# Development of *In Vivo* Raman Spectroscopy for the Diagnosis of Breast Cancer and Intra-Operative Margin Assessment

by

Abigail Susan Haka

A.B. Chemistry
Bryn Mawr College
(1998)

SUBMITTED TO THE HARVARD/MIT DIVISION OF
HEALTH SCIENCES AND TECHNOLOGY
IN PARTIAL FULFILLMENT OF THE REQUIREMENTS FOR THE DEGREE OF

**DOCTOR OF PHILOSOPHY IN CHEMISTRY AND MEDICAL PHYSICS**

at the

**Massachusetts Institute of Technology**

[February 2005]
January 2005





Signature of Author_____
Division of Health Sciences and Technology
January 5, 2005

Certified by_____
Michael S. Feld
Professor of Physics
Thesis Supervisor

Accepted by_____
Martha L. Gray
Co-Director of Health Sciences and Technology
Edward Hood Taplin Professor of Medical and Electrical Engineering
Professor of Electrical Engineering and Computer Science
Chairman, Departmental Committee on Graduate Students

# Development of *In Vivo* Raman Spectroscopy for the Diagnosis of Breast Cancer and Intra-Operative Margin Assessment

by

Abigail Susan Haka

Submitted to the Harvard/MIT Division of Health Sciences and Technology
on January 5, 2005 in Partial Fulfillment of the Requirements for the Degree of
Doctor of Philosophy in Medical Physics

## ABSTRACT

Breast cancer is the most commonly diagnosed cancer among women in the United States. It is the most common cause of death in women ages 45-55. Optical techniques can potentially play a diagnostic role in several aspects of breast cancer evaluation and treatment. This thesis outlines progress on the use of Raman spectroscopy to diagnose breast cancer. Laboratory studies on fresh-frozen tissues are used to demonstrate that the detailed information provided by Raman spectroscopy yields accurate breast disease diagnosis. A Raman spectroscopic-based diagnostic algorithm was developed which classifies samples into four categories according to specific pathological diagnoses: normal, fibrocystic change, fibroadenoma, and infiltrating carcinoma. Cancerous lesions were separated from non-cancerous tissues with a sensitivity of 94% and a specificity of 95%. Further, use of a spectral model based on the morphological structures that comprise breast tissue allows increased understanding of the relationship between a Raman spectrum and tissue disease state. Based on the excellent results of our laboratory work, two clinical studies were undertaken. These studies translate Raman spectroscopy from a laboratory technique into a clinically useful tool. The first study tests the diagnostic algorithm in a prospective manner on freshly excised tissue. Preliminary results are promising. The second study is the first demonstration of *in vivo* data acquisition of Raman spectra of breast tissue. The culmination of this research is the demonstration of accurate intra-operative margin status assessment during partial mastectomy surgeries. Application of our previously developed diagnostic algorithm resulted in perfect sensitivity and specificity in this small *in vivo* data set. These preliminary findings indicate that Raman spectroscopy has the potential to lessen the need for re-excision surgeries resulting from positive margins and thereby reduce the recurrence rate of breast cancer following partial mastectomy surgeries. The experiments and theory presented throughout this thesis demonstrate that Raman spectroscopy is a viable clinical tool that can be used to accurately diagnosis breast cancer and breast disease.

Thesis Supervisor: Michael S. Feld, Ph.D.
Title: Professor of Physics

## ACKNOWLEDGEMENTS

*"He who seeks knowledge begins with humbleness."*
-- Buju Banton

I would like to thank my parents, Cliff and Sue, for their continual guidance, support, and love. They have devoted so much time, effort and thought to my development. It is often overwhelming but always appreciated. I love you mom and dad. I am also grateful to Josh. He endures my times of stress and provides me with much needed perspective on life. I love you very much and I can't wait to begin our lives together (finally). I would like to give a shout out to Aaron, I don't know what I would have done without you during my time at MIT. From late nights in the lab to blowing off steam, Aaron was my partner in crime during graduate school.

I would also like to thank Michael Feld. Michael has devoted innumerable hours (I never knew meetings could be so long) to my scientific development and taught me to think critically about my research. He encouraged me to venture into areas of science where I was less comfortable and patiently helped me to succeed once I was there. For someone who always claims to not know what he is talking about, I have certainly learned a great deal from Michael. Ramachandra Dasari has been an invaluable resource and friend. Maryann Fitzmaurice has been a second advisor to me. She has provided guidance and assistance in all aspects of my research as well as valuable and thoughtful career advice. I am also appreciative to my entire committee for generously giving their time and expertise.

Karen Shafer-Peltier provided much of my early training in the laboratory and I am grateful for her patience and trust. Jason Motz was a close friend and colleague throughout my time at MIT. From anatomy, to lab gossip, to support and advice, we have been through a lot and I cannot thank him enough. Joe Gardecki was my go-to-guy in the lab and endured hours of venting. Thanks to Karen, Jason, Joe, Tae-Woong, Obrad, Zoya, Saumil, Wei and Fran for making 6-018 so much fun. Tae-Woong's dancing, Obrad's gyrations and impressions, and everyone's open minds and hearts make the Raman crew the best group to work with in the lab. Finally, I would like to thank the entire Spectroscopy Laboratory. As a result of our interactions, I have grown as a scientist in my time at MIT.

## TABLE OF CONTENTS

## LIST OF FIGURES

## LIST OF TABLES

## ABBREVIATIONS USED THROUGHOUT THE THESIS

**AGE:** Advanced Glycation End-Products
$\alpha$: Polarizability
**BSE**: Breast Self-Examination
**BRCA1**: BReast CAncer 1
**BRCA2**: BReast CAncer 2
**CBE**: Clinical Breast Examination
**CCD**: Charge Coupled Device
**CLS**: Classical Least Squares
**DCIS**: Ductal Carcinoma In Situ
**DEH**: Ductal Epithelial Hyperplasia
**DOT**: Diffuse Optical Tomography
**DNA**: Deoxyribonucleic Acid
**DRS**: Diffuse Reflectance Spectroscopy
**EEM**: Excitation-Emission Matrix
**FDA**: Food and Drug Administration
**FDG**: F-fluorodeoxyglucose
**FT**: Fourier Transform
**FWHM**: Full Width at Half Maximum
**H&E**: Hematoxylin and Eosin
**HDL**: High Density Lipoprotein
$I_0$: Intensity of the excitation laser [W-cm$^{-2}$]
**IDC**: Invasive Ductal Carcinoma
**IFS** Intrinsic Fluorescence Spectroscopy
**ILC**: Invasive Lobular Carcinoma
**IR**: Infrared
**KD**: Kilodalton
**LCIS**: Lobular Carcinoma In Situ
**LDL**: Low Density Lipoprotein
**LSS**: Light Scattering Spectroscopy
**MCR**: Multivariate Curve Resolution
**MRI**: Magnetic Resonance Imaging
$\nu_L$: Excitation laser frequency [s$^{-1}$]
**NA**: Numerical Aperture
**NAD(P)H**: Nicotinamide Adenine Dinucleotide (Phosphate)
**NIR**: Near-Infrared
**NMBA:** N-nitrosomethylbenzylamine
**OCT**: Optical Coherence Tomography
**OLS**: Ordinary Least Squares
**OR**: Operating Room
**ORO**: Oil Red O
**OxLDL**: Oxidized Low Density Lipoprotein
**P**: Dipole Moment
**PBS**: Phosphate Buffered Saline
**PC**: Principal Component
**PCA**: Principal Component Analysis
**PCR**: Principal Component Regression
**PET**: Positron Emission Tomography
**PLS**: Partial Least-Squares
**PUFA**: Polyunsaturated Fatty Acid
**Q**: Normal coordinate of the vibration
**RMSEP**: Root Mean Standard Error of Prediction
**ROC:** Receiver Operator Characteristic
**Std:** Standard Deviation
**SERM:** Selective Estrogen Receptor Modulator
**SERS**: Surface Enhanced Raman Scattering
**SNR**: Signal-to-Noise Ratio
**SVD**: Singular Value Decomposition
**T**: temperature (K)
**t**: Time [s]
**TMS**: Tri-Modal Spectroscopy
**UV**: Ultraviolet
**VLDL**: Very Low Density Lipoprotein

# Chapter I. Introduction

The work in this thesis develops analytical Raman spectroscopy into a tool for the diagnosis of breast cancer. Laboratory studies on fresh-frozen tissues are used to demonstrate that the detailed information provided by Raman spectroscopy yields accurate breast disease diagnosis. Further, use of a spectral model based on the morphological structures that comprise breast tissue allows increased understanding of the relationship between a Raman spectrum and tissue disease state. Based on the excellent results of our laboratory work, two clinical studies were undertaken. These studies translate Raman spectroscopy from a laboratory technique into a clinically useful tool. The first study tests the diagnostic algorithm in a prospective manner on freshly excised tissue. Preliminary results are promising. In the second study, data was acquired *in vivo* during partial mastectomy surgeries. This is the first demonstration of *in vivo* collection of Raman spectra of breast tissue. These advances culminated in an approach that was employed intra-operatively during partial mastectomy surgeries to accurately assess margin status.

## *I. A. Objectives*

**Develop a Spectral Model for Diagnosing Breast Disease**

Statistical interpretations of the Raman spectra acquired from biological tissue can diagnose disease. Indeed, previous investigations using principal component analysis demonstrated that Raman spectroscopy is capable of accurately diagnosing breast cancer. Although it is possible to use statistical methods of analysis to provide diagnoses, there is a wealth of information in Raman spectra that enables enhanced understanding of disease etiology. One goal of this research is the development of a spectroscopic model based on tissue morphology. We utilize confocal Raman microscopy to examine the various morphological structures present in normal and diseased breast tissues. Our model identifies the morphological components present in breast tissue through their unique Raman spectra and uses them as basis spectra to describe the morphology of macroscopic data. Such a model translates spectroscopic analysis into terminology commonly used by pathologists and can be used to diagnose breast cancer.

**Derive of an Analytical Method of Estimating Chemometric Prediction Error**

Another aim of the research is the derivation and validation of an analytical formula that estimates the uncertainty in concentrations predicted by our spectral model. In biological samples, such as tissue, obtaining reference concentrations to assess measurement error is not straightforward. The ability to make predictions concerning the concentration error is valuable to the process of developing and refining analytical measurements.

**Develop an Algorithm for Breast Cancer Diagnosis Using our Spectral Model**

Development of an algorithm to diagnose breast cancer is a central objective of this thesis.

We employ our spectral model to diagnose normal, benign and malignant lesions in specimens of fresh-frozen human breast tissue, based on their morphological compositions.

**Assess the Diagnostic Importance of Microcalcifications**

In our *ex vivo* studies, we see relatively little contribution from the two types of calcifications found in breast tissue and included in our spectral model, calcium hydroxyapatite and calcium oxalate dihydrate. Due to their diagnostic importance, microcalcifications in fresh breast tissue are not typically made available for scientific research and thus our studies did not include lesions containing microcalcifications. For this reason, we investigate the diagnostic power of Raman microscopy of microcalcifications in thin sections of deparaffinized fixed breast tissue. Results can be coupled with the diagnostic algorithm developed using fresh-frozen tissues to create a powerful new tool for the diagnosis of benign and malignant breast lesions.

**Prospective Validation of the Diagnostic Algorithm**

The main goal of this study is to validate our diagnostic algorithm developed on fresh-frozen tissues with a large data set that closely mimics an *in vivo* environment. In this work, we utilize freshly excised tissues. Further, we aim to elucidate differences between the Raman spectra of fresh-frozen and fresh breast tissues. Additional goals include expanding our diagnostic algorithm to include pathologies not seen in our *ex vivo* laboratory data and incorporating microcalcifications into our diagnostic scheme.

**Demonstrate *In Vivo* Application of Raman Spectroscopy to Breast Cancer Diagnosis**

Ultimately, this thesis culminates in the translation of Raman spectroscopy from a laboratory technique to a clinical tool. To collect the first *in vivo* Raman spectra of breast tissue, we employ our Raman optical fiber probe to acquire data from patients undergoing partial mastectomy procedures. This study serves to demonstrate the feasibility of *in vivo* Raman spectroscopy for the diagnosis of breast cancer.

## *I. B. Accomplishments*

The experiments and theory presented throughout this thesis demonstrate that Raman spectroscopy can be used to accurately diagnosis breast cancer and breast disease. Furthermore, we have demonstrated extension of the technique to *in vivo* clinical applications with excellent results. We have developed a spectral model based on the major morphological structures in breast tissue, including epithelial cell cytoplasm, the cell nucleus, fat, β-carotene, collagen, calcium hydroxyapatite, calcium oxalate dihydrate, cholesterol-like lipid deposits and water. A diagnostic algorithm, which utilizes this spectral model, was developed in the laboratory with samples of fresh-frozen breast tissue. This diagnostic algorithm, which encompasses all data and classifies samples according to specific pathological diagnoses, results in high sensitivity and specificity.

Based on the excellent results of these laboratory studies, we sought to employ Raman spectroscopy clinically. Studies were undertaken to validate our algorithm on a large data set of freshly excised tissue as well as demonstrate *in vivo* data acquisition. Preliminary results in which the diagnostic algorithm is used in a prospective manner to examine fresh tissue are encouraging, although further data analysis is necessary. This thesis culminates in a demonstration of *in vivo* data acquisition during partial mastectomy surgeries. The study

was the first *in vivo* acquisition of Raman spectra of breast tissue and thus extends the technique from a laboratory to a clinical setting. Further, using our diagnostic algorithm developed on *ex vivo* tissues, we were able to accurately provide intra-operative margin assessment. The work demonstrates that Raman spectroscopy can be used for real-time breast cancer diagnosis in a clinical setting.

## *I. C. Outline*

The goals and accomplishments of this thesis are further elucidated as follows:

**Chapter II. Breast Cancer**

Raman spectroscopy can potentially play a diagnostic role in several aspects of breast cancer evaluation and treatment. Research to develop new diagnostic modalities must be grounded in knowledge of both the disease progression and current medical practices. Only with this information as a basis can diagnostic schemes be created that provide relevant information and are easily incorporated into clinical practice. This chapter details fundamentals of breast cancer. Anatomy and pathology of the breast are discussed, along with a critique of the current methods used for disease diagnosis.

**Chapter III. Raman Spectroscopy**

The Raman effect and its application to biomedical spectroscopy are presented along with the previous work that has been accomplished in this field. Competing research technologies for breast cancer diagnosis are also discussed. The experimental instrumentation used throughout this research is presented.

## Chapter IV. Data Processing

This chapter presents approaches that we use to analyze Raman spectra. The motivation for the development of a Raman spectroscopic morphological model is explained. Techniques for the development of this model and its application to disease diagnosis are described. In addition, an analytical formula that estimates the uncertainty in concentrations predicted by our spectral model is derived and validated. By understanding the sources of prediction error, efforts can be made to reduce it scientifically. Further analytic methods for calculating the concentration error allow smart experimental design to detect moieties of interest with the appropriate accuracy.

## Chapter V. Raman Spectroscopic Breast Cancer Diagnosis: *Ex Vivo* Studies

We employ Raman spectroscopy to diagnose normal, benign and malignant lesions in specimens of human breast tissue, based on their morphological compositions. The morphologic makeup of the tissue is determined through the application of our spectral model. A diagnostic algorithm is presented that was developed in the laboratory with samples of fresh-frozen human breast tissue. The diagnostic algorithm, which encompasses all data and classifies samples according to specific pathological diagnoses, is used to identify those lesions that would need to be excised. This algorithm results in a positive predictive value of 85% and a negative predictive value of 100%, indicating that no malignant lesions in our data set are left unexcised. The excellent results of this study thus supported moving the technique to a clinical setting for further testing of its efficacy in breast cancer diagnosis. Preliminary results in which the diagnostic algorithm is used in a prospective manner to examine fresh tissue are also presented.

## Chapter VI. Raman Microscopy of Microcalcifications

In our *ex vivo* studies, we see relatively little contribution from the two types of calcifications found in breast tissue and included in our spectral model, calcium hydroxyapatite and calcium oxalate dehydrate. Microcalcifications are a feature of particular diagnostic significance on a mammogram. However, due to their diagnostic importance, microcalcifications in fresh breast tissue are not typically made available for scientific research and thus our studies did not include lesions containing them. For this reason, we have investigated the diagnostic power of Raman microscopy of microcalcifications in thin sections of deparaffinized fixed breast tissue. We were able to distinguish microcalcifications occurring in benign and malignant ducts with a sensitivity of 88% and a specificity of 93%. This is a significant improvement over current X-ray mammography techniques which are unable to reliably differentiate microcalcifications in benign and malignant lesions.

## Chapter VII. Raman Spectroscopic Breast Cancer Diagnosis: *In Vivo* Studies

The final objective of this thesis, the *in vivo* application of Raman spectroscopy for diagnosing breast cancer, is described in this chapter. The culmination of this work is the demonstration of accurate intra-operative margin status assessment. Application of our previously developed diagnostic algorithm resulted in perfect sensitivity and specificity in this small data set. Significantly, we detected a grossly invisible cancer that, upon pathological review, required the patient to undergo a second surgical procedure. Had Raman spectroscopy been employed in a real-time fashion during the procedure, the additional re-excision surgery would have been avoided. These preliminary findings indicate that Raman spectroscopy has the potential to lessen the need for re-excision surgeries

resulting from positive margins and thereby reduce the recurrence rate of breast cancer following partial mastectomy surgeries.

## Chapter VIII. Other Applications of Raman and Fluorescence Spectroscopies

Although there are many advantages to Raman spectroscopy, other optical techniques may also play a role in breast cancer diagnosis. Preliminary investigations have examined the diagnostic potential of fluorescence and reflectance spectroscopies. Studies have also been conducted using spectroscopic techniques that have only recently been applied to tissue, such as surface enhanced Raman spectroscopy and fluorescence lifetime measurements. Finally, Raman and fluorescence spectroscopies are used in a synergistic manner to elucidate the mechanism of ceroid formation *in situ*. Ceroid is an insoluble lipid-protein complex characteristic of atherosclerotic plaques. The mechanism of ceroid formation has been extensively studied but despite intensive research, ceroid is only defined empirically through its fluorescence properties and its behavior during various staining processes. The synergy of these two types of spectroscopy allows for the identification of ceroid *via* its fluorescence signature and the subsequent elucidation of its chemical composition through the acquisition of a Raman spectrum. A better understanding of the mechanism of ceroid formation may suggest avenues to induce regression or prevent progression of atherosclerotic plaques with medical therapy

## Chapter IX. Future Directions

Future directions, comprised of both clinical and basic studies, are presented. With the successful demonstration of *in vivo* Raman spectroscopy for breast cancer diagnosis, there are many clinical applications that can be addressed. Clinical studies to further investigate

the role of Raman spectroscopy for intra-operative margin assessment are discussed. Also, development of a side-looking optical fiber Raman probe for transdermal needle measurements is detailed. Basic research will focus on quantitative analysis and spectral model refinement. Our current spectral model only provides relatively quantitative data and does not utilize the intensity information contained within the spectra. Studies to incorporate intensity information into our diagnostic schemes and to extract quantitative morphological information are presented. These studies simultaneously provide a basis for model refinement as well as insight into the lower detection limits of the approach. Finally, approaches to combining Raman spectroscopy with fluorescence and reflectance data are presented. The combination of these spectroscopic modalities may provide an even more powerful tool for guiding patient care.

# Chapter II. Breast Cancer

Breast cancer is the most common female cancer in the United States, the second most common cause of cancer death in women (after lung cancer), and the main cause of death in women ages 45 to 55 [Jemal *et al.* 2004]. Optical techniques can potentially play a diagnostic role in several aspects of breast cancer evaluation and treatment. Numerous spectroscopic modalities are currently under investigation for this purpose. This thesis outlines progress on the use of Raman spectroscopy to diagnose breast cancer. Research to develop new diagnostic modalities must be grounded in knowledge of both the disease progression and current medical practices. Only with this information as a basis, can diagnostic schemes be created that provide relevant information and are easily incorporated into a clinical setting. This chapter details fundamentals of breast cancer. Both breast anatomy and pathology are described, thereby providing a framework for interpretation of spectroscopic data. To astutely apply spectroscopy to breast cancer diagnosis, an extensive understanding of breast pathology and the morphologic changes associated with each disease is imperative. Also summarized in this chapter are current diagnostic strategies for breast cancer as well as breast cancer staging, prognosis, and treatment. With knowledge of the current biopsy and surgical approaches, areas where spectroscopic modalities can play beneficial roles in breast cancer diagnosis and treatment are evident. As spectroscopic techniques move into the clinic, a through understanding of surgical procedures also allows smart study designs that utilize existing procedures. Further, tissue changes induced by therapy and the effect this will have on spectroscopic data must be considered. Knowledge of the strengths and limitations of breast cancer diagnosis and treatment is key for developing new diagnostic modalities.

## *II. A. Breast Anatomy*

The mature breast serves as a secretory, milk producing, gland [Cotran *et al.* 1999]. Breast tissue extends from below the collarbone to the level of the sixth or seventh rib, and from the breastbone to the axilla. In the center of the breast are the nipple and areola. Fibrous connective tissue, called fascia, lies between the breast tissue and the skin, and separates breast tissue from the chest muscles. Cooper's ligaments, made of elastin, run from the deep fascia throughout the breast tissue and attach to the dermis providing a supportive network for the breast. Figure II.1 shows a schematic of the female breast. The internal mammary, axillary, and intercostal arteries supply the breasts with blood; and the internal mammary, axillary, and intercostal veins carry blood away from the breasts. The surface veins of the breast encircle the nipple and carry blood to the internal mammary, axillary, and intercostal veins, and to the lungs. Breast cancer cells can travel to the lungs via surface veins and form metastatic tumors. The intercostal veins join a complex network of vertebral veins in and around the spine, providing a path for breast cancer cells to spread to bone tissue. Most lymphatic vessels in the breast drain into a network of lymph nodes located around the breast's edges, in the underarm, and near the collarbone. Axillary lymph nodes are often the first site of breast cancer metastasis. The skin of the upper breast is innervated by nerves that branch from a network of nerves in

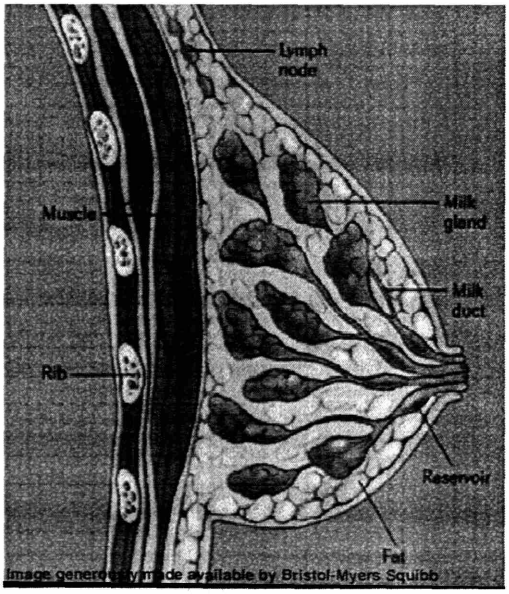


**Figure II.1.** Schematic of the female breast.

the neck. The long thoracic nerve innervates the muscle that helps move the upper arm. Surgeons must be careful not to sever or injure this nerve when operating near underarm lymph nodes. Chest muscles located under the breasts include the major and minor pectorals, the serratus magnus and the rectus abdominus. Some mastectomy procedures, excision of the entire breast, involve removing the fascia overlying the chest muscles, while others involve removing the muscles themselves.

### II. A. 1. Normal Breast Tissue

The breast itself is composed of three types of tissue; adipose, fibrous, and glandular. A microscopic image of a thin section of normal breast tissue stained with hematoxylin and eosin (H&E) is shown in Figure II.2a. The three tissue types comprising normal breast can be visualized in this image. In the histopathological diagnosis routine, tissue is fixed, sectioned, stained, visually examined by a pathologist and evaluated for abnormalities [Burkitt *et al.* 1996]. H&E is applied to tissues fixed in formalin or alcohol and is the most commonly used technique in routine pathology. The basic dye, hematoxylin, stains acidic structures a purplish blue. Nuclei, ribosomes and the rough endoplasmic reticulum have a strong affinity for this dye owing to their high DNA and RNA content, respectively. In contrast, eosin is an acidic dye that stains basic structures red or pink. Most cytoplasmic proteins are basic and hence the cytoplasm usually stains pink or pinkish red. Fibrous tissue is also composed of basic proteins and thus stains pink, as can be seen in Figure II.2a. Also seen in the image, are the purplish appearing ducts and lobules that are lined with glandular epithelium. Epithelium is membranous tissue composed of one or more layers of cells separated by very little intercellular substance. It forms the covering of most internal and

external surfaces of the body and its organs. The epithelium appears purple due to the abundance of cell nuclei. Adipose tissue can be visualized as clear spaces in Figure II.2a because fat is washed away during the tissue processing.

The primary composition of normal breast is fatty tissue interspersed with fibrous or connective tissue. Together, these two types of tissue make up the stroma, or tissue lying between the glands. The fatty tissue contains cells, called adipocytes, which harbor copious amounts of cytoplasmic fat. The fibrous tissue is mainly composed of collagen and small amounts of glycosaminoglycans. The stroma also contains fibroblasts and blood vessels [Sternberg, 1997]. Fibroblasts are stellate or spindle-shaped cells capable of producing connective tissue by forming collagen fibers. The glandular tissue is comprised of several lobes or milk glands connected to a conduit of ducts that carry milk to the nipples. Each lobe is autonomous and empties into its own excretory duct. The lobes themselves are divided into smaller units called lobules, which in turn are made up of acini. The lobules are the functional, milk producing, units of the mammary parenchyma. The lobular units and the ducts that connect them are separated from the stroma by a basement membrane, primarily composed of collagen. Figure II.2b depicts the high magnification appearance of a normal breast acinus. In the image, a low, flattened layer of contractile cells, some slightly vacuolated, can be identified beneath the more prominent lining epithelium. Indeed, the larger ducts in the breast consist of a double layer of cuboidal cells, an inner layer of epithelial cells surrounded by a layer of myoepithelial cells. The myoepithelial cells are smooth muscle like cells found in between the epithelium and the basement membrane. They contain myofilaments, are flatter than epithelial cells and are oriented parallel to the

long axis of the duct, enabling them to control the transport of milk. As the ducts become smaller, they are reduced to a single layer of epithelial cells.

### II. A. 2. Menstrual Cycle, Pregnancy and Menopause

The breast undergoes significant changes in response to hormonal influences, such as during the menstrual cycle, pregnancy, and menopause [Cotran *et al.* 1999]. In the first half of the menstrual cycle, the lobules are relatively quiescent. After ovulation, under the influence of estrogen and rising progesterone levels, cell proliferation increases as does the number of acini per lobule. When menstruation occurs, the fall in estrogen and progesterone levels is followed by apoptosis, a form of programmed epithelial cell death. It is only with the onset of pregnancy that the breast assumes its complete morphologic maturation and functional activity. During pregnancy, the female breast undergoes lobular hypertrophy, resulting in dense clusters of epithelial cells, so that following birth lactation can occur. As such, there is a reversal of the usual stromal-epithelial relationship so that by the end of the pregnancy the breast is composed almost entirely of lobules. The breast, which histologically is a modified sweat gland, secretes milk by budding off portions of cell cytoplasm. The epithelial cells lining the lumen in Figure II.2b demonstrate apocrine secretion with snouting, or cytoplasmic extrusions, into the lumen. About 15 to 20 ducts come together near the areola to form reservoirs of milk to be drawn from the nipple. After cessation of lactation, the lobules regress and atrophy, and the total breast size diminishes remarkably. Female breast also undergoes substantial biochemical alterations at menopause. The ducts and lobules atrophy with concurrent shrinkage of the stroma and a large amount of collagen is replaced by fat. The lobular acini and stroma may almost disappear in the very aged, leaving only ducts to

create a morphologic pattern that resembles that of the male breast. Males have a small amount of breast tissue, but it consists of just a few ducts, without lobules, in a fibrous stroma.

## *II. B. Breast Pathology*

### II. B. 1. Benign Breast Lesions

Fibrocystic changes account for the majority of "breast lumps" that are found in women of reproductive years, particularly between age 30 and menopause [Cotran *et al.*, 1999]. Table II.1 displays the typical distribution of findings in women seeking evaluation of breast lumps, an important consideration when developing a diagnostic modality. Fibrocystic change is a benign condition which can manifest itself as fibrosis (formation of fibrous tissue), adenosis (increase in the number of ductules) or cyst formation (dilation of ducts and lobules with semi-transparent fluid). Each of these changes can occur with or without the presence of others. Figure II.2c depicts the histologic appearance of fibrocystic changes in the breast. Cystically dilated ducts lined by a single layer of epithelial cells can be seen. There are also areas of lobules that are laced with abundant fibrous connective tissue (sclerosing adenosis), and stromal fibrosis. Additionally, there is a small area of microcalcification, highlighted with an arrow. Microcalcifications form as a result of either calcified secretory material or necrotic debris. No atypical changes are seen in Figure II.2c.

| | |
|---|---|
| **No Disease** | **30%** |
| **Benign** | **60%** |
| Fibrocystic Change | 40% |
| Miscellaneous Benign | 13% |
| Fibroadenoma | 7% |
| **Cancer** | **10%** |

**Table II.1.** Distribution of the findings in women seeking evaluation of breast lumps.

Atypia refers to abnormality of a cell, which may or may not be associated with later malignancy.

Fibroadenoma, illustrated in Figure II.2d, is the most common benign tumor of the human female breast. Its growth is induced by estrogen and often stimulated by lactation and pregnancy. Most cases of fibroadenoma arise in younger women. Because of the lack of estrogen after menopause, regression occurs which can result in mucoid degeneration, hyalinization, involution of the epithelial component and calcification. On physical examination, the mass feels firm because of proliferative fibrous stroma and its glandular composition. The tumor is relatively mobile because it does not induce peripheral fibroblast proliferation, and is rarely tender and painful. To the right in Figure II.2d, compressed breast connective tissue forming a "capsule" to the mass can be seen. The tumor itself is composed of a fibroblastic stroma that contains elongated compressed ducts lined by benign appearing epithelium. Lesions diagnosed as fibroadenoma show an accumulation of collagen due to fibroblast proliferation which results in expansion of the stroma. Thus, although fibroadenoma is a benign lesion, it often grows rapidly resulting in significant morbidity, and thus is typically excised [Khan *et al.* 2001]. Fibroadenoma is most closely related to phylloides tumors, the malignant counterpart of which is not carcinoma but cystosarcoma phylloides, in which the stroma rather than the epithelium is malignant.

Intraductal papilloma, a benign epithelial tumor projecting from the ductal surface, is often associated with a serous or bloody nipple discharge. In Figure II.2e, a small intraductal papilloma appears in a breast duct. They are typically in one of the main lactiferous ducts beneath the areola and thus may cause some nipple retraction. Figure II.2e demonstrates a

fine pink collagenous stroma within the papilloma and epithelial cells that do not show atypia.

Fat necrosis of the breast is a less prevalent benign pathology descriptive of focal areas of fat destruction. The most common etiology is trauma but fat necrosis can also occur with surgery and radiation therapy. It can be a localized, firm area with scarring that may mimic a breast carcinoma. Microscopically, fat necrosis consists of irregular steatocytes with no peripheral nuclei and intervening pink amorphous necrotic material. Steatosis refers to abnormal accumulation of triglycerides within a parenchymal cell, in this case the adipocyte. Inflammatory cells, including foreign body giant cells, responding to the necrotic fat cells are also present. A foreign body giant cell is a very large cell, containing several nuclei and formed by the fusion of multiple macrophages. Macrophages are large, phagocytic cells that engulf dead and dying cells as well as antigens that enter the body. Figure II.2f shows fat necrosis at high magnification. Some lipid-laden macrophages can be seen between the necrotic adipose tissue cells.

Ductal epithelial hyperplasia (DEH), shown in Figure II.2g, is a pathology characterized by intraductal proliferation of epithelial cells. In DEH, the epithelial cells encroach into the duct lumen, producing solid masses, whereas in sclerosing adenosis, also characterized by epithelial cell proliferation, the epithelial cells continue to form well-defined glandular units despite somewhat distorted cells. Epithelial hyperplasia is defined by an increase in the layers of cells and may be due to increased proliferation or, more likely, failure of cells to undergo apoptosis. Here it is florid and occurs in the setting of fibrocystic change. DEH confers a slightly increased risk, 1.5 to 2 times normal, for breast carcinoma [Page *et al.* 1990]. Figure II.2h shows atypical DEH of the breast. Atypical DEH is

recognized by its histologic resemblance to ductal carcinoma *in situ*. However, the lesions are characteristically limited in extent, and the cells are not completely monomorphic in type or fail to completely fill ductal spaces. Monomorphic refers to cells that have the same phenotype. This occurs in tumors as the neoplastic cells often arise from a single progenitor cancerous cell. In breasts with invasive cancer, multiple independent atypical clones may be present, suggesting that this is a multicentric process and that only a minority of these lesions progress to malignancy [Cotran *et al.* 1999]. However, a significantly increased risk, 5 times normal, for breast carcinoma occurs with cytologically atypical epithelial hyperplasia [Page *et al.* 1990].

Like the female breast, the male breast is subject to hormonal influences which can cause gynecomastia, a benign condition characterized by enlargement of the male breast. It is estimated that 15% of men have gynecomastia [Cotran *et al.* 1999]. It can be characterized by DEH or prominent periductular edema and may be unilateral or bilateral. Gynecomastia results from an imbalance between estrogens, which stimulate breast tissue, and androgens, which counteract these effects. It can occur at puberty or with aging. Gynecomastia may also occur as a result of cirrhosis of liver, Leydig cell tumors of the testis, or drugs.

### II. B. 2. Breast Cancer

The incidence of breast carcinoma increases with age, with 85% of cases arising in women older than 30 years. The largest proportion of cases, 50% of breast carcinomas, occur in the upper outer quadrant of the breast. Most breast cancer develops in glandular tissue, epithelium, and is classified as adenocarcinoma. Cancer is characterized by abnormal cell proliferation as well as abnormal maturation of cells. Genetic mutations often override the

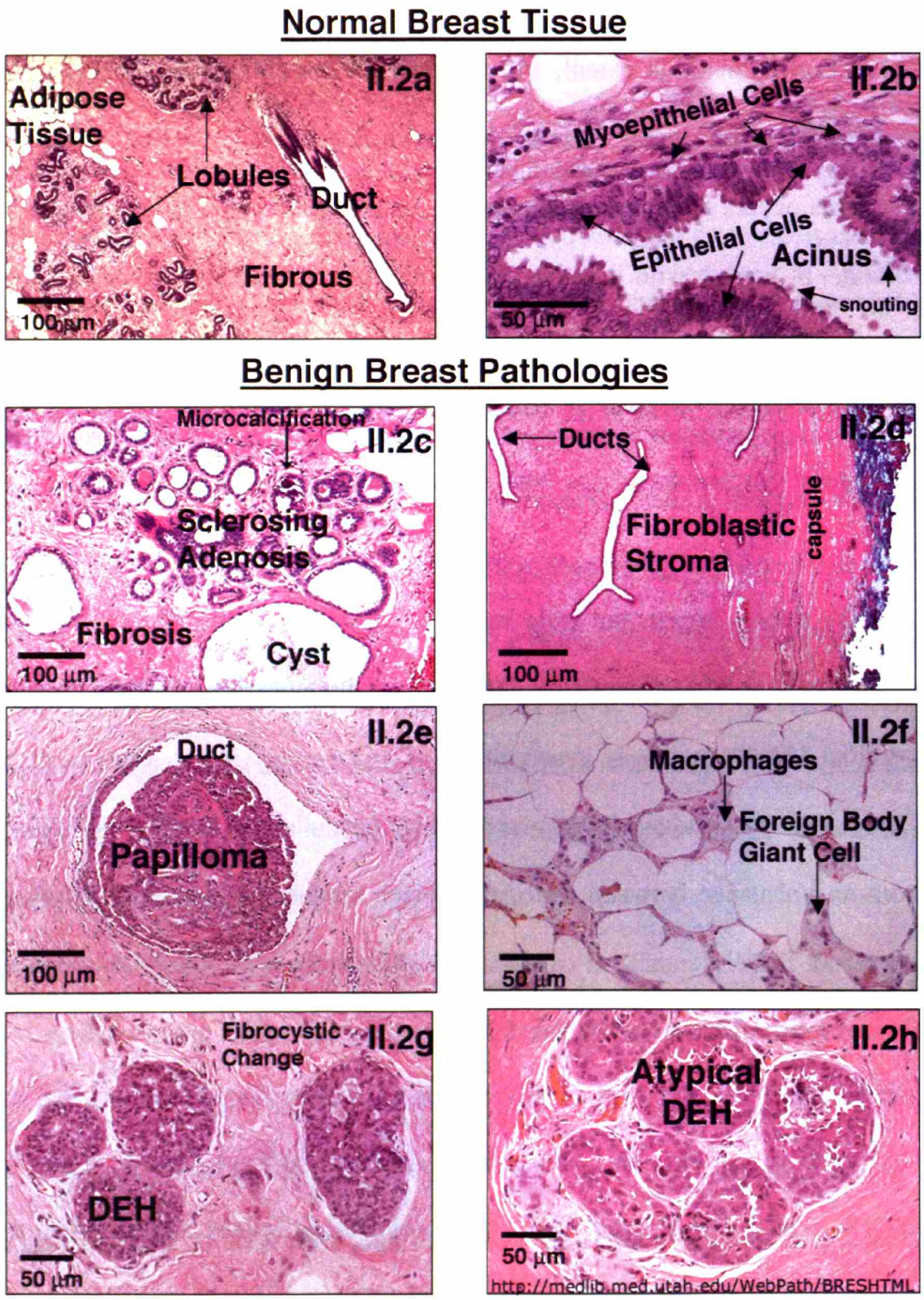


**Figure II.2.** H&E images of a-b) normal and c-h) benign tissues.

normal cell signaling system allowing cellular proliferation and growth to occur in the absence of any external stimulus. Thus, unlike normal cells, malignant cells do not stop reproducing after they have doubled 50 or 60 times. They may also become more resistant to

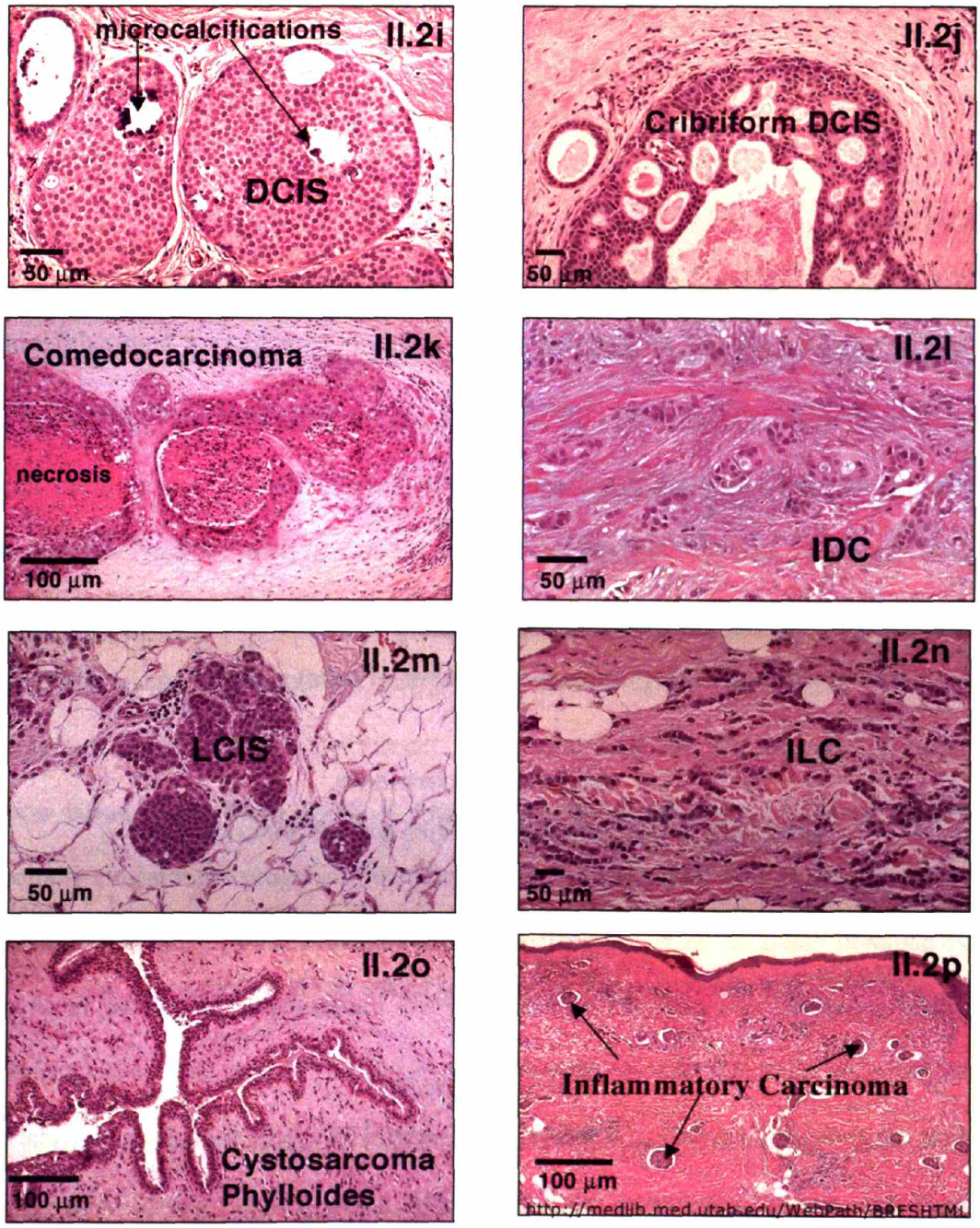


**Figure II.2.** i-p) H&E image of malignant breast tissues.

apoptosis than normal cells, thereby ultimately forming a monomorphic tumor that is made up of billions of copies of the original cancerous cell. A schematic illustrating the start of this process is shown in Figure II.3. Differentiation, a feature of normal tissue growth, refers

to the maturation of cells into a form adapted to a specific function. Thus, a fully mature cell of any particular cell line is described as highly differentiated, whereas stem cells are relatively undifferentiated. Cancerous cells exhibit variable states of differentiation and often fail to achieve a highly differentiated state. Poorly differentiated cancers typically confer a worse prognosis. In general, the cells of benign lesions are well differentiated. A simple flowchart detailing the breast cancer "continuum" is shown in Figure II.4.

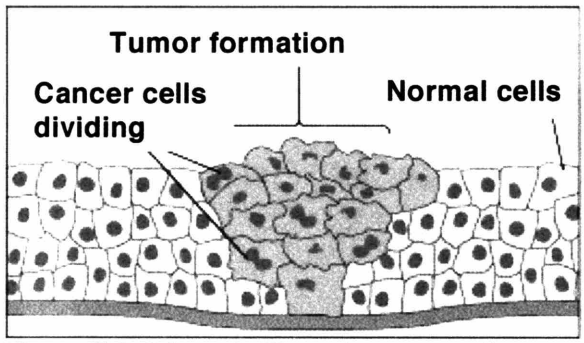


**Figure II.3.** Schematic illustrating uncontrolled neoplastic cell growth and monomorphic expansion.

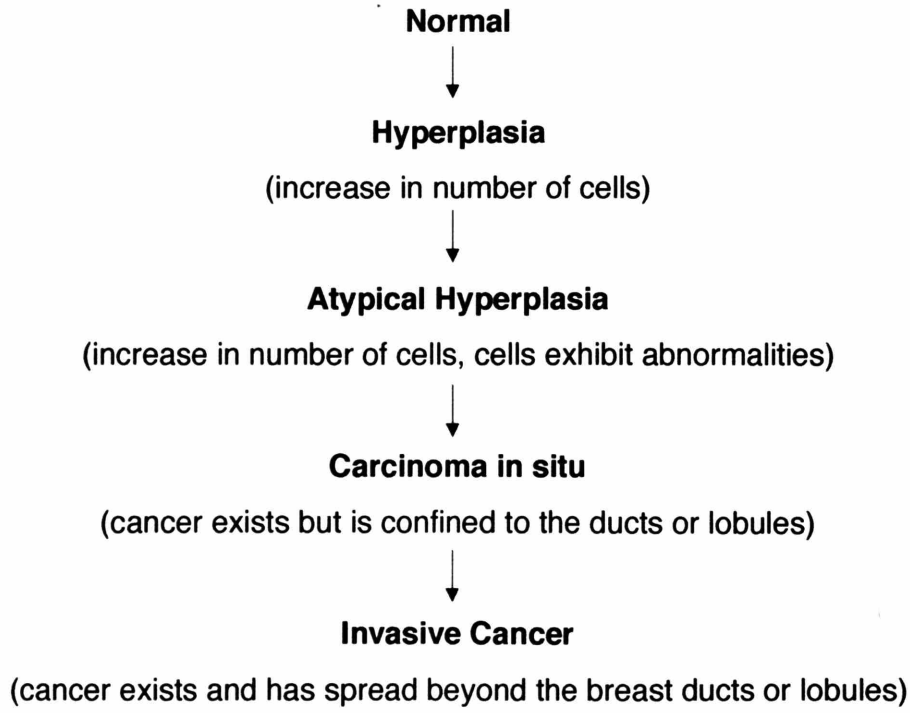


**Figure II.4.** Flowchart describing the breast cancer 'continuum'.

The earliest form of breast cancer, ductal carcinoma in situ (DCIS), develops solely in the milk ducts. Figure II.2i is a high power microscopic view demonstrating DCIS. Malignant cells are still within the ductules and have not broken through the basement membrane and into the stroma. The two large lobules in the center contain microcalcifications. The classic cribriform pattern of DCIS of the breast, shown in Figure II.2j, is characterized by holes with sharp margins as though punched out by a cookie cutter. The neoplastic epithelial cells within the duct show minimal hyperchromatism and pleomorphism. Hyperchromatism is an increase in the chromatin content in the cell nucleus. It can be visualized as an increased staining capacity of the cell nuclei for hematoxylin. Pleomorphism refers to cells of the same species which occur in more than one morphological form, in other words cells which have a variety of shapes and sizes. Hyperchromatism, pleomophism, atypical mitoses, DNA aneuploidy and nuclear enlargement are all hallmarks of cancer. However, they are not observed in this tissue section because cribriform DCIS is typically a low grade lesion. Tumor grade is an important indicator of prognosis, with low grade cancers behaving less aggressively than high grade tumors. Comedocarcinoma, shown in Figure II.2k, is a less common type of intraductal carcinoma characterized by the presence of rapidly proliferating, high grade malignant cells. The cells in the center of ducts with comedocarcinoma are often necrotic and calcify, as can be seen in Figure II.2k. This central necrosis leads to the gross characteristic of extrusion of cheesy material from the ducts with pressure, comedone-like. Comedocarcinoma is much more likely to exhibit hyperchromatism, pleomorphism, atypical mitoses, DNA aneuploidy and nuclear enlargement than cribriform DCIS due to its high grade.

The most common type of breast cancer, invasive ductal carcinoma (IDC), develops from DCIS, spreads through the duct walls, and invades the breast tissue. Lesions diagnosed as infiltrating carcinoma exhibit increases in cellularity and often increases in collagen due to fibroblast proliferation in response to stromal invasion by the malignant epithelial cells. IDC arises from breast ducts and accounts for 70-80% of cases of breast cancer [Cotran *et al.* 1999]. The IDC of the breast, shown in Figure II.2l, is poorly differentiated with very pleomorphic cells.

Lobular carcinoma in situ (LCIS) consists of neoplastic proliferation in the terminal breast ducts and acini. The cells are small and round. LCIS is seen in Figure II.2m. Though these lesions are low grade, they confer a 30% risk for development of invasive carcinoma in the same or the opposite breast [Cotran *et al.* 1999]. Invasive lobular carcinoma (ILC) accounts for 5-15% of invasive breast cancers. ILC of the breast is shown in Figure II.2n. There is roughly a 20% chance that the opposite breast will also be involved, and many ILCs arise multicentrically in the same breast. ILCs often have a diffusely invasive pattern causing tumors to be difficult to detect by either physical examination or mammography.

There are several less common types of breast cancer. A phyllodes tumor of the breast, the malignant counterpart to fibroadenoma, is shown in Figure II.2o. They arise from interlobular stroma, but unlike fibroadenomas are not common and are much larger. They are low-grade neoplasms which are more cellular than fibroadenomas but rarely metastasize. From the Greek word phyllodes, meaning leaf-like, these tumors are characterized by projections of stroma into the ducts which create a leaf-like pattern. Inflammatory carcinoma, shown in Figure II.2p, tends to spread quickly. It is characterized by breast tissue that is warm and appears red. The hallmark of inflammatory carcinoma can be seen in the

skin overlying the breast which has prominent lymphatic spaces filled with small metastases from breast carcinoma. Medullary carcinoma originates in central breast tissue. Interestingly, it has a slightly better prognosis than do most carcinomas, despite the almost universal presence of poor prognostic factors. Mucinous carcinoma, also called colloid carcinoma, is a rare type of invasive cancer that usually occurs in postmenopausal women. It arises from mucin producing cells and tends to grow slowly. Mucinous carcinoma is characterized by abundant extracellular mucin surrounding nests of carcinoma cells. Paget's disease of the nipple originates in the milk ducts and spreads to the skin of the nipples or areola. Table II.2 shows

| Histologic Type | Total Cancers |
|---|---|
| ***In Situ* Carcinoma** | **15%-30%** |
| Ductal carcinoma *in situ* | 80% |
| Lobular carcinoma *in situ* | 20% |
| **Invasive Carcinoma** | **70%-85%** |
| Ductal carcinoma | 79% |
| Lobular carcinoma | 10% |
| Tubular/cribriform carcinoma | 6% |
| Mucinous carcinoma | 2% |
| Medullary carcinoma | 2% |
| Papillary carcinoma | 1% |

**Table II.2.** Frequency of histologic types of breast cancer.

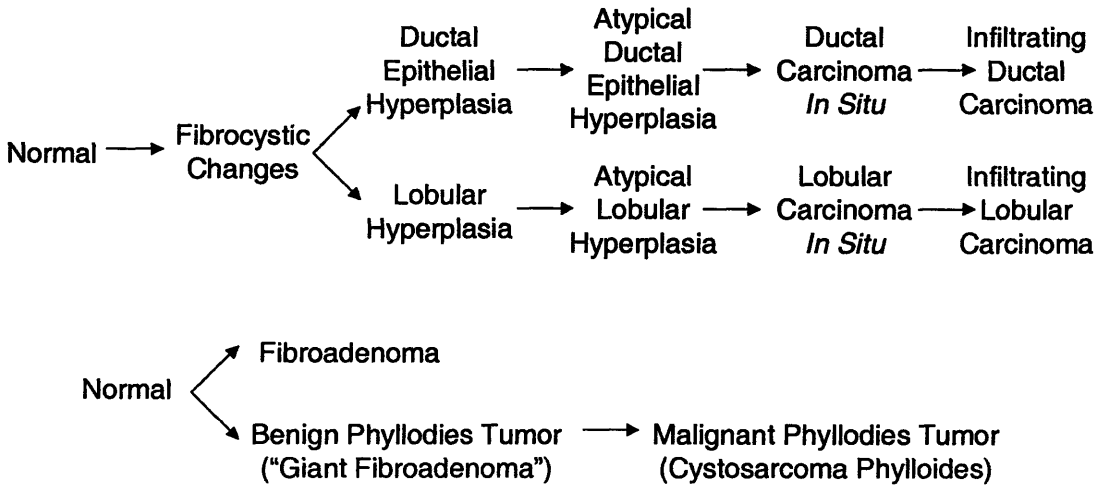


**Figure II.5.** Flowchart depicting the relationship between the breast lesions encountered in our studies.

the distribution of the histologic types of breast cancer. Tubular carcinoma is a small tumor that is often undetectable by palpation. It is a well differentiated form of invasive breast carcinoma and is usually associated with foci of DCIS. Tubular carcinomas are almost always less than 2 cm in greatest dimension. Sarcomas, cancer of the connective tissue, and lymphomas, cancer of the lymph tissue, rarely develop in the breasts. Figure II.5 shows a flowchart depicting the relationship of breast lesions encountered in our studies.

Although the majority of breast cancers are confined to women, carcinoma in the male breast does arise. It is a rare occurrence, with a frequency ratio to breast cancer in the female of less than 1:100. The dearth of glandular tissue in the male breast is a significant reason for the rarity of male breast cancer. However, the scant amount of breast tissue in men also results in malignant neoplasms that rapidly infiltrate to become attached to the overlying skin and underlying thoracic wall. Metastasis follows the same pattern as in women, and axillary lymph node involvement is present in about half of the cases of male breast cancer at the time of lesion discovery. Although men present at higher stages, when they are matched by stage, prognosis is similar in men and women [Cotran *et al.* 1999].

## *II. C. Breast Cancer Risk Factors*

Most women who develop breast cancer have no identifiable risk factors other than their gender. The growth of breast cancer tumors is often affected by the presence of estrogen and progesterone. The following risk factors result from exposure to these hormones: age greater than 50 years, first pregnancy after age 30 years, long-term hormone replacement therapy (more than 5 years), menstruation before age 12 years, menopause after age 50 years, and nulliparity (not bearing children). Other risk factors include a family history of the disease,

which means a mother or sister has been affected with premenopausal breast cancer, a genetic link, a history of breast biopsy or chest radiation, moderate alcohol use (2 to 5 drinks daily), obesity, a personal history of disease (women with a history of breast cancer are 3 to 4 times more likely to have a recurrence), race (breast cancer is slightly more common in Caucasians), and a sedentary lifestyle.

Approximately 5% of breast cancer cases have a genetic link that results from an inherited mutation in genes identified as BRCA1 (BReast CAncer 1) and BRCA2 (BReast CAncer 2) [Radford *et al.* 1996]. BRCA1, on chromosome 17, and BRCA2, on chromosome 13, are autosomal dominant tumor suppressor genes first identified in 1994 [Miki *et al.* 1994; Wooster *et al.* 1995]. Until recently, the function of these genes was not known. However, studies on a related protein in yeast revealed that the genes code for proteins which participate in repairing radiation-induced breaks in deoxyribonucleic acid (DNA) [Zhang *et al.* 1998]. It is thought that mutations in BRCA1 or BRCA2 disable this mechanism, leading to more errors in DNA replication and ultimately to cancerous growth. Patients who inherit an altered BRCA1 or BRCA2 gene have an increased risk for developing premenopausal breast cancer and are more likely to have family members with the condition. Studies have shown that for women who inherit a BRCA1 or BRCA2 mutation, breast cancer risk could be as high as 80% to 90% by the age of 70. These mutations are particularly prevalent in the Ashkenazi Jewish population [Beller *et al.* 1997]. Both mutations also carry an increased risk of developing ovarian cancer. Genetic testing can be performed to determine BRCA1 and BRCA2 status and patients carrying the genes may choose preventative measures such as prophylactic mastectomy or prophylactic medication. Prophylactic mastectomy, which can reduce the risk of breast cancer by 90%, is the removal of one or both breasts [Hartmann *et*

*al.* 1999]. However, surgeons can never be certain that they have removed all of a patient's breast tissue and in 10% of cases tissue that eventually develops cancer is left behind. In 1998, tamoxifen became the first drug approved by the U.S. Food and Drug Administration (FDA) to prevent breast cancer. Research has shown that it reduces the chance of developing breast cancer by 49% in women at high risk [Fletcher *et al.* 1998]. While tamoxifen reduces the chance of breast cancer in women with the BRCA2 mutation, it doesn't appear to work for women with the BRCA1 mutation [King *et al.* 2001]. Tamoxifen is discussed in more detail in section II.F.5.

Genetic screening for breast cancer is complicated by the fact that both BRCA genes are extremely large and may harbor hundreds of possible mutations. Therefore genetic testing is often performed with affected and unaffected family members and comparison is used to pinpoint the exact location of the mutation. For people of Ashkenazi Jewish descent genetic testing is somewhat simplified. This is because in 90% of cases, an Ashkenazi Jewish family with a pattern of hereditary breast and ovarian cancer will have one of three specific mutations [Roa *et al.* 1996]. This has made it possible to develop a test that looks for the presence or absence of these three specific mutations, rather than the hundreds that can be associated with these types of cancer in other populations.

## *II. D. Breast Cancer Screening*

The American Cancer Society recommends these guidelines for women who do not have symptoms of breast cancer:

- Women at age 20 should learn about the benefits and limitations of breast self-examination (BSE). The American Cancer Society considers performing BSE to be optional.

- Women between the ages of 20 and 39 should have a clinical breast examination by a physician or other health care practitioner every 3 years.
- Women age 40 and older should have a clinical breast examination and mammogram annually.
- Older women with serious health problems should evaluate the benefit of screening with their physician.
- Women with a family history of breast cancer should discuss early detection testing, breast ultrasound, and MRI with their physician.

## *II. E. Breast Cancer Diagnosis*

Cancers of the breast are usually first discovered by a woman or her physician as a solitary, painless mass in the breast or because of mammographic abnormalities during screening. On average, palpable invasive carcinomas are 2 to 3 cm in size when they are first found, and approximately one third have already spread to axillary or other lymph nodes. In contrast, mammographically detected invasive carcinomas average 1 cm in size and less than one fifth will have axillary metastases. The older the patient at the time of discovery, the more likely the lesion is to be cancer. Diagnosis of breast cancer is made through a process called triple assessment, which includes:

- clinical examination,
- imaging procedures (mammogram, breast ultrasound), and
- biopsy of a mass detected by clinical examination or mammogram.

However, it is important to note that biopsy and pathological review are the final arbiters of clinical condition.

### II. E. 1. Clinical Examination

During clinical breast examination (CBE), the health care provider examines the breasts including the nipples and areola for retractions, skin changes, and discharge [Donegan and Spratt, 1995]. Next, the breasts and underarms are palpated. If a mass is found, texture and mobility are assessed. On physical examination, benign lesions are typically mobile while cancers are often firm and immovable due to stromal invasion. If a lesion is identified during CBE, the health care provider will likely order additional studies. Typically, health professionals perform a CBE once every three years between the ages of 20 and 40 and once a year for patients over 40 years of age.

### II. E. 2. Imaging Techniques

Mammography and ultrasound are important counterparts to physical examination that allow many cancers to be discovered at an early stage. Both are imaging techniques, which rely on density changes in the breast to detect cancers.

#### II. E. 2. a) Mammography

Mammography is a non-invasive imaging procedure that uses x-rays to create images of breast tissue [Dahnert 1999; Feig and Piccoli 1997]. During a mammogram, the breast is compressed between a compression paddle and a film holder or digital detector that is used to record the attenuation of x-rays as they traverse the tissue. Compression of the breast reduces tissue thickness, thereby producing improved images. However, the compression causes moderate discomfort. A mammogram is a screening test, not a diagnostic test. An abnormal mammographic result cannot alone indicate cancer. In most cases further testing

shows masses detected via mammography to be benign, and in 10% of cases, radiologists can interpret normal tissue as abnormal [NCI 2002]. An abnormal screening mammogram indicates that further testing should be done, such as a diagnostic mammogram, ultrasound, or biopsy. There are two basic forms of mammography: screening and diagnostic.

A screening mammogram is used to look for cancer in women with no symptoms and no history of breast surgery. The mammogram is first checked by the technologist and then read by a diagnostic radiologist. The radiologist looks for unusual shadows, masses, distortions, special patterns of tissue density, and differences between the two breasts. Mammograms are used for comparative study, that is, the left breast is compared to the right breast, and current films are compared to older films. The goal of regular mammographic screening is to detect small breast cancers because they are easier to treat and present a better prognosis for the patient. How often women under age 50 should have a screening mammogram continues to be controversial. However, most prominent health organizations (e.g., World Health Organization, National Cancer Institute, American Cancer Society) agree that women between the ages of 40 and 69 can significantly reduce their risk for dying of breast cancer by having a mammogram every 1 or 2 years. Women who have significant risk factors for breast cancer should discuss whether to begin screening earlier, and how often, with their physicians.

In standard mammography studies two images of each breast are obtained for evaluation: a mediolateral oblique view, side, and a cranial-caudal view, from above. Different tissues in the breast absorb different amounts of x-rays, producing varying shades of black, gray, and white on the film. Fatty tissue absorbs a relatively small amount of x-rays and thus appears black or dark gray. Normal fibrous and glandular tissues contain water that

causes absorption of a moderate amount of x-rays and thus appear light gray. Dense breast tissue, with more collagen, can make mammogram evaluation difficult because the tissue can obscure small cancers. Younger women and those with fibrocystic change typically have a more dense breast stroma, however there is significant variation. Many mammograms show nontransparent white specks. These are calcium deposits known as calcifications and they are a key component that radiologists look for in a mammogram. Although there is no reliable way to distinguish between calcifications occurring in benign and malignant lesions in a clinical mammogram, their presence does provide some insight into the underlying tissue pathology. Changing of mammographic views may cause disappearance of the calcifications.

If there is a new mass, has been a change in the size or the shape of the edges of a mass, or if a suspicious calcification within a mass is seen, the radiologist is likely to order additional studies. An area in one breast that has a distinctly different appearance than the same area in the other breast is referred to as asymmetric density. In Figure II.6 an asymmetric density can be seen in both the mediolateral oblique and cranial-caudal views.

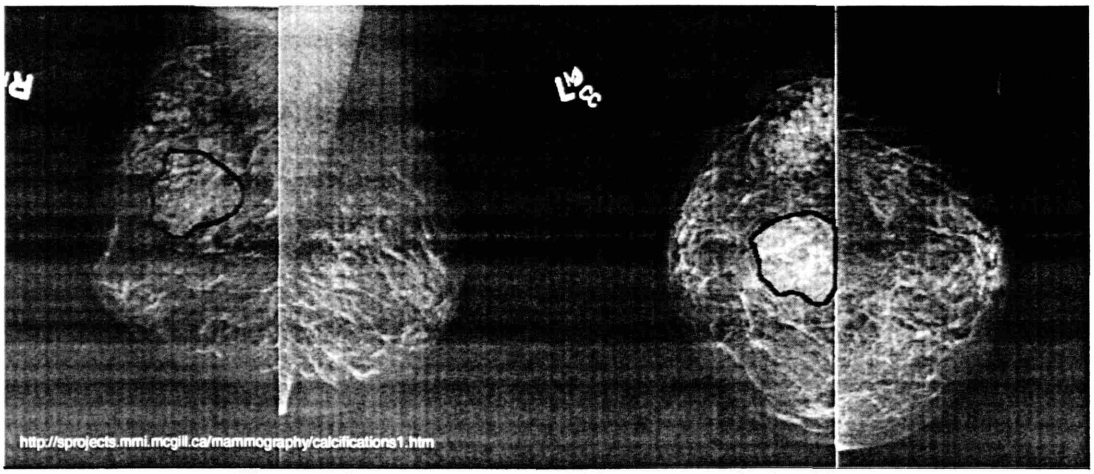


**Figure II.6.** Mammograms exhibiting asymmetric densities.

This finding necessitates additional studies. A new mass or a mass that has grown since the last mammogram was taken is usually evaluated with ultrasound to assess cyst formation, as cancers do not typically grow so rapidly. The shape of a mass detected by mammography is important for differentiating benign and malignant lesions.

A growth that is benign, such as a cyst or fibroadenoma, generally looks smooth, round and has a clearly defined edge. Figure II.7 displays a mammogram of a cystic lesion. Several masses may be seen in women who harbor fibrocystic change and microcalcifications may be present in foci of fibrocystic change containing cysts. When the calcium sediments at the bottom of a cyst, crescent-shaped calcification is produced. The calcification evident in Figure II.8a appears to rim the entire cyst. In a breast lobule, epithelial hyperplasia may also appear as crescent-shaped calcification as it

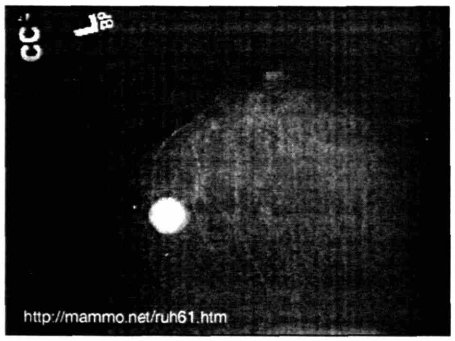


**Figure II.7.** Mammogram showing a cyst.


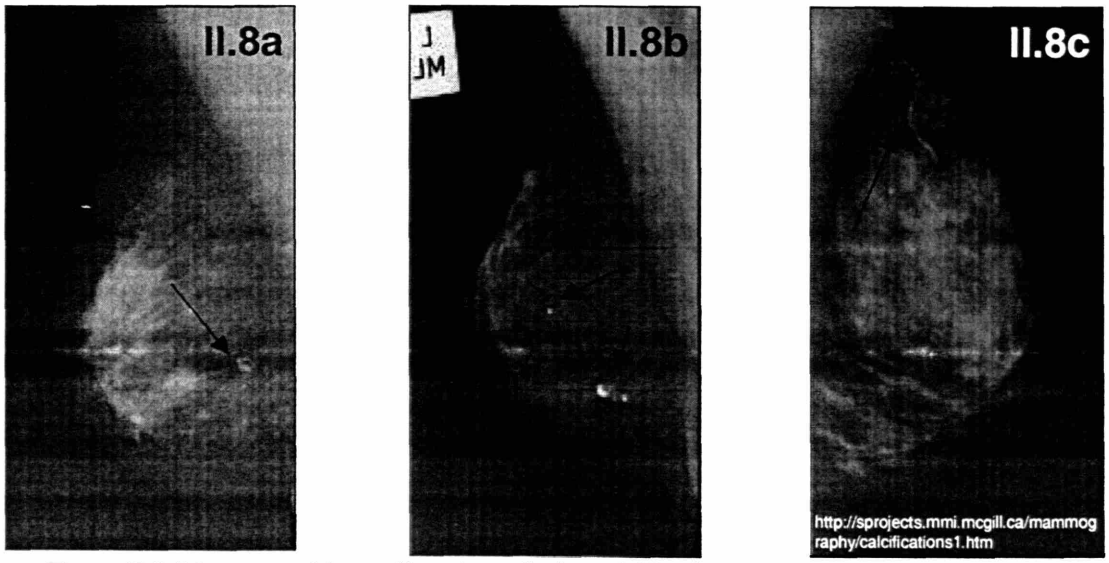


**Figure II.8.** Mammographic manifestations of microcalcifications, highlighted by arrows, occurring in a) a cystic lesion, b) fibroadenoma, and c) Monkeburg's arteriosclerosis.

often causes dilatation of acini and formation of cysts. The mammogram in Figure II.9a demonstrates a suspicious area with microcalcifications that could be a carcinoma or just an area of fibrocystic changes. On biopsy, this lesion had areas of fibrocystic change with epithelial hyperplasia. Sclerosing adenosis, another manifestation of fibrocystic change, is often difficult to distinguish from cancer. Its gross and mammographic appearance may mimic carcinoma, and the two can be difficult to distinguish on frozen section. The mammogram in Figure II.9b demonstrates a suspicious lesion that could be a carcinoma or just an area of pronounced sclerosis with fibrocystic changes. On biopsy it was found to be benign. In older woman with fibroadenoma, atrophy may give rise to calcification. As a result, the "pop-corn" calcification, seen in Figure II.8b, is considered a pathognomonic feature of fibroadenoma. Benign calcifications are usually associated with clusters of apocrine cysts, sclerosing adenosis, fat necrosis, or hyalinized fibroadenomas. Idiopathic arterial calcification, Monkeburg's arteriosclerosis, is common on mammograms and attributed to the ageing process. On mammography, arterial calcifications are observed as two parallel continuous or discontinuous calcific lines along the vessel wall, as seen in Figure II.8c. These calcifications are unrelated to breast lesion formation.

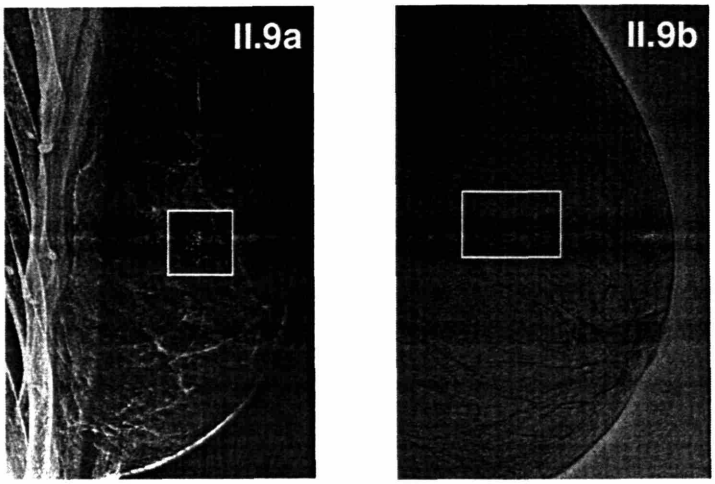

**Figure II.9.** Mammograms demonstrating suspicious lesions.

In contrast to well circumscribed lesions, breast cancer often has an irregular outline with finger-like extensions. On

mammography, a spiculated carcinoma is seen as a star-shaped mass with irregular borders due to a desmoplastic process in conjunction with a possibly infiltrating tumor. Postsurgical scarring (from a previous biopsy), trauma, and infection may also produce a lesion with spiculated margins. IDC and ILC exhibit irregular borders, as can be seen in Figure II.10. However, many breast cancers appear circumscribed and thus may resemble benign lesions. Medullary carcinoma, papillary carcinoma and some of the ductal carcinomas show this feature. Higher density, irregular and non-homogeneous opacities, disruption of normal architecture, increased vascularity, and perifocal haziness are features which assist in distinguishing them from a benign lesion. Microcalcification due to necrotic debris can often be seen within or outside a cancerous mass. This type of calcification is much finer than that of fibroadenoma. Calcifications associated with malignancy are more commonly small, irregular, numerous, and clustered or linear and branching. About half of the cancers found by mammography are detected as clusters of microcalcifications. Clusters of numerous microcalcifications in one area are often a sign of DCIS. In fact, DCIS is most commonly detected as mammographic calcifications and only rarely as a palpable or radiographic mass. DCIS is important to detect because it is limited to the breast and most cases can be cured by local treatment. Any mammographic abnormality suggestive of cancer indicates that further testing should be done, such as a diagnostic mammogram, ultrasound, or biopsy.


**Figure II.10.** Mammogram demonstrating a spiculated mass.

Diagnostic imaging refers to special mammographic views and ultrasound. It may be necessary in patients with breast implants, severe fibrocystic disease, or surgery for early breast cancer that did not remove the entire breast. Diagnostic imaging is required for an abnormal finding on a screening mammogram and a new finding during CBE. If the findings obtained from diagnostic imaging indicate that there is a solid lesion, a biopsy is recommended for final diagnosis. Special mammographic views include magnification and spot compression. Magnification produces an enlarged image of a portion of the breast that contains small calcifications or small masses. Spot compression applies pressure to a small region in the breast. This is used to thin out an area of dense tissue so that a clearer image is produced. Sometimes, views of the breast from different angles are required to better visualize a questionable area. Typical additional views include: cleavage view (both breasts are compressed between a set of panels at the same time providing a top-to-bottom view), rolled view (the breast is rolled to the right or left, compressed, and a top-to-bottom view is taken), mediolateral view (from the center of the chest to the outer side of the breast), lateromedial view (from the outer side of the breast to the center of the chest).

Because small cancers are difficult to distinguish from normal breast tissue on a mammogram and may not be palpable, some go undetected. Cases that elude diagnosis are referred to as false-negatives. Other conditions in the breast may look similar to cancer, such as calcifications or cysts. In this situation, additional studies that focus on the area of the breast where the suspicious lesion is located will be performed. If additional studies are inconclusive, a biopsy is recommended. If the biopsy proves to be benign, the finding is called a false-positive. The high rate of false-positive readings in mammography is why it is not a diagnostic modality and must be followed by biopsy. Age of the patient as well as

breast tissue characteristics are factors in the false-positive rate. Most women who have received false-positive readings are younger women whose breasts tend to be dense, women with a history of breast biopsies, women with a family history of breast cancer, and women who are taking hormone replacement therapy. There is also the possibility of misreading of a mammogram by an unskilled or inexperienced radiologist. Research reports a correlation between a radiologist inaccurately reading a mammogram and his or her experience and training [Elmore *et al.* 2002]. A recent ten year study found that when subjects underwent a median of four mammograms and five CBEs, approximately 32% experienced at least one false-positive from either test [Elmore *et al.* 1998]. Consequently, each year a large number of unnecessary breast biopsies are performed.

II. E. 2. b) Digital Mammography

Digital mammography promises to be a significant improvement over conventional mammography in the early detection of breast cancer. In digital mammography, the film normally used for recording the image is replaced by an electronic x-ray detector [Wu *et al.* 1992]. Instead of acquiring an image on film, a digital image is generated. This image can be displayed and adjusted by the radiologist to facilitate detection of small breast cancers. With digital mammography, the magnification, orientation, brightness, and contrast of the image may be altered after the exam is completed to help the radiologist more clearly see certain areas without having to take an additional image. Further, digital mammography allows correction for under or over exposure after the exam is completed. Advances in image registration, allow doctors to view the entire breast in one image. Digital mammograms also offer the potential for more efficient access to past mammograms as they can be

electronically transmitted to another hospital. This is important as mammograms are most effective when used for comparative study.

Several studies have demonstrated that digital mammography is at least as accurate as standard mammography and the FDA has recently approved a digital mammography system to screen for breast cancer. Small studies have shown that digital mammography may provide additional benefits, such as lower radiation doses and higher sensitivity to abnormalities. Also, research efforts are focusing on use of automated programs to search the digital images for telltale patterns of cancer, enabling radiologists to make diagnoses based on subtle patterns in tumor architecture. The largest U.S. federally-funded clinical trial on medical imaging will soon be underway to determine whether digital mammography is equal or superior to standard film mammography in helping to detect breast cancer.

While digital mammography is quite promising, it still has additional hurdles to undergo before it replaces conventional mammography. Digital mammography lacks the spatial resolution of standard mammography. High resolution is especially useful for imaging microcalcifications and very small abnormalities that may indicate early breast cancer. While digital mammography lacks the spatial resolution of film, clinical trials have shown it to be at least equivalent to standard film screening mammography. This is thought to be because digital mammography has the benefit of providing improved contrast, which may make abnormalities easier to see. Efforts to develop digital mammography systems with resolution equivalent to standard film mammography are underway. The high cost of digital mammography is another obstacle in its implementation. Standard mammography systems are currently installed in over 10,000 locations across the United States. It may take years for

this current equipment to be updated or replaced and for digital mammography to become widespread.

II. E. 2. c) Ultrasound

Ultrasound uses high-frequency sound waves to create an image of the breast. It is performed with a small, handheld device called a transducer. A gel is spread on the skin of the breast and the radiologist passes the transducer over the breast, directing sound waves through the skin and into the body. Thus, ultrasound allows significant freedom in obtaining images of the breast from almost any orientation. It is typically used to determine if a mass is a cyst or a solid lesion, possibly a cancer. Figure II.11a shows an ultrasound of a breast cyst with sharp walls and internal septation while Figure II.11b displays a large cyst with layered debris and a solid component. The ultrasound image in Figure II.11c shows ductal invasion associated with a malignant breast mass. Ultrasound is also useful when evaluating dense fibrous breasts where contrast is limited. Though breast ultrasound has excellent contrast, it lacks the spatial resolution of mammography. As a consequence, it is unable to reliably image microcalcifications. Therefore, ultrasound is not approved by the FDA as a screening tool for breast cancer. Rather, ultrasound is used as an adjunct to further investigate an abnormality detected by mammography or during a CBE [Gordon 2002].

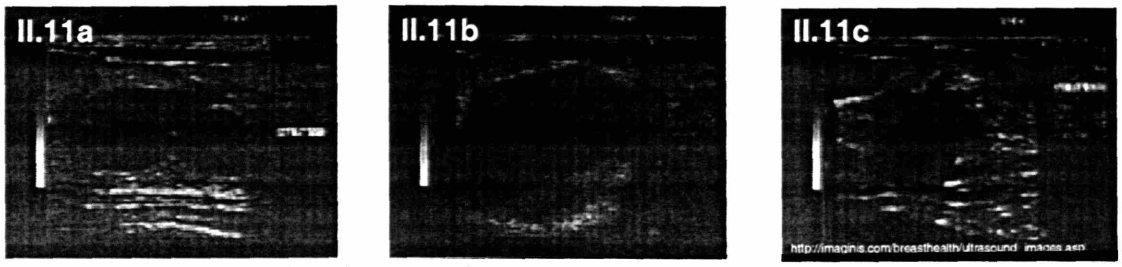


**Figure II.11.** Ultrasound of a) a breast cyst, b) a large cyst with layered debris, and c) an infiltrating ductal carcinoma.

## II. E. 3. Biopsy

### II. E. 3. a) Excisional Biopsy

Biopsy refers to the process of removing tissue from patients for diagnostic examination. Traditionally, suspicious lesions undergo open excisional biopsy under general anesthesia in the operating room. This procedure is preformed by a surgeon. Excisional biopsy removes the entire lesion, which can range from a spheroid several centimeters in diameter to the entire breast. With the increasing use of mammographic screening, a growing number of breast biopsies are performed because of an abnormality detected by mammography in the absence of a palpable mass. Nonpalpable lesions are surgically identified by mammographic placement of a localizing wire within the lesion [Schnitt and Connolly 1992; Bennginton and Lagios 1992]. A radiologist performs needle localization prior to surgery and the wire is used as a guide to precisely locate the mammographic abnormality for excision. The most frequent mammographic abnormalities prompting biopsy are microcalcifications, a soft tissue density or a combination of the two. Specimen radiography, acquiring an x-ray of the excised lesion, is used to document the presence of the lesion or microcalcifications detected by mammography in the excised tissue. It is also used to localize the suspicious area for histologic examination. An example of a specimen radiograph is shown in Figure II.12. The localizing wire can be seen in the upper right of the image. Specimen radiographs are compared with the preoperative mammograms to be certain that the lesion of concern has been excised.

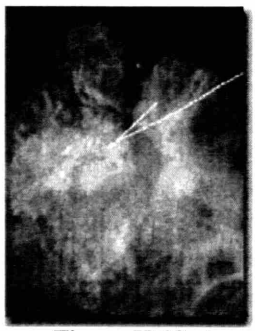

**Figure II.12.** A specimen radiograph.

After radiography of the intact specimen has demonstrated that the lesion of interest is present within the specimen, this area must be identified by the pathologist. Some

specimens will contain a grossly evident tumor, in which case further efforts to demonstrate the lesion are not necessary. If, however, there is no grossly evident lesion, a number of methods can be used to identify the location of the lesion within the specimen. One simple method consists of comparing the gross specimen with the specimen radiograph and placing a pin or needle into the specimen at the site of the mammographic lesion to permit the identification of its location by the prosector. Another method consists of performing the initial specimen radiograph after placing the tissue in a specimen holder that incorporates a grid that is visible on the radiograph. The holder containing the specimen and the specimen radiograph are then compared to precisely locate the target lesion using the X and Y coordinates of the grid. Once the excised lesion is located, the suspicious tissue is placed in a cassette to be sectioned, stained, and examined microscopically by a pathologist. Pathology is the gold standard for disease diagnosis and diagnostic algorithm development.

II. E. 3. b) Needle Biopsy

In recent years, less invasive needle based biopsy techniques have been developed and are being used more frequently. Needle biopsies are performed in a radiologist's office on an outpatient basis under local anesthesia. Needle procedures are less intrusive and less disfiguring than excisional biopsy and yield equal diagnostic accuracy [Parker *et al.* 1994]. In light of the fact that up to 80% of breast biopsies are found to be benign upon tissue excision, needle biopsy is an attractive alternative to excisional biopsy [Johnson *et al.* 1999]. If the lump to be biopsied cannot be felt, stereotactic mammography or ultrasound may be utilized to help the physician guide the biopsy needle. Patient positioning depends on the imaging method employed. If the procedure uses ultrasound, a doctor will obtain images of

the breast tissue while the patient lies on her back. In stereotactic procedures, patients lie facedown on a special table, shown in Figure II.13. The woman's breast protrudes through a hole in the table's surface, where it is compressed and immobilized while mammograms are taken from two angles and a computer maps the precise location of the lesion to be biopsied. The sensitivity of the needle biopsy procedure is in large part related to the size of the needle. In one study, for example, the sensitivity for malignancy was 65%, 92%, and 100% for 18, 16, and 14-gauge needles, respectively [Nath *et al.* 1995]. Spectroscopic modalities have the ability to provide minimal invasiveness, similar to fine needle aspiration, with sensitivity to a larger tissue volume. Several types of needle biopsy will now be described.

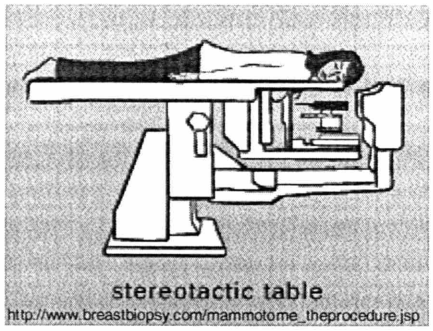


**Figure II.13.** Instrumentation used in stereotactic biopsy procedures.


II. E. 3. c) Fine Needle Aspiration

In fine needle aspiration the doctor uses a hollow needle that is attached to a syringe to extract fluid from a cyst or cells from a solid lesion. The needle used in this procedure is very small, 20-25 gauge (0.89-0.51 mm). The procedure is performed under local anesthesia and requires a small incision. The procedure takes a few minutes and typically leaves no scarring and does not require stitches. Fine needle aspiration is the easiest and fastest method of obtaining a breast biopsy, and is very effective for women who have fluid filled cysts. However, the pathological evaluation can be incomplete because the tissue sample is extremely small. As with many procedures, the effectiveness of fine needle aspiration

depends on the skill of the surgeon or radiologist who performs it. Needle placement can be guided by stereotactic mammography or ultrasound, but even with this guidance, insufficient sampling is a problem. A study of fine needle aspiration found that 34% of patients were insufficiently sampled, requiring further biopsy [Pisano *et al.* 1998].

II. E. 3. d) Core Needle Biopsy

Core needle biopsy is similar to fine needle aspiration, but the needle is larger, 14-18 gauge (2.11-1.25 mm), enabling a larger sample to be obtained. It removes a cylinder of tissue typically 1 mm in diameter and several centimeters long. Although less invasive than excisional biopsy, core needle biopsy requires the collection of at least five specimens to ensure proper sampling [Liberman *et al.* 1994]. The needle, shown in Figure II.14, is deployed by a spring-loaded device. Also shown in Figure II.14 is a schematic of tissue removal procedure. Repeated needle insertions are necessary to obtain each biopsy sample.

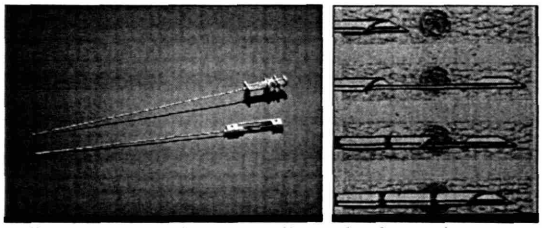

**Figure II.14.** Biopsy needle and schematic of the tissue removal procedure.

Core needle biopsy is also performed under local anesthesia and ultrasound or stereotactic mammography is used if the lump cannot be felt. The procedure takes a few minutes and no stitches are required. Core needle biopsy may provide a more accurate analysis and diagnosis than fine needle aspiration because tissue is removed, rather than just cells. However, this procedure is not accurate in patients with very small or hard lumps. Specimen radiography is also used to document the presence of the lesion or microcalcifications in tissue excised via core needle biopsy. In biopsies performed for microcalcifications, the likelihood that the pathologist will

be able to render a specific diagnosis is significantly greater when calcifications are identified on the specimen radiograph than when they are not [Mainiero *et al.* 1996]. In one study, a specific diagnosis was rendered in 81% of core biopsies in which calcifications were present on the specimen radiograph compared with only 38% of cases in which calcifications were not radiographically identified in the core biopsy specimens [Liberman *et al.* 1994].

II. E. 3. e) Vacuum-Assisted Biopsy

This method utilizes a vacuum-like device to remove breast tissue. Under local anesthesia, following manual incision of the skin, a canula between 0.5 to 2 cm in diameter containing a circular blade is advanced to the lesion position as identified by digital spot view mammography. The needle is inserted only once to obtain multiple samples. As depicted in Figure II.15, when suction is applied, the breast tissue is drawn into the needle and a blade sections the trapped tissue. The suction also draws out the breast tissue and the samples are passed through the hollow chamber of the probe and into a collection chamber. Successive biopsies can be performed over 360° around the axis of the needle without any need to withdraw the needle between biopsies. Typically twelve cores of tissue are removed and in some cases, the entire lesion may be excised. 11 or 14 gauge needles are used. At the completion of the procedure, a small metallic clip may be deployed through the needle to mark the biopsy site in case therapeutic lumpectomy and/or radiation therapy, both described in section II.F, need to be performed for invasive cancer. Vacuum-assisted biopsy is safe, reliable, and valuable for patients who wish to avoid excisional biopsy.

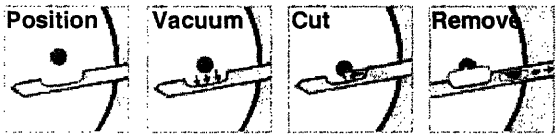


**Figure II.15.** Schematic of vacuum-assisted biopsy.

II. E. 3. f) Large Core Biopsy

Presently, large core biopsy, also called advanced breast biopsy instrumentation (ABBI), has been FDA approved for diagnostic biopsy only. However, in the future ABBI may provide an alternative for patients who prefer a less invasive procedure than surgery. This technique can completely excise small lesions from the breast with clear histologic margin. ABBI assemblies are available which can provide core tissues of 5, 10, 15, or 20 mm in diameter. In this procedure, the radiologist localizes the lesion with a needle in the center of the device. A surgeon then removes a core of tissue from the breast using a circular oscillating blade which is advanced concentrically over the initial localization needle. The procedure is performed through a skin incision, large enough to accommodate the blade, made under local anesthesia and sutured closed by the surgeon at the completion of the procedure.

II. E. 3. g) Sentinal Node Biopsy and Axillary Node Dissection

Sentinal node biopsy and axillary node dissection are performed following a positive biopsy to determine if cancer has spread beyond the breast. The axillary lymph nodes are located under the arm. The sentinel node is the first axillary lymph node that filters fluid from the breast. Cancer cells found in the lymph nodes suggest that the cancer has metastasized and the patient may need more aggressive treatment. Many cancer experts believe that malignant cells reach the sentinel node first and that this lymph node is more likely to contain cancer cells. If the sentinel node is free of cancer cells, then it is highly unlikely that the other nodes are positive. The results of this test are important for the patient and physician to plan the best course of therapy.

Sentinal node biopsy, combined with lumpectomy, is easily performed as an outpatient procedure and causes less pain and deformity than an axillary node dissection. After the patient is given general anesthesia in the operating room, a radioactive tracer or blue dye is injected into and around the tumor. The material passes naturally through the nearby lymphatics to the sentinal node for that area of the breast. With a small, hand-held Geiger counter or by eye, the surgeon tracks the path the tracer takes as it travels away from the breast and under the arm to the sentinal lymph node. Once located, the sentinel node is removed and sent for histopathology and diagnosis. If the results are negative, it is assumed that the cancer has not spread and there is no need for further surgery. If the sentinel node is positive, the surgeon may perform an axillary node dissection to assess how many other lymph nodes are affected. Because sentinel node biopsy removes fewer lymph nodes than axillary lymph node dissection, many patients have no side effects. Pain, nerve damage, and lymphedema (swelling of the arm caused by scarring of the lymph vessels) are more common when additional lymph nodes are removed with the sentinel node.

After the sentinel node has been removed, it is examined by a pathologist. There are two stains typically employed, H&E and an immunohistochemical stain for cytokeratin. The standard test has always been the H&E stain, and prognostic estimates have been based on seeing cancer cells in a lymph node through this method of staining. However, the cytokeratin IHC stain is more sensitive than the H&E stain, and thus it picks up nodes that are negative by H&E. Initially, it was thought this would allow more accurate diagnosis. However, there are often a few cells dislodged during surgery that make it to the lymph nodes, called micrometastases. Micrometastases do not appear to be the same as cancer cells that find their own way to the lymph nodes, called macrometastases, and do not appear to

affect overall survival [Ollila *et al.* 2001]. There are two clinical trials currently underway to determine whether cytokeratin IHC staining should become a routine part of the sentinel node analysis. Researchers experience with IHC staining has taught us that increases in sensitivity do not necessarily translate into increases in a technique's efficacy. This lesson is important to keep in mind when developing a new diagnostic modality.

An axillary node dissection removes all of the axillary lymph nodes and may be done at the same time as a lumpectomy or a mastectomy. The surgeon makes an incision under the arm and removes a pad of fat in which 10 to 20 lymph nodes are embedded. The incision is sutured and a drain may be put in to remove excess fluid. The procedure takes between 1 and 2 hours. Complications include, permanent numbness under the arm, lymphedema and infection of the incision site. An axillary dissection removes many of the lymph nodes that protect against infection, and the hand and arm on the affected side may become more susceptible. Blood should not be drawn from this arm, and minor injuries should be reported to a physician. The hand and arm should be checked regularly for inflammation or cuts.

## *II. F. Breast Cancer Treatment*

### II. F. 1. Staging and Prognosis

The prognosis and therapeutic course for patients with breast cancer depends on the stage of the disease at diagnosis as well as a number of other factors. If a diagnosis of breast cancer is made, the cancer is staged. The American Joint Committee on Cancer Staging divides the clinical stages as follows:

**Stage 0.** DCIS or LCIS, 5-year survival rate 92%.

**Stage I.** Invasive carcinoma 2 cm or less in size without nodal involvement and no distant metastases, 5-year survival rate 87%.

**Stage II.** Invasive carcinoma 5 cm or less in size with involved but movable axillary nodes and no distant metastases, or a tumor greater than 5 cm without nodal involvement or distant metastases, 5-year survival rate 75%.

**Stage III.** Breast cancers greater than 5 cm in size with nodal involvement; or any breast cancer with fixed axillary nodes; or any breast cancer with involvement of the ipsilateral internal mammary lymph nodes; or any breast cancer with skin involvement, pectoral and chest wall fixation, edema, or clinical inflammatory carcinoma, if distant metastases are absent, 5-year survival rate 46%.

**Stage IV.** Any form of breast cancer with distant metastases, 5-year survival rate 13%.

Axillary lymph node status is a key prognostic factor used in stage determination. Lymphovascular invasion, in which tumor cells are seen within vascular spaces surrounding the lesion, is strongly associated with the presence of lymph node metastases. The presence of tumor cells in lymphatics of the dermis is strongly associated with the clinical appearance of inflammatory cancer and bodes a very poor prognosis, with 3-year survival only 3% to 10%. Also, tumors invading skin or skeletal muscle are frequently associated with concurrent or subsequent distant disease. Tumor size is another important prognostic factor also used in staging a lesion, as a larger tumor increases the risk of axillary and systemic metastasis. However, although rare, very small tumors are capable of distant metastasis.

There are a number of additional factors that influence the prognosis and clinical course of women with breast cancer [Cotrain *et al.* 1999]. Histologic subtype plays a role in prognosis. The 30-year survival of women with special types of invasive carcinomas (tubular, colloid, medullary, lobular, and papillary) is more than 60%, compared with less than 20% for women with cancers of no special type (ductal carcinomas).

Tumor grade as well as receptor status are also important indicators of prognosis. A low grade cancer is likely to be less aggressive in its behavior than a high grade tumor. The most commonly used grading system, the modified Bloom and Richardson grading system shown in Table II.3, combines nuclear grade, tubule formation (percentage of cancer

| Grade | Description | Score | 5 yr. survival | 7 yr. survival |
|---|---|---|---|---|
| **Grade 1** | Well-differentiated breast cells; cells generally appear normal and are not growing rapidly; cancer arranged in small tubules. | 3,4,5 | 95% | 90% |
| **Grade 2** | Moderately-differentiated breast cells; have characteristics between Grade 1 and Grade 3 tumors. | 6,7 | 75% | 63% |
| **Grade 3** | Poorly differentiated breast cells; Cells do not appear normal and tend to grow and spread more aggressively. | 8,9 | 50% | 45% |

**Table II.3.** Bloom-Richardson grade system.

composed of tubular structures), and mitotic rate (rate of cell division). In general, each element is given a score of 1 to 3 (1 being the best prognosis and 3 the worst) and the score of all three components are added together to give the "grade" [Bloom and Richardson 1957; Scarff *et al.* 1968; Elston and Ellis 1991]. The lowest possible score (1+1+1=3) is given to well differentiated tumors that all form tubules and have a low mitotic rate. The highest possible score is 9 (3+3+3=9). However, several large-scale studies suggest that mitotic rate alone can be as predictive as the grading system [Clayton 1991]. Cancers with high levels of hormone receptors, such as estrogen and progesterone, have a slightly better prognosis than those without receptors.

DNA ploidy (amount of DNA) is another important prognostic factor. Cancers with the same amount of DNA as normal cells are called diploid and those cancers with either more or less than that amount are called aneuploid. About two-thirds of breast cancers are aneuploid. Several studies have shown that aneuploid cancers tend to be more aggressive

than normal cancers. Expression of oncogenes (Her2/neu, c-myc, ras p21) or loss of expression of tumor-suppressor genes (INT2, p53, NM23), angiogenesis (blood vessel formation), and proteases (stromal proteases are thought to be involved in tumor invasion by degrading extracellular matrix) also influence prognosis. All biopsies are tested for Her2 over-expression since results of the test may help determine a course of treatment.

The course of treatment depends on both the stage of the disease and the patient's preference. Treatment options include, surgery, radiation therapy, chemotherapy, hormone therapy, and immunotherapy. If no axillary metastases are present, some patients may not receive systemic therapy, depending on the characteristics of the tumor. Almost all women with one to three positive axillary nodes receive some form of standard systemic treatment, either hormonal therapy or chemotherapy. Women with four to nine positive axillary nodes are eligible for clinical trials using high-dose chemotherapy. If ten or more nodes are positive, women are eligible for other experimental treatments, such as autologous bone marrow transplantation.

### II. F. 2. Surgery

Surgery combined with radiation and/or chemotherapy is the most common treatment for breast cancer. The type of surgical procedure recommended to the patient depends on the stage of the disease. Lumpectomy and mastectomy are both commonly performed surgical procedures.

A lumpectomy, also known as a partial mastectomy or breast conserving surgery, is the surgical removal of a tumor. Lymph nodes may also be removed during this procedure, depicted in Figure II.16a. When excising the tumor, the surgeon strives to encase the lesion in normal tissue to ensure that all of the cancerous tissue has been removed. In routine

practice, the evaluation of breast lumpectomy specimens to ensure complete excision is assisted by the use of various tissue marking inks to delineate surgical margins and preserve tissue orientation. If cancer cells are found touching or near (2 to 5 mm although definitions

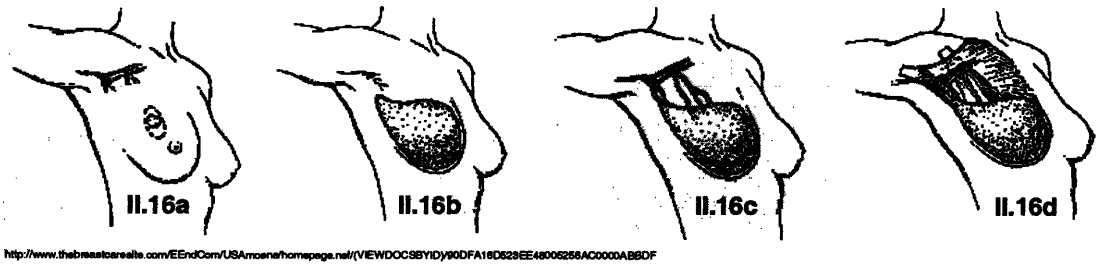


**Figure II.16.** Schematic representations of breast cancer surgeries: a) lumpectomy or partial mastectomy, b) simple mastectomy, c) modified radical mastectomy, and d) radical mastectomy.


vary) the inked regions, it is assumed that malignant cells are likely still present in the patient. The color of ink harboring the malignant cells identifies their location in the patient. Many surgeons also remove several small samples of tissue, called margins, from different areas of the surgical cavity. Following surgery, the margins are examined by a pathologist to see if any cancer cells are present in the presumed normal tissue. If no cancer cells are found in the margins they are called "clean margins". If cancer cells are found in the margin tissue or near the inked region of the excised tumor, the surgeon will recommend additional steps, which typically include another surgical procedure, called a re-excision, in which remaining cancerous tissue is removed. The area to be excised is identified by which margin or which face of the tumor the cancerous cells are found in. In general, lumpectomy procedures take 60 to 90 minutes. After a lumpectomy with clean margins, most women receive six to seven weeks of radiation therapy, in order to eliminate any cancer cells that may remain after surgery.

There are three types of mastectomies: simple, modified radical and radical mastectomies, depicted in Figure II.16b-d. A simple mastectomy includes removal of the

breast tissue, skin and nipple but rarely lymph nodes. This procedure is often performed for prophylactic reasons when a strong probability of developing breast cancer exists, for instance in patients who harbor a BRCA mutation. A modified radical mastectomy is the most common form of mastectomy performed. This procedure includes removal of the entire breast, nipple and areola and varying amounts of lymph nodes in the underarm region. The procedure can also be performed through a much smaller incision near the areola to create a skin sparing mastectomy. Skin sparing mastectomies work well if immediate reconstruction is planned. A radical mastectomy includes the removal of the breast tissue, skin, nipple, areola, underlying chest muscles and varying numbers of lymph nodes in the underarm region. Prior to 1970 this was a common surgery used for breast cancer but is now reserved for treatment of advanced disease as studies have shown survival rates are equal with that of the less invasive modified radical mastectomy [Papatestas and Lesnick 1975]. Radical mastectomy typically creates more difficulty with range of motion in the arm and shoulder on the operative side. All mastectomies require general anesthesia and a hospital stay. Drains are often placed in the breast and underarm area and are removed two weeks after the surgery. A woman may opt for breast reconstruction or choose to wear a breast prosthesis following a mastectomy. Patients often receive breast reconstruction immediately following the mastectomy and as part of the same surgical procedure. Breast reconstruction falls into two general categories: implant type restorations and those using the patient's own tissues. For procedures using the patient's own tissues, the most common donor site is the abdomen, the Transverse Rectus Abdominus skin-Muscle, or TRAM.

### II. F. 3. Radiation Therapy

Radiation therapy uses high-energy x-rays to destroy cancer cells. Treatment is delivered externally or by radioactive "seeds" that are placed directly into the tumor, called brachytherapy. Breast cancer is usually treated using highly focused and targeted external radiation [Fletcher 1972]. Radiation may be used to shrink the tumor before surgery, called neoadjuvant therapy, or may be used after surgery to destroy cancer cells that remain in the breast, chest wall, or underarm, called adjuvant therapy [Ragaz *et al.* 1997; Overgaard *et al.* 1997; Overgaard *et al.* 1999]. Radiation therapy is performed in a hospital or outpatient center. Each treatment lasts a few minutes and treatment is usually given 5 days per week, for 6 weeks. Side effects include fatigue, reddening of the skin, and swelling.

### II. F. 4. Chemotherapy

Chemotherapy is a systemic treatment that travels throughout the body via the bloodstream. It often relies on a combination of drugs to slow tumor growth and destroy cancer cells. Drugs may be administered orally or intravenously. Chemotherapy is also used as both neoadjuvant and adjuvant therapy [Eifel *et al.* 2001; Goldhirsch *et al.* 2001]. One of the main advantages of neoadjuvant chemotherapy is that it allows for assessment of pathologic response to treatment. There are several pathologic changes associated with response to neo-adjuvant chemotherapy. Tumor replacement by loose fibrosis is the most common pathologic event. In most cases, the intensity of fibrotic change is proportional to the degree of clinical-mammographic reduction of the tumor mass. Studies have also observed a decrease in tumor cellularity, from 40% in core needle biopsy to 10% in resection specimens [Rajan *et al.*

2004]. These changes in tissue morphology must be considered when collecting spectra from patients who have undergone neo-adjuvant chemotherarpy.

The combination most commonly prescribed to treat breast cancer is doxorubicin and cyclophosphamide. Paclitaxel (Taxol®) is often prescribed after this combination treatment, when breast cancer has metastasized to the lymph nodes. It is also often prescribed following breast cancer surgery. Other chemotherapy drugs include docetaxel and gemcitabine. Side effects are typically severe and include fatigue, fever, alopecia (hair loss), infection, anemia (low red blood cell count), neutropenia (low neutrophil count), thrombocytopenia (low platelet count), and nausea.

### II. F. 5. Hormone Therapy

Endocrine manipulations are among the most effective, and least toxic, of the systemic therapies currently available for the management of hormone-responsive breast cancers. Estrogen, a hormone produced by women's ovaries, promotes the growth of some breast cancers, particularly those with detectable amounts of estrogen receptor protein. Estrogen and progesterone receptors are intracellular steroid-hormone receptor proteins. 50% to 85% of tumors exhibit estrogen receptors. Such tumors are more commonly found in postmenopausal women. Hormone therapy involves blocking the effect of estrogen or lowering estrogen levels. It can be used to treat breast cancer as both a neoadjuvant and adjuvant therapy and to treat cancer that has spread or come back after it was first treated. 75% of tumors with estrogen receptors regress after hormonal manipulation, whereas only 5% of those that are negative respond [Early Breast Cancer Trialists' Collaborative Group

2004]. The highest response rates are in patients with tumors exhibiting both estrogen and progesterone receptors.

Several drugs, classified as anti-estrogen therapy, have been developed to treat breast cancer that is responsive to estrogen. Selective estrogen-receptor agonists, such as tamoxifen and raloxifene, inhibit the effects of estrogen on breast cancer cells [Early Breast Cancer Trialists' Collaborative Group 1998]. Tamoxifen works by competing with estrogen to bind to estrogen receptors in breast cancer cells. Tamoxifen is formally known as a selective estrogen receptor modulator (SERM). By blocking estrogen in the breast, it helps slow the growth and reproduction of breast cancer cells. Tamoxifen is taken in pill form, usually for 5 years after breast cancer surgery to prevent recurrence. After 5 years medication must be discontinued because patients taking tamoxifen have an increased risk for uterine cancer. The most common side effect of this medication is hot flashes. Other side effects include depression, dizziness, alopecia, headache, and swelling. Fulvestrant destroys estrogen receptors. It is used to treat metastatic breast cancer in postmenopausal women who have been treated unsuccessfully with tamoxifen. This treatment is administered once a month by intramuscular injection. Side effects include nausea, hot flashes, and weight gain. Aromatase inhibitors, such as anastozole, letrozole and exemestane, are also prescribed for postmenopausal women with advanced breast cancer that has been unsuccessfully treated with tamoxifen [Goss *et al.* 2003]. They inhibit the action of the enzyme aromatase, involved in small amounts of estrogen production in postmenopausal women. Side effects include cough, depression, diarrhea, dizziness, fatigue, headache, hot flashes, increase appetite, nausea, and pain. Goserelin is a synthetic form of luteinizing hormone-releasing hormone that is prescribed to treat metastatic breast cancer in premenopausal women. This

medication is a pituitary downregulator, signaling the body to stop producing estrogen, thereby depriving the tumor of the estrogen it needs to grow. This therapy is not appropriate for postmenopausal women because their ovaries no longer produce estrogen. Several weeks of treatment are needed before tumor growth slows. Side effects include hot flashes, sexual dysfunction, increased pain, and rash.

### II. F. 6. Immunotherapy

Immunotherapy involves using trastuzumab (Herceptin®) to inhibit tumor growth and enhance the immune system's ability to fight cancer. The Her2/neu oncogene encodes for a 185 KD transmembrane glycoprotein with intracellular tyrosine kinase activity [King *et al.* 1985]. The Her2 receptor belongs to the epidermal growth factor receptor family of receptors, which are critical in the activation of subcellular signal transduction pathways controlling epithelial cell growth and differentiation [Karunagaran *et al.* 1996; Klapper *et al.* 1999]. Amplification of Her2 or overexpression of its protein product is observed in 20% to 40% of human breast cancers [Slamon *et al.* 1987; Slamon *et al.* 1989]. All biopsies are tested for Her2 over-expression since results of the test may help determine a course of treatment. Her2 receptor protein overexpression correlates with several negative prognostic variables in breast cancer, including estrogen receptor-negative status and high nuclear grade [Sjogren *et al.* 1998]. Breast cancers that overexpress the Her2 receptor protein can be therapeutically targeted with trastuzumab anti-Her2 monoclonal antibody therapy [Burstein *et al.* 2003]. It also may be combined with chemotherapy as a first line treatment for metastatic breast cancer and may be used after chemotherapy or anti-estrogen therapy to improve the effectiveness of the treatment. When used alone or in combination, side effects

include cardiac dysfunction resulting in headache, fever and chills, weakness, nausea and vomiting, and anemia and neutropenia.

## *II. G. Summary*

The incidence of breast cancer has been increasing steadily from an incidence of 1:20 in 1960 to 1:8 women today. It is three times more common than all gynecologic malignancies put together. As such, breast cancer is truly an epidemic among women. Breast cancer is considered a heterogeneous disease, meaning that it is a different disease in different women, a different disease in different age groups and has different cell populations within the tumor itself. Due to its heterogeneity, complexity and numerous manifestations, an understanding of breast pathology is necessary for intelligent diagnostic algorithm development. Further, through knowledge of current approaches to breast cancer diagnosis and treatment, spectroscopic modalities can be developed to aid in numerous aspects of breast cancer management.

## *Acknowledgements*

I am grateful to Dr. Maryann Fitzmaurice for her patience in teaching me breast pathology. I also thank Dr. Daniel Kopans for educating me in current biopsy techniques and mammography during a one-week visit to the Massachusetts General Hospital Comprehensive Breast Center.

## *References*

Beller U, Halle D, Catane R, Kaufman B, Hornreich G and LevyLahad E (1997). "High Frequency of BRCA1 and BRCA2 Germline Mutations in Ashkenazi Jewish Ovarian Cancer Patients, Regardless of Family History." Gynecol Oncol **67**(2): 123-126.

Bennington JL, Lagios MD (1992). The Mammographically Directed Biopsy. Philadelphia, Hanley and Belfus.

Bloom HJ and Richardson WW (1957). "Histological Grading and Prognosis in Breast Cancer." Br J Cancer, **11**: 359-377.

Burkitt HG, Stevens A, Lowe JS, and Young B (1996). Wheater's Basic Histopathology. 3rd Ed., New York, Churchill Livingstone.

Burstein HJ, Harris LN, Marcom PK, Lambert-Falls R, Havlin K, Overmoyer B, Friedlander RJ, Gargiulo J, Strenger R, Vogel CL, Ryan PD, Ellis MJ, Nunes RA, Bunnell CA, Campos SM, Hallor M, Gelman R and Winer EP (2003). "Trastuzumab and Vinorelbine as First-Line Therapy for HER2-Overexpressing Metastatic Breast Cancer: Multicenter Phase II Trial With Clinical Outcomes, Analysis of Serum Tumor Markers as Predictive Factors, and Cardiac Surveillance Algorithm." J Clin Oncol **21**(15): 2889-2895.

Clayton F (1991). "Pathologic Correlates of Survival in 378 Lymph Node-Negative Infiltrating Ductal Breast Carcinomas. Mitotic Count is the Best Single Predictor." Cancer **68**: 1309-1317.

Cotran RS, Kumar V and Collins T (1999). Robbins Pathologic Basis of Disease. 6th Ed., Philadelphia, W. B. Saunders Company.

Dahnert W (1999). Radiology Review Manual. 4th Ed., Baltimore, Williams & Wilkins, 449-474.

Donegan WL and Spratt JS (1995). Cancer of the Breast. Philadelphia, W. B. Saunders Company.

Early Breast Cancer Trialists' Collaborative Group (1998). "Tamoxifen for Early Breast Cancer: An Overview of the Randomised Trials." Lancet **351**:1451.

Early Breast Cancer Trialists' Collaborative Group (2004). "Tamoxifen for Early Breast Cancer (Cochrane Review)." The Cochrane Library. **4**, Chichester, UK, John Wiley & Sons, Ltd.

Eifel P, Axelson JA, Costa J (2001). "National Institutes of Health Consensus Development Conference Statement: Adjuvant Therapy for Breast Cancer." J Natl Cancer Inst **93**: 979.

Elmore JG, Barton MB, Moceri VM, Polk S, Arena PJ and Fletcher SW (1998). "Ten-year Risk of False Positive Screening Mammograms and Clinical Breast Examinations." N Engl J Med **338**: 1089-1096.

Elmore JG, Miglioretti DL, Reisch LM, and Barton MB (2002). "Screening Mammograms by Community Radiologists: Variability in False-Positive Rates." J Natl Cancer Inst **94**: 1373-1380.

Elston CW and Ellis IO (1991). "Pathological Prognostic Factors in Breast Cancer. I. The Value of Histological Grade in Breast Cancer: Experience From a Large Study With Long-Term Follow-Up." Histopathology **19**: 403-410.

Feig SA, Piccoli CW (1997). "The Breast." Grainger & Allison's Diagnostic Radiology: A Textbook of Medical Imaging. Eds. Grainger RG and Allison DJ, Churchill Livingstone, Edinburgh, **3**:1995-2023.

Fisher B, Costantino JP, Wickerham DL, Redmond CK, Kavanah M, Cronin WM, Vogel V, Robidoux A, Dimitrov N, Atkins J, Daly M, Wieand S, Tan-Chiu E, Ford L and Wolmark N (1998). "Tamoxifen for Prevention of Breast Cancer: Report of the National Surgical Adjuvant Breast and Bowel Project P-1 Study." J Natl Cancer Inst **90**: 1371-1388.

Fletcher G (1972). "Local Results of Irradiation in the Primary Management of Localized

Breast Cancer." Cancer **29**: 545.

Goldhirsch A, Glick JH, Gelber RD, Coates AS and Senn HJ (2001). "Meeting Highlights: International Consensus Panel on the Treatment of Primary Breast Cancer. Seventh International Conference on Adjuvant Therapy of Primary Breast Cancer." J Clin Oncol **19**(18): 3817-3827.

Gordon PB (2002). "Ultrasound for Breast Cancer Screening and Staging." Radiol Clin North Am **40**: 431-441.

Goss PE, Ingle JN, Martino S, Robert NJ, Muss HB, Piccart MJ, Castiglione M, Tu D, Shepherd LE, Pritchard KI, Livingston RB, Davidson NE, Norton L, Perez EA, Abrams JS, Therasse P, Palmer MJ and Pater JL (2003). "A Randomized Trial of Letrozole in Postmenopausal Women After Five Years of Tamoxifen Therapy for Early-Stage Breast Cancer." N Engl J Med **349**(19): 1793-1802.

Hartmann LC, Schaid DJ, Woods JE, Crotty TP, Myers JL, Arnold PG, Petty PM, Sellers TA, Johnson JL, McDonnell SK, Frost MH, Jenkins RB, Grant CS and Michels VV (1999). "Efficacy of Bilateral Prophylactic Mastectomy in Women with a Family History of Breast Cancer." N Engl J Med **340**(2): 77-84.

Jemal A, Tiwari RC and Murray T (2004) "Cancer statistics 2004." CA Cancer J Clin **54**: 8.

Johnson JM, Dalton RR, Wester SM, Landercasper J and Lambert PJ (1999). "Histological Correlation of Microcalcifications in Breast Biopsy Specimens." Archiv Surg **134**: 712-716.

Karunagaran D, Tzahar E, Beerli RR, Chen XM, GrausPorta D, Ratzkin BJ, Seger R, Hynes NE and Yarden Y (1996). "ErbB-2 is a Common Auxiliary Subunit of NDF and EGF Receptors: Implications for Breast Cancer." Embo J **15**: 254-264.

Khan SA and Badve S (2001). "Phyllodes Tumors of the Breast." Curr Treat Options Oncol **2**(2): 139-147.

King CR, Kraus MH and Aaronson SA (1985). "Amplification of a Novel v-erbB-Related Gene in a Human Mammary Carcinoma." Science **229**: 974-976.

King MC, Wieand S, Hale K, Lee M, Walsh T, Owens K, Tait J, Ford L, Dunn BK, Costantino J, Wickerham L, Wolmark N and Fisher B (2001). "Tamoxifen and Breast Cancer Incidence Among Women With Inherited Mutations in *BRCA1* and *BRCA2*." JAMA **286**: 2251-2256.

Klapper LN, Glathe S, Vaisman N, Hynes NE, Andrews GC, Sela M and Yarden Y (1999). "The ErbB-2/HER2 Oncoprotein of Human Carcinomas May Function Solely as a Shared Coreceptor for Multiple Stroma-Derived Growth Factors." Proc Natl Acad Sci USA **96**: 4995.

Liberman L, Dershaw DD, Rosen PP, Abramson AF, Deutch BM and Hann LE (1994). "Stereotaxic 14-Gauge Breast Biopsy - How Many Core Biopsy Specimens are Needed." Radiology **192**(3): 793-795.

Liberman L, Evans WP 3rd, Dershaw DD, Hann LE, Deutch BM, Abramson AF and Rosen PP (1994). "Radiography of Microcalcifications in Stereotaxic Mammary Core Biopsy Specimens." Radiology **190**:223-225.

Mainiero MB, Philpotts LE, Lee CH, Lange RC, Carter D and Tocino I (1996). "Stereotaxic Core Needle Biopsy of Breast Microcalcifications: Correlation of Target Accuracy and Diagnosis with Lesion Size." Radiology **198**(3):665-669.

Moreno A, Escobedo A, Benito E, Serra JM, Guma A and Riu F (2002). "Pathologic

Changes Related to CMF Primary Chemotherapy in Breast Cancer. Pathological Evaluation of Response Predicts Clinical Outcome." Breast Cancer Res Treat **75**(2): 119-25.

Miki Y, Swensen J, Shattuck-Eidens D, Futreal PA, Harshman K, Tavtigian S, Liu Q, Cochran C, Bennett LM, Ding W (1994). "A Strong Candidate for the Breast and Ovarian Cancer Susceptibility Gene BRCA1." Science **266**(5182): 66-71.

National Cancer Institute Web Site. Cancer Facts: Screening Mammograms: Questions and Answers. Accessed November 3, 2004.

Nath ME, Robinson TM, Tobon H, Chough DM and Sumkin JH (1995). "Automated Large-Core Needle Biopsy of Surgically Removed Breast Lesions: Comparison of Samples Obtained With 14-, 16-, and 18 Gauge Needles." Radiology **197**(3): 739-742.

Ollila DB and Stitzenberg KB (2001). "Breast Cancer Sentinel Node Metastases: Histopathologic Detection and Clinical Significance." Cancer Control **8**(5): 407-414.

Overgaard M, Hansen PS, Overgaard J, Rose C, Andersson M, Bach F, Kjaer M, Gadeberg CC, Mouridsen HT, Jensen MB and Zedeler K (1997). "Postoperative Radiotherapy in High-Risk Premenopausal Women With Breast Cancer Who Receive Adjuvant Chemotherapy." N Engl J Med **337**(14): 949-955.

Overgaard M, Jensen MB, Overgaard J, Hansen PS, Rose C, Andersson M, Kamby C, Kjaer M, Gadeberg CC, Rasmussen BB, Blichert-Toft M and Mouridsen HT (1999). "Postoperative Radiotherapy in High-Risk Postmenopausal Breast-Cancer Patients Given Adjuvant Tamoxifen: Danish Breast Cancer Cooperative Group DBCG 82c Randomised Trial." Lancet **353**(9165): 1641-1648.

Page DL and Dupont WD (1990). "Anatomic Markers of Human Premalignancy and Risk of Breast Cancer." Cancer **66**(6): 1326-1335.

Papatestas AE and Lesnick GJ (1975) "Treatment of the Breast by Modified Radical Mastectomy." Surg Gynecol Obstet **140**(1): 22-26.

Parker SH, Burbank F, Jackman RJ, Aucreman CJ, Cardenosa G, Cink TM, Coscia JL Jr, Eklund GW, Evans WP 3rd, Garver PR (1994). "Percutaneous Large Core Breast Biopsy: Multi-Institutional Study." Radiology **193**(2): 359-364.

Pisano ED, Fajardo LL, Tsimikas J, Sniege N, Frable WJ, Gatsonis CA, Evans WP, Tocino I and McNeil BJ (1998). "Rate of Insufficient Samples for Fine-Needle Aspiration for Nonpalpable Breast Lesions in a Multicenter Clinical Trial." Cancer **82**: 679-688.

Radford DM and Zehnbauer BA (1996). "Inherited Breast Cancer." Surg Clin North Am **76**(2): 205-220.

Ragaz J, Jackson SM, Le N, Plenderleith IH, Spinelli JJ, Basco VE, Wilson KS, Knowling MA, Coppin CM, Paradis M, Coldman AJ and Olivotto IA (1997). "Adjuvant Radiotherapy and Chemotherapy in Node-Positive Premenopausal Women With Breast Cancer." N Engl J Med **337**(14): 956-962.

Rajan R, Poniecka A, Smith TL, Yang Y, Frye D, Pusztai L, Fiterman DJ, Gal-Gombos E, Whitman G, Rouzier R, Green M, Kuerer H, Buzdar AU, Hortobagyi GN and Symmans WF (2004). "Change in Tumor Cellularity of Breast Carcinoma After Neoadjuvant Chemotherapy as a Variable in the Pathologic Assessment of Response." Cancer **100**(7): 1365-73.

Roa BB, Boyd AA, Volcik K and Richards CS (1996). "Ashkenazi Jewish Population

Frequencies for Common Mutations in BRCA1 and BRCA2." Nat Genet **14**(2):185-187.

Scarff RW and Torloni H (1968). "Histological Typing of Breast Tumors." International Histological Classification of Tumours, No. 2. World Health Organization, Geneva **2**: 13-20.

Schnitt SJ and Connolly JL (1992). "Processing and Evaluation of Breast Excision Specimens. A Clinically Oriented Approach." Am J Clin Pathol **98**(1): 125-137.

Slamon DJ, Clark GM, Wong SG, Levin WJ, Ullrich A and McGuire WL (1987). "Human Breast Cancer: Correlation of Relapse and Survival with Amplification of the HER-2/neu Oncogene." Science **235**(4785): 177-182.

Slamon DJ, Godolphin W, Jones LA, Holt JA, Wong SG, Keith DE, Levin WJ, Stuart SG, Udove J, Ullrich A (1989). "Studies of the HER-2/neu Proto-Oncogene in Human Breast and Ovarian Cancer." Science **244**(4905): 707-712.

Sjogren S, Inganas M, Lindgren A, Holmberg L and Bergh J (1998). "Prognostic and Predictive Value of c-erbB-2 Overexpression in Primary Breast Cancer, Alone and In Combination with other Prognostic Markers." J Clin Oncol **16**(2): 462-469.

Sternberg SS (1997). Histopathology for Pathologists. Philadelphia, Lippincott-Raven.

Wooster R, Bignell G, Lancaster J, Swift S, Seal S, Mangion J, Collins N, Gregory S, Gumbs C and Micklem G (1995). "Identification of the Breast Cancer Susceptibility Gene BRCA2." Nature **378**(6559): 789-792.

Wu Y, Doi ML, Giger ML and Nishikawa RM (1992). "Computerized Detection of Clustered Microcalcifications in Digital Mammograms: Application of Artificial Neural Networks." Med Phys **19**: 555-560.

Zhang H, Tombline G and Weber BL (1998). "BRCA1, BRCA2, and DNA Damage Response: Collision or Collusion?" Cell **92**(4): 433-436.

# Chapter III. Raman Spectroscopy

In this thesis we employ Raman spectroscopy to diagnose breast cancer. This chapter outlines the general theory of Raman spectroscopy as well as its strengths and weaknesses. Biomedical considerations of Raman spectroscopy are also presented. Previous work applying Raman spectroscopy to breast cancer diagnosis is summarized and competing research technologies for breast cancer diagnosis are discussed. Finally, the experimental instrumentation used throughout this work is presented.

## *III. A. General Theory*

### III. A. 1. Raman Spectroscopy

Raman scattering, discovered by the Indian physicist C.V. Raman in 1928, is a relatively new effect [Raman and Krishnana 1928]. It arises when a photon incident on a molecule interacts with the electron cloud of that molecule. In classical terms, the interaction can be viewed as a perturbation of the molecule's electric field. In quantum mechanics, the Raman effect describes a scattering interaction between light and matter. When light is scattered from a molecule the majority of photons are elastically scattered. In elastic scattering, the scattered photons have the same energy and, therefore, wavelength, as the incident photons. In Raman spectroscopy, the wavelength and intensity of light inelastically scattered from a sample is measured. Inelastic scattering refers to the process in which the energies of the incident and scattered photons are different. In Raman spectroscopy an incident photon, with energy $h\nu_L$ where h is Planck's constant (J s) and $\nu_L$ is the frequency of the excitation laser ($s^{-1}$), excites a molecule into a virtual state that is lower in energy than an electronic transition. A new photon is created and scattered from this virtual level [Diem 1993; McCreery 2000]. The scattering event occurs almost instantaneously, typically in $10^{-14}$ s. or less. If a molecule begins in the vibrational ground state, then the final state can be either the vibrational ground state (elastic scattering), called Rayleigh scattering, or an excited vibrational state, called Stokes-Raman scattering. In Stokes-Raman scattering photons lose energy by exciting a vibration within the sample molecule and thus the scattered light appears at a lower frequency than the incident photon. In this case, the Raman scattered light will have an energy of $h(\nu_L-\nu_R)$, where $\nu_R$ is the frequency of the Raman scattered light ($s^{-1}$). The molecule can also begin in an excited vibrational state and proceed, via the virtual state, to

the vibrational ground state. This process is called anti-Stokes-Raman scattering and in this case photons gain energy from the molecular vibrations and the scattered signal appears at a higher frequency. In anti-Stokes-Raman scattering the Raman scattered light will have an energy of $h(\nu_L+\nu_R)$. At room temperature the thermal population of vibrational excited states is low, although not zero. The number of scattering molecules in a given state, N, is governed by the Boltzmann distribution, $e^{-h\nu/kT}$, in which $h\nu$ is the energy of the state, k is the Boltzmann factor ($J\ K^{-1}$), and T (K) is the temperature. Therefore, at room temperature anti-Stokes-Raman scattering is only strong enough to be useful for vibrational frequencies less than about 1500 $cm^{-1}$, defined in Eq. III.1. The Stokes and anti-Stokes Raman spectra contain identical frequency information. Thus, the ratio of anti-Stokes to Stokes intensity at any vibrational frequency can be used as a measure of temperature.

Individual bands in the Raman spectrum are characteristic of specific molecular motions. By measuring the energy of the emitted photon after the scattering event, and

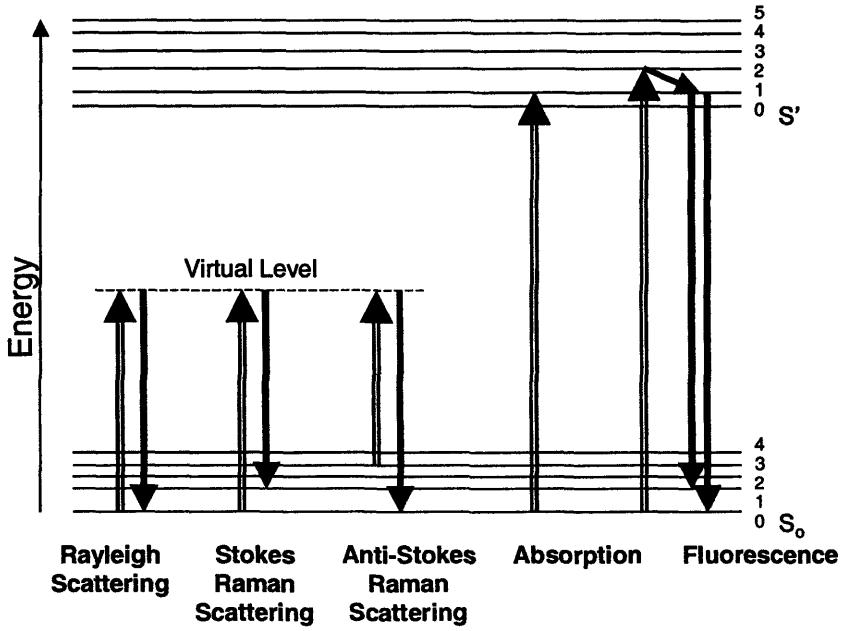


**Figure III.1.** Molecular energy level diagram depicting several light-matter interactions.

knowing the energy of the incident photon, one can assess the structure of the molecule being probed. Because the Raman effect is weak and comprises a very small fraction, about 1 in $10^7$, of the incident photons, the intense Rayleigh background must be suppressed so that it does not overwhelm the Raman scattered light. The processes of Rayleigh, Stokes-Raman, and anti-Stokes Raman scattering are depicted schematically in Figure III.1. Also shown for comparison are the processes of absorption and fluorescence. The lower energy levels in Figure III.1 represent the ground electronic state, $S_o$, while the upper levels represent the first excited electronic state, S'. Within the ground and excited electronic states are vibrational and rotational energy levels. The open arrows represent the incident light, $\nu_L$, and the solid arrows the re-emitted light.

Numerically, the energy difference between the initial and final vibrational levels, $\bar{\nu}$, or Raman shift in wavenumbers ($cm^{-1}$), is calculated through Eq.III.1:

$$\bar{\nu} = (\nu_L c^{-1}) - (\nu_R c^{-1}) \qquad \text{(III.1)}$$

in which c is the speed of light (cm $s^{-1}$). Raman frequency shifts are always the same, regardless of the frequency of the incident light. The vibrational energy is ultimately dissipated as heat. Because of the low probability of Raman scattering, the heat dissipation does not cause a measurable temperature rise in the material, allowing safe biomedical application. In clinical implementation, the largest source of heating is absorption of the excitation light by the surrounding tissue. The energy of a particular vibrational mode depends on molecular structure and environment. Atomic mass, bond order, molecular substituents, molecular geometry and inter-molecular interactions, such as hydrogen bonding, all effect the vibrational force constant which, in turn dictates the vibrational energy.

Vibrational Raman spectroscopy is not limited to intra-molecular vibrations. Crystal lattice vibrations and other motions of extended solids are also Raman active. Their spectra are important in such fields as polymers and semiconductors. In the gas phase, rotational structure is resolvable on vibrational transitions. The resulting vibration/rotation spectra are widely used to study combustion and gas phase reactions. Vibrational Raman spectroscopy in this broad sense is an extraordinarily versatile probe into a wide range of phenomena ranging across disciplines from materials science to medicine.

### III. A. 2. Raman Selection Rules and Intensities

A simple classical electromagnetic field description of Raman spectroscopy can be used to explain many of the important features of Raman band intensities. The dipole moment, P, induced in a molecule by an external electric field, E, is proportional to the field as shown in Eq. III.2.

$$P=\alpha E \qquad \text{(III.2)}$$

The proportionality constant $\alpha$ is the polarizability of the molecule. The polarizability measures the ease with which the electron cloud around a molecule can be distorted. The induced dipole emits or scatters light at the optical frequency of the incident light wave. Raman scattering occurs because a molecular vibration can change the polarizability of the molecule. The selection rule for a Raman-active vibration, that there be a change in polarizability during the vibration, is given in Eq. III.3, where Q is the normal coordinate of the vibration.

$$\partial\alpha/\partial Q \neq 0 \qquad \text{(III.3)}$$

The Raman selection rule is analogous to the more familiar selection rule for an infrared-active vibration, which states that there must be a net change in permanent dipole moment during the vibration. From group theory it is straightforward to show that if a molecule has a center of symmetry, vibrations which are Raman-active will be silent in infrared spectroscopy, and vice versa.

The Raman effect is weak, comprising a very small fraction, about 1 in $10^7$, of the incident photons. Typical non-resonant Raman cross-sections are on the order of $10^{-30}$ $cm^2$ per molecule. The Raman scattering cross-section indicates the strength of the Raman signal of a particular moiety at unit concentration. The Raman scattered intensity is given by

$$I \cong \nu_L^4 I_0 N f(\alpha^2) \qquad \text{(III.4)}$$

where $I_0$ is the intensity and $\nu_L$ is the frequency of the excitation light, N is the number of scattering molecules in a given state, and $\alpha$ is the polarizability of the sample. $f(\alpha^2)$ describes a function in which scattering intensity is proportional to the square of the induced dipole moment, that is to the square of the polarizability derivative, Eq. III.3. If a vibration does not greatly change the polarizability, then the polarizability derivative will be close to zero, and the intensity of the Raman band will be low. The vibrations of a highly polar moiety, such as the O-H bond, are usually weak because an external electric field cannot induce a large change in the dipole moment. This is advantageous for biomedical Raman spectroscopy, as water signals do not overwhelm the spectrum. Typical strong Raman scatterers are molecules with distributed electron clouds, such as those containing double bonds. The pi-electron cloud of the double bond is easily distorted in an external electric field.

Raman scatter is partially polarized, even for molecules in a gas or liquid, where the individual molecules are randomly oriented. The effect is most easily seen with an exciting source that is plane polarized. In isotropic media, polarization arises because the induced electric dipole has components that vary spatially with respect to the coordinates of the molecule. Raman scatter from totally symmetric vibrations will be strongly polarized parallel to the plane of polarization of the incident light. The scattered intensity from non-totally symmetric vibrations is 3/4 as strong in the plane perpendicular to the plane of polarization of the incident light as in the plane parallel to it.

### III. A. 3. Resonance Enhanced Raman Scattering

Raman spectroscopy is conventionally performed with green, red or near-infrared (NIR) lasers. These excitation wavelengths are below the first electronic transitions of most molecules. However, if the wavelength of the exciting laser is within the electronic spectrum of a molecule, the intensity of some Raman active vibrations increases by a factor of $10^2$-$10^4$. This is known as resonance enhanced Raman scattering.

Vibrations whose Raman bands are resonance enhanced fall into two general classes. The most common case is Franck-Condon enhancement, in which a component of the normal coordinate of the vibration is in a direction in which the molecule expands during an electronic excitation. The more the molecule expands along this axis when it absorbs light, the larger the enhancement factor. The in-plane ring breathing expansion modes of porphyrins fall into this class. Vibrations which couple two electronic excited states are also resonance enhanced. This mechanism is called vibronic enhancement. In both cases enhancement factors roughly follow the intensities of the absorption spectrum [Myers and Mathies 1987]. Resonance enhancement does not begin at a sharply defined wavelength. In

fact, enhancements of 5x to 10x are commonly observed if the exciting laser is even a few hundred wavenumbers below the electronic transition of a molecule. β-carotene exhibits this type of pre-resonance enhancement in our experimental data. Resonance enhancement can also be implemented in the deep UV.

The resonance Raman effect can be quite useful. Because the spectrum of a particular molecule is resonance enhanced and that of the surrounding sample is not, selective monitoring of that moiety, without spectral interference from other components, is easily attainable. This allows biological molecules to be examined in their natural environments. Metalloporphyrins, carotenoids and several other classes of biologically important molecules have strongly allowed electronic transitions in the visible. These molecules often make up the active site of enzymes. Resonance Raman spectroscopy has been successfully employed *in vivo* to quantitatively measure macular carotenoids. Levels were compared in patients with age-related macular degeneration and normal subjects to assess the role of dietary carotenoids in protecting against age-related visual loss [Bernstein *et al.* 2002].

### III. A. 4. Surface Enhanced Raman Spectroscopy

The Raman scattering from a compound adsorbed on or within a few Angstroms of a structured metal surface can be $10^3$ to $10^{10}$ times greater than in solution. This technique, called surface enhanced Raman scattering (SERS), arises from two mechanisms. The first is an enhanced electromagnetic field produced at the surface of the metal [Otto 1984; Campion and Kambhampati 1998; Kneipp *et. al* 1999]. When the wavelength of the incident light is close to the plasma wavelength of the metal, conduction electrons in the metal surface are

excited into an extended surface electronic excited state called a surface plasmon resonance. Thus, molecules adsorbed or in close proximity to the surface experience an exceptionally large electromagnetic field. Vibrational modes normal to the surface are most strongly enhanced. In addition to this "electromagnetic field enhancement," the electronic interaction between the molecule and the metal can result in an increase of the Raman scattering cross-section itself, called "chemical or electronic enhancement." Several mechanisms are discussed to account for this chemical SERS enhancement, such as a resonance Raman effect, which becomes operative due to possibly shifted and broadened electronic levels in the adsorbed molecule compared to the free molecule or due to a new electronic transition in the metal-molecule system [Otto 1984; Campion and Kambhampati 1998]. In many experiments, the "chemical effect" provides a very small contribution and the total SERS enhancement is determined by electromagnetic field enhancement [Kniepp *et al.* 1997].

SERS is strongest on silver, but is observable on gold and copper as well. The intensity of the surface plasmon resonance is dependent on many factors including the wavelength of the incident light and the morphology of the metal surface. The wavelength should match the plasma wavelength of the metal. This is about 382 nm for a 5 μm silver particle [Kerker *et al.* 1982], but can be as high as 600 nm for larger ellipsoidal silver particles. The plasma wavelength is to the red of 650 nm for copper and gold [Morris 1992], the other two metals which exhibit SERS at wavelengths in the 350-1000 nm region. The best morphology for surface plasmon resonance excitation is a small (<100 nm) particle or an atomically rough surface. Molecules with lone pair electrons or pi-electron clouds show the strongest SERS.

SERS was first used to study monolayers of materials adsorbed on metals, including

electrodes, however, many other formats can be used. The most popular include colloids, metal films on dielectric substrates and, recently, arrays of metal particles bound to metal or dielectric colloids through short linkages. The effect was first discovered with pyridine [Jeanmaire and Van Duyne 1977]. Other aromatic nitrogen or oxygen containing compounds, such as aromatic amines or phenols, are strongly SERS active. The effect can also been seen with other electron-rich functionalities such as carboxylic acids. Recently, SERS has been applied to the detection of glucose [Shafer-Peltier *et al.* 2003]. Although SERS allows easy observation of Raman spectra from solution concentrations in the micromolar range, slow adsorption kinetics and competitive adsorption have limited its application in analytical chemistry.

## *III. B. Biomedical Considerations*

Raman shifts are independent of excitation wavelength. This gives an important degree of flexibility in generating a Raman spectrum; ultraviolet (UV), visible or infrared excitation light can all be used, and in each case the Raman fingerprints will be the same. Thus, in contrast to many spectroscopic techniques, the excitation frequency can be chosen such that it is tailored to the specific application. For biological samples, NIR radiation is typically employed, 770 nm to 1500 nm. The use of NIR excitation light confers three advantages to biomedical Raman spectroscopy: a reduction of background fluorescence, deeper sampling depths (>1 mm), and less laser-induced photothermal degradation. Reduced fluorescence occurs because the lowest lying excited electronic state of biological molecules, responsible for fluorescence, correspond to visible wavelengths and therefore cannot be excited by lower energy NIR light. Background fluorescence is a competing process that can often obscure

the Raman bands. It adds shot noise to the data, thereby degrading the signal-to-noise ratio (SNR). Because Raman scattering is a weak process and clinical implementation necessitates rapid data acquisition, attention must be paid to maintaining adequate SNR. Further, the background must be removed prior to data analysis, which inherently results in distortion of the Raman spectrum. We have found that excitation with 785 nm, employed by several laboratories for biological Raman spectroscopic studies, results in at least a four-fold increase in tissue fluorescence when compared with 830 nm excitation. Although excitation wavelengths longer than 830 nm further reduce tissue fluorescence, the Raman scattering cross-sections are simultaneously reduced because they depend on the excitation frequency to the fourth power. Also, longer excitation wavelengths prohibit the use of CCD detectors. Large penetration depths, the second advantage of using NIR excitation light, are obtained by

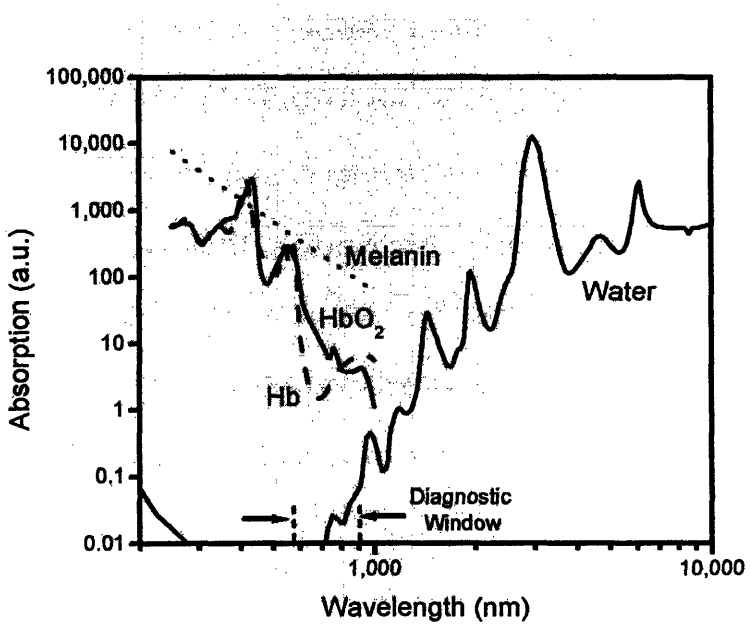


**Figure III.2.** Predominate absorption spectra in tissue.

working in a spectral region with minimal absorption. Figure III.2 shows spectra of the predominant tissue absorbers. A group of minima can be seen in the NIR region below 1000 nm. The large penetration depth conferred by working in this wavelength region, often referred to as the diagnostic window, provides the opportunity to observe subsurface structures, regions which cannot be examined using conventional white light techniques. Also, thermal and photochemical damage are minimized by the use of low energy NIR light. NIR wavelengths are not mutagenic and absorption is relatively low so tissue heating is minimized. Finally, when employing 830 nm frequency excitation, the resultant fingerprint region of Raman shifts falls in a wavelength range that is efficiently transmitted by fused silica optical fibers. Such fibers can be readily incorporated into optical fiber probes thereby allowing remote sensing for *in vivo* clinical applications.

Because each molecule possesses a unique pattern of Raman shifts, the chemical composition of the tissue can be determined via Raman spectroscopy. Raman spectra provide direct chemical information and are capable of characterizing a sample both qualitatively and quantitatively without the use of fluorescent tags or stains. Unlike fluorescence, reflectance, and NIR absorption spectroscopies, Raman spectroscopy provides narrow spectral bands, with high information content, that can be assigned to specific molecular vibrations. To illustrate this, Figure III.3 displays a fluorescence spectrum of NADH and a Raman spectrum taken from cholesterol. Raman spectral band widths for biological molecules are on the order of 10 $cm^{-1}$. Whereas there are relatively few endogenous biological fluorophores, many of whose spectra significantly overlap, there exist a multitude of Raman active chemicals in tissue that have unique spectra and which can be specifically related to healthy and diseased conditions. Table III.1 displays the Raman band

assignments for a number of biological moieties [Sadtler 1974; Manoharan *et al.* 1992; Baraga *et al.* 1992; Diem 1993; Manoharan *et al.* 1993; Manoharan *et al.* 1996]. Given the heterogeneity and complexity of breast disease, presented in Chapter II, the ability to measure several different chemicals is of particular importance in studying breast cancer. Although Raman spectra provide high information content, the signals are orders of magnitude weaker than fluorescence. However, with careful system design collection of clinical data in relevant times with safe levels of laser power can be accomplished. For these reasons, we have investigated the use of Raman spectroscopy as a clinical tool for the examination of a variety of breast pathologies.

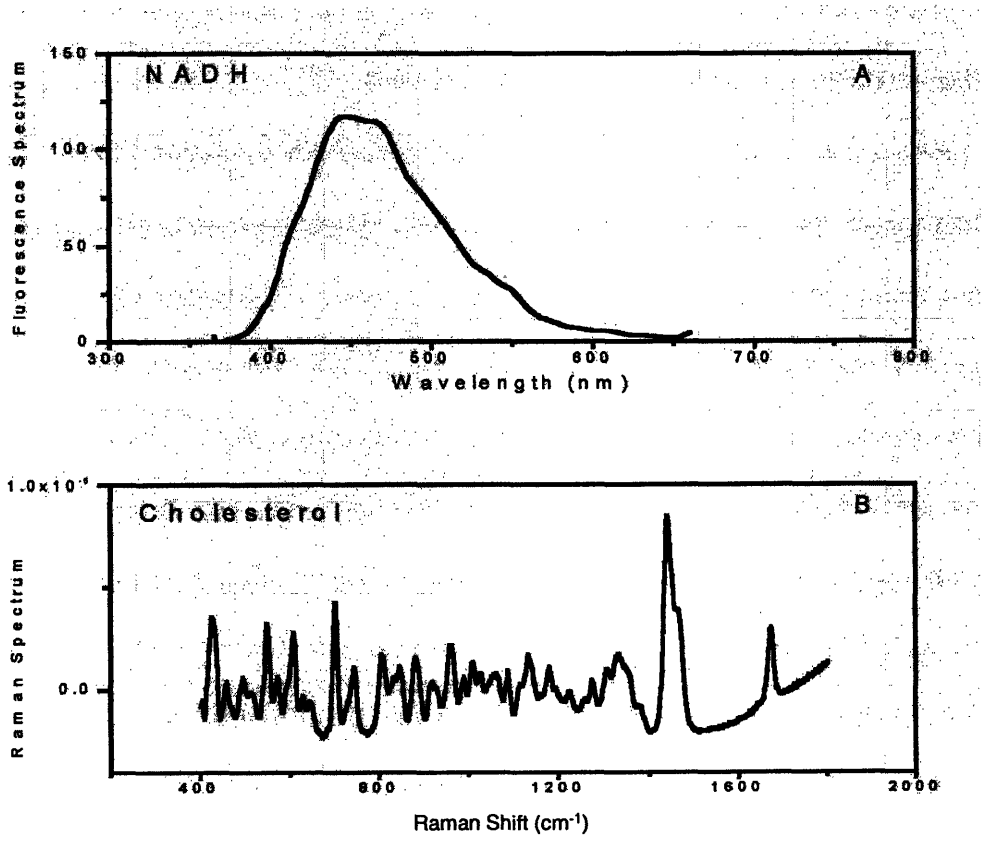


**Figure III.3.** Comparison of Raman and fluorescence spectra.

| Raman Shift ($cm^{-1}$) | | Molecule/Molecular Class | Group/Vibration |
|---|---|---|---|
| 702 | | Cholesterol/Cholesterol esters | Sterol ring breathing |
| 719 | | Phospholipids | Symmetric choline stretch |
| 762 | | Phospholipids | Symmetric O-P-O stretch |
| 801-805 | | Cholesterol/Cholesterol esters | Sterol ring breathing |
| 841-850 | | Cholesterol/Cholesterol esters | Sterol ring breathing |
| 853 | | Proteins | C-C tyrosine ring breathing |
| 855 | | (Hydroxy)Proline (collagen) | C-C stretch |
| 878 | | Cholesterol/Cholesterol esters | Sterol ring breathing |
| 878 | | Phospholipids | Asymmetric O-P-O stretch |
| 871-882 | | Cholesterol/Cholesterol esters | Sterol ring breathing |
| 923 | | Cholesterol/Cholesterol esters | Sterol ring breathing |
| 933 | | Proline (collagen) | C-C stretch |
| 940 | | Proteins | C-C or C-H stretch |
| 957 | | Cholesterol/Cholesterol esters | Sterol ring breathing |
| 959-962 | | Calcium hydroxyapatite | Symmetric $PO_4^{3-}$ |
| 1004 | | Phenylalanine | Phenyl ring breathing |
| 1034 | | Proteins | C-C or C-H stretch |
| 1071 | | Calcium carbonate | Symmetric $CO_3^{2-}$, asymmetric $PO_4^{3-}$ |
| 1085 | | Cholesterol | C-C stretch |
| 1104 | | Desmosine/Isodesmosine (elastin) | Ring breathing |
| 1160 | | β-carotenoids | C=C stretch |
| 1176 | | Cholesterol | C-C stretch |
| 1245 | | Proteins | Amide III, random coil |
| 1264 | | Proteins | Amide III (C-N stretch), α-helix |
| 1268 | | Proteins | Amide III, α-helix |
| 1270 | | Cholesterol/Cholesterol esters | $-CH_2$, $-CH_3$ bending |
| 1274 | | Cholesterol | $-CH_2$, $-CH_3$ bending |
| 1299 | | Cholesterol/Cholesterol esters | $-CH_2$, $-CH_3$ bending/twist |
| 1301 | | Triglycerides | $-CH_2$, $-CH_3$ bending/twist |
| 1328 | | Cholesterol | $-CH_2$, $-CH_3$ bending |
| 1336 | | Proteins | Amide III and $-CH_2$, $-CH_3$ wag |
| 1336 | | Desmosine/Isodesmosine (elastin) | -CH bending |
| 1439 | | Cholesterol/Cholesterol esters | $-CH_2$, $-CH_3$ bending |
| 1440 | | Triglycerides | $-CH_2$, $-CH_3$ bending |
| 1443 | | Lipids | $-CH_2$, $-CH_3$ bending |
| 1449 | | Proteins | $-CH_2$, $-CH_3$ bending |
| 1451-1455 | | Proteins | $CH_2$ deformation, C-H bend |
| 1523 | | β-carotenoids | C-C stretch |
| 1660 | | Proteins | Amide I |
| 1654 | | Triglycerides, Proteins | C=C stretch, Amide I, α-helix |
| 1664 | | Proteins | Amide I (C=0, C-N), α-helix |
| 1668 | | Lipids | C=C stretch |
| 1671 | | Cholesterol/Cholesterol esters | C=C stretch |
| 1735 | | Cholesterol esters | C=O stretch (ester) |
| 1747 | | Triglycerides | C=O stretch (ester) |

**Table III.1.** Raman band assignments for morphological structures.

## *III. C. Raman Spectroscopy for Breast Cancer Diagnosis: Previous Studies*

### III. C. 1. Raman Spectroscopy of Breast: Other Laboratories

The first Raman spectroscopy measurements of human breast tissue used 1064 nm excitation and a Fourier transform Raman system [Alfano *et al.* 1991]. Collection times were 4 to 5 min. and employed a power density of less than 10 watt/cm$^2$. The area probed was 6x6 mm. No depth information was provided. Histology of the tissue samples was performed before the measurements and spectra were acquired from formalin-fixed tissue. Fourteen breast tissue specimens were examined, 3 normal specimens, 4 benign tumors, and 7 malignant tumors. No more detailed pathology information was provided. Four to 15 spectra were collected per sample. Surprisingly, no significant changes in the Raman spectra were observed between different locations on a single sample. This may be a function of relatively noisy data provided by this now outdated experimental system. All specimens were found to have peaks at 1445 cm$^{-1}$ and 1651 cm$^{-1}$, while normal tissue also had peaks at 1078 cm$^{-1}$ and 1330 cm$^{-1}$ and benign at 1240 cm$^{-1}$. The 1445 cm$^{-1}$ peak results from the -$CH_2$ and -$CH_3$ bending modes and is indicative of lipids. The 1651 cm$^{-1}$ peak was assigned to the C=O stretching Amide I vibration, indicative of proteins. The 1240 cm$^{-1}$ band results from the Amide III vibration and the 1300 cm$^{-1}$ and 1078 cm$^{-1}$ bands were assigned to C-C and C-N stretching vibration modes. The relative intensities of the 1445 cm$^{-1}$ and 1651 cm$^{-1}$ bands were reported to correlate with disease classification although no diagnostic algorithm was presented. Table

| Pathology | $I_{(1651\ cm^{-1})}/I_{(1445\ cm^{-1})}$ |
|---|---|
| Normal | 0.80±0.09 |
| Benign | 1.08±0.03 |
| Malignant | 1.15±0.05 |

**Table III.2.** Summary of the results of Alfano and co-workers from their initial investigation of breast tissue using Raman spectroscopy.

III.2 summarizes these initial results.

In 1993, Redd *et al.* examined the application of Raman spectroscopy to 35 samples of breast tissue using visible excitation [Redd *et al.* 1993]. They employed <50 mW or 0.4 to 1.0 watt/cm$^2$ incident power and integration time was varied to optimize SNR, 2.5 to 50 s. Differences between normal, benign and malignant samples were examined, as well as the effects of excitation wavelength and formalin fixation on the Raman spectrum. Several Raman bands, which were not observed in the Alfano study, were reported. Further, unlike Alfano, Redd and coworkers observed variability of the Raman spectrum between different locations on a single sample. This is not surprising considering the anatomic heterogeneity of breast tissue. The additional peaks as well as the increased spectral variability observed in this study may be attributable to a higher SNR, evident through comparison of the spectra presented in each manuscript. Interestingly, Redd and coworkers debate several of the band assignments made in the study of Alfano *et al.* Among other discrepancies, they attribute the 1651 cm$^{-1}$ peak to lipids, C=C stretching from the hydrocarbon region, rather than to proteins. Due to the biochemical complexity of tissue, several chemicals often contribute intensity to a particular Raman band. Clearly, spectral analysis based on peak heights is not sufficient to elucidate the moieties responsible for the Raman signal.

The Raman spectra in Redd's study predominately contained features attributed to various amounts of carotenoids and lipids. A small contribution from a heme-type signal, at 1358 cm$^{-1}$, was detected in some samples of benign breast tissue, while a much stronger heme-type signal was detected in most of the breast cancers. Thus far, we have not observed contribution from heme containing species in our studies. The reason for this has not been investigated, but is likely explained by resonant enhancement of the heme signal at visible

excitation frequencies. Raman spectra of diseased breast tissue, both benign (fibrocystic change) and malignant (mammary carcinoma), also showed markedly diminished to absent contributions from lipids and reduced contributions from carotenoids. The concentration of carotenoids often mirrors that of lipids as they are typically extremely lipophilic moieties. This study also examined the effects of excitation wavelength on the Raman spectrum of normal breast tissue, varied from 406.7 to 647.8 nm. The contribution of lipids was best observed with 406.7 nm excitation while the contributions of carotenoids were found to be enhanced at longer excitation wavelengths. In accordance with theory, they observed a reduction in the fluorescence background with increasing excitation wavelength. Last, in an effort to document possible changes in breast tissue following formalin fixation, a specimen of normal breast tissue was studied in the fresh state, and then again after 24 hours of formalin fixation. No new spectral lines were noted and the formalin fixation showed no evidence of significant Raman features. However, the primary effect of fixation is cross-linking the collagen proteins, a component not present in significant quantities in normal breast tissue. Thus it is difficult to draw conclusions about the effect of formalin fixation from this study. All other tissues examined in this study were formalin-fixed.

Frank and coworkers also examined the optimal excitation wavelength, ranging from 406 nm to 830 nm, to employ for Raman spectroscopy of breast tissue. Their objective was to produce a detailed characterization of the Raman spectrum of normal human breast tissue samples with visible and NIR excitation. Consistent with the studies of Redd *et al.*, spectra of formalin-fixed breast tissue revealed features of lipids and carotenoids. However, in contrast to the results of Redd and coworkers, the best defined lipid features were observed for 782 nm and 830 nm excitation, while carotenoid features were strongest in the 488 nm to

515 nm range due to resonant enhancement. As expected, the fluorescence background was reduced when working at longer wavelengths, and thus 691 nm to 832 nm excitation was suggested for future breast studies. Lastly, a compact, portable, diode laser based system with fiber optic sampling was used to demonstrate the clinical potential of Raman spectroscopy. Using 7 mW of 782 nm light and a 60 s. integration time, they were able to collect a Raman spectrum of normal tissue. However, normal breast tissue is mainly composed of fat, which has a relatively strong Raman scattering cross-section. Again, normal breast tissue is naively used as a representative sample for all types of breast pathologies. The silica fiber background was clearly visible in the probe acquired spectra.

Frank *et al.* followed their preliminary investigations with a diagnostic study. In this work, Raman spectra of histologically normal human breast biopsy samples were compared to those exhibiting IDC and fibrocystic change. The study employed 784 nm excitation, 10-200 mW laser power, 300 to 600 sec. integration times and formalin-fixed tissue. A total of 123 spectra from 12 patients were examined. The Raman spectra changed dramatically in diseased specimens, with much weaker lipid bands being evident. This is consistent with our studies and the findings of Redd and coworkers. A shift of the prominent 1439 $cm^{-1}$ feature in normal tissue to 1450 $cm^{-1}$ in IDC was noted and attributed to different $CH_2$ deformation frequencies in fatty acids and proteins. The spectrum of IDC samples was similar to that of human collagen. Differences between fibrocystic and malignant lesions were smaller than those between normal and IDC specimens, but were still reproducible. The fibrocystic spectra had smaller amide I, 1656 $cm^{-1}$, and amide III, 1259 $cm^{-1}$, intensities relative to the 1449 $cm^{-1}$ $CH_2$ deformation band and the $CH_2$ deformation was shifted to a lower frequency (1446 $cm^{-1}$ vs. 1449 $cm^{-1}$). In addition, structure in the 850 $cm^{-1}$ to 950 $cm^{-1}$ region differed,

with only two resolvable peaks in the fibrocystic specimens and four in the case of IDC. However, the authors report that too few samples were evaluated to determine the statistical significance of their findings. Again, fiber optic sampling through a hypodermic needle and with a remote probe was demonstrated.

Treado and coworkers employed Raman imaging of breast tissue. Initially, they used the technique to identify foreign polymer inclusions anchored in fibrous breast tissue surrounding silicone implants [Schaeberle *et al.* 1996]. Their imaging system employed an acousto-optical tunable filter for wavelength selection. In this implementation, the Raman spectra obtained from breast tissue itself were extremely noisy. However, Dacron polyester, the foreign polymer inclusion, has a strong Raman signal and thus it was possible to image the polymer material within the breast tissue matrix. Using an improved device, outfitted with a liquid crystal tunable filter, they were able to image characteristic bands of lipid and protein in chicken breast, a poor model for human breast tissue [Kline and Treado 1997].

Although previous studies indicate the promise of Raman spectroscopy for breast cancer diagnosis, they are exploratory in nature, and none contain a diagnostic algorithm. These studies have consistently shown differentiation of normal and malignant breast specimens, however, none have demonstrated statistically meaningful differences between malignant and benign samples. Given the intended application, in which there is an *a priori* expectation of non-normal tissue, accurate differentiation of benign and malignant lesions is a crucial and significant step in the field. Both Alfano and Frank were able to distinguish malignant and normal tissue based on the 1654 $cm^{-1}$ and 1439 $cm^{-1}$ bands. This difference was attributed to increased protein concentrations in malignant samples and is consistent with the results presented in this thesis. Further, previous studies relied on simple peak height

ratios for analysis. The wealth of information available from Raman spectroscopy coupled with the biochemical complexity of tissue necessitates a method of analysis that utilizes the entire spectrum. Lastly, all of the previous work used formalin-fixed breast tissue. The fixation process chemically alters the tissue and thus the Raman spectrum. The primary effect of fixation is cross-linking the collagen proteins, a component which our studies show to be a key diagnostic feature. To address these concerns and to fully assess the ability of Raman spectroscopy to improve breast cancer diagnosis, especially the ability to distinguish benign lesions from malignant lesions, we have undertaken further studies.

### III. C. 2. Raman Spectroscopy of Breast: Our Laboratory

Our initial data set included 61 spectra obtained from 13 patients: 15 normal, 15 benign, and 31 malignant [Manoharan 1998]. Specifically, 11 normal, 4 normal glandular, 11 fibrocystic change, 4 adenosis, 2 carcinoma *in situ* and 29 IDC. Fat and glandular samples were grouped to form the normal category, fibrocystic change and adenosis into benign and carcinoma *in situ* and infiltrating ductal carcinoma comprised malignant. Spectra were acquired from fresh-frozen, but unfixed, samples of human breast tissue with 80 mW of 830 nm excitation and 100 sec. integration time. Absolute intensities were preserved by using ethanol as an intensity standard and keeping the light delivery/collection geometry fixed for all measurements. A third-order polynomial was fit to the spectra by least-square minimization to remove the fluorescence background. To assess the degree of agreement between our data and previous studies, we plotted the shift of the 1442 $cm^{-1}$ peak against the ratio of the 1445 $cm^{-1}$ and 1650 $cm^{-1}$ bands, shown in Figure III.4. Trends in our data were consistent with previous results. Specifically, $I_{(1650)}/I_{(1445)}$ generally increased from normal to

benign to malignant samples. Further, the $CH_2$ deformation band appeared at lower frequencies for normal and benign specimens. This algorithm, based on previous studies, used features of the Raman spectra that are sensitive to differenced in lipid and protein

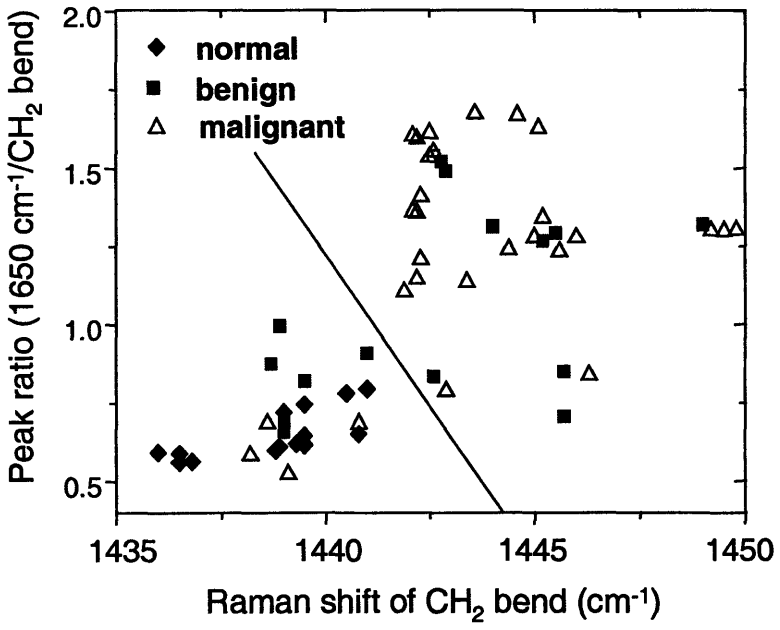


**Figure III.4.** Elementary breast cancer diagnostic plot.

modes. Because lipids dominate in normal tissue and proteins dominate in abnormal tissues, this simple empirical diagnostic algorithm can differentiate normal and malignant samples. However, it is clear that a more sophisticated approach in necessary to identify benign lesions. As discussed above, accurate differentiation of benign and malignant lesions is crucial for reducing the percentages of false positives and false negatives through Raman assisted diagnosis.

In order to capitalize on the wealth of information available from Raman spectroscopy, we employed principal component analysis (PCA). PCA is a multivariate statistical method of analysis, discussed in detail in Chapter IV. It does not assume any

knowledge about the chemical composition of the tissue. Rather, it resolves the spectra of the entire data set into a small number of principal components (PC) that accurately characterize the entire range of spectral variations. All 61 spectra in this study could be accurately modeled, above the noise level, using 12 principal components. The scores were then used to develop a diagnostic algorithm to classify the tissue into normal, benign and malignant categories. Logistic regression was used to correlate the fit coefficients with the pathological categories. This study did not employ cross-validation.

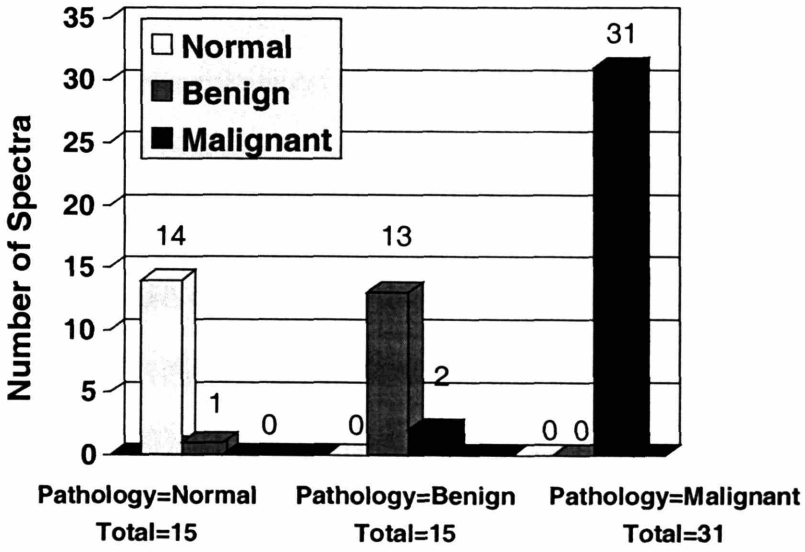


**Figure III.5.** Comparison of pathology and the PCA based Raman diagnosis.

Four PCs were found to be statistically significant classification indicators at the P=0.05 level. They account for 98.70% of the variance in the data. PC 1, accounting for 96.77% of the data variance, closely resembles the Raman spectrum of fat while PC 4, 0.60% of the variance, exhibits features indicative of carotenoids. PC 2, which accounts for 1.24% of the data variance, is somewhat reminiscent of cholesterol and PC 6, 0.09% of the variance, has features of both collagen and epithelial cell cytoplasm. The 4 PCs were used to estimate the probability for each sample that it belongs to one of the above three diagnostic categories.

Figure III.5 shows the resulting predicted classifications, determined using the algorithm, versus the pathologic diagnosis. This decision algorithm enabled us to diagnose correctly 14 out of 15 normal samples, 13 out of 15 benign samples and 31 out of 31 malignant samples. This initial success indicated there are consistent spectral differences among normal, benign and malignant breast tissue samples and opened the possibility that NIR Raman spectroscopy can be used for clinical diagnosis. Although PCA does not provide information about the chemical basis responsible for diagnosis, this initial success demonstrated that there are consistent spectral differences among normal, benign and malignant breast tissue samples and motivated the development of our Raman spectral model of breast tissue, discussed in Chapter IV.

## *III. D. Research Technologies for Breast Cancer Diagnosis*

New technologies for breast cancer detection fall primarily into two categories: adapted technologies and novel technologies. Adapted technologies are those that involve the adaptation of devices used elsewhere in the clinic to the breast, such as ductal lavage, ductoscopy, MRI and PET. Novel technologies refer to those that have not been employed clinically outside of the research setting. Currently, a variety of optical imaging and spectroscopic techniques are being explored to improve breast cancer diagnosis. They employ visible or near-infrared light, have the potential to provide chemical information and are less invasive than current diagnostic procedures. Optical techniques are only now being introduced clinically and represent relatively new lines of research.

### III. D. 1. Ductal Lavage

The majority of breast cancers begin in the epithelium lining the breast ducts. It can take many years for these cells to grow into a tumor large enough to be detected by mammography, ~1 cm in diameter, or felt during a physical breast exam. Ductal lavage is a minimally invasive procedure that involves collecting samples of cells washed out from the breast ducts and pathological examination to determine whether they are normal, atypical, or malignant. The idea of testing fluid from the nipple was first suggested in the 1950s by Dr. Papanicolaou, the physician who developed the pap smear to test for cervical cancer.

In the procedure, gentle suction is applied to identify which milk ducts produce droplets of fluid on the nipple surface. Next, a microcatheter is inserted into the milk duct and sterile saline is slowly infused to rinse the duct and collect cells. The collected ductal fluid is then stained and microscopically analyzed by a pathologist. A schematic detailing the ductal lavage procedure is shown in Figure III.6. Ductal lavage is not a replacement for standard breast cancer detection tools such as mammography or physical exam.

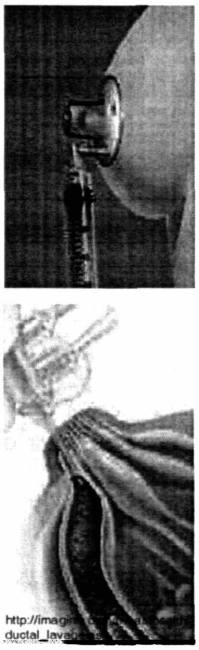

**Figure III.6.** Ductal lavage schematic. © Pro-Duct Health.

A multi-center clinical study of over 500 high-risk women in the United States and Europe examined ductal lavage. All of the women enrolled had normal mammograms and physical exams within 12 months prior to their participation in the study. Preliminary results showed that ductal lavage detected atypical cells in 23.5% of the breasts studied and malignant cells in 0.5% of the breasts studied. However, the presence of atypical cells does not necessarily

signify subsequent breast cancer. In fact, it is believed that, in most cases, these cells don't progress to cancer.

### III. D. 2. Ductoscopy

Fiberoptic ductoscopy adapts endoscopes developed to detect cancer in organs such as the colon, cervix, and esophagus to the study of breast ducts [Berna *et al.* 1991]. It is used to directly visualize the epithelial lining of the breast ducts as well as provide access for retrieval of epithelial cells, by lavage. Because the majority of both benign and malignant breast disease originates in the epithelium, development of a minimally invasive procedure which can directly assess early epithelial changes has important applications to the detection and treatment of these conditions. In the ductoscopy procedure, the breast is first massaged to promote nipple-aspirate fluid, serving to visually identify a ductal orifice. The duct is then dilated and the ductoscope advanced under direct visualization. The ductoscope is typically 0.9 mm in diameter and contains an outer sheath, through which insufflation can occur during the procedure and aspiration can be performed to retrieve epithelial cells for cytologic analysis. The interior of the duct is illuminated, viewed via fiberoptics, and catalogued by videotape [Shen *et al.*, 2000]. If an intraluminal pathology is identified, it can be surgically removed or marked with a small metallic clip for image-guided core biopsy. The limitations of this approach stem from the fact that early cancers are difficult to identify visually, even in organs where clinicians have significant experience using endoscopic devices.

Ductoscopy is primarily used in patients with pathologic nipple discharge [Yamamoto *et al.* 2001]. This population is ideally suited for the ductoscopy procedure, as they generally demonstrate single-duct discharge, making identification of the ductal orifice harboring the

pathology straightforward. Additionally, many of these patients have ductal dilation or ectasia, which makes maneuvering of the scope easier. Over 70% of patients undergoing ductoscopy for nipple discharge are found to have an intraductal papilloma. The papilloma can be localized and excised with the ductoscope. An example of typical findings during mammary ductoscopy in a patient with pathologic nipple discharge are shown in Figure III.7. Ductoscopy is also being evaluated for intra-operative surgical margin assessment and in patients who are at high-risk for developing cancer but have a normal breast exam and imaging studies. There is an isolated report of a series of patients with known breast cancer who underwent intra-operative ductoscopy to assess surgical margins with promising results [Dooley 2000]. The use of ductal lavage for risk assessment has generated a population of high-risk patients who have no imaged evidence of breast malignancy yet are found to have atypical cells within one or more ductal systems. There are a small number of reports of patients who have had mammary ductoscopy of the same ductal system that yielded atypical cytology from ductal lavage, and a variety of pathologic lesions have been identified which range from intraductal papillomas to DCIS and atypical DEH [Dooley *et al.* 2001].

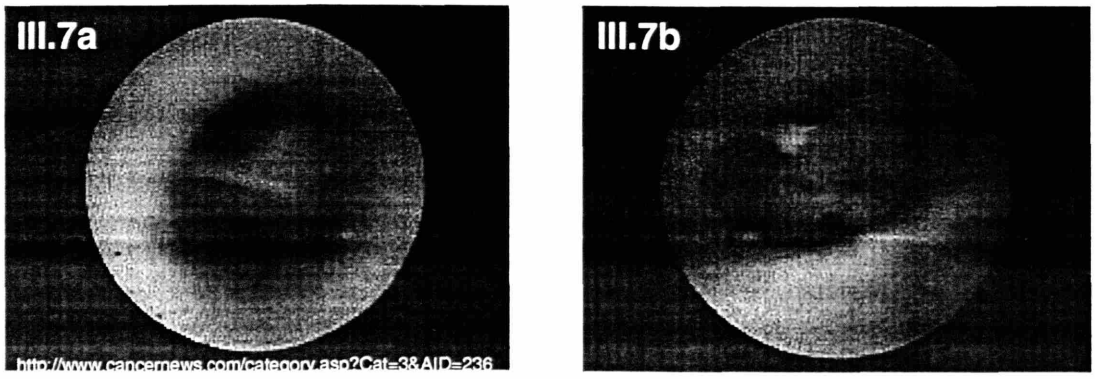


**Figure III.7.** Ductoscopy images: a) a normal bifurcation and b) an intraductal papilloma obstructing the ductal lumen.

However, the clinical significance of these findings has not yet been elucidated. Ductoscopy may provide a means for spectroscopic access to the breast and identification of pre-cancerous changes.

### III. D. 3. Magnetic Resonance Imaging

Magnetic Resonance Imaging (MRI) non-invasively monitors the distribution of water in the body. MRI machines operate through high powered magnets in two groups, a stable field, produced by a main magnet, and a variable field, produced by three gradient magnets. These magnets manipulate the spin properties of hydrogen contained in the water comprising the majority of the human body. A hydrogen atom without an external field will spin on its own in random alignment. In an external magnetic field, the atoms spin will align parallel to the applied field. In an MRI, the main magnet produces an applied magnetic field that aligns the hydrogen atoms in the patient's body parallel to the field. When the magnetic field is turned off, the hydrogen atoms return to regular alignment. In making this spin alignment shift, a change in magnetization results and is detected.

MRI has been considered the imaging procedure of choice in the evaluation of breast implant rupture. Some investigators have found that MRI increased sensitivity for the detection of breast cancer as compared with conventional imaging techniques [Orel 2000]. MRI has been successful in detecting cancers that are mammographically and clinically occult. The ability to detect cancer by MRI relies almost exclusively on the fact that tumors exhibit angiogenesis to support their growth. In order to effectively distinguish small cancers from fatty tissue, contrast material must be administered intravenously. Detection of invasive breast cancer by MRI has sensitivity approaching 100%, but some breast lesions,

such as DCIS, may have much lower rates of detection, 40% sensitivity, due to variable angiogenesis [Morris *et al.* 1997]. MRI is emerging as a valuable diagnostic test for young women in whom the sensitivity of mammography is reduced and appears more accurate than mammography in annual breast cancer surveillance in women with a hereditary risk of breast cancer. In a cohort of 179 women at high risk for developing cancer, mammography detected 7 cancers while MRI detected 13 cancers [Stoutjesdijk *et al.* 2001]. In addition, MRI appears equally sensitive, 99.2%, to the triple diagnostic technique in detecting breast cancer [Drew *et al.* 1999].

Several problems with MRI imaging will require future resolution. Signals from many benign lesions and even normal breast tissue may be enhanced following contrast administration, thereby degrading specificity. Further, there is no universally accepted standard or optimal technique for MRI imaging of the breast and there are no commercial needle localization systems for use with MRI. Lastly, MRI is more expensive than other currently used imaging techniques.

The history of MRI provides a relevant framework for the development of new medical technologies. MRI has become the primary technique throughout the body in the routine diagnosis of many disease processes. Similar to Raman spectroscopy, MRI developed out of a laboratory technique, nuclear magnetic resonance (NMR). During the 1950's and 1960's NMR spectroscopy became a widely used technique for the non-destructive analysis of small samples. Like Raman spectroscopy, many of its applications were at the microscopic level. Initially, MR images were noisy and it took close to five hours to produce a single image. Today, it is possible to image in seconds what used to take hours. The term MRI was adopted soon after imaging of the human body became possible as the public could

more easily adopt a term for an imaging modality without the word "nuclear" in it.

### III. D. 4. Positron Emission Tomography

Positron Emission Tomography (PET) is already in clinical use to image the brain, but its application to other organs is only now being explored. PET involves labeling biochemicals, such as sugars, with positron emitting isotopes, and imaging their uptake in the organ of interest [Phelps 2000]. Once a positron, an antielectron, is emitted, it combines with an electron and annihilation occurs producing two photons traveling in opposite directions. Detectors placed in a ring around the patient record the arrival of the photons. By monitoring the arrival time and positions, the origin of the photon can be calculated and three dimensional images constructed. In contrast to standard methods of anatomical imaging, such as mammography and MRI, PET represents a form of functional imaging of the breast. PET scanning exploits the metabolic difference between benign and malignant cells [Morris *et al.* 2001]. Tumor cells demonstrate increased glucose metabolism, and thus the labeled sugar molecules are proposed to preferentially accumulate in malignant tumors.

F-fluorodeoxyglucose (FDG)-PET imaging allows accurate diagnosis of breast carcinoma, with sensitivity and specificity for both ranging from 80% to 100% [Delbeke and Martin 2001]. By designing better molecular probes, improved diagnostic accuracy may be possible and significant research is focused on this area. However, PET scanning can produce false negative results with small lesions (< 1 cm in size) and well differentiated tumors, such as tubular carcinoma and carcinoma *in situ*. False positive results may occur with inflammatory breast conditions or in breast tissue soon after surgery. FDG-PET scanning may have its greatest value in the local and regional staging of newly diagnosed

breast cancer. Most women with primary invasive breast cancer undergo axillary lymph node dissection, a costly procedure that can be associated with complications. However, now many primary cancers are diagnosed as small invasive cancer without axillary node involvement. PET scanning may help evaluate the status of the axilla and stage patients with locally advanced disease.

### III. D. 5. Diffuse Optical Tomography

Diffuse Optical Tomography (DOT), a promising optical imaging technique, studies the propagation of amplitude modulated pulses of light through the breast. Similar in approach to traditional x-ray mammography, it is non-invasive and can detect lesions deep within the tissue [Tromberg *et al.* 1997; Fantini *et al.* 1998; Quaresima *et al.* 1998; Hebden *et al.* 2001]. An arrangement of sources and detectors in a measurement cup enables three-dimensional images to be constructed. By using light of several different wavelengths, information about the scattering and absorption can be extracted to measure oxy- and deoxy-hemoglobin concentrations and the presence of lipids. However, DOT can only detect a limited number of chemicals and is generally of low resolution, causing small lesions to go undetected. Resolutions of 4 to 13 mm, depending on measurement geometry and a number of other factors, have been reported [Culver *et al.* 2001]. Furthermore, in order to obtain the sensitivity and specificity required for lesion detection in vivo, exogenous agents to improve contrast are often employed [Ntziachristos *et al.* 2000]. Based on this approach, ViOptix, Inc., has developed an instrument which provides two-dimensional maps of hemoglobin distribution and oxygen saturation. The device was employed to 50 mammogram-positive

patients. As an adjunct to mammography, the approach resulted in 92% sensitivity and 67% specificity for detecting ductal carcinoma [Cheng *et al.* 2003].

### III. D. 6. Fluorescence and Diffuse Reflectance Spectroscopies

Optical spectroscopic techniques are also under investigation for breast cancer diagnosis. Unlike DOT, these techniques sample the tissue locally. Light delivery and collection can be accomplished by means of optical fibers that could readily be incorporated into a biopsy needle. As the needle was inserted or withdrawn, depth information would be obtained. As opposed to standard biopsy, a spectroscopic transdermal needle measurement has the advantage of providing immediate diagnosis. As a result, spectroscopy has the potential to reduce both the likelihood of a non-diagnostic biopsy that would require repeat needle or surgical biopsy, and patient anxiety by eliminating the currently unavoidable wait for a traditional histopathology diagnosis. Furthermore, with the development of minimally invasive breast cancer therapies, such as radiofrequency ablation which relies on insertion of a thin metal probe into the breast, there is the potential that diagnosis and treatment could be performed in a single procedure [Fornage *et al.* 2004]. Optical spectral techniques that have been applied to breast tissue analysis include fluorescence, diffuse reflectance, and Raman spectroscopies.

Fluorescence is emission of light from a singlet excited state, in which the electron in the excited orbital has the same spin orientation as the ground state electron. The fluorescing molecule stays in the excited state for a finite time, usually 1-10 nanoseconds. Fluorescence spectra can be used to identify fluorophores and their concentrations in the tissue. Various endogenous tissue flourophores include metabolic substances such as the reduced form of

nicotinamide adenine dinucleotide (phosphate) NAD(P)H and flavins, aromatic amino acids such as tryptophan, tyrosine and phenylalanine, structural proteins such as collagen and elastin, several porphyrins, and some lipids such as ceroid and lipofuscin. Each of these fluorophores is excited and emits at a specific wavelength in the near UV/visible range of light. Fluorescence spectroscopy has been applied to *ex vivo* breast tissue for disease diagnosis and trends which correlate with disease have been observed [Gupta and Majumder 1997; Yang *et al.* 1996; Majumder *et al.* 1998]. Fluorescence produces relatively large signals. However, the small number of endogenous fluorophores present in breast tissue coupled with their broad spectral lineshapes are limiting factors. Fluorescence spectroscopy of breast has the potential to provide information not available from Raman data and is discussed in greater detail in Chapter VIII. However, fluorescence spectra can be distorted by the interplay of tissue scattering and absorption.

Preliminary studies have examined the efficacy of diffuse reflectance spectroscopy in the diagnosis of breast lesions, as well as in the assessment of tumor margins and sentinel lymph node metastasis [Bigio *et al.* 2000]. These studies monitor changes in the absorption and reduced scattering coefficients among tissues with different pathologies. Combining fluorescence and diffuse reflectance spectroscopies has shown promise in the breast [Yang *et al.* 1996]. Studies are currently underway in our laboratory to assess the power of fluorescence and diffuse reflectance spectroscopies for breast cancer diagnosis. The preliminary data analysis is presented in Chapter VIII.

## *III. E. Raman Instrumentation*

### III. E. 1. General Considerations

Despite its rich information content, Raman spectroscopy has not experienced extensive clinical investigation because the Raman effect is weak, comprising a very small fraction, about 1 in $10^7$, of the incident photons. However, within the past few decades a variety of instrumental developments, primarily new lasers, detectors and methods for rejecting elastically scattered light, have expanded the utility of Raman spectroscopy for biomedical applications. Compact diode lasers can provide stable narrow-line excitation over a range of wavelengths in the NIR region. Silicon deep-depletion charge coupled device (CCD) detectors are best suited for tissue Raman spectroscopy, because of their relatively high sensitivity and lack of fixed-pattern noise [Murray and Dierker 1986].

Advances in thermoelectrically cooled detectors may soon allow them to replace liquid nitrogen cooled cameras, allowing easier clinical implementation. The application of holographic filter technology to Raman spectroscopy has also led to increased utilization of the technique in medical settings [Carabba *et al.* 1990]. Because the Raman effect is weak, the intense elastically scattered light must be removed so that it does not overwhelm the Raman signal. Holographic notch filters are devices for rejecting scattered light and are specific for the excitation wavelength employed. These new technologies make rapid data acquisition as well as the design of compact, robust Raman instruments, needed for clinical applicability, a reality.

### III. E. 2. Laboratory Raman System: Confocal Microscope and Macroscopic System

The experimental system, shown in Figure III.8, utilized for our *in vitro* Raman spectroscopy

studies, is designed for versatility. It is capable of collecting spectra from both macroscopic size biopsies and thin microscopic sections of tissue. It is also capable of collecting data at a wide range of wavelengths given the appropriate beamsplitters and notch filters. The versatility of this system is ideal for exploring new approaches to studying Raman spectroscopy of human tissue. Raman excitation is provided by an argon ion laser-pumped Ti:sapphire laser (Coherent Innova 90C/Spectra Physics 3900S, Coherent Inc., Santa Clara, CA). The Ti:sapphire laser is tunable from 720 nm to 1000 nm, however for biological Raman studies we employ 830 nm excitation. Laser power is continuously monitored by a PDA55 photodiode (ThorLabs, Newton, NJ). The excitation laser beam traverses a bandpass

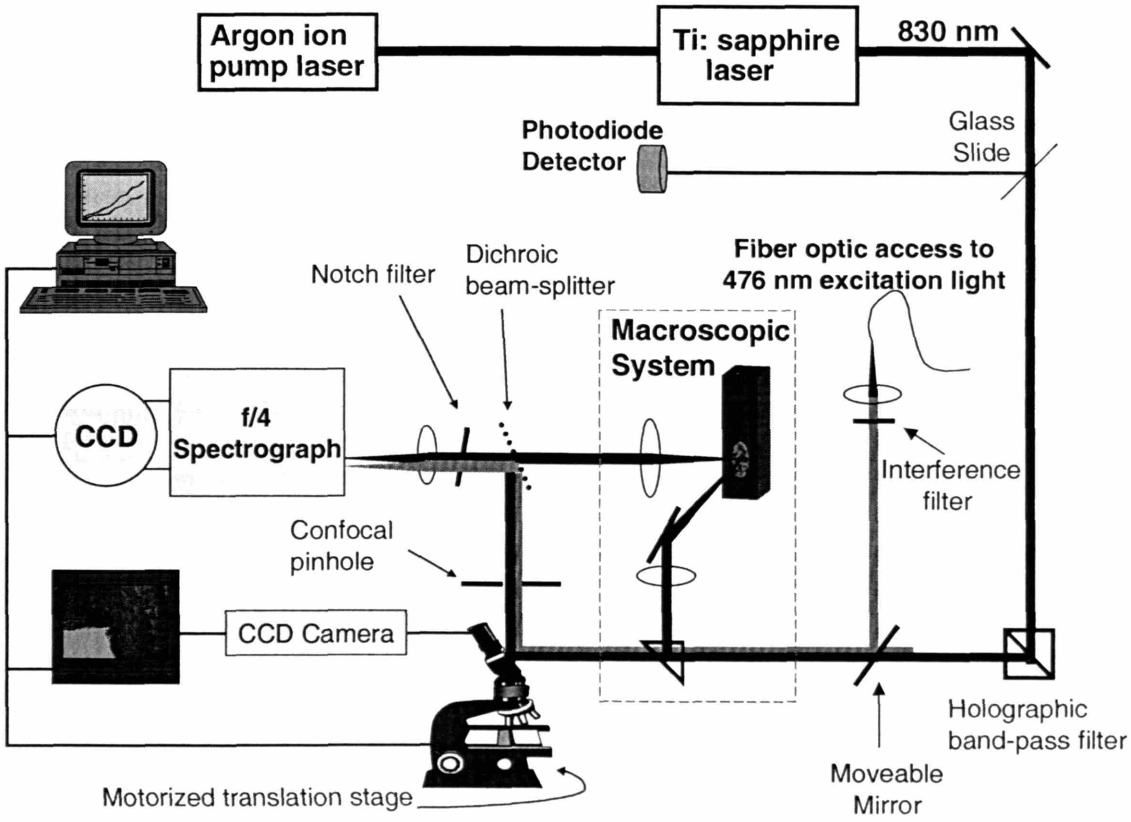


**Figure III.8.** Schematic of the laboratory Raman system.

filter (Kaiser Optical Systems, Ann Arbor MI) and is collimated by two lenses to improve the spatial resolution of the confocal Raman microscope. The excitation laser beam can either be focused onto a macroscopic sample or launched into the microscope via a prism that can be translated in and out of position.

III. E. 2. a) Confocal Raman Microscope

When the prism is out of position, the collimated laser is coupled into a microscope (Zeiss Axioscope 50, Zeiss, Thornwood, NY) and deflected towards the sample via a dichroic beamsplitter. A CCD camera atop the microscope allows for registration of the focused laser spot with a white light image to verify the morphologic structures from which the spectra were collected. The microscope is fitted with two phase contrast objectives (10x and 63x) which are used for visual inspection of the samples. By adjusting the flip-mirror so that the light is directed towards the CCD camera, a VCR and frame-grabber can be used to record image.

The microscope itself is equipped with a range of objectives, both normal and phase contrast. For the studies presented here we used a 63x infinity-corrected water immersion objective (Zeiss Achroplan, NA 0.9). This microscope objective both focuses the excitation and collects the Raman scattered light in a backscattering geometry. Lateral resolution of this lens is ~2 μm. The Raman microscope is equipped with a mapping stage enabling Raman micro-imaging. As both the detector and the microscope stage are computer controlled, spectral maps of the tissue can be created by moving the translation stage in a raster-scan pattern under the microscope objective. The minimum step size of the motorized translation stage (Prior Scientific) is 1 μm in the x direction and 1.1 μm in the y direction. A

dichroic beamsplitter and mirror combination redirect the Raman-scattered light to the spectrograph system. The light is passed through a confocal pinhole to increase axial resolution, filtered by a holographic Raman notch filter (Kaiser Optical Systems, Ann Arbor MI) for laser line removal, and coupled into an f/4 0.25 m Czerny-Turner spectrograph (Chromex 250IS/SM spectrograph monochromator, Albuquerque, NM) with an f/4 achromatic lens. At the smallest confocal aperture diameter, ~300 μm, the spatial resolution of the microscope is ~$(2\ \mu m)^3$.

The spectrograph itself has an adjustable slit and a turret, which holds three gratings for a range of measurements. For the Raman studies a 600 grooves/mm grating blazed at 1 μm, linear dispersion of 4.3 nm/mm, was used along with the 140 μm spectrograph entrance slit setting, providing ~ 8.5 $cm^{-1}$ resolution. The grating disperses the light onto a back-illuminated, deep depletion, liquid nitrogen cooled CCD detector (Princeton Instruments, Princeton, NJ). The CCD is composed of a 256x1024 array of 27 μm x 27 μm pixels and is controlled by WinSpec software (Roper Scientific). A spectral range of ~200-2000 $cm^{-1}$ is typically collected.

Simply by changing the excitation source, the filters/beamsplitters, and spectrograph grating, the system can be adapted for fluorescence spectroscopy. Fluorescence measurements can be obtained at a variety of excitation wavelengths. In particular 352 nm, 476 nm, and 647 nm excitation light can be delivered to the system via fiber optics from an argon ion laser (Coherent Innova 700, Coherent Inc., Santa Clara, CA) in an adjacent laboratory. The switch between Raman and fluorescence can be made in less than one minute.

III. E. 2. b) Raman Macroscopic System

The excitation laser light can also be diverted from the microscope via a prism to study macroscopic samples. In this case, the light is focused and directed to the sample via a mirror at a 60° angle. The excitation spot is ~100 μm in diameter. Diffusion in the tissue results in a sampling volume of ~1mm$^3$, depending on the sample properties. The Raman scattered light is collected with an f/1.2 camera lens, notch filtered and then focused onto the spectrograph. The switch between the Raman macroscopic and microscopic systems involves considerably more system realignment than the switch between Raman and fluorescence.

## III. E. 3. Clinical Raman System: Raman Optical Fiber Probe

For clinical studies, we have developed portable compact instrumentation including a Raman

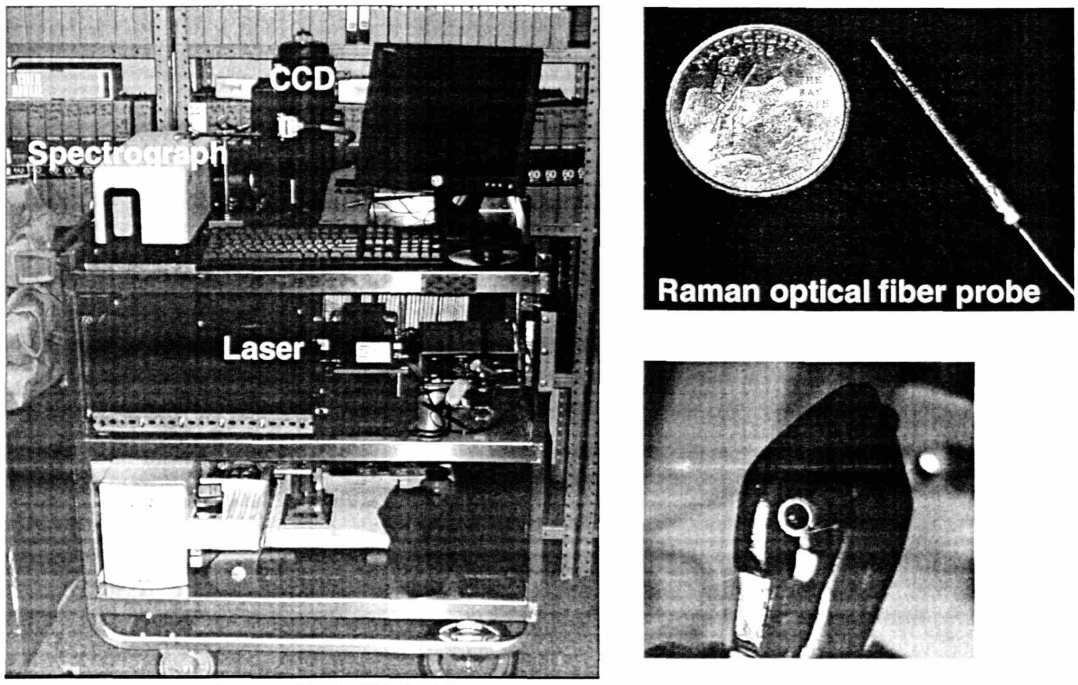


**Figure III.9.** Clinical Raman system and Raman optical fiber probe.

optical fiber probe for remote sampling during surgical procedures. Photographs of the instrumentation and Raman probe are shown in Figure III.9. A schematic of the

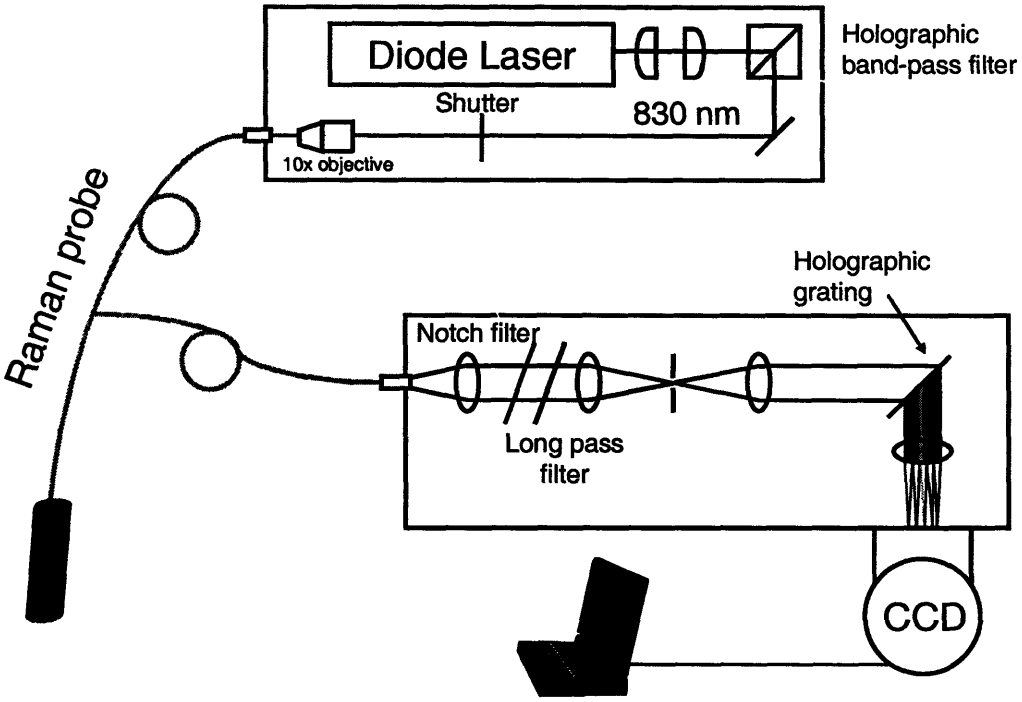


**Figure III.10.** Schematic of the clinical Raman system.

experimental system used in the clinical studies, Chapters V and VII, is shown in Figure III.10. Light from an InGaAS diode laser (Process Instruments, Salt Lake City, UT), tuned to 830 nm, is collimated by two cylindrical lenses, directed through a bandpass filter (Kaiser Optical Systems, Inc., Ann Arbor, MI), redirected by a gold coated mirror and focused into the Raman probe excitation fiber by a 10x microscope objective (Newport, Irvine, CA). The laser output is under computer control. A shutter (Uniblitz, Rochester, NY) is employed prior to the microscope objective to prevent laser light from emerging from the probe except when collecting data. The shutter is also under computer control and is triggered by the onset of data collection. The proximal linear array of collection fibers from the Raman probe are input to the f/1.8 spectrograph (Kaiser) which collimates the light before it passes through

an RG850 long wavelength-pass filter (Schott, Elmsford, NY), to reduce an intense portion of the silica fiber background, and the Rayleigh line removed with a notch filter. The light is then focused onto a slit and re-collimated for dispersion by the holographic grating. Finally, the dispersed light is focused onto a liquid nitrogen cooled, back-illuminated, deep depletion CCD detector. The CCD is interfaced with a computer and controlled with code written in LabVIEW (v. 6.1, National Instruments, Inc., Austin, TX). The grating dispersion of 0.04 $cm^{-1}$/mm yields a two pixel spectral resolution of 9.4 $cm^{-1}$ for the 200 μm collection fiber/ slit diameter.

III. E. 3. a) Raman Optical Fiber Probe

Minimally invasive clinical applications of Raman spectroscopy require remote sampling via optical fiber probes. These probes must be able to collect high SNR spectra in clinically relevant timeframes with safe levels of laser exposure. This requires maximizing signal collection and efficiency while minimizing all sources of noise. Our Raman optical fiber probe implements an optical design strategy to fully utilize system throughput by characterizing the Raman distribution from tissue [Motz *et al.* 2004]. The approach optimizes collection efficiency, minimizes noise and has resulted in a small diameter, highly efficient Raman probe capable of collecting high-quality data in 1 s.

The design of Raman fiber optic probes is quiet challenging. Efficient transmission of NIR light for remote detection requires the use of fused silica optical fibers [Shim and Wilson 1997]. However, even with low laser excitation powers, below 10 mW, the fused silica fiber background is intense and saturates the detector for collection times under 0.1 s. The fiber background is comprised of Raman light from the fused silica core, fluorescence

from impurities and dopants used to produce fibers of a particular numerical aperture (NA), and signal from various jacket materials. This fiber background, generated from 2 to 3 feet traversed in the fibers, masks the tissue Raman signal which is generated from only a 1 mm depth of tissue. In addition to obscuring and distorting the spectrum of interest, the intense fiber background adds shot-noise to the signal.

To remove much of this background, we employ dielectric filters at the distal end of the probe. The delivery fiber is terminated with a short wavelength-pass, or band-pass, filter that transmits the laser excitation light while blocking the longer wavelength spectral background generated in the delivery fiber. Also, the distal end of the collection fibers are preceded by a long wavelength-pass, or notch, filter, which transmits the tissue Raman

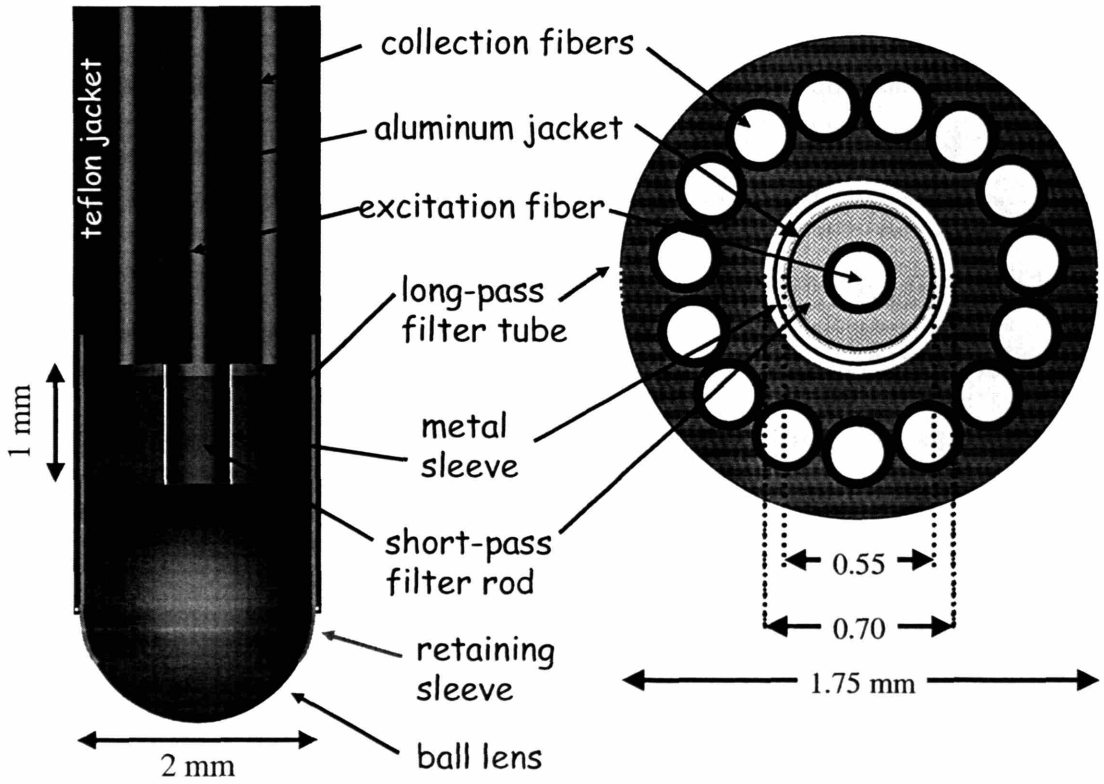


**Figure III.11.** Schematic of the Raman optical fiber probe.

spectrum, while blocking backscattered laser light. The filters must perform these functions over the range of angles corresponding to the NA of the fibers they serve.

The laboratory currently has two prototype versions of Raman optical fiber probes that are front-viewing. The first, shown in Figure III.11, contains 15 collection fibers, resulting in a probe diameter of 2.5 mm. The second is a smaller diameter probe with 9 collection fibers and a 2.0 mm diameter. The probes are otherwise identical. The left hand side of Figure III.11 is a longitudinal view of the probe tip, while the right hand side is a cross-sectional view at the level of the fiber-filter interface. There is a central excitation fiber with an aluminum jacket for optical isolation. The central excitation fiber has a 200 μm core with a 0.22 NA. The collection fibers are also 200 μm core, but have a 0.27 NA which is closely matched to that of the spectrograph. The filters are secured to the fibers with sodium silicate and the entire fiber bundle/filter module is encased with black Teflon for binding and protection. The distal tip of the probe contains an anti-reflection coated sapphire ball lens (MKPhotonics, Albuquerque, NM) secured in a crimped stainless steel tube with epoxy. Sapphire was chosen as it exhibits no fluorescence and has sharp prominent Raman bands, only one of which falls within the spectral range utilized for data analysis. The steel tube is also affixed to the fiber-bundle/filter assembly. The probe length is 4 meters. All components of the probe are constructed of medical grade materials that can withstand standard cold gas ethylene oxide sterilization for surgical procedures.

The proximal end of the excitation fiber is terminated with a standard FC connector that provides a relatively reproducible fiber geometry and straightforward laser coupling in the clinical environment. The linear array of collection fibers are terminated with a modified BNC connector and coupled to the spectrograph with a customized adaptor plate that was

built in house. The BNC connector snaps into place on the adaptor plate, however, this coupling is problematic for a number of reasons and is currently being updated. The coupling does not ensure precise alignment of the linear array with the spectrograph slit and alignment must be checked prior to data collection. Perpendicular alignment of the linear area of collection fibers can usually be achieved with operating room (OR) lights. However, OR lights are bright and can saturate the detector. Further, the BNC connector is the portion of the clinical instrumentation that allows the majority of light to enter the system. Thus, when acquiring data with a light tight box, as in Chapter V.B, the BNC coupling to the spectrograph must be covered with a black cloth.

The first Raman optical fiber probe contained a dual ring of collection fibers. This may prove useful for obtaining depth information on Raman scatterers by collecting light from the inner and outer rings separately. The laboratory also has a side viewing probe prototype. It is based on a design which replaces the sapphire ball lens with a half-ball lens backed by a mirror. Lens and mirror are configured at 45° providing collection capabilities similar to the front viewing probe. The performance of the side-viewing probe is currently being tested. There are some problems with heating of the stainless steel tube associated with the side viewing Raman probe.

## *Acknowledgements*

Jason Motz was responsible for the development of the Raman optical fiber probe as well as the clinical instrumentation. Many of the images in this chapter have been reproduced from *Applied Optics* [Motz *et al.* 2003] with permission from The Optical Society of America, *Photochemistry and Photobiology* [Manoharan *et al.* 1998] with permission from The American Society for Photobiology, and *Techniques in Gastrointestinal Endoscopy* [Tunnell *et al.* 2003] with permission from Elsevier.

## *References*


Alfano RR, Liu CH, Sha WL, Zhu HR, Akins DL, Cleary J, Prudente R and Cellmer E (1991). "Human Breast Tissues Studied by IR Fourier Transform Raman Spectroscopy." Lasers Life Sci **4**: 23-28.

Baraga JJ, Feld MS and Rava RP (1992). "*In situ* Optical Histochemistry of Human Artery Using near Infrared Fourier Transform Raman Spectroscopy." Proc Natl Acad Sci **89**(8): 3473-3477.

Berna JD, Garcia-Medina V and Kuni CC (1991). "Ductoscopy: A New Technique for Ductal Exploration." Eur J Radiol **12**(2): 127-9.

Bernstein PS, Zhao DY, Wintch SW, Ermakov IV, McClane RW and Gellermann W (2002). "Resonance Raman Measurement of Macular Carotenoids in Normal Subjects and in Age Related Macular Degeneration Patients" Opthalmology **109**(10): 1780-7.

Bown SG, Briggs G, Kelley C, Lakhani S, Pickard D, Ripley PM, Rose IG and Saunders C and Bigio IJ (2000). "Diagnosis of Breast Cancer Using Elastic-Scattering Spectroscopy: Preliminary Clinic Results." J Biomed Opt **5**: 221-228.

Campion A and Kambhampati P (1998). "Surface-Enhanced Raman Scattering." Chem Society Reviews **27**(241): 241-250.

Carabba MM, Spencer KM, Rich C, and Rauh D (1990). "The Utilization of a Holographic Bragg Diffraction Filter for Rayleigh Line Rejection in Raman Spectroscopy," Appl Spectrosc **44**: 1558-1561.

Cheng XF, Mao JM, Bush R, Kopans DB, Moore RH and Chorlton M (2003). "Breast Cancer Detection by Mapping Hemoglobin Concentration and Oxygen Saturation." Appl Opt **42** (31): 6412-6421.

Culver JP, Ntziachristos V, Holboke MJ and Yodh AG (2001). "Optimization of Optode Arrangements for Diffuse Optical Tomography: A Singular-Value Analysis." Opt Lett **26**: 701-703.

Diem M (1993). Introduction to Modern Vibrational Spectroscopy. New York, Wiley.

Dooley WC (2000). "Endoscopic Visualization of Breast Tumors." JAMA **284**(12): 1518.

Dooley WC, Ljung BM, Veronesi U, Cazzaniga M, Elledge RM, O'Shaughnessy JA, Kuerer HM, Hung DT, Khan SA, Phillips RF, Ganz PA, Euhus DM, Esserman LJ, Haffty BG, King BL, Kelley MC, Anderson MM, Schmit PJ, Clark RR, Kass FC, Anderson BO, Troyan SL, Arias RD, Quiring JN, Love SM, Page DL and King EB (2001). "Ductal Lavage for Detection of Cellular Atypia in Women at High Risk for Breast Cancer." J Natl Cancer Inst **93**:1624-32.

Drew PJ, Turnbull LW, Chatterjee S, Read J, Carleton PJ, Fox JN, Monson JRT and Kerin MJ (1999). "Prospective Comparison of Standard Triple Assessment and Dynamic Magnetic Resonance Imaging of the Breast for the Evaluation of Symptomatic Breast Lesions." Ann Surg **230**(5): 680-685.

Fantini S, Walker SA, Franceschini MA, Kaschke M, Schlag PM and Moesta KT, (1998). "Assessment of the Size, Position, and Optical Properties of Breast Tumor *In Vivo* by Noninvasive Optical Methods." Appl Opt **37**: 1982-1989.

Fornage BD, Sneige N, Ross MI, Mirza AN, Kuerer HM, Edeiken BS, Ames FC, Newman LA, Babiera GV and Singletary SE (2004). "Small (<= 2 cm) Breast Cancer Treated with US-Guided Radiofrequency Ablation: Feasibility Study." Radiology **231**(1): 215-224.

Frank CJ, McCreery RL and Redd DCB (1995). "Raman Spectroscopy of Normal and Diseased Human Breast Tissues." Anal Chem **67**: 777-783.

Frank CJ, Redd DCB, Gansler TS and McCreery RL (1994). "Characterization of Human Breast Biopsy Specimens with Near-IR Raman Spectroscopy." Anal Chem **66**: 319-326.

Gupta PK, Majumder SK and Uppal A (1997). "Breast Cancer Diagnosis Using $N_2$ Laser Excited Autofluorescence Spectroscopy." Lasers Surg Med **21**: 417-422.

Hebden J, Veenstra H, Dehghani H, Hillman E, Schweiger M, Arridge S and Delpy D (2001). "Three-Dimensional Time-Resolved Optical Tomography of a Conical Breast Phantom." Appl Opt **40**: 3278-3287.

Jeanmaire DL and Van Duyne RPV (1977). "Surface Raman Spectroelectrochemistry .1. Heterocyclic, Aromatic, and Aliphatic-Amines Adsorbed on Anodized Silver Electrode." J Electroanal. Chem **84**(1): 1-20.

Kerker M, Wang DS, Chew H, Siiman O and Bumm LA (1982). Surface Enhanced Raman Scattering. Chang RK and Furtak TE Eds., New York, Plenum Press:109-128.

Kline NJ and Treado PJ (1997). "Raman Chemical Imaging of Breast Tissue." J Raman Spectrosc **28**: 119-124.

Kneipp K, Wang Y, Kneipp H, Perelman LT, Itzkan I, Dasari RR and Feld MS (1997). "Single Molecule Detection Using Surface-Enhanced Raman Scattering (SERS)." Phys Rev Lett **78**, 1667-1670.

Kneipp K, Kneipp H, Itzkan I, Dasari RR and Feld MS (1999). "Ultrasensitive Chemical Analysis by Raman Spectroscopy." Chemical Reviews **99**: 2957.

Majumder SK, Gupta PK, Jain B and Uppal A (1998). "UV Excited Autofluorescence Spectroscopy of Human Breast Tissues for Discriminating Cancerous Tissue from Benign Tumor and Normal Tissue." Lasers Life Sci **00**: 1-16.

Manoharan R, Baraga JJ, Feld MS asnd Rava RP (1992). "Quatitative Histochemical Analysis of Human Artery using Raman Spectroscopy." Photochem Photobio B: Biol **16**: 211-233.

Manoharan R, Baraga JJ, Rava RP, Dasari RR, Fitzmaurice M and Feld MS (1993). "Biochemical Analysis and Mapping of Atherosclerotic Human Artery Using FT-IR Microspectroscopy." Atherosclerosis **103**: 181-193.

Manoharan R, Wang Y and Feld MS (1996). "Review: Histochemical Analysis of Biolgical Tissues uing Raman Spectroscopy." Spectroschim Acta Part A **52**: 215-249.

Manoharan R, Shafer K, Perelman L, Wu J, Chen K, Deinum G, Fitzmaurice M, Myles J, Crowe J, Dasari RR and Feld MS (1998). "Raman Spectroscopy and Fluorescence Photon Migration for Breast Cancer Diagnosis and Imaging." Photochem Photobiol **67**: 15-22.

McCreery RL (2000). Raman Spectroscopy for Chemical Analysis. New York, Wiley.

Morris EA, Schwartz LH, Dershaw DD, van Zee KJ, Abramson AF and Liberman L (1997). "MR Imaging of the Breast in Patients with Occult Primary Breast Carcinoma." Radiology **205**:437-40.

Morris MD (1992). Applied Laser Spectroscopy. Andrews, DL Ed., VCH Publishers Inc. New York, Chapter 6.

Motz JT, Hunter M, Galindo LH, Gardecki JA, Kramer JR, Dasari RR and Feld MS (2003). "Optical Fiber Probe for Biomedical Raman Spectroscopy." Appl Opt **43**: 542-554.

Murray CA and Dierker SB (1986). "Use of an Unintensified Charge-Coupled Device Detector for Low-Light-Level Raman Spectroscopy," J Opt Soc Am **3**: 2151-2159.

Myers AB and Mathies RA "Biological Applications of Raman Spectroscopy" Resonance Raman Spectra of Polyenes and Aromatics. Vol. 2, Spiro TG Ed., John.

Ntziachristos V, Yodh AG, Schnall M and Chance B (2000). "Concurrent MRI and Diffuse Optical Tomography of Breast After Indocyanine Green Enhancement." P Natl Acad Sci USA **97**: 2767-2772.

Orel SG (2000). "MR Imaging of the Breast." Radiol Clin North Am **38**: 899-913.

Otto A (1984). "Surface- Enhanced Raman Scattering: 'Classical' and 'Chemical' Origins." Light Scattering in Solids IV. Cardona M and Guntherodt G Eds. Berlin, Germany, Springer-Verlag, **1984**: 289.

Phelps ME (2000). "Positron Emission Tomography Provides Molecular Imaging of Biological Processes." PNAS **97**: 9226-9233.

Quaresima V, Matcher SJ and Ferrari M (1998). "Identification and Quantification of Intrinsic Optical Contrast for Near-Infrared Mammography." Photochem Photobiol **67**(1): 4-14.

Raman CV, Krishnan KS (1928). "A New Type of Secondary Radiation." Nature **121**: 501-502.

Redd DCB, Feng ZC, Yue KT and Gansler TS (1993). "Raman Spectroscopic Characterization of Human Breast Tissues: Implications for Breast Cancer Diagnosis." Appl Spectrosc **47**: 787-791.

Sadtler (1974). Sadtler Standard Spectra. Philadelphia, Sadtler Research Laboratories.

Schaeberle MD, Kalasinsky VF, Luke JL, Lewis EN, Levin IW and Treado PJ (1996). "Raman Chemical Imaging: Histopathology of Inclusions in Human Breast Tissue." Anal Chem **68**: 1829-1833.

Shah N, Cerussi A, Eker C, Espinoza J, Butler J, Fishkin J, Hornung R and Tromberg B (2001). "Noninvasive Functional Optical Spectroscopy of Human Breast Tissue." P Natl Acad Sci USA **98**(8): 4420-4425.

Shafer-Peltier KE, Haynes CL, Glucksberg MR, Van Duyne RP (2003). "Toward a Glucose Biosensor Based on Surface-Enhanced Raman Scattering." J Am Chem Soc **125**: 588-593.

Shen KW, Wu J, Lu JS, Han QX, Shen ZZ, Nguyen M, Shao ZM and Barsky SH (2000). "Fiberoptic Ductoscopy for Patients with Nipple Discharge." Cancer **89**(7): 1512-1519.

Shim M and Wilson B (1997). "Development of an *In Vivo* Raman Spectroscopic System for Diagnostic Applications." J Raman Spectrosc **28**: 131-142.

Stoutjesdijk MJ, Boetes C, Jager GJ, Beex L, Bult P, Hendriks JHCL, Laheij RJF, Massuger L, van Die LE, Wobbes T and Barentsz JO (2001). "Magnetic Resonance Imaging and Mammography in Women with a Hereditary Risk of Breast Cancer." J Natl Cancer Inst **93**(14):1095-1102.

Tromberg BJ, Coquoz O, Fishkin JB, Pham T, Anderson ER, Butler J, Cahn M, Gross JD, Venugopalan V and Pham D (1997). "Non-Invasive Measurements of Breast Tissue Optical Properties Using Frequency-Domain Photon Migration." Philos Trans R Soc Lond B **352**(1354), 661-668.

Yamamoto D, Shoji T, Kanawashi H, Nakagawa H, Haijima H, Gondo H and Tanaka K

(2001). "A Utility of Ductography and Fiberoptic Ductoscopy for Patients with Nipple Discharge." Breast Cancer Res Treat **70**(2): 103-108.

Yang Y, Katz A, Celmer EJ, Zurawska-Szczepaniak M and Alfano RR (1997). "Fundamental Differences of Excitation Spectrum Between Malignant and Benign Breast Tissues." Photochem Photobiol **66**(4): 518-522.

# Chapter IV. Data Processing

Raman spectroscopy is a powerful tool for determining chemical information about a biological specimen. It has been used in numerous applications to obtain both qualitative and quantitative analyses of samples. As a result, many analytical techniques of varying degrees of sophistication have emerged for analyzing Raman spectra. The challenge is to condense the large amount of spectral information provided by Raman spectroscopy into an accurate and easily interpretable form. Researchers have applied a range of techniques, from peak-height ratios to multivariate models, to extract chemical information about a sample. The purpose of this chapter is to discuss approaches that are commonly used to analyze Raman spectra.

## *IV. A. Data Preprocessing*

Proper interpretation of Raman spectra requires several preprocessing steps to calibrate the data and configure it into its most useful form. The Raman data acquired undergoes similar preprocessing whether it is collected using the macroscopic laboratory system, the microscope, or the clinical Raman system *via* the Raman probe. This ensures reproducibility of the data between systems, users, and daily conditions.

### IV. A. 1. Wavenumber Calibration

Each day, a wavenumber calibration must be performed to determine the Raman band frequencies. Significant changes may occur in the pixel position of a particular band with changes in the alignment of the instrumental system. The linear relationship between wavelength and dispersion by the spectrograph provides an easy method for wavelength calibration by using the spectral lines from atomic emissions, which are readily available from pen lamps containing gases such as neon. However, accurate conversion from wavelength (nm) to Raman shift ($cm^{-1}$) requires precise knowledge of the excitation laser wavelength. Even slight day-to-day drift in the laser wavelength can cause errors on the order of a few wavenumbers, depending on the wavelength region used. For example, a change from 830 nm to 830.2 nm, which is a typical daily variation observed with diode lasers, results in a 2.9 $cm^{-1}$ shift. Thus in Raman spectroscopy, a wavenumber calibration can either be performed by measuring both the laser line frequency and spectral lines or more simply the bands from a well-characterized Raman scatterer can provide calibration in a single measurement. This single measurement automatically accounts for variations in laser frequency because the Raman shifts are measured relative to the excitation wavelength.

Toluene, a liquid, and 4-acetamidophenol, a solid, both provide excellent standards for wavenumber calibration in our region of analysis. Their Raman spectra, acquired with 830 nm excitation, are shown in Figure IV.1. Because of the inverse relationship between Raman shift and wavelength, the correlation of CCD pixel to wavenumber is most accurately established by calibration through a forth order polynomial. This relationship is then applied to the data, providing Raman band assignments.

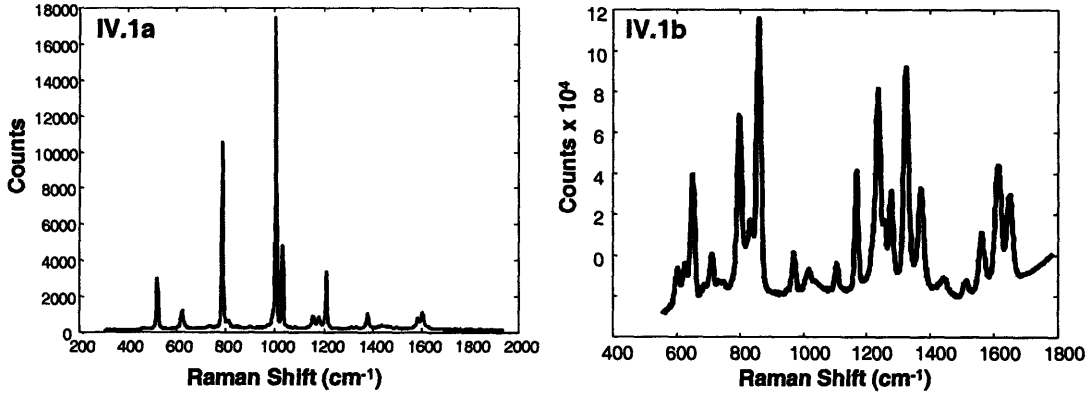


**Figure IV.1.** Raman spectra of species used for wavenumber calibration: a) toluene and b) 4-acetamidophenol.

## IV. A. 2. Spectral Response Correction

It is also necessary to correct Raman spectra for the system wavelength response. This allows comparison of spectra taken from different experimental systems or from the same system on different days. Correction is accomplished by collecting light from a wavelength-calibrated tungsten white light source. Our current white light source is a tungsten halogen lamp (LS-1, Ocean Optics, FL). The light is scattered from a reflectance standard that has a flat spectral response, typically $BaSO_4$. The reflectance standard is tightly packed and placed in the sample position. Division of the data by this calibration white light spectrum corrects

for spectral variations induced by optical component absorption losses, filter responses, notch filter position or angle, the grating efficiency, the quantum efficiency of the CCD detector, and fixed pattern noise. White light spectra from the macroscopic and microscopic laboratory systems as well as the clinical Raman system are shown in Figure IV.2.

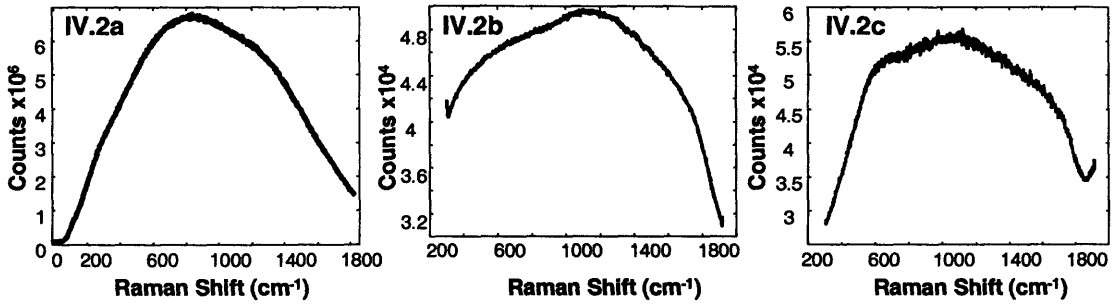


**Figure IV.2.** White light spectra acquired with different instruments: a) the clinical system and Raman optical fiber probe, b) the macroscopic and c) microscopic laboratory systems.

## IV. A. 3. Filtering

When a cosmic ray, a particle from outer space such as a helium nucleus, interacts with the CCD, it creates charge in those pixels it passes through. As a result, sharp spectral features often appear in the data in addition to the Raman bands. Cosmic rays distort the intensity of Raman bands and produce errors in data analysis. Contributions from cosmic rays are removed using a derivative filter. Derivative filters provide a quantitative measurement for the rate of change in pixel brightness. Because cosmic rays are quite narrow compared to Raman peaks, derivative filtering is an effective method for their removal. Specifically, if any term in the derivative of the spectrum is greater than 2.5 times the average derivative of the neighboring 15 pixels, then the corresponding term in the spectrum is replaced with the average of the two values 3 pixels away on either side.

## IV. A. 4. Fluorescent Background Removal

Raman spectra of biological samples are often accompanied by strong background fluorescence. This background fluorescence varies from sample to sample and when particularly strong inhibits our ability to interpret the Raman spectrum. The origin of the fluorescence from tissue at 830 nm excitation is presently unknown, although collagen, elastin, calcifications, ceroid, and necrotic materials are all thought to fluoresce at this excitation wavelength. The background fluorescence interferes with multivariate analysis methods and must be removed prior to data analysis. This can be accomplished by a variety of methods including Fourier transforms, differential Raman spectroscopy, point difference derivatives, spline fitting, and Savitsky-Golay derivatives [Baraga *et al.* 1992; Shaver 2001]. Since the fluorescence background has much broader features than the Raman bands, we typically employ a fifth order polynomial fit and subtraction for background removal. Previous experiments in our laboratory have shown that the background can be satisfactorily removed by using this approach and that a fifth-order polynomial accurately emulates the slowly varying fluorescence spectrum [Brennan 1995; Brennan *et al.* 1997]. Resultant

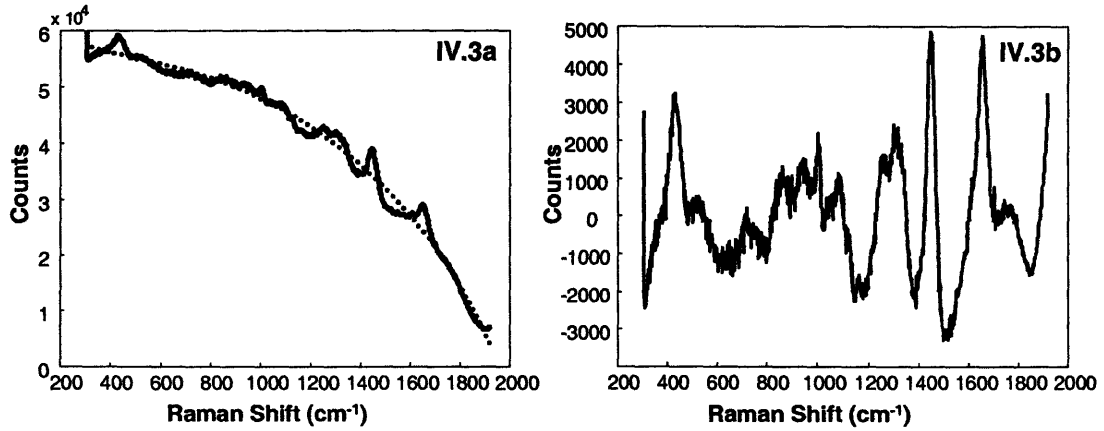


**Figure IV.3.** Background removal: a) Raman spectrum (solid line), fifth order polynomial fit (dotted line) and b) resultant Raman spectrum with fluorescence background removed.

Raman spectra will always have negative regions when using this approach. Figure IV.3 shows a measured Raman spectrum of breast tissue, acquired on the macroscopic laboratory system. Also shown are the fifth order polynomial fit and resultant Raman spectrum with background removed. The models used to interpret the Raman data, discussed in section IV.C, must be processed in the same manner, using fifth order polynomial subtraction. However, the process of background removal produces slight distortions in the Raman spectrum resulting in errors in analysis. There are ongoing investigations in our laboratory to quantify the effect of increasing background fluorescence on the prediction error. Also, methods are under development to reduce the slight error induced by the fifth order polynomial background removal.

### IV. A. 5. Normalization

There are many approaches to intensity normalization that can be taken, depending on the application. Strict quantitative analysis requires accurate normalization. This can be accomplished through the use of an internal standard that produces a well-defined Raman band of known intensity for the experimental setup in use. Such an internal standard can be included in the sample preparation or in the case of optical fiber probes, can potentially be introduced into the optical design [Zheng *et al.* 2001]. An external standard may also be used. However, great care must be taken to ensure standard sample position reproducibility. Qualitative or relatively quantitative analyses are not as restrictive and alternative normalizations can be used to provide intra-model calibrations. For example, Raman spectra can be normalized to the area of a particular vibration or the spectra can be scaled to have a particular maximum intensity. Thus far, we have scaled our spectra to have a maximum

intensity of one and have not included intensity information in our data analysis. The Raman optical fiber probe, discussed in Chapter III, provides a reproducible geometry for data collection, allowing examination of spectral data that has not been normalized. However, as long as the normalization technique is standardized and consistent, the data can be appropriately interpreted.

### IV. A. 6. Mean Centering

It is often useful to mean center data prior to the application of many analytical algorithms other than ordinary least squares (OLS) and classical least squares (CLS), discussed below. Mean centering refers to subtracting the mean spectrum of the data set from each spectrum in the data set. Conceptually, mean centering accentuates the differences among spectra. Mathematically, it reduces the complexity of the data by one degree of freedom and prevents certain spectra in the data set from being weighed more than other spectra. Statistically, it maps the data onto an abstract space where the mean of the mean centered data does not have any directionality [Kramer 1998]. For certain techniques, such as principal component analysis (PCA) and partial least squares (PLS), mean centering is recommended. In the absence of mean centering, the first spectral component of analysis will be the statistical mean of the data set.

### IV. A. 7. System Specific Calibrations

Certain experimental systems have additional calibration steps specific to the instrumentation or application. In the case of data collected with the confocal Raman microscope, the substrate background, typically $MgF_2$, must be subtracted prior to fluorescence background

removal. Although a confocal data collection geometry minimizes contributions from the substrate background, its removal is still necessary. Similarly, data collected on the clinical system with the light tight box employs a background removal step. Data collected on the clinical system using the Raman probe must also utilize methods for dealing with confounding signals from optical fibers. Although more than 95% of the Rayleigh scattered excitation light is eliminated via long-pass filters on the collection fibers, the remaining fiber background, mainly quartz, must be removed from the raw tissue data. The fiber background is characterized by collecting the laser light reflected from a block of aluminum. This spectrum is then subtracted from the white light corrected tissue data to remove the probe background. A sixth order polynomial is employed for fluorescence background removal when using the Raman optical fiber probe [Motz 2003].

## *IV. B. Chemometric Techniques*

The general term for techniques used to derive chemical information from data is chemometrics. Such analysis methods can be separated into two distinct classes, univariate and multivariate. A time honored technique for extracting sample information is by examination of a particular peak height. This is an example of a univariate technique as the analysis depends on the value of a single variable of interest [Shaver 2001]. However, this approach only takes advantage of a small portion of the data available. In complex biological samples, where several distinct moieties may contribute intensity to a particular Raman band, it is necessary to incorporate all of the spectral information in order to differentiate moieties. Further, to capitalize on the high information content provided by Raman spectroscopy, more sophisticated modeling techniques that incorporate the full spectral range of data available

are required. The key is to compress the information into a manageable, yet still informative form.

The notation for the equations in this thesis uses bold upper case letters to denote matrices, bold lower case letters for vectors and lower case letters to indicate scalars. The superscript T denotes matrix transposition while the superscript (–1) indicates matrix inversion.

Extracting meaningful information from a complex data set, such as that of biological tissue, can be accomplished by use of a set of mathematical techniques known as multivariate analysis. Raman data can be modeled using linear analysis. Two assumptions are associated with this type of modeling. One is that the Raman spectrum of a mixture of chemicals is a linear superposition of the mixture's component spectra. The second is that there is a linear relationship between signal intensity and chemical concentrations [Manoharan *et al.* 1992]. Manoharan and co-workers conducted a study on Raman spectra of mixtures similar in composition to that of biological tissue and verified that both of these conditions hold within experimental accuracy. For breast tissue, the linear superposition can be formulated:

$$S_{\text{breast tissue}} = c_{\text{fat}} \bullet P_{\text{fat}} + c_{\text{collagen}} \bullet P_{\text{collagen}} + c_{\beta\text{-carotene}} \bullet P_{\beta\text{-carotene}} + \ldots . \qquad \text{(IV.1)}$$

Where $S_{\text{breast tissue}}$ is the Raman spectrum of breast tissue, $c_i$ is the concentration of component i, and $P_i$ is the Raman spectrum of component i. For an entire data set, Eq. IV.1 can be expressed in matrix form:

$$\mathbf{S} = \mathbf{C} \bullet \mathbf{P} \qquad \text{(IV.2)}$$

Where **S** is the matrix of Raman spectra, **C** is the matrix of component concentrations and **P** is the matrix of basis spectra. When the number of samples is n, the number of components is p, and the number of wavelength points in each spectrum is m, **S** is an nxm matrix, **C** is an

nxp matrix and **P** is a pxm matrix. The basis spectra, **P**, can be the Raman spectra of the pure chemical constituents in the mixture, the Raman spectra of individual morphological components of the tissue, or even mathematically derived lineshapes. The spectral matrix **S** is a measured set of data for which we want to obtain the concentration information **C**. This can be obtained through a series of matrix manipulations, resulting in

$$\mathbf{C}=\mathbf{S}\cdot\mathbf{B} \qquad \text{(IV.3)}$$

Where **B** is the matrix of orthogonal projection vectors (or b-vectors). For each chemical in the data set, there exists only one ideal projection vector that models the data set most accurately. When each multivariate technique is applied carefully, the projection vectors obtained with different methods of analysis should all closely approximate the ideal projection vector.

Multivariate analysis for extracting concentrations is typically performed in two steps, calibration and prediction. Calibration is the process of developing a mathematical relationship between physical quantities, for example the spectra and concentrations or the fit coefficients and disease classification. Prediction is the process of applying the mathematical model developed during calibration to extract information from spectra. Choice of the optimal linear multivariate calibration technique depends upon the extent of the calibration data. Explicit techniques are those in which the linear model is completely defined, and therefore the linear superposition properties can be directly applied. Some examples are OLS and CLS [Haaland and Thomas 1988]. In other techniques, called implicit techniques, not all of the component spectra or concentrations are known [Geladi and Kowalski 1986]. PCA and PLS are examples of implicit techniques. Explicit methods are more robust, but they require the composition of the mixture to be completely characterized. Implicit and explicit

models each have their advantages. Because explicit models use information about every species, they are capable of providing superior calibrations. However, implicit models require information only about a single species and thus they can be significantly easier to implement. In addition, explicit models suffer when a species is mischaracterized or omitted or when spectral artifacts such as baselines are present. In these cases, implicit models tend to be more robust [Thomas and Haaland 1990]. We will be concerned with only those methods that have been applied to the analysis of breast tissue. These include PCA and OLS. The quantitative methods of CLS, PLS, and principal component regression (PCR) all require concentration information from a reference technique for model calibration, which is difficult to obtain for solid tissue, such as breast.

### IV. B. 1. Principal Component Analysis

PCA is useful when it is not possible to identify all of the component spectra or concentrations *a priori*. It can be used as a proof-of-principal analysis to demonstrate that there is sufficient information contained within a data set to yield accurate disease diagnosis. PCA has been used to classify diseased tissue samples in several organ systems [Mahadevan and Richards-Kortum 1996; Manoharan *et al.* 1998; Denium *et al.* 1999]. It uses the entire Raman spectrum and does not assume any knowledge about the chemical composition of the tissue. PCA resolves the spectra of an entire data set into a small number of orthogonal principal component (PC) basis spectra. These PC spectra can have negative and positive components and form a complete basis set that accurately describes all the data (within limitations imposed by noise) if the PCs are multiplied by the proper weighting coefficients.

These weighting coefficients, called fit coefficients, are analogous to chemical concentrations however they provide much less direct chemical information.

We use a singular value decomposition (SVD) algorithm (Matlab V.6.5.0, The Mathworks, Natick, MA) to determine the PCs of our data sets. SVD computes all n PCs, one for each spectrum or CCD pixel. In SVD the data, **S**, an mxn matrix, can be reconstructed by multiplying its eigenvectors, **Q**, by their **k** eigenvalues (also call scores or fit coefficients).

$$\mathbf{S}=\mathbf{U}\bullet\mathbf{X}\bullet\mathbf{Q}^{T} \qquad \text{(IV.4)}$$

Here, $\mathbf{U}\bullet\mathbf{X}$ are the fit coefficients and $\mathbf{Q}^{T}$ is a (kxn) matrix whose columns are the PCs, analogous to **P** in Eq. IV.2. **X** is a diagonal matrix containing square roots of the eigenvalues, and **U** is an (mxk) matrix.

Data sets are typically mean centered prior to performing PCA in order to remove features common to all spectra, thereby highlighting spectral variance. The first PC will contain the maximum amount of variation in the data, with each subsequent PC spectrum representing sequentially less variation. The contributions of each PC to subsequent samples can then be calculated:

$$\mathbf{C}\equiv\mathbf{U}\bullet\mathbf{X}=\mathbf{S}\bullet\mathbf{Q}\bullet(\mathbf{Q}^{T}\bullet\mathbf{Q})^{-1}=\mathbf{S}\bullet\mathbf{Q} \qquad \text{(IV.5)}$$

PCA provides little physical information in and of itself; however, it is adept at isolating spectral trends that correlate with physical information and thereby provides a basis for development of diagnostic algorithms. Furthermore, by comparing the lineshapes of the diagnostic PC spectra with the spectra of pure chemicals, it is possible to ascribe some meaning to them. For example, features related to Raman bands of particular chemicals can

be identified in the PCs used for breast cancer diagnosis. A detailed discussion is presented in section III.C.2.

To further illustrate the information conveyed by PCA, an analysis was preformed on the fresh-frozen breast data presented in Chapter V. Figure IV.4 displays the first 3 PCs of the data set. The data was not mean centered prior to PCA and thus the first PC, shown in Figure IV.4a is the statistical mean of the data set. PC 1 represents 41% of the data variance and is very similar to the morphologically derived Raman spectrum of fat. PC 2 also resembles a morphologically derived Raman spectrum, that of collagen. It represents 11% of the data variance. PC 3, shown in Figure IV.4c, accounts for less than 1% of the data variance. It exhibits more complex structure as well as negative and positive components thus illustrating the difficulty in interpreting PCs and the limitations of this approach. Interestingly, collagen and fat are the two components found to be diagnostic in our modeling studies, presented in Chapter V.

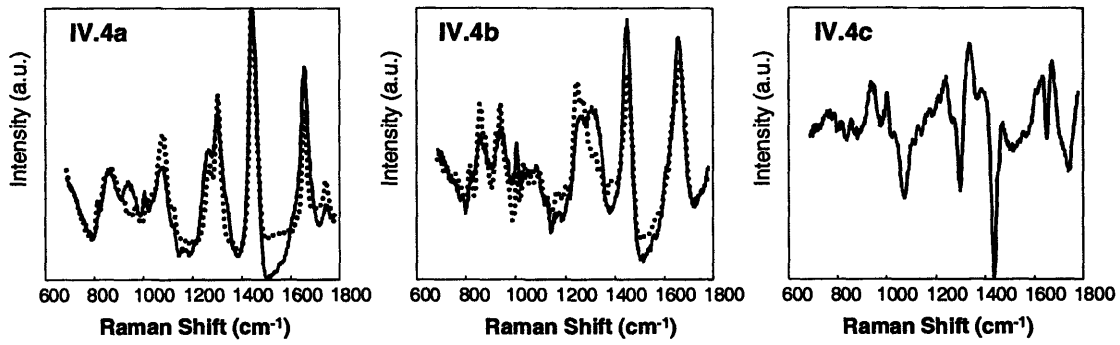


**Figure IV.4.** Principal component basis spectra of fresh-frozen breast data set. a) PC 1 (solid line) and fat (dotted line). b) PC 2 (solid line) and collagen (dotted line). c) PC 3

## IV. B. 2. Ordinary Least Squares Regression

OLS is used to extract concentrations of all important components present in the samples. As input, it requires Raman spectra of all components that contribute signal to the spectral data

set. When the number of spectra and the number of variables in the spectra are equal and the matrix **P** is invertible, we can directly obtain concentrations from

$$\mathbf{C}=\mathbf{S}\bullet\mathbf{P}^{-1} \tag{IV.6}$$

However, the number of spectra and the number of variables in the spectra are rarely equal resulting in a matrix **P** that is not invertible. In fact, it is preferable to have a data set composed of many more spectra than variables. To obtain the concentration in this case, we multiply Eq. (IV.2) by the transpose of **P**:

$$\mathbf{S}\bullet\mathbf{P}^{T}=\mathbf{C}\bullet\mathbf{P}\bullet\mathbf{P}^{T} \tag{IV.7}$$

If $\mathbf{P}\bullet\mathbf{P}^{T}$ is invertible, we can derive an equation for the concentration matrix, **C**:

$$\mathbf{C}=\mathbf{S}\bullet\mathbf{P}^{T}\bullet(\mathbf{P}\bullet\mathbf{P}^{T})^{-1} \tag{IV.8}$$

And thus via comparison with Eq. VI.3, a matrix of projection vectors:

$$\mathbf{B}=\mathbf{P}^{T}\bullet(\mathbf{P}\bullet\mathbf{P}^{T})^{-1} \tag{IV.9}$$

OLS is a simple but powerful technique in spectral analysis. However, an error in the number of model components can result in erroneous regression results. Additionally, spectra of certain chemicals vary with environment, which can also lead to inaccurate OLS analysis. In the next section, development of our spectral model used in OLS analysis is presented.

## *IV. C. Spectral Modeling: A Morphologic Assay of Breast Tissue*

### IV. C. 1. Motivation and Assumptions

Although it is possible to use simple correlation analyses of particular Raman bands or lineshapes to diagnose disease, there is a wealth of information in the spectra that enables enhanced understanding of disease etiology. Thorough understanding of the

chemical/morphological Raman spectrum of breast tissue is a necessary step in developing Raman spectroscopy as a tool for breast cancer diagnosis. To understand the relationship between the Raman spectrum of breast tissue and its disease state we developed a Raman spectroscopic model [Shafer-Peltier *et al.* 2002]. This model is based on the morphological structures that comprise breast tissue.

Construction of a morphological model of breast tissue relies on three assumptions. First, as discussed above, that the Raman spectrum of a mixture is equal to the weighted sum of the individual components of the mixture. Second, that biological morphological features, such as cells, have a similar Raman spectrum from one patient to another. Finally, that the elements included in the model are sufficiently distinct to enable their differentiation based on their Raman spectrum and a given SNR in the data.

Our model identifies the morphological components present in breast tissue through their unique Raman spectra and uses them as basis spectra to describe the morphological features of macroscopic spectra. These basis spectra are derived from Raman microscopy of the epithelial cell cytoplasm, the cell nucleus, fat, β-carotene, collagen, calcium hydroxyapatite, calcium oxalate dihydrate, cholesterol-like lipid deposits and water. The resulting fit coefficients yield the contribution of each basis spectrum to the macroscopic tissue spectrum, thereby elucidating the chemical/morphological makeup of the lesion. The model explains the spectral features from a range of normal and diseased human breast tissue samples, thereby relating the Raman spectrum of a breast tissue sample to diagnostic parameters used by pathologists.

Morphologically derived basis spectra have several advantages over spectra obtained from pure chemicals. First, the spectra are collected *in situ* and are therefore subject to

perturbations naturally present when tissue is examined *in vivo*. In other words, pure chemicals are not identical to those found in tissue. For example, most proteins are commercially available in a powdered form, not hydrated as they are in human tissue. Second, the number of components in the model is reduced to spectra of a few key morphological features, rather than the large number of chemicals that are present in tissue. This simplification has the potential to reduce error in the model fits by limiting the spectral overlap of the model. For instance, collagen is present in human tissue in many different forms, each producing a slightly different Raman spectrum. The collagen found in breast tissue is predominately composed of type I collagen with minor contributions from types III, IV, and V [Alini and Losa, 1991]. To avoid data over-fitting, a morphological spectrum of collagen, encompassing the average of the different types, is included in our model. Also, identifying each chemical present in a complex biological environment, such as cell cytoplasm, is challenging. Finally, the model interprets the traditional chemical information contained in Raman spectra into terms that are commonly used by pathologists during histologic analysis. However, Raman spectra of pure chemicals do provide insight into the make up of morphological features and when necessary, synthesized or commercially available chemicals were used.

### IV. C. 2. Samples Preparation and Data Acquisition

Samples of breast tissue were obtained from surgical biopsy specimens, snap frozen in liquid nitrogen, and stored at -85 C until spectroscopic examination. Samples were then mounted on a cryostat chuck using Histoprep and sliced into 6 μm to 8 μm thick sections using a microtome. These sections were mounted on $MgF_2$ flats, selected because of their small

Raman background signal, and kept moist with phosphate buffered saline (PBS) at physiological pH.

Raman spectra underwent processing to ensure reproducibility of the data from day to day. First, they were corrected for the spectral response of the system using a tungsten light source. The data were frequency calibrated using the known Raman lines of toluene. The $MgF_2$ background spectrum was subtracted and the broad fluorescence background was removed by fitting the spectrum to a fifth order polynomial and subsequent subtraction of this polynomial. Also, contributions from cosmic rays were removed, if necessary, using a derivative filter.

Our model was built using the phase contrast microscope, discussed in Chapter III, to identify morphological features and collect confocal Raman spectra from those features. Raman maps were also employed for comparison with serial H&E stained sections. This allows identification of morphological features difficult to locate with phase contrast alone, for example fibroblasts buried in the extracellular matrix. As an example of this approach, a Raman map of a normal breast duct and the corresponding phase contrast image are shown in Figure IV.5. The circular structure of the duct can be discerned in the phase contrast image, Figure IV.5a, however the image shows few other features. By plotting the contribution of certain morphological features to the Raman map, we observe a supportive collagen network surrounding the duct. The single layer of epithelial cells forming the duct itself and the location of the nuclei within these cells can be seen in images IV.5c and IV.5d. Also the presence of fat in the lumen of the duct is visible in image IV.5e.

Libraries of spectra for each morphological feature were generated. When possible, examples of each morphological element were identified from a variety of patients and

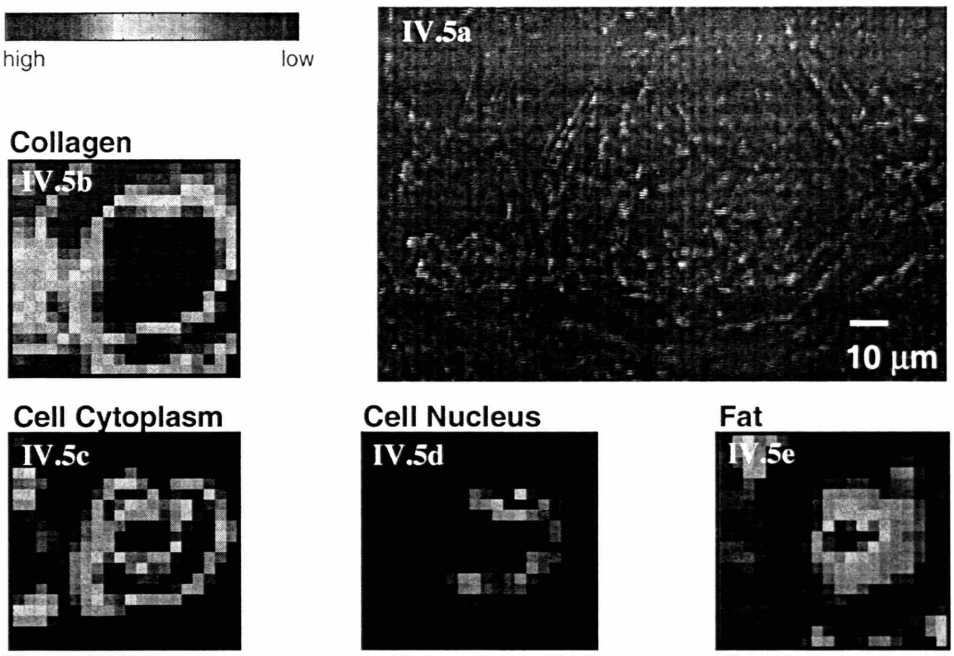


**Figure IV.5.** Raman map of a normal breast duct with the corresponding a) phase contrast image. Each Raman image represents the contribution of a specific morphological element to the region mapped: b) collagen, c) cell cytoplasm, d) cell nucleus and e) fat.

disease states. Raman spectra from normal, benign and malignant samples were collected into separate libraries for analysis. Each library typically contained 60 to 80 spectra from 5 or 6 patients. If spectra in a library did not vary greatly or consistently, the spectra were averaged to create the morphologically derived basis spectrum used in our model. If consistent differences were observed, as was the case for the cellular components, the number of independently varying contributors was identified with PCA and used to extract independent basis spectra. In cases where single spectra had unique Raman bands when compared with other spectra in that morphological category, those spectra were removed from the category and analyzed independently to ensure that their spectral features could be explained by other elements in the model. If the spectral features could not be explained by the current morphological model, a new category was added and the database of Raman maps was searched for similar spectral signatures. When matches were found, phase contrast images and serial stained sections corresponding to the Raman map were reviewed.

Using our library of Raman maps, 9 key basis spectra were identified to comprise our spectral model. Their Raman spectra are shown in Figure IV.6. Some features identified during the Raman mapping experiments were not included in the model because they were not found to contribute appreciably to macroscopic data (1 $mm^3$ volume) acquired from biopsy samples. This could be because they are not present in large quantities or because

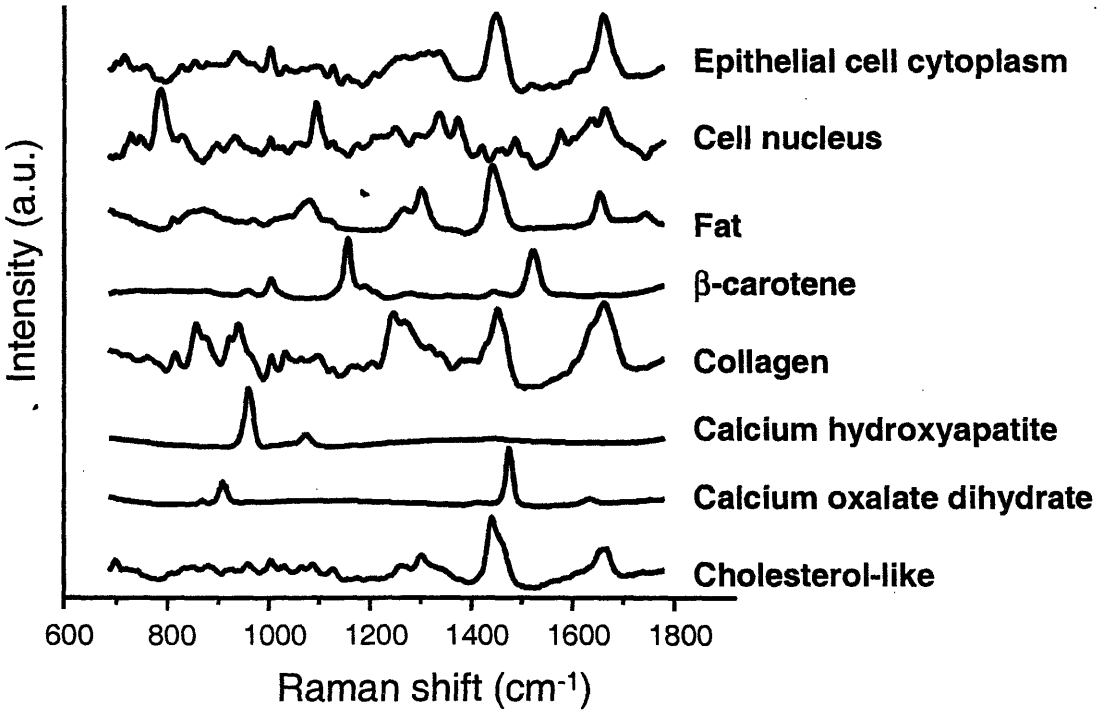


**Figure IV.6.** Morphological spectral model of breast tissue.

they have small Raman scattering cross-sections and thus do not contribute appreciably to bulk tissue spectra.

### IV. C. 3. Epithelial Cell Cytoplasm and Cell Nucleus

There are several types of cells in normal breast tissue: epithelial, myoepithelial, and fibroblasts. Inflammatory cells are present when there is a host response to an irritant. Malignant cells are typically derived from epithelial cells that have undergone a number of

genetic transformations. Thus, the degree of inter-patient and disease dependent variation was largest for the epithelial cell cytoplasm basis spectrum. Figure IV.7 displays Raman spectra of different cells occurring in the breast. Shown are the spectra of an epithelial cell in a normal duct, an epithelial cell in a focus of fibrocystic disease, a malignant epithelial cell, and a fibroblast occurring in normal stroma. The main difference among Raman spectra of a range of cells was determined to result from varying ratios of the cell cytoplasm to the cell nucleus. Differences in this ratio are most emphasized when comparing normal and malignant cells.

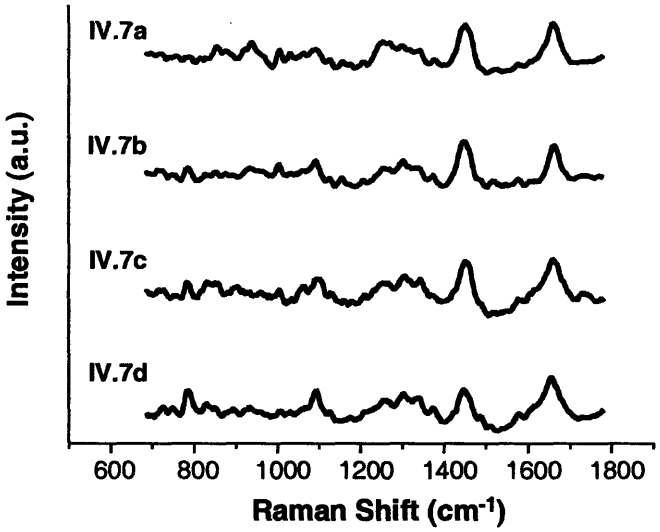


**Figure IV.7.** Raman spectra of cells occurring in the breast: a) a fibroblast occurring in normal stroma, b) an epithelial cell in a focus of fibrocystic disease, c) an epithelial cell in a normal duct, and d) a malignant epithelial cell.

Because the ability to collect pure spectra from the cell cytoplasm and the cell nucleus is somewhat limited by the collection volume of the Raman confocal microscope, the two basis spectra were separated mathematically. To separate the two components, spectra of hundreds of cells from 8 different patients were collected using the Raman microscope. Initially areas in the Raman map corresponding to cell nucleus and cell cytoplasm were identified by comparison to the Raman spectrum of DNA, purchased from Sigma. Next, two libraries were constructed, one high in DNA, corresponding to spectra acquired from nuclear regions and one with little or no DNA, collected from regions in the cytoplasm. The mean DNA-rich spectrum was then subtracted from the mean cytoplasm spectrum, thereby

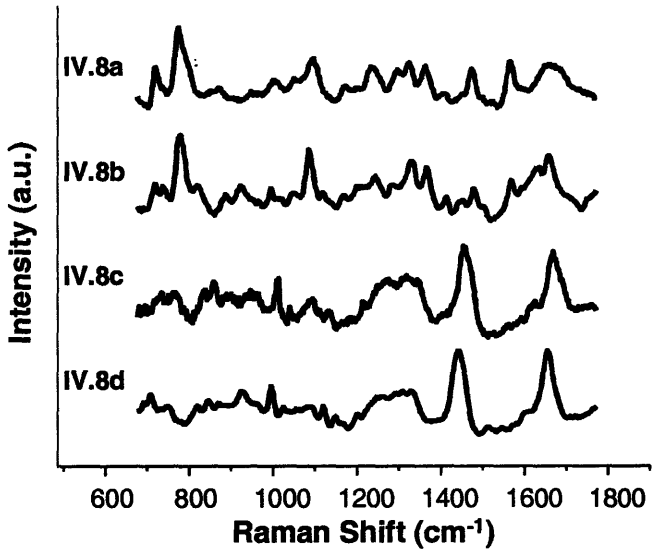


**Figure IV.8.** Raman spectra of cellular components. a) DNA, b) cell nucleus, c) actin and d) epithelial cell cytoplasm.

removing all the residual cell nucleus bands from the cytoplasm rich spectrum and all the cytoplasm contributions from the cell nucleus spectrum. The resultant two spectra, cell nucleus and epithelial cell cytoplasm, were used to re-fit the original cell spectral data. The final cell nucleus model basis spectrum was derived by subtracting the epithelial cell cytoplasm model fit from each Raman spectrum in the original cell data set and calculating the mean of the residual spectrum. The same procedure was followed to produce the epithelial cell cytoplasm spectrum. This iterative process minimizes artifacts due to the inability of the Raman spectrum of commercially available DNA to accurately model the cell nucleus. The model basis spectra representing epithelial cell cytoplasm and cell nucleus are shown in Figure IV.8. Shown for comparison, are Raman spectra acquired from commercially available actin and DNA

Other differences between the cells found in breast tissue are incorporated into other model components. For instance, signal from collagen can be seen in the Raman spectrum from a fibroblast. Fibroblasts are cells responsible for making and maintaining the extracellular matrix. In order to do so, they produce collagen, fibrinogen, and glycosaminoglycans.

### IV. C. 4. Fat

Fat is one of the strongest contributors to the Raman spectrum of normal breast tissue. Fat is present in large quantities and has a large Raman scattering cross-section. Fat storage in humans primarily takes the form of triglycerides, especially triolein. The morphological spectrum of fat is very similar to the Raman spectrum of triolein. The fat spectrum included in our model is the average of 28 spectra collected from 5 patients. There was little variability in the Raman spectrum of fat with either patient or disease state.

### IV. C. 5. β-Carotene

β-carotene is resonance enhanced when excited with 830 nm light. As a result, it has an extremely strong Raman signal. It is lipophillic and is often found in conjunction with fat throughout the breast. To eliminate the need for extracting the fat content from the hundreds of morphologically-derived β-carotene spectra, we used the spectrum acquired from commercially available β-carotene. Using our morphologically-derived Raman spectra of β-carotene, we confirmed that the commercially available sample was an accurate representation of the β-carotene found in tissue.

### IV. C. 6. Collagen

Collagen is the major protein of the white fibers of connective tissue, cartilage, and bone. It is insoluble in water, but can be altered to a soluble gelatin form by boiling in water, dilute acids, or alkalies. It is high in glycine, alanine, proline and hydroxyproline, but is low in sulfur and has no tryptophan. Collagen comprises a family of genetically distinct molecules all of which have a unique triple helix configuration of three polypeptide subunits known as

α-chains. Different types of collagen are comprised of different polypeptide chains. In breast tissue, both the extracellular matrix and the basement membrane are composed primarily of collagen. Other structural proteins, such as fibrinogen, fibronectin, and proteoglycans, are also present but in minute quantities and with such small Raman scattering cross-sections that they do not contribute significantly to the bulk Raman spectra. Figure IV.9 compares the mean spectrum of morphologically-derived collagen, mainly type I with minor contributions from types III, IV, and V with the Raman spectrum of commercially available collagen type I [Alini and Losa, 1991]. The morphologically-derived collagen spectrum is the mean of 215 spectra taken from 7 different patients.

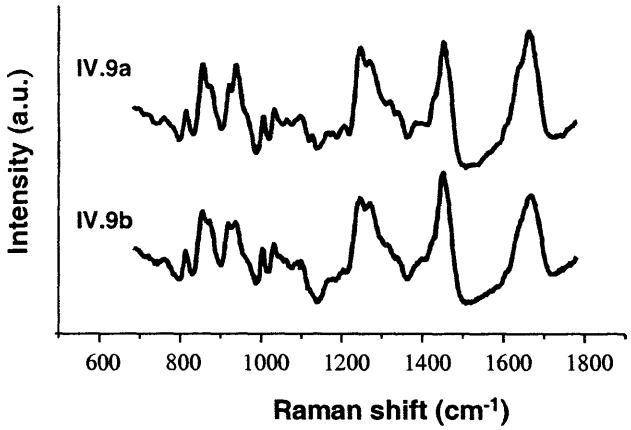


**Figure IV.9.** Raman spectra of collagen: a) commercially available collagen type I and b) morphologically-derived collagen, mainly type I with minor contributions from types III, IV, and V.

## IV. C. 7. Microcalcifications

Two major types of microcalcifications are found in breast tissue. Type I deposits consist of calcium oxalate dihydrate, a birefringent colorless crystal, while type II deposits are composed of calcium phosphates, mainly calcium hydroxyapatite. Type II microcalcifications are typically basophilic on light microscopic examination of H&E stains and nonbirefringent. Both type I and type II microcalcifications are strong Raman scatterers. There is no reliable way to distinguish between type I and type II microcalcifications in a

clinical mammogram, but the type is thought to correlate with disease [Radi 1989]. Calcium oxalate dihydrate crystals are most frequently seen in benign ductal cysts and are rarely found in foci of carcinoma, while calcium phosphate deposits are most often seen in proliferative lesions, including carcinoma. This distribution is consistent with the hypothesis that type I microcalcifications are a product of secretions, whereas type II calcium deposits result from cellular degradation or necrosis. The Raman spectra of type I and II microcalcifications are distinct and shown in Chapter VI.

Despite the significant role they play in breast cancer, microcalcifications are not commonly found in our frozen breast tissue specimens. This is because calcifications are important for medical diagnosis and therefore tissue containing calcifications is not commonly released for scientific study. As a result, we expanded our studies to include deparaffinized tissue sections. Calcium hydroxyapatite was identified in fresh frozen specimens from 3 patients and in deparaffinized tissue sections from 11 patients. The calcium hydroxyapatite basis spectrum included in the model is an average of these spectra. Calcium oxalate was only observed in one deparaffinized tissue sample. Therefore, calcium oxalate dihydrate was synthesized for incorporation into our model [Kontoyannis *et al.* 1997]. In subsequent microcalcification studies on deparaffinized sections, the spectrum of calcium oxalate dehydrate was found to be very reproducible. Both calcification spectra resemble Raman spectra published in the literature [Kodati *et al.* 1990, Kodati *et al.* 1991].

### IV. C. 8. Cholesterol-like Lipid Deposits

The necrotic core is essentially the product of cellular degradation. Consequently, its composition varies significantly from location to location even within a single duct. Necrosis

can occur within a malignant duct or in the center of a tumor. Analysis of Raman spectra from three patients indicated that the necrotic core contains: fat, collagen, calcium hydroxyapatite, cholesterol, cholesterol linoleate and cellular material. As the ratios of these elements can vary significantly, the spectrum included in our model, cholesterol-like, represents the common elements of these spectra not represented elsewhere in the model. The spectrum includes features indicative of cholesterol and cholesterol linoleate, although there are small contributions from cellular material and triglycerides. The necrotic core is not the only element in breast tissue containing cholesterol and cholesterol linoleate, for example, the cell membrane contains both these chemicals.

### IV. C. 9. Water

Although not a strong Raman scatterer, water constitutes ~80% of human tissue by weight and thus our data contains contributions from water. The Raman spectrum of water is well known and in our region of data acquisition has a single, relatively broad Raman band centered at 1650 $cm^{-1}$. The Raman spectrum of water is shown in Figure IV.10. Also shown in Figure IV.10 is the Raman spectrum used in the Raman artery studies. The two spectra exhibit different background structure and SNRs. Studies to determine which spectrum more accurately fits our Raman data should be undertaken.

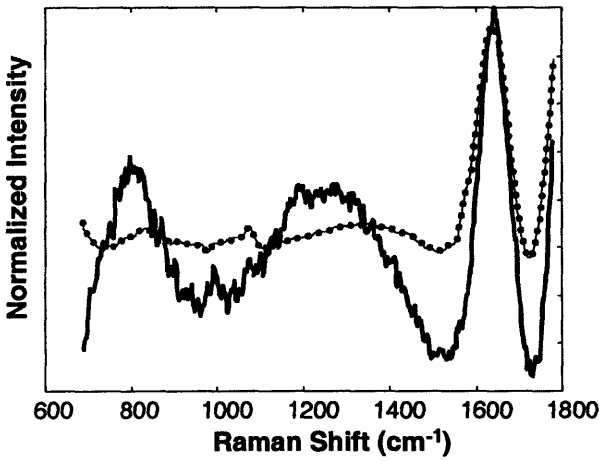


**Figure IV.10.** Raman spectra of water: in the breast spectral model (solid line) and in the artery spectral model (dotted line).

### IV. C. 10. Inter-patient Variation of Elements

Model development via averaging spectra from many patients and pathologies ensures that our model includes the common elements to all morphological features. However, one of the keys to successful morphological modeling is that there is minimal inter-patient variation in the model elements. For some model components there is very little inter-patient variation. For instance, the extracellular matrix spectrum is primarily collagen, regardless of the patient. Likewise the fat spectrum is similar to triolein, although small variations can be seen across samples. For other model components, such as calcium hydroxyapatite and cholesterol-like, more variation is observed. In our present clinical data, subtle variations are typically overwhelmed by noise. However, as instrumentation and data analysis techniques improve, new components corresponding to smaller chemical variations will need to be included in our model.

### IV. C. 11. Future Directions: Quantitative Analysis

In order to collect Raman spectra for truly quantitative analysis, data must be independent of the experimental system. In addition to the steps discussed above, the system throughput must be assessed and data must be corrected for the CCD gain so that the number of collected photoelectrons is determined. Our current morphological model of breast only provides relatively quantitative data and is therefore, not subject to these more advanced considerations. Although strict quantification is desirable, it is challenging to establish Raman scattering cross-sections for the components present in biological tissue. However, with instrumental advances and a deeper understanding of the theoretical accuracy of our

approach we have planned a study to make our morphological models quantitative. In this study, data will be acquired from thin sections of fresh-frozen breast tissue using our Raman microscope. This data will be acquired using a low magnification objective to ensure that the spectroscopic signal is representative of the entire breast tissue section. Data will not be collected confocally and spectra will be acquired for long integration times, conferring high SNR Raman data. Addition of a photodiode to the laboratory microscopy system allows for correction for laser intensity variations. Each thin section of breast tissue spectroscopically examined will then be reviewed by a pathologist. A combination of staining techniques and morphometric analysis will be used to obtain an estimate of the volume occupied by each morphological feature represented in our Raman spectral model. These volumes will then be correlated with the fit coefficients from the corresponding spectrum. Half of the data will be used to scale the basis spectra such that the fit coefficients are representative of the pathologically determined volumes. The remaining data will be used for validation of the intensity corrected model. I anticipate that some model elements, such as fat and microcalcifications, will quite accurately reflect their morphological volumes while others, such as epithelial cell cytoplasm and cholesterol-like, will not. This will allow us to identify areas of the model which are representative of several morphological features and provide a basis for model refinement. The prediction error equation, presented below, can be used to estimate reasonable errors.

## *IV. D. Diagnostic Algorithm Development*

### IV. D. 1. Calibration

Many techniques have been developed to aid researchers in producing decision algorithms to classify data according to specific parameters. These include discriminant analysis [Fisher and Van Belle, 1993], logistic regression [Fisher and Van Belle, 1993; Pagano and Gauvereau, 1993], and neural networks [Robb and Munk, 1990]. Discriminant analysis and logistic regression are very similar linear techniques. Both assume that the samples are binomially distributed within each classification. Discriminate analysis, which applies Bayes' Theorem, is the more restrictive in its assumptions. It allows only for normally distributed input variables, whereas logistic regression allows for discrete (e.g. only integer values) or categorical (e.g. cancerous/non-cancerous) variables. We typically employ logistic regression in our algorithm development as it can easily incorporate binary categorical information into the decision scheme. Neural networks simulate the processing of signals in the brain. In such a system, information is processed by a network of interconnected units according to a pattern established during the calibration process. Neural networks do not require the data to be normally distributed and can be used to describe non-linear systems as well as linear ones. However, it is especially important to perform proper calibration and validation of neural network based decision algorithms because physical interpretation of the coefficients is difficult and robustness is not always easy to achieve.

### IV. D. 2. Logistic Regression

Logistic regression is well suited to the purpose of developing classification algorithms from Raman spectral data as it allows us to classify samples according to discrete categories [Sharma 1996]. It is used to correlate the fit coefficients, obtained via modeling, with disease classifications provided by a pathologist. Pathology serves as the gold standard in all of our diagnostic algorithm development. Logistic regression is used extensively throughout this thesis for algorithm development. The underlying assumption of logistic regression is that the probability, $p_i$, that the $i^{th}$ sample in a set of spectral data belongs to a particular category, for example that the sample is malignant, is described by the logistic function of the form:

$$p_i=(1+\exp(\alpha+\Sigma\beta_j x_j))^{-1} \qquad \text{(IV.10)}$$

With $x_j$ the score or fit coefficient associated with the $j^{th}$ basis spectrum. The parameters $\beta_j$ and $\alpha$ are to be determined. $p_i$ varies from zero to one in a sigmoidal fashion as a function of $x_j$. It is small for large values of $x_j$ and approaches unity for small values. Logistic regression introduces the likelihood function, L, defined as the probability of observing a specific set of diagnoses in a set of samples. This can be calculated as the product of the probabilities, $p_i$, that each individual sample belongs to a given category:

$$L= p_1 \cdot p_2 \cdot p_3 \cdot \ldots p_n \qquad \text{(IV.11)}$$

The first step in implementing logistic regression is to choose a particular basis set and apply these basis spectra to a set of calibration data to obtain a set of fit coefficients, $x_j$, for each of the i samples. In this thesis we use both the spectral model, described above, as well as PCA to generate fit coefficients for algorithm development. To determine values for the $\beta_j$s and $\alpha$, the maximum likelihood principle is used. It states that the values for the parameters of the likelihood function should be chosen to maximize the probabilities predicted for obtaining

the specific set of diagnoses for the sample set. The expression for L is obtained by inserting Eq. IV.10 into Eq. IV.11 and the values for the $\beta_j$s and $\alpha$ are found by applying this expression to the calibration data set. The values for the $\beta_j$s and $\alpha$ are chosen to maximize the agreement between L and the known classifications of the calibration data set. Once the values for the $\beta_j$s and $\alpha$ have been obtained, Eq. IV.10 can be used to predict the probability that a new sample falls into a given category. Different combinations and numbers of spectral components should be assessed in selecting the relevant number of parameters with diagnostic potential.

Once a diagnostic algorithm is developed, its performance must be assessed. This can be accomplished by calculating the sensitivity and specificity of the approach. Sensitivity refers to the proportion of individuals with the disease who are correctly identified by the diagnostic algorithm. Specificity is the proportion of individuals without the disease who are correctly identified by the diagnostic algorithm. Sensitivity and specificity are typically expressed as percentages. If the sensitivity and specificity are both 100%, then the diagnostic algorithm is equivalent to the gold standard. However, in practice, sensitivity is gained at the expense of specificity and vice versa. The trade off between sensitivity and specificity is often displayed as a Receiver Operator Characteristic (ROC) curve. Whether we aim for a high sensitivity or high specificity depends on the condition we are trying to detect and the implications for the patient of a false negative or false positive test result. For conditions that are easily treatable, a high sensitivity is preferable. However, for conditions that are serious and untreatable, a high specificity is preferable in order to avoid making a false positive diagnosis.

### IV. D. 3. Validation

It is necessary to check the accuracy of a diagnostic algorithm after it is built. An independent data set, which does not include the data used for calibration, is often used for testing the robustness of a diagnostic algorithm. If the diagnoses obtained by using a prediction scheme in a prospective manner and the diagnoses provided by a pathologist are statistically similar, the diagnostic algorithm is validated and considered clinically accurate. This process of testing an algorithm is called validation.

Although it is desirable to use an independent data set for validation, this requires a large number of samples, often difficult to achieve with biological tissues. When the number of samples is not sufficient to perform an independent validation, cross-validation can be performed. Cross-validation allows for the efficient use of a data set because only a small number of samples are reserved, and the spectra of the remaining samples are used for calibration. The developed algorithm is then used to extract diagnoses from the spectra of the reserved samples and the disease classifications are compared with the pathological diagnosis. One example of cross-validation is the leave-one-out method, in which one spectrum at a time is left out of the calibration. In this process, the diagnostic algorithm is calibrated using logistic regression excluding a single spectrum. The excluded datum is used for validation and the prediction made on it is compared to the diagnosis provided by a pathologist. Each spectrum is, in turn, excluded and the procedure repeated. By cycling through left-out samples in this way, a relatively small data set can be used efficiently and without bias to establish the robustness of a model. Several other variations of cross-validation analysis exist. Data from a single patient may be omitted or the data can be divided into a number of sets. In these versions of cross-validation, the diagnostic algorithm

is calibrated using logistic regression on all spectra except those from a single patient or a single .set. Again the excluded data is used for validation. The patients or sets are then rotated, with each in turn serving as the validation set. When separating data into sets, it is important that multiple spectra from a single patient are kept as part of the same data set and also that data collected during different acquisition time periods is carefully mixed between the sets. Finally, normal, benign, and malignant samples should be evenly distributed among the sets. All algorithm development presented in this thesis employs leave-one-out cross-validation in which a single spectrum is excluded. Algorithms are also validated prospectively on independent data sets.

## *IV. E. Real-Time Analysis*

A final step in the development of clinical Raman spectroscopy is the ability to provide real-time diagnosis. Real-time analysis is also a useful experimental tool. As such, we have developed clinical Raman instrumentation that provides real-time diagnoses [Motz *et al.* in press]. Following accumulation of the data, the spectrum is analyzed with the appropriate model. Data, model fit, and fit coefficients are then displayed. A diagnostic plot is also shown indicating the samples' disease state. Different diagnostic algorithms and spectral models can be chosen depending on the application. LabVIEW is the primary platform for data acquisition and analysis in the real-time clinical Raman system. In addition to providing flexibility for interfacing with various devices in the system, LabVIEW allows automation of spectral calibration and data analysis in Matlab, V.6.5.0 (The Mathworks, Natick, MA). Diagnosis is obtained in less than 1 sec. following data acquisition.

Real-time feedback can be used to direct biopsy, thereby reducing the likelihood of a non-diagnostic biopsy that would require repeat needle or surgical biopsy. Also, with the development of minimally invasive breast cancer therapies, such as radiofrequency ablation, which relies on insertion of a thin metal probe into the breast, there is the potential that diagnosis and treatment of some lesions could be performed in a single procedure. Our real-time Raman system has been used successfully for a variety of preliminary clinical studies. Applications include targeting moieties of interest during data collection and real-time *in vivo* diagnosis. The system was used *ex vivo* to target microcalcifications in breast biopsies, discussed in Chapter V.B.5, and *in vivo* to provide margin assessment at breast cancer surgery, Chapter VII.

## *IV. F. Analytical Method of Estimating Chemometric Prediction Error: $\Delta c$*

We present an analytical formula that estimates the uncertainty in concentrations predicted by linear multivariate calibration, particularly OLS. We emphasize the analysis of spectroscopic data. The formula is expressed in terms of easily quantifiable experimental parameters and is straightforward to evaluate. To test this formula, we performed OLS analysis upon simulated spectra and upon experimental Raman spectra of dissolved biological analytes in water. In each instance, the root-mean-squared error of prediction was compared to the estimate from the formula. We observe excellent agreement between the formula and data for these simple systems. The ability to make predictions concerning the concentration error is valuable to the process of developing and refining analytical measurements.

## IV. F. 1. Introduction

Raman spectroscopy provides detailed quantitative information about sample composition and thus is a promising technique for the examination of biological systems [Raman and Krishnan 1928; Pupples *et al.* 1990; Mahadevan-Jansen and Richards-Kortum 1996; Hanlon *et al.* 2000]. However, it is often difficult to interpret Raman spectra of biological samples due to their complexity. Noise as well as the presence of multiple components, resulting in overlapping Raman bands, complicates attempts to use Raman peak intensities for accurate quantitative analysis. This has led to the application of multivariate techniques, which utilize the entire spectral range, to the analysis of Raman spectra [Shaver 2001]. Multivariate analysis is part of the general field used to derive chemical information from data, known as chemometrics. The goal of multivariate methods of analysis is to find a projection vector that extracts concentration information from the data. The concentration errors resulting from chemometric analysis are typically assessed by comparison with a reference measurement. Reference measurements have the disadvantage of introducing an additional source of error, contained in the reference concentration. Further, in many biologic samples, such as tissue, obtaining reference concentrations is not straightforward. Although, reference measurements can be used to assess the overall error of an approach, they provide little insight into the origins of that error.

We have derived a formula for the chemometric prediction error in a noise-limited data set. This formula relates easily measurable experimental parameters to concentration uncertainty. These parameters are the noise in the data, the signal of the component of interest at unit concentration and the overlap factor. The overlap factor accounts for the similarity between the Raman spectrum of the component of interest and the spectra of all

other moieties present in the sample. By understanding the sources of prediction error, efforts can be made to reduce it scientifically. Further analytic methods for calculating the concentration error allow smart experimental design to detect moieties of interest with the appropriate accuracy. Most importantly, the formula provides a means to predict the smallest concentrations measurable or the signal to noise ratio necessary to observe a moiety of interest with the appropriate accuracy.

The prediction error formula presented in this manuscript is derived for OLS regression. OLS is a simple, yet powerful technique in spectral analysis [Haaland and Thomas 1988]. It is useful when it is desirable to know the concentrations of all constituents present in the sample. Although OLS provides detailed information about sample composition, it requires knowledge of the number of important components in the sample as well as their Raman spectra. The Raman spectra of the constituents form a set of basis spectra that are fit to the data in a linear least-squares fashion. In this procedure, the sum of the squares of the residual, the difference between the model fit and the data, are minimized to obtain the optimal fit. The amount that each basis spectrum is weighted in order to achieve this fit, the fit coefficient, provides the concentration of that species.

Although derived for OLS, the formula can readily be extended to other multivariate techniques, as long as the projection vectors for OLS and the other method of analysis are similar. For each species in the data set, there exists only one ideal projection vector that models the data set most accurately. When distinct multivariate methods are applied successfully, the projection vectors obtained with different techniques should closely approximate each other. If there are differences between the projection vectors, this methodology will not provide accurate errors for other multivariate techniques.

In this section we derive an analytical formula for the prediction error. The concentration errors given by this formula are compared with those provided by a chi-squared analysis, a standard but more cumbersome method of calculating error. Next, the analytical expression is validated through both simulated and experimental data. In the simulations, excellent agreement is obtained for various levels of noise, as well as different concentration mixtures. Experimental data, acquired from biological analytes dissolved in water, also exhibits good agreement with the analytical formula. The ability to predict the smallest concentrations measurable or the signal to noise ratio necessary to observe a moiety of interest is an important step towards quantitative biomedical Raman spectroscopy.

## IV. F. 2. Sample Preparation and Data Acquisition

### IV. F. 2. a) Raman Spectroscopic Measurements

Data were acquired using the macroscopic Raman laboratory system that has been described in Chapter III. In short, the excitation laser beam, 830 nm, is focused and directed to the sample via a mirror at a 60° angle. The Raman scattered light is detected by a deep-depletion CCD detector cooled to –110 °C. Raman spectra in this study were acquired with a 500 s. integration time for basis spectra (1s. per frame x 500 frames) and a 1 s. integration time for data. Data and basis spectra were collected with the same integration time per frame in order to remove distortions in intensity caused by the shutter. All data have a spectral resolution of 8 $cm^{-1}$. The average laser excitation power was 100 mW. Laser power was continuously monitored by a PDA55 photodiode (ThorLabs) which reads out every 10 ms. Photodiode values were averaged for the time of data collection.

IV. F. 2. b) Simulated Data

Basis spectra, collected during this study or previously, were used as 'noiseless' Raman spectra to generate simulated data. Both the amount of noise and the basis spectra mixtures were varied in our simulations. Simulated data corresponding to different concentration mixtures were obtained from mathematical manipulation of basis spectra. In order to attain sufficient sample statistics and avoid statistical abnormalities sometimes encountered with small data sets, 500 sources of noise were added to the basis spectra for each simulation. To generate uncorrelated spectral noise of varying magnitudes, values returned by the randn function in Matlab (The Math Works, Inc., Natick, MA) were multiplied by a constant. The data was then analyzed using OLS and the root mean standard error of prediction (RMSEP) was compared to the prediction error given by the analytical formula.

IV. F. 2. c) Experimental Data

All chemicals used in this study were purchased from Sigma (St. Louis, MO). Glucose and creatinine were chosen for experimental data as they are water soluble and do not appear to interact with one another. Stock solutions of both analytes at 0.4 M were created with deionized water. These stock solutions were then used to obtain basis spectra as well as create all mixtures examined in this study. Data were acquired from mixtures of varying concentrations of glucose and creatinine. For each mixture examined, 500 Raman spectra were sequentially collected. Errors in reference concentrations of the mixtures, resulting from fluctuations in pipeting volumes, were probably less than a part in 500. The magnitude of noise was calculated from the experimental residuals, which were devoid of Raman features.

IV. F. 2. d) Data Processing

Data processing was preformed in Matlab 5.31. Spectra were Raman shift frequency-calibrated using known spectral lines of toluene. Individual spectra were divided by the photodiode output to correct for fluctuations in laser power. A fifth order polynomial was fit to the spectra by least-square minimization and subsequently subtracted to remove the slowly varying background [Brennan *et al.* 1997]. Cosmic rays were removed through the use of a derivative filter. Model fitting was performed using a linear combination of basis spectra with a non-negativity constraint. The fit coefficients, provided by the model, were used to predict sample concentrations and calculate RMSEP values.

## IV. F. 3. Theory

Multivariate methods of analysis provide concentration measurements via a projection vector that extracts concentration information from the spectral data set, as in Eq. IV.3. We assume that the noise in the spectral data set is the only source of error. This is an appropriate assumption for Raman spectra of biological tissues as the shot noise resulting from the fluorescence background is the dominant source of noise. If we have an accurate **B** matrix, the noise in matrix **S** induces errors in the predicted concentration. The errors can be expressed:

$$\mathbf{C}+\Delta\mathbf{C}_{noise}=(\mathbf{S}+\mathbf{S}_N)\bullet\mathbf{B} \qquad \text{(IV.12)}$$

where $\Delta\mathbf{C}_{noise}$ is the matrix of error in concentration and $\mathbf{S}_N$ is the matrix of noise in the signal matrix **S**. By subtracting Eq. IV.3 from Eq. IV.12, we obtain:

$$\Delta\mathbf{C}_{noise} = \mathbf{S}_N\bullet\mathbf{B} \qquad \text{(IV.13)}$$

Since the projection vector **B** is universal, we can insert the projection vector for OLS, given in Eq. IV.9 into Eq. IV.13 to obtain:

$$\Delta \mathbf{C}_{noise}=\mathbf{S}_N \bullet \mathbf{P}^T \bullet (\mathbf{P} \bullet \mathbf{P}^T)^{-1} \quad \text{(IV.14)}$$

When the number of samples is r, the number of components p and the number of wavelength points in each spectrum m, **S** is an rxm matrix, **C** is an rxp matrix, and **P** is a pxm matrix.

In concentration predictions, prediction errors indicate the quality of the approach. For each sample, the prediction error is the difference between the predicted concentration and the concentration measured by a reference technique. This is formulated:

$$\Delta c_i = \left| c_{prediction,i} - c_{reference,i} \right| \quad \text{(IV.15)}$$

where $\Delta c_i$ is the prediction error for the i-th sample, $c_{prediction,i}$ is the predicted concentration for the i-th sample, and $c_{reference,i}$ is the concentration measured by the reference technique for the i-th sample. For a set of samples, the prediction error for a data set is the standard deviation of the prediction errors for all samples:

$$\Delta C = \sqrt{\sum (c_{prediction,i} - c_{reference,i})/N} \quad \text{(IV.16)}$$

Where $\Delta C$ is the predicted error for the data set and N is the number of samples in the data set. $\Delta C$ is also called the RMSEP. The prediction accuracy is defined as the ratio of the mean concentration to the prediction error ($C/\Delta C$). By using the definition of standard deviation, the prediction error of the k-th element due to noise, $\Delta c_{noise}$, is expressed:

$$\Delta \mathbf{C}_{noise,k} = \sqrt{diag_k(\Delta \mathbf{C}_{noise}^T \bullet \Delta \mathbf{C}_{noise})/N} \quad \text{(IV.17)}$$

where $diag_k(\mathbf{X})$ is the diagonal k-th element of matrix **X**. Each diagonal element of the $\Delta \mathbf{C}_{noise}^T \bullet \Delta \mathbf{C}_{noise}$ is related to the error in the concentration measurement of each component. Inserting Eq. IV.14 into Eq. IV.17, we obtain:

$$\Delta \mathbf{C}_{noise,k} = \sqrt{diag_k\{[(\mathbf{P} \bullet \mathbf{P}^T)^{-1}]^T \bullet \mathbf{P} \bullet \mathbf{S}_N^T \bullet \mathbf{S}_N \bullet \mathbf{P}^T \bullet (\mathbf{P} \bullet \mathbf{P}^T)^{-1}\}/N} \quad \text{(IV.18)}$$

In the covariance matrix of shot noise, the diagonal elements are dominant. By using an approximation which neglects the off diagonal elements of the covariance matrix:

$$\mathbf{S}_N^T \bullet \mathbf{S}_N \cong n^2 \bullet N \bullet \mathbf{I} \tag{IV.19}$$

where n is the magnitude of the noise and **I** is the N-by-N identity matrix, Eq. IV.19 can be greatly simplified:

$$\Delta C_{noise,k} \cong n\sqrt{diag_k\{(\mathbf{P} \bullet \mathbf{P}^T)^{-1}\}} \tag{IV.20}$$

The matrix of basis spectra, **P**, contains spectra of pure components at unit concentrations. We can expand the matrix **P** so that:

$$\mathbf{Q} = \mathbf{P}/\mathbf{s} \tag{IV.21}$$

where **Q** is the matrix of generalized component spectra and **s** is the signal intensity. **P/s** is purely lineshape without intensity information. The signal intensity is the Euclidean norm of the spectrum of the k-th pure component [Strang 1988].

$$\mathbf{s} = \sqrt{diag_k(\mathbf{P} \bullet \mathbf{P}^T)} \tag{IV.22}$$

By inserting Eq. IV.21 into Eq. IV.20 we obtain:

$$\Delta c_k \cong (n\sqrt{diag_k(\mathbf{Q} \bullet \mathbf{Q}^T)^{-1}})/\mathbf{s} \tag{IV.23}$$

The ratio of concentration $c_k$ and error in concentration $\Delta c_k$ is the prediction accuracy. In this equation, there are two significant factors that determine the prediction error: the signal to noise ratio and the spectral overlap. The first term, s/n, is the signal to noise ratio of the target chemical. It is determined by the integrated signal (norm) of the component of interest at unit concentration and the noise (standard deviation) in the data set. The prediction accuracy increases linearly with the SNR, which has been confirmed previously [Berger and Feld 1997]. The second term describes the effect of overlap in basis spectra. **Q** is the matrix of generalized component spectra, the basis spectra without intensity information. When the

covariance matrix of **Q** has dominant diagonal elements, the spectral overlap is small and the overlap factor is close to 1, its maximum possible value. When the non-diagonal elements are comparable in magnitude to the diagonal elements, the spectral overlap is significant and the overlap factor is close to 0. The spectral overlap is affected by the number of basis spectra as well as their resolution and spectral range. Defining the overlap factor, olf, as:

$$olf=1/\sqrt{diag_k(\mathbf{Q}\bullet\mathbf{Q}^T)^{-1}} \qquad \text{(IV.24)}$$

The prediction error equation can be written as:

$$\Delta c_k \cong n/(s \bullet olf) \qquad \text{(IV.25)}$$

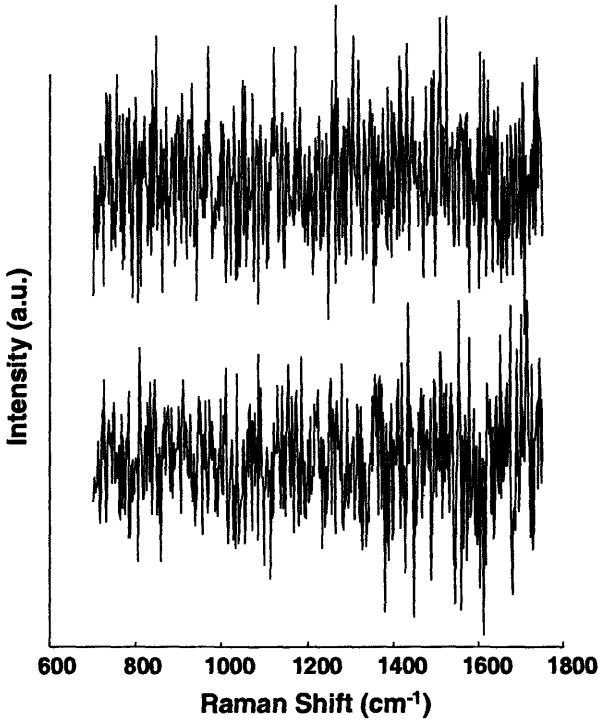


**Figure IV.11.** Comparison of the experimentally observed noise (below) and the simulated noise (above).

The formula assumes that the noise in the spectral data set is the only source of error and that the basis spectra are noise free [Koo 1996]. These are reasonable assumptions, as the shot noise resulting from the fluorescence background is the dominant source of noise in the Raman spectrum of biological tissues and basis spectra are collected for long integration times and may be averaged over many samples. The formula also assumes that the noise is uncorrelated. In other words, the noise behaves as white-noise, which is evenly distributed throughout the spectral range. Although our spectra are governed by shot-noise, the broad fluorescence background we observe with tissue measurements slopes gently

across our spectral region of interest. This background produces the dominant source of noise in our data and thus our experimental noise is similar to white- noise. A comparison between the uncorrelated noise used in the simulations and the experimentally observed noise is shown in Figure IV.11.

### IV. F. 4. Comparison with Chi-Square Analysis

Chi-square analysis is a well established method for assessing the accuracy of a modeling technique. We compare this approach with our analytical formula for calculating concentration error. A simple simulation using only the spectrum of glucose, at a signal of 4.97 counts, is examined. In this simulation, noise is the only source of concentration error, there is no overlap factor. Shown in Figure IV.12, is the parabola generated by constraining the glucose fit to the simulated spectrum with a magnitude of noise of 0.094 counts. The equation of this parabola is given by $\chi^2=(5.6(C-1)^2+1)546$, where 546 represents the degrees of freedom in our system. The error for a one component system, is inversely one half of the second derivative of $\chi^2$ with respect to C [Bevington and Robinson 1992]. This results in a concentration error of 0.018 comparable with that given by the prediction error formula, 0.019.

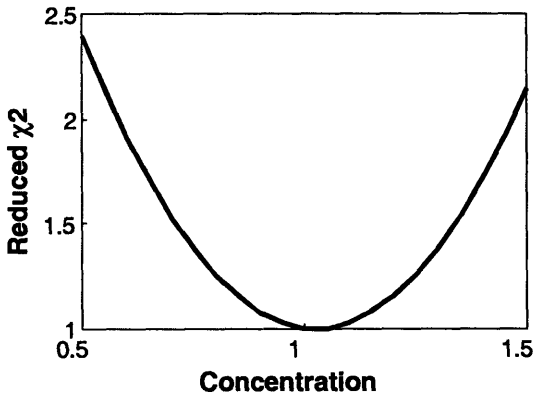

**Figure IV.12.** Chi-square error analysis.

Although the chi-square approach provides a means to calculate concentration error, complex systems with several basis spectra result in time consuming and cumbersome

analysis. The formula presented in this thesis allows rapid and straightforward calculation of prediction error and relates this error to quantifiable experimental parameters.

### IV. F. 5. Simulated Data

The prediction error expression can easily be validated with simulated data. Further, simulations are used as a direct comparison with experimental data. Simulations also allow examination of deviations from the formula due to system drift and data pre-processing techniques. Both the amount of noise and the basis spectra mixtures were varied in our simulations.

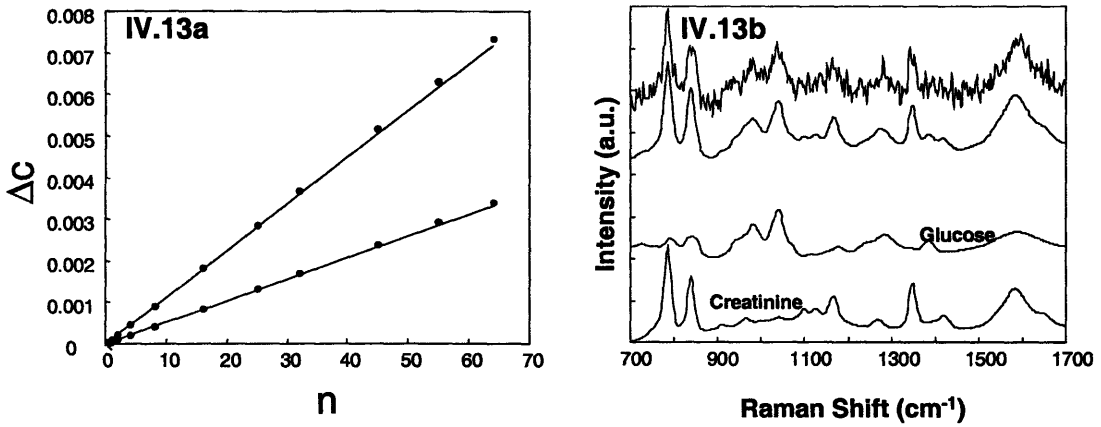


**Figure IV.13.** Results of a simulation with a low amount of spectral overlap. a) Comparison of the RMSEP of the simulated data (dots) and the prediction error given by the analytical formula (line) as a function of noise. b) Basis spectra of creatinine and glucose used in the simulation. Shown above are simulated mixture spectra with the minimum and maximum amounts of noise employed in the analysis.

Figures IV.13 and IV.14 show plots of prediction error as a function of the magnitude of noise in the data. These Figures correspond to simulations with different degrees of spectral overlap. The signals have been scaled to be comparable between the two simulations, shown in Figures IV.13 and IV.14, in order to highlight the effects of noise and spectral overlap. Figure IV.13a displays results of a simulation using glucose and creatinine in equal proportions. These two basis spectra have little spectral overlap, seen in Figure

IV.13b, and thus an overlap factor of 0.99. Also shown in Figure IV.13b are the simulated mixture data with the maximum and minimum magnitudes of noise examined. The solid lines in Figure IV.13a represent concentration errors given by the analytical formula while the dots are the RMSEP values obtained from OLS modeling of the simulated data. The simulated data exhibits excellent agreement with the prediction error formula. Figure IV.14a displays results of a simulation using cholesterol and two cholesterol esters, cholesterol linoleate and cholesterol oleate, in equal proportions. As seen in Figure IV.14b, these three basis spectra are very similar and have a large amount of spectral overlap. The overlap factors of cholesterol, cholesterol linoleate, and cholesterol oleate are 0.54, 0.37 and 0.34, respectively. The concentration errors in this analysis are much larger due to the high degree of spectral similarity in the system. Again, we obtain excellent agreement between the simulated data and the analytical formula. As expected, the prediction error increases linearly with the amount of noise in both simulations. From these simulations, we conclude that Eq. IV.25 provides accurate error estimates over a wide range of experimental conditions.

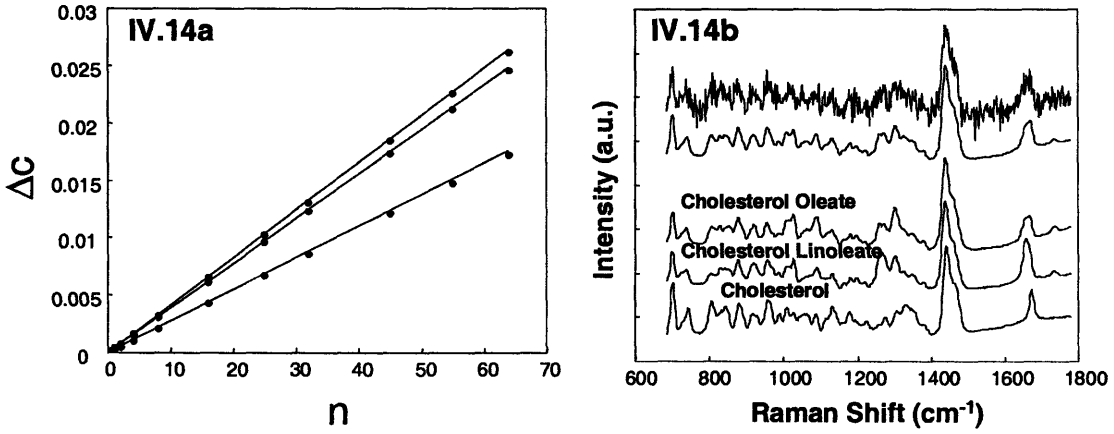


**Figure IV.14.** Results of a simulation with a high amount of spectral overlap. a) Comparison of the RMSEP of the simulated data (dots) and the prediction error given by the analytical formula (line) as a function of noise. b) Basis spectra of cholesterol, cholesterol linoleate and cholesterol oleate used in the simulation. Shown above are simulated mixture spectra with the minimum and maximum amounts of noise employed in the analysis.

Simulated data sets were constructed to closely mimic the experimental data presented below. An amplitude of noise consistent with the noise observed experimentally was used (n=13.4 counts). In this simulation, basis spectra mixtures are varied. Results are displayed in Table IV.1. Concentrations are obtained by averaging the fit coefficients for all 500 spectra and thus are expected to be within known concentrations by a factor of the prediction error divided by the square root of 500. Again, these simulations agree well with the prediction error formula and provide a means for direct comparison with experimental data.

### IV. F. 6. Experimental Data

Experimental results are also displayed in Table IV.1. Although simulated data confirms the

| | | Simulated Data | | Experimental Data | |
|---|---|---|---|---|---|
| Glucose (mM) | Creatinine (mM) | Glucose (mM) | Creatinine (mM) | Glucose (mM) | Creatinine (mM) |
| 400.0 | 0.0 | 400.0 | 0.3 | 399.9 | 0.2 |
| 0.0 | 400.0 | 0.7 | 400.0 | 1.2 | 400.6 |
| 100.0 | 300.0 | 100.1 | 300.0 | 99.2 | 299.8 |
| 200.0 | 200.0 | 200.1 | 200.0 | 197.2 | 201.1 |
| 300.0 | 100.0 | 300.1 | 100.0 | 294.3 | 100.4 |
| $\Delta c_{glucose}$ | $\Delta c_{creatinine}$ | $RMSEP_{glucose}$ | $RMSEP_{creatinine}$ | $RMSEP_{glucose}$ | $RMSEP_{creatinine}$ |
| 1.5 | 0.7 | 1.5 | 0.4 | 2.8 | 0.5 |
| 1.5 | 0.7 | 0.9 | 0.7 | 1.6 | 1.5 |
| 1.5 | 0.7 | 1.5 | 0.7 | 2.3 | 1.4 |
| 1.5 | 0.7 | 1.5 | 0.7 | 2.3 | 1.1 |
| 1.5 | 0.7 | 1.5 | 0.7 | 2.0 | 0.9 |

**Table IV.1.** Comparison of theory, simulations and experimental data of different concentration mixtures of glucose and creatinine.

accuracy of the formula, rarely are the ideal assumptions about errors observed with real data. Many factors cause these deviations such as spectrometer drift and nonlinear response as well as distortions due to data pre-processing. Experimental data tests our ability to achieve the theoretical error, provided by the analytical formula, with our instrumentation and data pre-processing techniques. As expected, the experimental data shows deviations from the theoretical predictions. However, the experimental results exhibit reasonable agreement with the analytical formula. The RMSEP is typically within a factor of two of theory and the absolute concentration is bracketed by the prediction error, although not by the prediction error divided by 500. It should be noted that the values in Table IV.1. represent ideal experimental conditions and cannot be reliably collected using our current instrumentation. Deviations are thought to be due to limitations in the ability to correct for fluctuations in laser power, pipeting errors and data pre-processing techniques, such as background and cosmic ray removal. Studies are currently underway to assess the impact of each of these factors.

### IV. F. 7. Conclusions

We have derived an analytical formula that estimates the uncertainty in concentrations predicted by linear multivariate calibration, particularly OLS. The equation is expressed in terms of easily quantifiable experimental parameters and is straightforward to evaluate. Both simulated spectra and experimental data have been used to validate the formula. This approach allows calculation of the ideal concentration error and is not subject to errors introduced from reference measurements or data pre-processing techniques. Thus, it provides insight into the fundamental limits of concentration accuracy as well as the sources

of prediction error. The ability to predict concentration errors without the use of a reference measurement is particularly useful in biological systems. With this formula, one can calculate, *a priori*, the level of signal to noise ratio needed in order to achieve a specified level of prediction accuracy. The ability to predict the smallest concentrations measurable or the signal to noise ratio necessary to observe a moiety of interest is an important step towards quantitative biomedical Raman spectroscopy.

## *Acknowledgements*

Karen Shafer-Peltier was responsible for the development of the morphological model as well as the laboratories Raman mapping techniques. Further, Karen provided much of my early training in the laboratory and I am grateful for her patience. Saumil Gandhi implemented the real-time analysis. Derivation of the prediction error formula was accomplished by Tae-Woong Koo. Finally, I would like to thank Professor Michael Feld for the numerous hours we spent discussing prediction error. Many of the images in this chapter have been reproduced from *The Journal of Raman Spectroscopy* [Shafer-Peltier *et al.* 2002] with the permission of Wiley.

## *References*

Alini M and Losa GA (1991). "Partial Characterization of Proteoglycans Isolated from Neoplastic and Nonneoplastic Human Breast Tissues." Cancer Res **51**: 1443-1447.

Baraga JJ, Feld MS and Rava RP (1992). "Rapid Near-Infrared Raman Spectroscopy of Human Tissue with a Spectrograph and CCD Detector." Appl Spectrosc **46**(2): 187-190.

Berger AJ and Feld MS (1997). "Analytical Method of Estimating Chemometric Prediction Error." Appl Spectrosc **51**: 725-732.

Bevington PR and Robinson DK (1992). Data Reduction and Error Analysis for the Physical Sciences. New York, McGraw-Hill.

Brennan JFB (1995). "Near-Infrared Raman Spectroscopy for Human Artery Histochemistry and Histopathology." Electrical Engineering Ph.D. Thesis. Cambridge, Massachusetts Institute of Technology: 124.

Brennan JF, Wang Y, Dasari RR and Feld MS (1997). "Near-Infrared Raman Spectrometer Systems for Human Tissue Studies." Appl Spectrosc **51**(2):201-208.

Buschman HP, Deinum G, Motz JT, Fitzmaurice M, Kramer JR, van der Laarse A, Bruschke AV and Feld MS (2001). "Raman Microspectroscopy of Human Coronary Atherosclerosis: Biochemical Assessment of Cellular and extracellular Morphologic structures *In Situ*." Cardiovascular Pathology **10**: 69-82.

Denium G, Rodriquez D, Römer TJ, Brennan JF, Fitzmaurice M., Myles JL, Kramer J, Lees RS and Feld MS (1999). "Principal Component Analysis as a Method to Correlate the Raman Spectrum and the Pathology of Human Coronary Artery Tissue". Appl Spectrosc **53**: 938-942.

Fisher L and Van Belle G (1993). Biostatistics: A Methodology for the Health Sciences. New York, Wiley.

Geladi L and Kowalski BR (1986). "Partial Least-Squares Regression: A Tutorial." Anal Chim Acta **185**: 1-17.

Haaland DM and Thomas EV (1988). "Partial Least-Squares Methods for Spectral Analysis I. Relation to Other quantitative Calibration Methods for Spectral Extractions of Qualitative Information." Anal Chem **60**: 1193-1202.

Hanlon EB, Manoharan R, Koo TW, Shafer KE, Motz JT, Fitzmauric M, Kramer JR, Itzkan I, Dasari RR and Feld MS (2000). "Prospects for *In Vivo* Raman Spectroscopy." Phys Med Biol **45**(2): R1-R59.

Kodati VR, Tomasi GE, Turumin JL and Tu AT (1990). "Raman Spectroscopic Identification of Calcium-Oxalate-Type Kidney Stone." Appl Spectrosc **44**: 1408-1411.

Kodati VR, Tomasi GE, Turumin JL and Tu AT (1991). "Raman Spectroscopic Identification of Phosphate-Type Kidney Stones." Appl Spectrosc **45**: 581-583.

Kontoyannis CG, Bouropoulos NC and Koutsoukos PG (1997). "Use of Raman Spectroscopy for the Quantitative Analysis of Calcium Oxalate Hydrates: Application for the Analysis of Urinary Stones." Appl Spectrosc **51**: 64-67.

Koo TW (1996). "Measurement of Blood Analytes in Turbid Biological Tissue Using Near-Infrared Raman Spectroscopy." Mechanical Engineering Ph.D. Thesis. Cambridge, Massachusetts Institute of Technology: 137-140.

Kramer R (1998). Chemometric Techniques for Quantitative Analysis. New York, Marcel Dekker.

Mahadevan A and Richards-Kortum R (1996). "Raman Spectroscopy for the Detection of Cancers and Precancers." J Biomed Opt **1**: 31-70.

Manoharan R, Baraga JJ, Feld MS and Rava RP (1992). "Quantitative Histochemical Analysis of Human Artery Using Raman Spectroscopy." J Photochem Photobiol B: Biol **16**: 211-233.

Manoharan R, Shafer K, Perelman L, Wu J, Chen K, Deinum G, Fitzmaurice M, Myles J, Crowe J, Dasari RR and Feld MS (1998). "Raman Spectroscopy and Fluorescence Photon Migration for Breast Cancer Diagnosis and Imaging." Photochem Photobiol **67**: 15-22.

Motz JT (2003). "Development of *In Vivo* Raman Spectroscopy of Atherosclerosis." Medical Physics Ph.D. Thesis. Cambridge, Massachusetts Institute of Technology.

Motz JT, Gandhi SJ, Haka AS, Galindo L, Kramer JR, Dasari RR and Feld MS (2004). "Real-Time Raman System for *In Vivo* Disease Diagnosis" JBO in press.

Pagano M and Gauvreau K (1993). Principles of Biostatistics. Belmont, CA, Duxbury.

Puppels GJ, de Mull FFM, Otto C, Greve J, Robert-Nicoud M, Arndt-Jovin DJ, Jovin TM (1990). "Studying Single Living Cells and Chromosomes by Confocal Raman Microspectroscopy." Nature **372**(301).

Radi MJ (1989). "Calcium Oxalate Crystals in Breast Biopsies." Arch Pathol Lab Med **113**: 1367-1369.

Raman C and Krishnan K (1928). "A New Type of Secondary Radiation." Nature **121**: 501-502.

Robb EW and Munk ME (1990). "A Neural Network Approach to Infrared Spectrum Interpretation." Microchim Acta **1**:131-155.

Shafer-Peltier KE, Haka AS, Fitzmaurice M, Crowe J, Myles J, Dasari RR and Feld MS (2002). "Raman Microspectroscopic Model of Human Breast Tissue: Implications for Breast Cancer Diagnosis *In Vivo*." J Raman Spec **33**(7): 125-137.

Sharma S (1996). Applied Multivariate Techniques. New York, Wiley.

Shaver JM (2001). *Chemometrics for Raman Spectroscopy*. Handbook of Raman Spectroscopy. 275-306. Lewis IR and Edwards HGM, Ed. New York, Marcel Dekker, Inc.

Strang G (1988). Linear Algebra and its applications. Orlando, Harcourt College Publisher.

Thomas EV and Haaland DM (1990). "Comparison of Multivariate Calibration Methods for Quantitative Spectral Analysis."Anal Chem **62**:1091-1099.

Zheng X, Fu W, Albin S, Wise KL, Javey A and Cooper JB (2001). "Self-Referencing Raman Probes for Quantitative Analysis." Appl Spectrosc **55**(4): 382-388.

# Chapter V. Raman Spectroscopic Breast Cancer Diagnosis: *Ex Vivo* Studies

We employ Raman spectroscopy to diagnose normal, benign and malignant lesions in specimens of human breast tissue. In this Chapter, Raman spectra are acquired from intact, *ex vivo* samples of human breast tissue. The volume sampled is 1 $mm^3$. Data are fit to a linear combination of the model basis spectra. The resulting fit coefficients provide insight into the chemical/morphological makeup of the tissue and are used to develop diagnostic algorithms. A diagnostic algorithm was developed in the laboratory with samples of fresh-frozen breast tissue. 130 tissue sites from 58 patients are examined with four pathologies predominating: normal, fibrocystic change, fibroadenoma, and infiltrating carcinoma. The fit coefficients corresponding to fat and collagen, represented by two basis spectra, are found to be the key diagnostic parameters in distinguishing pathologies. The resulting diagnostic algorithm, that encompasses all data and classifies samples according to specific pathological diagnoses, yields a sensitivity of 94% (29/31), a specificity of 95% (90/95) and an overall accuracy of 85% (107/126). The excellent results of this study thus supported moving the technique to a clinical setting for further testing of its efficacy in breast cancer diagnosis. As such, we undertook two clinical studies. The first, presented in this Chapter, was preformed immediately following tissue excision. Motivation and preliminary results are presented in Section V.B. The second, presented in Chapter VII, demonstrates *in vivo* data collection.

## *V. A. Raman Spectroscopy of Fresh-Frozen Breast Tissue*

Breast cancer accounts for nearly one in every three cancers diagnosed in American women. In the US, approximately 212,600 new cases are diagnosed each year and 40,000 women die from the disease [NCI 2003]. Mammography is the most common technique for detecting non-palpable, highly curable breast cancer. It employs x-rays to quantitatively probe density changes in breast tissue. However, these density changes are not uniquely correlated with the probability of breast cancer. Because of this, mammography serves as a screening technique rather than a diagnostic tool. This is evidenced by the fact that 70 to 90% of mammographically detected lesions are found to be benign upon biopsy [Johnson *et al.* 1999]. Thus, if a lesion is found through either clinical breast examination or mammography, the suspect tissue is always biopsied. Breast biopsy is often performed by a surgical excision to remove the entire lesion, but more recently, a less invasive procedure using a needle to remove a core sample of the lesion has gained acceptance. Core needle biopsy removes only a cylinder of tissue typically 1 mm in diameter and several centimeters long. Although less invasive than surgical biopsy, it requires the collection of at least five specimens to ensure proper sampling and often as many as twelve cores of tissue are removed [Lieberman *et al.* 1994]. As a consequence of the limitations of current techniques, each year a large number of breast biopsies are performed on lesions ultimately diagnosed as benign. The complete diagnostic process, from start to finish, may take months and include multiple biopsies.

The desirability of reducing the number of benign excisional biopsies preformed, patient trauma, time delay, and the high medical costs associated with biopsy has motivated researchers to explore minimally invasive optical methods for diagnosing breast lesions. The

studies below assess the ability of Raman spectroscopy to diagnose breast cancer.

### V. A. 1. Sample Preparation and Data Acquisition

All studies involving human tissue were approved by the University Hospitals of Cleveland and Case Western Reserve University Institutional Review Board and the Massachusetts Institute of Technology Committee On the Use of Humans as Experimental Subjects. Samples were provided by the Cooperative Human Tissue Network from surgical biopsy specimens, reduction mammoplasties and prophylactic mastectomies.

#### V. A. 1. a) Tissue Preparation

Breast tissue was obtained from patients undergoing surgical procedures. Upon removal, the samples were snap frozen in liquid nitrogen and stored at –80 °C until examination. Samples were passively thawed at room temperature and kept moist with phosphate buffered saline (PBS). Following spectral acquisition, specimens were marked with India ink to indicate the region sampled, and fixed in formalin. The fixed tissue samples were routinely processed, paraffin embedded, cut through the marked locations in 5 μm thick sections, and stained with H&E. The histological slides were examined by an experienced breast pathologist who was blinded to the outcome of the Raman spectroscopy analysis. A total of 130 spectra from 58 patients was examined using Raman spectroscopy, 49 spectra from normal breast tissue, 47 from benign lesions, 3 from lesions diagnosed as DEH, and 31 from malignant lesions. Normal tissue from 25 patients was examined (20 female/2 male/3 unknown; 8 Caucasian/12 Black/5 unknown) with a mean age of 34.3 years and an age range of 13-75 years. Fibrocystic change was studied in 16 patients (10 female/1 male/5 unknown; 5 Caucasian/3

Black/8 unknown) with a mean age of 40.3 years and an age range of 13-75 years. Tissue diagnosed as fibroadenoma was obtained from 6 patients (4 female/2 unknown; 2 Black/4 unknown) with a mean age of 20.8 years and an age range of 13-40 years. All malignant samples were diagnosed as infiltrating carcinoma (10 ductal/2 lobular/1 ductal and lobular/ 1 mammary, not otherwise specified). Infiltrating carcinoma was examined in 16 patients (8 female/8 unknown; 5 Caucasian/2 Black/9 unknown) with a mean age of 57.6 years and an age range of 46-77 years. DEH was encountered in 2 female Caucasian patients with ages of 11 and 49 years. Patient information was not available for the sample diagnosed as fat necrosis.

The mean ages and age ranges for the patients in this study reflect the natural age incidence of each lesion [Rosen and Oberman 1992]. The peak age of incidence for stromal fibroplasia, the predominant manifestation of fibrocystic change encountered in this study, is in the 4th and 5th decades (30's and 40's). The peak age of incidence of fibroadenoma is much earlier, the 3rd decade (20's), and fibroadenomas account for the majority of breast lesions requiring biopsy in that age range. The peak age of incidence for infiltrating carcinoma is the 6th decade (50's).

As multiple spectra are collected from each patient, some tissue samples are included in both the normal and diseased categories, depending on the pathology underlying the exact region of data collection. Specifically, three tissue samples with fibrocystic change also contained normal breast tissue, one sample with fibrocystic change also contained DEH, one sample with fibroadenoma contained adjacent fibrocystic change, and one sample contained foci of infiltrating carcinoma, fibrocystic change and normal breast tissue.

V. A. 1. b) Raman Spectroscopic Measurements and Data Processing

Data were acquired using the laboratory Raman macroscopic system shown in Figure III.8 and detailed in Chapter III.E.2. Raman spectra in this study were acquired with a 10 to 30 sec. integration time, depending on signal intensity, with a spectral resolution of 8 $cm^{-1}$. The average laser excitation power varied between 100 and 150 mW. No tissue damage was observed, either grossly or upon histological review.

Data processing was preformed in Matlab 5.30. Spectra were Raman shift frequency-calibrated using known spectral lines of toluene. A fifth order polynomial was fit to the spectra by least-square minimization and subsequently subtracted to remove the slowly varying fluorescence background. Cosmic rays were removed through the use of a derivative filter. Raman spectra were divided by a white light spectrum to account for the spectral response of the system. Model fitting was performed using a linear combination of basis spectra with a non-negativity constraint. The contribution of each basis spectrum, obtained from the spectral model described in Chapter IV.C, to the breast tissue specimens was acquired by normalizing the fit coefficients (excluding water, as it is applied exogenously) such that they sum to one. Logistic regression, a discriminate analysis technique, was used to correlate the normalized fit coefficients with the diagnostic categories. Using logistic regression, we examined the diagnostic capability of all combinations of the eight morphological components in the model. The diagnostic algorithm presented below resulted in the highest sensitivity and specificity. In order to cross validate our algorithm, we employed a leave-one-out cross validation analysis. The diagnostic decision lines displayed in the figures were obtained using logistic regression with all samples included. However, to obtain the sensitivities and specificities reported in this thesis, logistic regression with leave-

one-out cross validation was used. These methods of data analysis and diagnostic algorithm development are detailed in Chapter IV.

Receiver operating characteristic (ROC) curves were generated by changing the probability threshold for assigning a classification (e.g. changing the probability threshold for cancer:non-cancer discrimination from 50%:50% to 45%:55%). Sensitivity and specificity were calculated in increments of 5% from 0% to 100%. Figures display unique values of sensitivity and specificity.

### V. A. 2. Model Fits

To understand the relationship between a tissue sample's Raman spectrum and its disease state, we examined the contribution of each model basis spectrum to spectra acquired from a variety of pathologies. Model fits to Raman spectra acquired from normal, benign, and malignant samples of breast tissue are shown in Figure V.1, along with the corresponding images from H&E stained sections used to make the histopathologic diagnosis. The India ink used to record the region of spectral examination can be seen as a black line on the tissue surface in the H&E images. The difference between the measured spectrum and the model fit, the residual, is shown below each spectrum in Figure V.1. The lack of significant structure in the residuals demonstrates that the model accounts for the majority of the spectroscopic features observed and describes the data well. The fit coefficients, also displayed in Figure V.1, represent the amount that each model basis spectrum must be weighted in order to recreate the tissue spectrum, thereby providing insight into the chemical/morphological makeup of the tissue. Fit coefficients are a function of both the concentration of a particular model component and its Raman scattering cross-section.

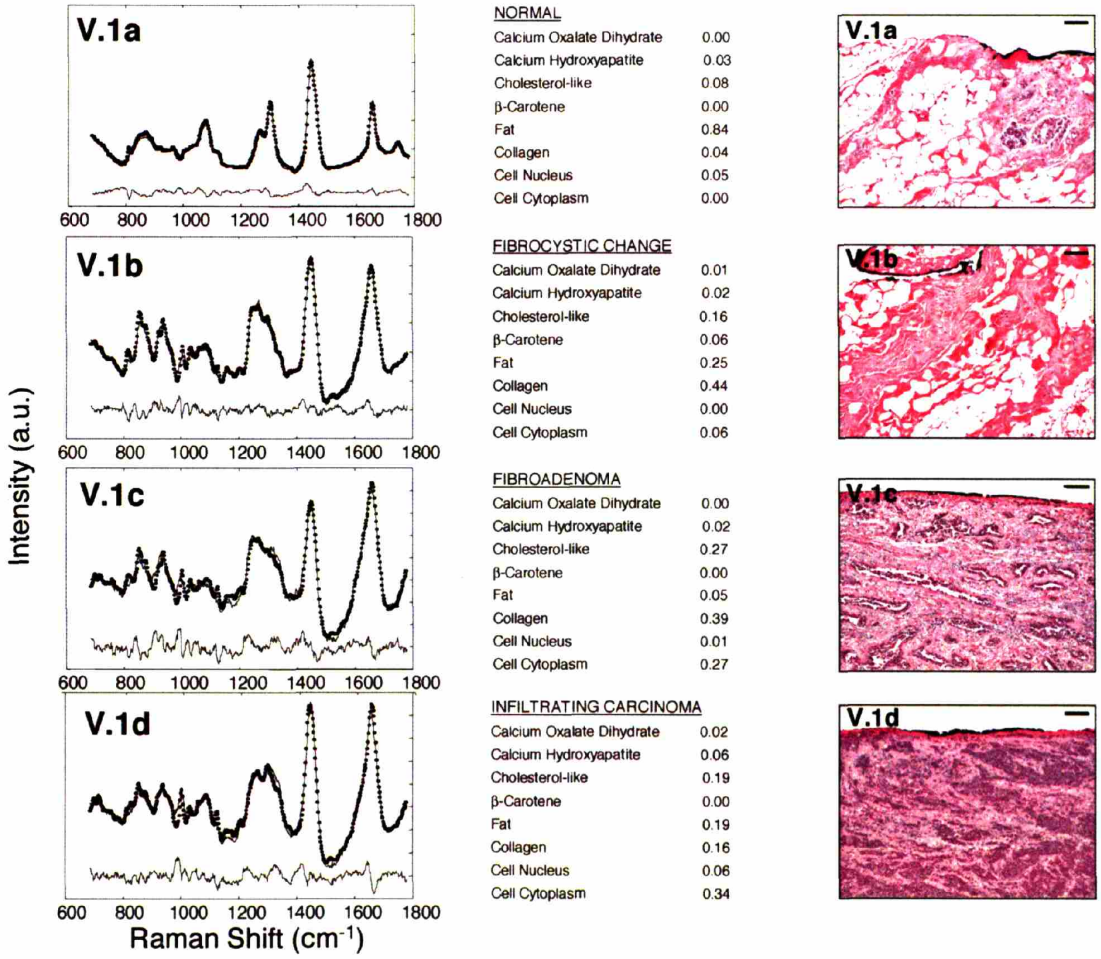


**Figure V.1.** Normalized Raman spectra (solid line), model fit (dotted line), residual (shown below), fit coefficients, and H&E images (size bars 100 μm) representative of a) normal breast tissue, b) fibrocystic change, c) fibroadenoma, and d) infiltrating carcinoma.

Four of the 130 spectra in our data set were excluded from the analysis due to an insufficient number of samples. Three of these spectra were acquired from samples diagnosed by histopathology as DEH and one was acquired from a benign sample diagnosed as fat necrosis. The sample diagnosed as fat necrosis exhibited an intense fluorescent background. This is most likely due to lipids oxidized during tissue necrosis and, with a larger data set, may prove to be diagnostic of fat necrosis.

### V. A. 3. Spectral Fit Coefficients and Tissue Morphology

The fit coefficients given by the model and normalized to sum to one, represent contributions of chemicals and morphological features to the macroscopic tissue spectrum. Figures V.2a and V.2b display histograms of the average fit coefficients associated with normal breast tissue, fibrocystic change, fibroadenoma, and infiltrating carcinoma. In Figure V.2a data are grouped according to pathologic diagnosis while in V.2b data are clustered by model component. In Figure V.2b, each histogram cluster is normalized to the largest of the four values in order to highlight the relative changes between pathologies. The amount of water present in the lesions has been excluded, as PBS is applied to keep the samples moist during examination, and thus the amount of water is not indicative of disease state. The presence or absence and variation in concentration of a particular model component between samples with similar pathologies is displayed in Figure V.2 as error bars which represent the root mean square of the fit coefficients of the data set.

Examination of the fit coefficients for each pathology provides insight into the chemical changes associated with breast disease. The fit coefficients of normal breast tissue indicate that it is primarily composed of fat. Normal breast tissue contains both glandular and adipose tissues [Rosen 1997]. Glandular tissue consists of ducts lined by epithelial cells and a supportive collagenous extracellullar matrix. Adipose tissue is primarily composed of adipocytes, cells containing large amounts of cytoplasmic fat, although small quantities of extracellular matrix are mixed throughout. In most women, ducts represent only a small volume of the breast tissue and thus our model accurately characterizes normal breast tissue as predominately comprised of fat with small contributions from collagen. Contributions from fat are particularly prominent because relative to most other model components,

adipose tissue has a large Raman scattering cross-section. The model does not show a contribution from epithelial cells to normal breast tissue. However, this does not mean that the normal samples do not contain epithelial cells, simply that they are not present in sufficient quantities or with a strong enough Raman scattering cross-section to appreciably contribute to the macroscopic Raman spectrum. The fit coefficients of the breast lesions indicate a markedly different chemical/morphological composition than that of normal breast tissue. First, the amount of collagen increases in all abnormal breast pathologies. This is consistent with known breast pathology, as lesion formation is often accompanied by fibrosis, a scarring process characterized by an increased stromal component, and thus by both proliferation of fibroblasts and accumulation of collagen. The relative increase in collagen is most pronounced in fibrocystic change, a benign condition which can manifest itself as fibrosis, adenosis (increase in the number of ductules) or cyst formation (dilation of ducts and lobules with fluid). Each of these changes can occur with or without the presence of the others. In the fibrocystic lesions examined in the present study an increase in the fit coefficients of the collagen, epithelial cell cytoplasm and cholesterol-like basis spectra replace the large contribution from fat in normal breast tissue.

Fibroadenoma is a benign tumor of a completely different lineage than all other lesions in this study [Houssami *et al.* 2001]. It is most closely related to phylloides tumors, the malignant counterpart of which is not carcinoma but cystosarcoma phylloides, in which the stroma rather than the epithelium is malignant. Lesions diagnosed as fibroadenoma show an increased contribution from collagen due to fibroblast proliferation and accumulation of collagen that results in expansion of the stroma [Cotran *et al.* 1989]. They also show an increased contribution from both the cell nucleus and epithelial cell cytoplasm

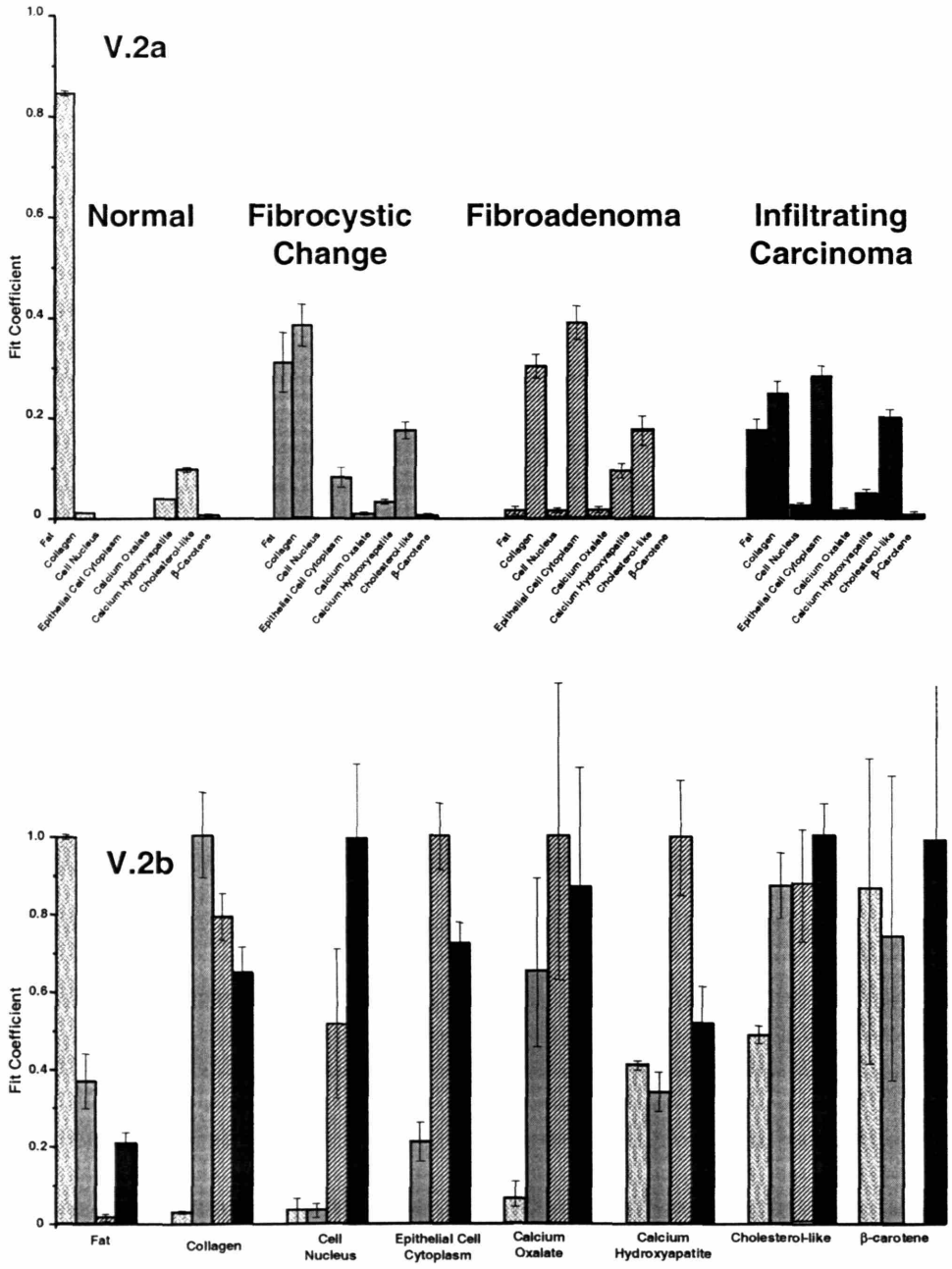


**Figure V.2.** Histogram displaying the average composition of samples diagnosed as normal (hatched), fibrocystic change (gray), fibroadenoma (striped), and infiltrating carcinoma (solid). A) Data are grouped according to pathologic diagnosis. B) Data are clustered by model component and each cluster is normalized to the largest of the four values.

basis spectra as a consequence of the number of fibroblasts and epithelial cells present.

Similar to fibroadenoma, lesions diagnosed as infiltrating carcinoma show an increased contribution from collagen, in this case due to fibroblast proliferation in response

to stromal invasion by the malignant epithelial cells [Cotran *et al.* 1989]. The fit coefficients of such lesions also display an increase in the amount of epithelial cell cytoplasm and cell nucleus. Both infiltrating carcinomas and fibroadenomas exhibit large increases in the number of cells relative to other lesions. However, a key signature of carcinoma is enlargement of cell nuclei, and thus a higher nuclear to cytoplasm (N/C) ratio than in benign conditions. Nuclear enlargement and atypia are hallmarks of cancer, thus the N/C ratio is a diagnostic criterion routinely used by pathologists [Elston and Ellis 1991; Hoda and Rosen 2002]. In our studies, the spectroscopic parameter characterizing the N/C ratio is obtained by dividing the fit coefficient of the cell nucleus basis spectrum by the fit coefficient of the epithelial cell cytoplasm basis spectrum. Fibrocystic change has a mean N/C parameter of 0.01, fibroadenoma 0.04, and infiltrating carcinoma a much higher mean N/C parameter of 0.08.

Further differences between lesions diagnosed as fibroadenoma and infiltrating carcinoma exist in the amount of fat present. Samples diagnosed as fibroadenoma have less fat than those diagnosed as infiltrating carcinoma, as can be seen in Figure V.2. This is because fibroadenoma is an expansile lesion that grows by pushing the fatty breast tissue aside. Infiltrating carcinoma, on the other hand, infiltrates in between the fat cells, so some adipocytes will be retained within the carcinoma.

Other breast pathologies are much less common and were not represented in the study specimens. Three samples diagnosed as DEH have not been included in the diagnostic analysis due to their small number. DEH is a proliferation of the ductal epithelium which confers a significantly increased risk for breast cancer [Page and Dupont 1990]. The mean N/C parameter of these three lesions is 0.05, intermediate between those of normal breast and

infiltrating carcinoma, indicating the potential for detecting pre-cancerous changes in the breast using Raman spectroscopy.

The histograms in Figure V.2 exhibit relatively little contribution from the two types of calcifications found in breast tissue, calcium hydroxyapatite and calcium oxalate dihydrate. Due to their diagnostic importance, microcalcifications in fresh breast tissue are not typically made available for scientific research, and thus our study did not include lesions containing microcalcifications. For this reason, we undertook a parallel study to examine the diagnostic information contained in Raman spectra of microcalcification, discussed in Chapter VI. Although small contributions from microcalcifications can be seen in some of our data, as this technique moves into a clinical setting microcalcifications will be encountered more frequently and in greater abundance.

Table V.1 displays the fit coefficient error associated with each model component.

| Model | Signal | OLF | $\Delta c_{normal}$ | $\Delta c_{fibrocystic\ change}$ | $\Delta c_{fibroadenoma}$ | $\Delta c_{cancer}$ |
|---|---|---|---|---|---|---|
| | | | N=0.0091 | N=0.0406 | N=0.0113 | N=0.0337 |
| Calcium Oxalate Dihydrate | 2.68 | 0.96 | 0.004 | 0.016 | 0.004 | 0.013 |
| Calcium Hydroxyapatite | 2.85 | 0.93 | 0.003 | 0.015 | 0.004 | 0.013 |
| Cholesterol-like | 4.48 | 0.28 | 0.007 | 0.032 | 0.009 | 0.027 |
| Water | 7.04 | 0.64 | 0.002 | 0.009 | 0.003 | 0.008 |
| β-Carotene | 3.67 | 0.84 | 0.003 | 0.013 | 0.004 | 0.011 |
| Fat | 4.97 | 0.40 | 0.005 | 0.020 | 0.006 | 0.017 |
| Collagen | 8.12 | 0.45 | 0.003 | 0.011 | 0.003 | 0.009 |
| Cell Nucleus | 5.96 | 0.69 | 0.002 | 0.010 | 0.003 | 0.008 |
| Epithelial Cell Cytoplasm | 6.32 | 0.31 | 0.005 | 0.021 | 0.006 | 0.017 |

**Table V.I.** Fit coefficients errors for the fresh-frozen Raman breast data.

The method used for calculating prediction error is presented in section IV.F. Errors are broken down by diagnosis, as spectra corresponding to different pathologies contained

dissimilar amounts of noise. It is important to note that these errors represent the lowest attainable accuracy and are not achieved experimentally.

### V. A. 4. Diagnostic Algorithm

The fit coefficients not only provide insight into the composition of the tissue but are also used to develop diagnostic algorithms. The morphological changes that characterize breast disease are manifested as chemical changes that can be reproducibly assessed. We begin with a pairwise analysis in which cancerous specimens are separately distinguished from normal breast tissue, fibrocystic change, and fibroadenoma, respectively. We then employ the insight gained through these individual comparisons to develop a single diagnostic algorithm encompassing all pathologies. Logistic regression was used to correlate the fit coefficients, obtained via modeling, with the diagnostic categories provided by a pathologic examination. A leave-one-out cross validation analysis was also employed. In each case, the diagnostic power of all 8 model components, alone and in combination, was assessed.

Normal breast and infiltrating carcinoma can be differentiated with 100% sensitivity and 100% specificity using the fit coefficients for collagen and fat, FC(Coll) and FC(Fat), respectively. Figure V.3

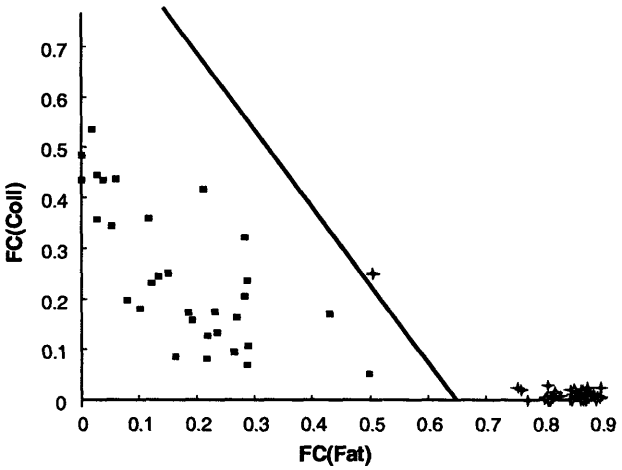


**Figure V.3.** Diagnostic plot illustrating the excellent separation between infiltrating carcinoma (squares) and normal breast tissue (stars).

shows a scatter plot of FC(Coll) and FC(Fat) corresponding to each of the normal and malignant samples examined. The decision line for separating normal and malignant samples is given by FC(Coll)=-1.71FC(Fat)+1.11. These two parameters result in the ability to separate normal and malignant tissues and they are consistent with known architectural changes that accompany breast disease. The normal data point that lies closest to the diagnostic decision line was acquired from a specimen that contains adjacent fibrocystic change. This may explain the increase in collagen and reduction in fat seen in this sample compared to other normal samples. Although the diagnostic algorithm depicted in Figure V.3 results in exact separation, any other model component, when combined with fat, also provides perfect discrimination. This is because our model characterizes normal breast tissue as composed almost exclusively of fat.

Figure V.4 displays the diagnostic algorithm resulting in the highest sensitivity and specificity for distinguishing fibrocystic change from infiltrating carcinoma. Again, we are able to separate fibrocystic change and malignant lesions based on the amount of collagen and fat. In this case, the equation for the decision line is FC(Coll)=-0.71FC(Fat)+0.51. Based on these two parameters, we are able to correctly predict 29 out of 31 malignant samples and 29 out of 31 samples diagnosed as fibrocystic change. This results in a sensitivity

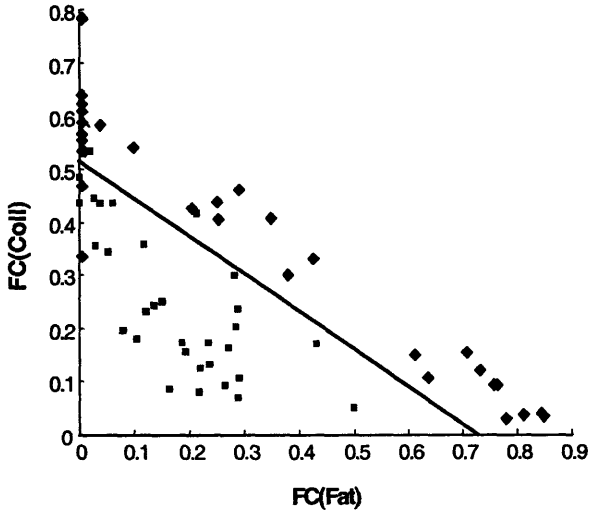


**Figure V.4.** The diagnostic algorithm for infiltrating carcinoma (squares) and fibrocystic disease (diamonds).

of 94%, a specificity of 94%, and a positive predictive value of 94%. Although clear differences in the spectroscopic parameter characterizing the N/C ratio exist between fibrocystic change and infiltrating carcinoma, inclusion of the fit coefficients for epithelial cell cytoplasm and cell nucleus did not improve the sensitivity and specificity of the diagnostic algorithm. The sensitivity and specificity for differentiating fibrocystic change and infiltrating carcinoma based solely on the N/C parameter are 65% and 90%, respectively.

Figure V.5 displays a scatter plot of the diagnostic algorithm resulting in the highest sensitivity and specificity for differentiating fibroadenoma and infiltrating carcinoma. In this case, fat is the only diagnostic parameter. Collagen is no longer diagnostic in differentiating between these two data sets. Using the amount of fat, the two pathologies can be differentiated with a sensitivity of 90% and a specificity of 80%. Thus, the algorithm provides a positive predictive value of 90% and accurately predicts 28 out of 31 malignant samples and 12 out of 15 samples diagnosed as fibroadenoma. The equation for the decision line is given by FC(Fat)=0.03.

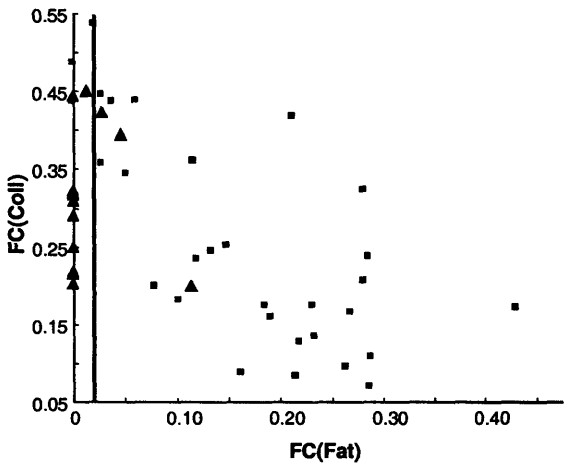


**Figure V.5.** The diagnostic algorithm for infiltrating carcinoma (squares) and fibroadenoma (triangles).

As discussed above, fibroadenoma and infiltrating carcinoma have distinct natural ages of incidence. Thus, age could provide useful information to enhance the diagnostic algorithm. Unfortunately, in the present study we did not have patient information for all of our samples. In future studies, it will be interesting to see the extent to which the inclusion of patient age improves the diagnostic algorithm. Based on insight gained through the pairwise

diagnostic comparisons, a single diagnostic algorithm encompassing all pathologies was developed. The algorithm examines all the data simultaneously and separates samples according to specific pathological diagnoses. As noted from the diagnostic algorithms displayed in Figures V.3, V.4, and V.5, all pathologies can be separated based on the same two parameters, fat and collagen. Further, in our studies there are clearly two tissue types with relatively low fat and collagen values and two pathologies with higher values. From this observation, the samples were initially divided into two groups based on their collagen and fat contents. The equation for the decision line, drawn by logistic regression, is FC(Coll)=-0.80FC(Fat)+0.55. The inclusion of additional model components did not

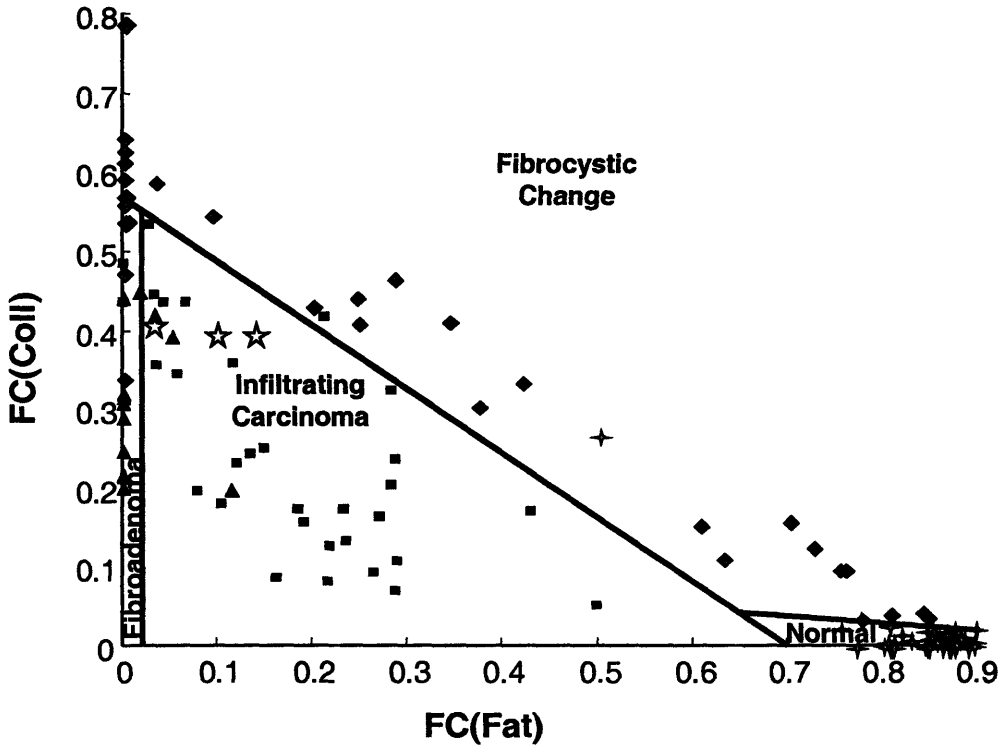


**Figure V.6.** Diagnostic algorithm displaying the fat and collagen content for all pathologies encountered in this study. Normal (gray stars), Fibrocystic Change (diamonds), Fibroadenoma (triangles), Infiltrating Carcinoma (squares), Ductal Epithelial Hyperplasia (white stars).

improve the accuracy of this separation. The resulting two clusters, one containing infiltrating carcinoma and fibroadenoma lesions, which have relatively less collagen and fat, and the second composed of normal and fibrocystic lesions, were then further subdivided. Fibrocystic change and normal tissue were separated based on their fat and collagen contents. The decision line for separating fibrocystic change and normal tissue is given by FC(Coll)=-0.06FC(Fat)+0.10. As in Figure V.5, fibroadenoma and infiltrating carcinoma are separated based on their fat content. The decision line for this separation, FC(Fat)=0.02, is based on a different probability threshold than that in the individual comparison of fibroadenoma and infiltrating carcinoma. This was done because of the prognostic importance of correct cancer diagnosis and was accomplished by moving to a different location on the ROC curve.

| **Pathology Diagnosis** / **Raman Diagnosis** | Normal (49 spectra) | Fibrocystic Change (31 spectra) | Fibroadenoma (15 spectra) | Infiltrating Carcinoma (31 spectra) |
|---|---|---|---|---|
| Normal | 45 | 1 | 0 | 0 |
| Fibrocystic Change | 4 | 22 | 0 | 0 |
| Fibroadenoma | 0 | 7 | 11 | 2 |
| Infiltrating Carcinoma | 0 | 1 | 4 | 29 |

**Table V.2.** Comparison of pathologic diagnosis with that of the Raman diagnostic algorithm. The Raman diagnostic algorithm results in an overall accuracy of 85% (107/126).

Figure V.6 displays a scatter plot of FC(Coll) and FC(Fat) for all pathologies encountered in this study, as well as the decision lines that separate samples according to diagnoses. Table V.2 compares the pathologic diagnosis with that of the Raman diagnostic algorithm for our data set. The algorithm results in a sensitivity for detecting infiltrating carcinoma of 94% (29/31), a specificity of 95% (90/95), and an overall accuracy of 85% (107/126). Also shown in Figure V.6 are the fat and collagen fit coefficients for the three

samples diagnosed as DEH. The sample diagnosed as fat necrosis was not analyzed due to a poor SNR resulting from excessive shot noise generated via the intense fluorescent background. In future applications, this diagnostic algorithm will be used in a prospective manner, and the fit coefficients of collagen and fat simply plotted to determine where they fall in the diagnostic plane.

Figure V.7 displays a ROC curve, shown as a dotted line, that illustrates the ability of Raman spectroscopy to separate lesions diagnosed as infiltrating carcinoma from benign and normal breast tissues. A ROC curve illustrates the tradeoff between sensitivity and specificity by plotting the true positive rate against the false positive rate for the different possible probability thresholds of a diagnostic test. The closer the curve comes to the 45-degree diagonal, shown as a dashed line in Figure V.7, the less accurate the diagnostic test.

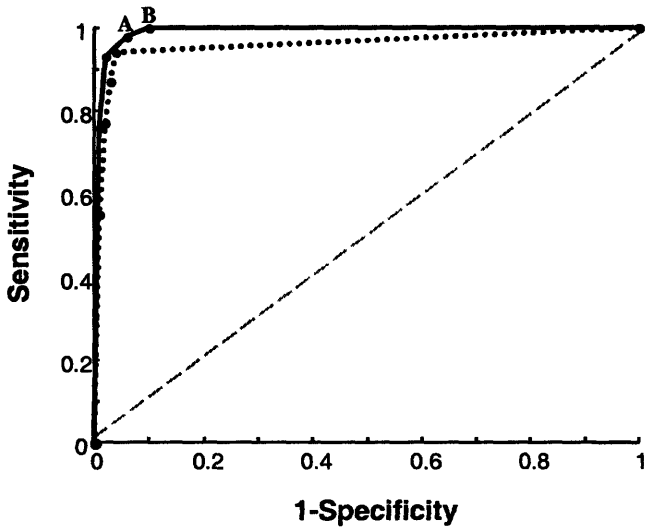


**Figure V.7.** Receiver operating characteristic (ROC) curves illustrating the ability of Raman spectroscopy to separate lesions diagnosed as infiltrating carcinoma from benign and normal breast tissues, dotted line and lesions which need to be excised (infiltrating carcinoma and fibroadenoma) from those which don't (normal and fibrocystic change), solid line.

This ROC curve clearly illustrates the ability of Raman spectroscopy to accurately diagnose breast cancer and demonstrates how the diagnostic scheme can be adjusted to obtain the desired degree of sensitivity at the cost of specificity.

From a practical clinical standpoint, Raman spectroscopy is well suited to identify lesions that need to be excised. Malignant lesions such as infiltrating carcinoma need to be excised, whereas most benign lesions, such

as fibrocystic change, do not. However, fibroadenomas, although benign, continue to grow and produce significant morbidity unless excised [Kahn and Badve 2001]. Results using the overall diagnostic algorithm to differentiate infiltrating carcinoma and fibroadenoma (lesions to be excised) from fibrocystic change and normal breast tissue are displayed in Figure V.7 as a solid line. In this case, sensitivity and specificity, identified on the ROC curve by the letter A, are 98% and 94%, respectively. This corresponds to a positive predictive value of 90% and a negative predictive value of 99%, indicating that if a lesion is not excised there is only a 1% chance that it is cancerous. Alternatively, a different threshold can be set in which all malignant lesions are excised, identified in Figure V.7 with the letter B. Using this threshold, 10 out of every 100 benign lesions examined will be unnecessarily removed. This results in a positive predictive value of 85% and a negative predictive value of 100% in this small data set, signifying that if a lesion is not excised there is no chance that it is malignant. This indicates that Raman spectroscopy has the potential to safely reduce the number of excisional biopsies performed on lesions eventually diagnosed as benign.

### V. A. 5. Effect of Age/Menopause on Diagnostic Algorithm

Female breast undergoes substantial biochemical alterations at menopause. Specifically, a large amount of collagen is converted to fat, resulting in breast tissue that is overall less dense on mammography. Because our diagnostic algorithm is based on the fat and collagen content as assessed by Raman spectroscopy, we investigated trends in these two parameters as a function of patient age (female breast density typically decreases with age). It is notable that although the normal samples span a wide age range, our technique characterizes them as predominately composed of fat. As explained above, this is because the Raman scattering

cross-section is much higher for fat than for collagen. Thus, we only observe significant contributions from collagen when it is present in large quantities, for instance in the setting of dense stromal fibrosis. To rigorously confirm that our diagnostic algorithm is not influenced by patient age, we examined the correlation between the spectroscopic parameter characterizing the fat to collagen ratio, obtained by dividing FC(Fat) by FC(Coll), and age. Fibroadenoma was excluded from this analysis because it is a juvenile disease and has a much different age range than the other pathologies in our study. We found a correlation coefficient of -0.140 for the spectroscopic parameter characterizing the fat to collagen ratio and age. We also examined the relationship between the fat to collagen ratio and age within individual pathologies. For invasive carcinoma, fibrocystic change, and normal samples, we obtained correlation coefficients of -0.104, 0.137, and -0.025, respectively. Thus, we do not observe age dependent trends in the fat and collagen contents of our data. Our results indicate that Raman spectroscopy is much less sensitive to breast density and menopausal status than many other optical techniques.

## *V. B. Raman Spectroscopy of Fresh Breast Tissue*

The excellent results of our studies on fresh-frozen tissue demonstrated that Raman spectroscopy can classify breast lesions with high accuracy. The study thus supported moving the technique to a clinical setting for further testing of its efficacy in breast cancer diagnosis. As a result, we expanded our studies to the examination of fresh breast tissue. Data was collected in the University Hospitals of Cleveland pathology suite, typically within half an hour of surgical tissue excision. The main goals of this study are to validate our *ex vivo* diagnostic algorithm on a large data set which closely mimics an *in vivo* environment

and to elucidate differences between the Raman spectra of fresh-frozen and fresh breast tissues. Additional goals include expanding our diagnostic algorithm to include pathologies not seen in our *ex vivo* laboratory data and targeting microcalcifications.

### V. B. 1. Sample Preparation and Data Acquisition

This study was carried out in collaboration with Drs. Fitzmaurice, Shenk, Wang, and Klein at University Hospitals of Cleveland and Case Western Reserve University. All studies involving human tissue were approved by the University Hospitals of Cleveland and Case Western Reserve University Institutional Review Board and the Massachusetts Institute of Technology Committee On the Use of Humans as Experimental Subjects. Informed consent was obtained from all subjects prior to the surgical procedures.

#### V. B. 1. a) Tissue Preparation

Breast tissue was obtained from patients immediately following surgical lumpectomy, re-excision, or mastectomy procedures. Upon removal, the samples were sectioned per the normal pathology protocol and Raman spectra acquired from locations chosen by the pathologist. The number of spectra taken per patient was extremely variable, depending primarily on the pathological manifestations grossly visible. Because it was not possible to turn the lights off in the pathology suite, samples were placed in a light tight box prior to examination. Following spectral acquisition, specimens were marked with India ink to indicate the region sampled, and fixed in formalin. The fixed tissue samples were routinely processed, paraffin embedded, cut through the marked locations in 5 μm thick sections, and stained with H&E. The histological slides were examined by an experienced breast

pathologist who was blinded to the outcome of the Raman spectroscopy analysis. A total of 150 spectra from 25 patients was examined using Raman spectroscopy, 42 spectra from normal breast tissue, 82 from benign lesions, and 26 from malignant lesions. Benign pathologies consisted of 73 fibrocystic lesions and 9 fibroadenoma tumors. Malignant pathologies consisted of 6 infiltrating ductal carcinomas (IDC) and 20 lesions diagnosed as ductal carcinoma *in situ* (DCIS). DCIS is a pathology we did not encounter in our fresh-frozen studies.

V. B. 1. b) Raman Spectroscopic Measurements and Data Processing

Data were acquired using the clinical Raman system and Raman optical fiber probe shown in Figure III.9 and detailed in Chapter III.E.3. Raman spectra in this study were acquired with a 10 to 30 s. integration time, depending on signal intensity, and a spectral resolution of 8 $cm^{-1}$. The average laser excitation power varied between 100 and 150 mW. No tissue damage was observed, either grossly or upon histological review.

At the start of each day, calibration data were collected for spectral corrections. Wavenumber calibration was established with a spectrum of 4-acetamidophenol. Chromatic intensity variations were corrected by collecting the spectrum of a tungsten white light source diffusely scatted by a reflectance standard ($BaSO_4$). The remaining probe background generated in the optical fibers was characterized by collecting the scattered excitation light off of a roughened aluminum surface. This background was optimally subtracted from the data in an iterative loop by using a scaling factor related to the tissue's optical properties [Motz *et al.* 2004]. The tissue fluorescence background was modeled with a sixth-order polynomial. Finally, the data was fit via non-negativity constrained least-squares minimization with the spectral model developed previously for the diagnosis of breast cancer

[Shafer-Peltier *et al.* 2002]. In order to accurately model the data, spectra of probe components, epoxy and sapphire, were included in the model. Also, a background acquired in the light tight box with no sample was included in the model. This background mainly consisted of features due to light contamination. In accordance with our initial diagnostic study, the contribution of each basis spectrum, obtained from the spectral model described in Chapter IV.C, to the breast tissue specimens was obtained by normalizing the fit coefficients such that they sum to one. However, in the present analysis, the two types of microcalcifications, calcium hydroxyapatite and calcium oxalate dihydrate, were excluded from this normalization as these species were not present in the tissue samples used for the diagnostic algorithm development. We also observed increased contributions from cholesterol-like in this data set and thus this component was excluded from normalization.

### V. B. 2. Agreement with Fresh Frozen Diagnostic Algorithm

Data was analyzed with the diagnostic algorithm developed on fresh-frozen tissues, shown in Figure V.8. Application of this algorithm in a prospective manner resulted in a sensitivity of 83%, correctly diagnosing 5 of 6 IDCs, and a specificity of 89% for separating cancerous

| **Pathology Diagnosis** / **Raman Diagnosis** | Normal (42 spectra) | Fibrocystic Change (73 spectra) | Fibroadenoma (9 spectra) | Infiltrating Carcinoma (6 spectra) |
|---|---|---|---|---|
| Normal | 38 | 13 | 0 | 0 |
| Fibrocystic Change | 4 | 54 | 0 | 0 |
| Fibroadenoma | 0 | 0 | 1 | 1 |
| Infiltrating Carcinoma | 0 | 6 | 8 | 5 |

**Table V.3.** Comparison of pathologic diagnosis with that of the Raman diagnostic algorithm. The Raman diagnostic algorithm results in an overall accuracy of 75% (98/130).

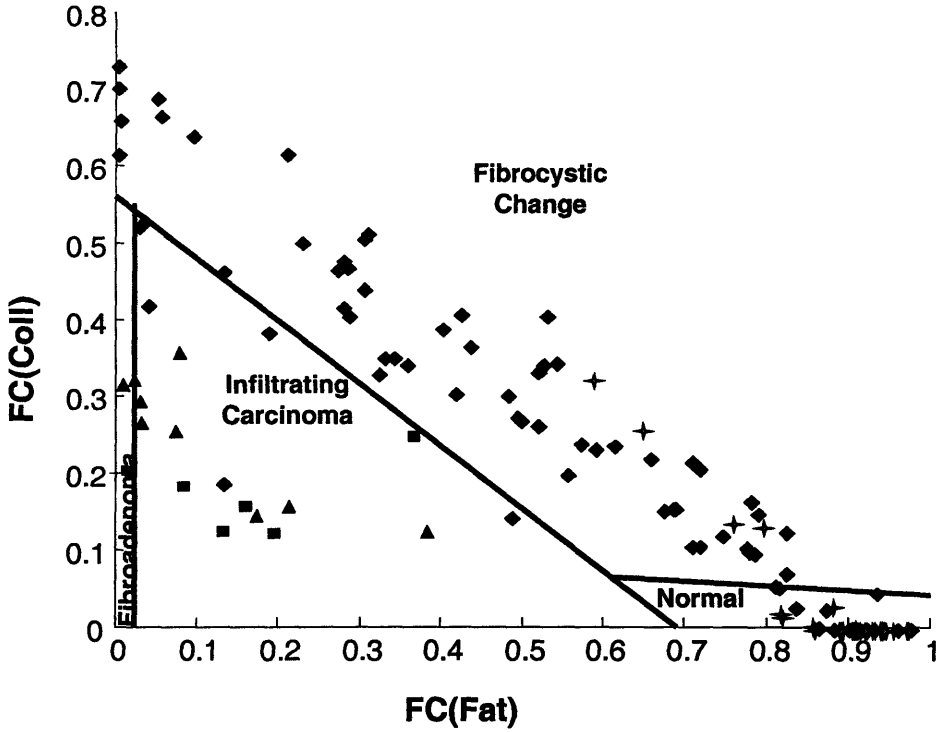


**Figure V.8.** Diagnostic algorithm displaying the fat and collagen content for all pathologies encountered in this study. Normal (stars), Fibrocystic Change (diamonds), Fibroadenoma (triangles), Infiltrating Carcinoma (squares).

lesions from benign and normal tissues. This corresponds to an overall accuracy of 75%, (98/130). As expected, the prospective use of the diagnostic algorithm yields results, summarized in Table V.3, which are degraded when compared with the initial performance of the diagnostic algorithm. The reduction in sensitivity in the fresh tissue studies may be due to the small number of cancerous samples encountered. Although the algorithm only incorrectly diagnoses 1 malignant sample, this results in a sensitivity of 83% due to the dearth of cancerous data points in this study. The overall accuracy may be affected by encountering a broader range of manifestations of each pathology. For example, in the fresh-frozen studies, the predominant manifestation of fibrocystic change in our data set was stromal fibrosis. In the clinical study of fresh tissue, all three manifestations of fibrocystic change were observed, stromal fibrosis, cyst formation, and adenosis. This increase in tissue

heterogeneity may contribute to the degradation of the overall accuracy in the fresh tissue studies. Results may also have been degraded by a lower SNR in this data set. Most notably, a reduced SNR may have affected the diagnosis of fibroadenoma because its area in the diagnostic plane is smallest. Thus slight variations in FC(Fat) will result in misdiagnosis. This effect may be evident in Figure V.8 as the 3 samples diagnosed as fibroadenoma that lie slightly to the right of the diagnostic line. Analysis using the equation derived in Chapter IV will shed light on the effect of error on algorithm performance.

Although the performance of the diagnostic algorithm is degraded when it is used prospectively to distinguish cancerous and non-cancerous lesions, it remains quite robust when used to identify those lesions which need to be excised. Prospective application of the diagnostic algorithm to differentiate infiltrating carcinoma and fibroadenoma (lesions to be excised) from fibrocystic change and normal breast tissue results in a sensitivity of 100% (15/15) and a specificity of 95% (109/115). As in the fresh-frozen studies, this signifies that if a lesion is not excised there is no chance that it is malignant.

This initial analysis excludes patients who have undergone pre-operative chemotherapy or are undergoing re-excision surgery. Such patients harbor pathological tissue changes that we have not previously examined. Pre-operative chemotherapy is used as a neo-adjuvant therapy to shrink large tumors. Tumor

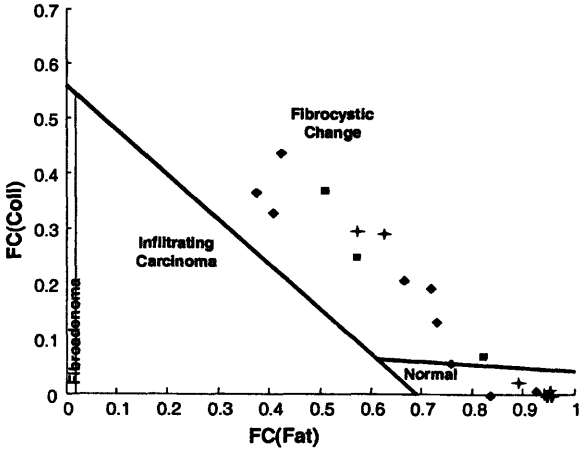


**Figure V.9.** Scatter plot displaying the fat and collagen content for data acquired from patients who underwent pre-operative chemotherapy. Normal (stars), Fibrocystic Change (diamonds), Infiltrating Carcinoma (squares).

replacement by loose fibrosis is the most common pathologic event resulting from neo-adjuvant chemotherapy [Moreno *et al.* 2002]. An increase in collagen is seen in all samples from patients receiving pre-operative chemotherapy, shown in Figure V.9. A similar, although less pronounced trend in collagen is seen in patients undergoing a re-excision surgery, seen in Figure V.10. Pathological changes induced by surgical procedures depend on the interval between the initial and re-excision surgeries. Variability in this interval may account for the heterogeneity in fit coefficients observed in the re-excision specimens. Early pathological findings are local hemorrhage, disrupted tissue and epithelial cell displacement, whereas, fibrosis, fat necrosis and inflammatory reaction are observed later in time [Tardivon *et al.* 2002]. Because both pre-operative chemotherapy and prior surgery are known in advance of data collection, these patients may be treated separately and a distinct diagnostic algorithm developed.

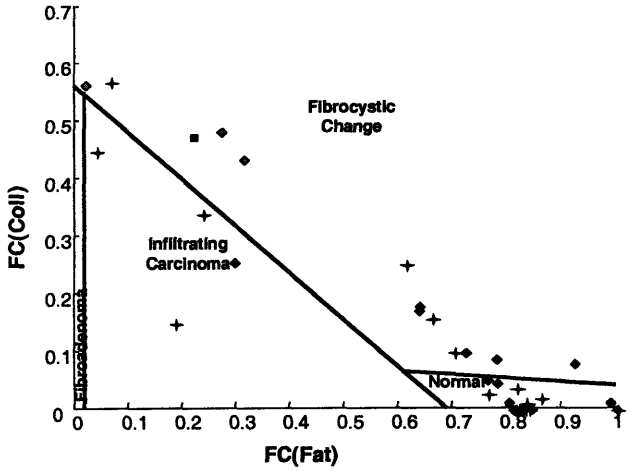


**Figure V.10.** Scatter plot displaying the fat and collagen content for data acquired from patients undergoing re-excision surgeries. Normal (stars), Fibrocystic Change (diamonds), Infiltrating Carcinoma (square).

## V. B. 4. Diagnostic Algorithm Encompassing New Pathologies

In this study, we acquired Raman spectra from 20 lesions diagnosed as DCIS. Although DCIS was not a pathology encountered in our laboratory studies, the spectra were analyzed with the diagnostic algorithm developed on fresh-frozen tissues, shown in Figure V.11. The DCIS samples are widely distributed throughout the diagnostic plane. It is clear that

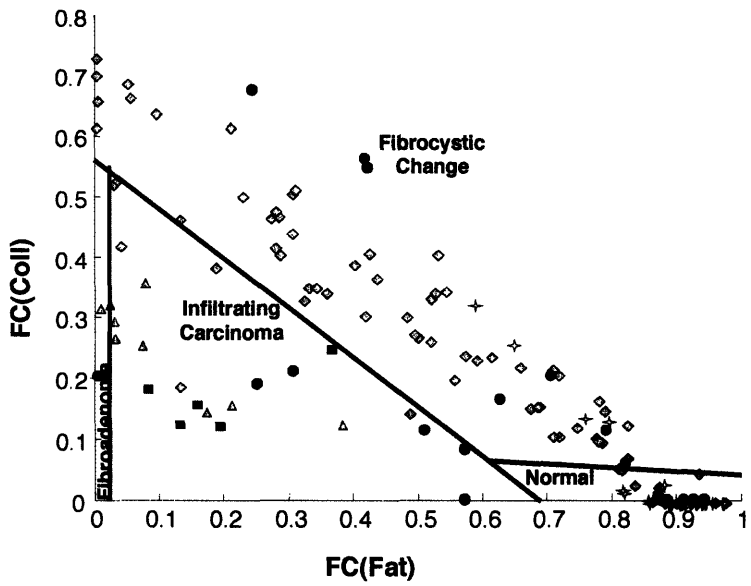


**Figure V.11.** Scatter plot displaying the fat and collagen content for all pathologies encountered in this study. Normal (stars), Fibrocystic Change (diamonds), Fibroadenoma (triangles), Infiltrating Carcinoma (squares), Ductal Carcinoma In Situ (circles).

additional model parameters need to be investigated for the accurate diagnosis of DCIS. Studies to incorporate additional fit coefficients and intensity information into the diagnostic scheme are currently underway.

### V. B. 5. Stereotactic Needle Biopsy to Target Microcalcifications

In the *ex vivo* study, the real-time Raman system was used to acquire data from microcalcifications contained in stereotactic needle biopsies of mammographically suspicious breast lesions. Microcalcifications are a feature of particular diagnostic significance on a mammogram and often geographically identify the location of the most important abnormality within the breast to be targeted at biopsy [Johnson *et al.* 1999]. Due to their diagnostic importance, microcalcifications in fresh breast tissue are not typically made available for scientific research. Thus, our laboratory studies on the use of Raman spectroscopy to diagnose breast disease have not included lesions containing microcalcifications [Haka *et al.* submitted]. For this reason, we investigated the ability of Raman spectroscopy to diagnose microcalcifications by performing confocal microscopy of

microcalcifications in thin sections of deparaffinized fixed breast tissue, detailed in Chapter VI [Haka *et al.* 2002]. This study resulted in high sensitivities and specificities and demonstrated the diagnostic potential of Raman spectroscopy to differentiate microcalcifications found in benign and malignant breast lesions that cannot currently be distinguished by mammography. Our recent studies have focused on extension of these results to unfixed microcalcifications contained in freshly excised breast tissue.

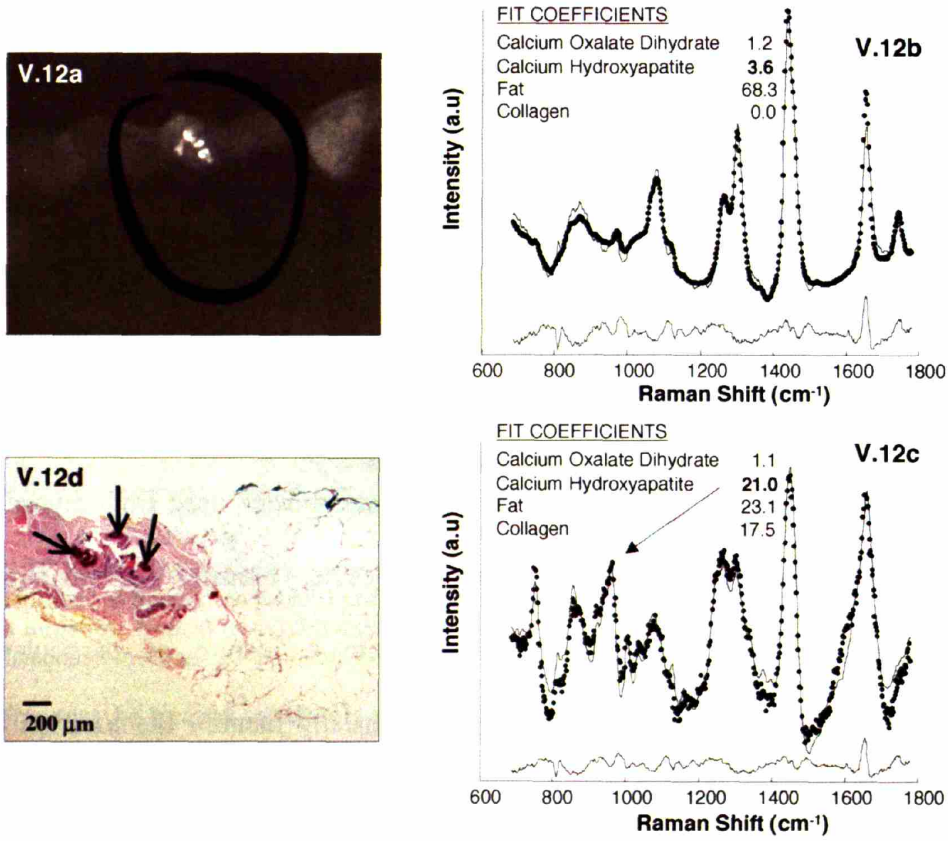


**Figure V.12.** a) Specimen radiograph of a stereotactic needle biopsy of the breast with microcalcifications (circle). b) Raman spectrum acquired from the needle biopsy c) Raman spectrum also acquired from the tissue demarcated by a box in figure V.12a. The spectrum exhibits features indicative of calcium hydroxyapatite, particularly a peak at 960 cm-1 (arrow). d) Histopathology corresponding to the Raman spectrum with a large contribution from calcium hydroxyapatite showing microcalcifications (arrow) within a benign lesion.

In our clinical studies of fresh tissue, stereotactic biopsies are examined with the real-time Raman system, allowing us to acquire Raman spectra from microcalcifications in fresh

breast tissue. Stereotactic biopsy, often used when mammography shows a cluster of microcalcifications, is performed under x-ray guidance using intersecting coordinates to ensure precise sampling of a mammographic abnormality. Radiography is routinely performed on these needle biopsy samples to ensure that the microcalcifications seen at mammography were sampled during the biopsy. Thus, by comparison with the corresponding radiograph, the approximate location of microcalcifications within the sample can be ascertained. Acquisition and real-time analysis of a Raman spectrum allows pinpointing the exact position of the microcalcifications. Figure V.12a is a specimen radiograph of a stereotactic biopsy that exhibits microcalcifications. A Raman spectrum obtained from this specimen in the approximate region of the microcalcifications is shown in Figure V.12b. Also shown are the real-time model fit, residual and relevant fit coefficients. The lack of significant contribution from calcium hydroxyapatite or calcium oxalate dihydrate, the two types of microcalcification found in breast, indicates that the probe is not placed directly over the microcalcifications. By translating the probe along the biopsy specimen and examining the calcification contribution at various locations, we were able to identify the exact position of the microcalcifications and collect a Raman spectrum. The Raman spectrum, acquired from the microcalcification highlighted by a small box in Figure V.12a, is shown in Figure V.12c. The fit coefficient of 21% for calcium hydroxyapatite signifies the presence of a type II microcalcification. This is evident in the spectrum as a band at 960 $cm^{-1}$, the $\nu_1(PO_4)$ totally symmetric stretching mode. We also see contributions from fat and collagen. Histopathology, shown in Figure V.12d, confirmed the presence of microcalcifications at this site. The green ink in Figure V.12d indicates the region of data acquisition for spectrum V.12b while the orange ink marks the position where spectrum

V.12c was collected. As the diagnostic importance of microcalcifications has been shown in our previous Raman microscopy studies, their inclusion in our current analysis should result in increased sensitivity and specificity. The real-time Raman system provides a means to obtain data from microcalcifications in fresh biopsy samples, allowing us to couple the results from our Raman microscopy studies of microcalcifications with our *ex vivo* diagnostic algorithm to create a powerful new tool for the diagnosis of benign and malignant breast lesions.

### V. B. 6. Future Directions

Upcoming studies will focus on further analysis of the clinical data set containing Raman spectra of fresh tissues. New diagnostic algorithms will be developed which incorporate additional model parameters, microcalcifications, and intensity information. These algorithms will be used to identify DCIS and possibly different manifestations of a single pathology. The incorporation of microcalcifications and intensity information are expected to strengthen the performance of our diagnostic algorithms. The Raman optical fiber probe provides a reproducible geometry for data collection, allowing examination of spectral data that has not been normalized. Ultimately, we strive to obtain quantitative information by incorporating the Raman scattering cross-sections of the model components into the data analysis routine. Studies to extract quantitative morphological information will correlate fit coefficients with the percent morphology as determined via pathology. This information can also be used to provide insight into the lower detection limits of the approach.

## *V. C. Summary*

In this chapter our Raman spectroscopic model of breast tissue is used to characterize the chemical/morphological composition of different breast pathologies. We analyze Raman spectra from a range of *ex vivo* tissue specimens and pathologies to assess the ability of the model to predict breast tissue disease state. The data demonstrate the efficacy of the model in both diagnosing breast disease and in understanding the chemical/morphological variations associated with disease progression. The results indicate that the technique has the potential to be applied *in vivo* to accurately classify breast lesions.

## *Acknowledgements*

Dr. Maryann Fitzmaurice provided the pathological diagnoses found in this chapter. More importantly, she supplied invaluable guidance throughout the projects detailed herein. She also helped devise the clinical protocol and collect data from freshly excised tissue. The Cleveland studies would not have occurred without Maryann's help. Jonathan Nazemi was also invaluable in executing the studies carried out in Cleveland. He assisted with data acquisition, study planning, equipment transportation, and general troubleshooting. Luis Galindo constructed the Raman probes used in the study of fresh tissues. Zoya Volynskaya helped to collect and analyze the data from freshly excised tissues. Funding has been provided by the NIH grants RR02594 and HL51265. Financial support was also contributed by the Pathology Associates of University Hospitals of Cleveland.

## *References*

Cotran RS, Kumar V and Collins T (1999). Robbins Pathologic Basis of Disease. 4th Ed., Philadelphia, W. B. Saunders Company: 1189,1195.

Elston CW and Ellis IO (1991). "Pathological Prognostic Factors in Breast Cancer. I. The Value of Histological Grade in Breast Cancer: Experience from a Large Study with Long-Term Follow-Up." Histopathology **19**(5): 403-410.

Fantini S, Walker SA, Franceschini MA, Kaschke M, Schlag PM and Moesta KT (1998). "Assessment of the Size, Position, and Optical Properties of Breast Tumors *In Vivo* by Noninvasive Optical Methods." Appl. Opt. **37**(10), 1982-1989.

Haka AS, Shafer-Peltier KE, Fitzmaurice M, Crowe JP, Dasari RR and Feld MS

"Diagnosing Breast Cancer Using Raman Spectroscopy." P Natl Acad Sci USA (submitted).

Haka AS, Shafer-Peltier KE, Fitzmaurice M, Crowe J, Dasari RR and Feld MS (2002). "Identifying Microcalcifications in Benign and Malignant Breast Lesions By Probing Differences in their Chemical Composition Using Raman Spectroscopy." Cancer Res **62**: 5375-5380.

Hoda SA and Rosen PP (2002). "Practical Considerations in the Pathologic Diagnosis of Needle Core Biopsies of Breast." Am J Clinical Pathol **118**(1): 101-108.

Houssami N, Cheung MN and Dixon JM (2001). "Fibroadenoma of the breast." Med J Aust **174**(4): 185-188.

Johnson JM, Dalton RR, Wester SM, Landercasper J and Lambert PJ (1999). "Histological Correlation of Microcalcifications in Breast Biopsy Specimens." Archiv Surg **134**: 712-716.

Khan SA and Badve S (2001). "Phyllodes Tumors of the Breast." Curr Treat Options Oncol **2**(2): 139-147.

Liberman L, Dershaw DD, Rosen PP, Abramson AF, Deutch BM and Hann LE (1994). "Stereotaxic 14-Gauge Breast Biopsy - How Many Core Biopsy Specimens are Needed." Radiology **192**(3): 793-795.

Moreno A, Escobedo A, Benito E, Serra JM, Guma A and Riu F (2002). "Pathologic Changes Related to CMF Primary Chemotherapy in Breast Cancer. Pathological Evaluation of Response Predicts Clinical Outcome." Breast Cancer Res Treat **75**(2): 119-25.

Motz JT, Hunter M, Galindo LH, Gardecki JA, Kramer JR, Dasari RR and Feld MS (2003). "Optical Fiber Probe for Biomedical Raman Spectroscopy." Appl Opt **43**: 542-554.

National Cancer Institute Web Site. Cancer Facts. Accessed July 26, 2003.

Page DL and Dupont WD (1990). "Anatomic Markers of Human Premalignancy and Risk of Breast Cancer." Cancer **66**(6): 1326-1335.

Rosen PP and Oberman HA (1992). Atlas of Tumor Pathology. Tumors of the Mammary Gland Third Series, Fascicle 7. Armed Forces Institute of Pathology, Washington, D.C.: 101, 157.

Rosen PP (1997). Breast Pathology Philadelphia, PA, Lippincott-Raven.

Shafer-Peltier KE, Haka AS, Fitzmaurice M, Crowe J, Myles J, Dasari RR and Feld MS (2002). "Raman Microspectroscopic Model of Human Breast Tissue: Implications for Breast Cancer Diagnosis *In Vivo*." J Raman Spec **33**(7): 125-137.

Tardivon AA, Guinebretiere JM, Dromain C, Deghaye M, Caillet H and Georgin V (2002). "Histological Findings in Surgical Specimens After Core Biopsy of the Breast." Eur J Radiol **42**(1): 40-51.

Tromberg BJ, Coquoz O, Fishkin JB, Pham T, Anderson ER, Butler J, Cahn M, Gross JD, Venugopalan V and Pham D (1997). "Non-Invasive Measurements of Breast Tissue Optical Properties Using Frequency-Domain Photon Migration." Philos Trans R Soc Lond B **352**(1354), 661-668.

# Chapter VI. Raman Microscopy of Microcalcifications

In our *ex vivo* studies, we see relatively little contribution from the two types of calcifications found in breast tissue and included in our spectral model, calcium hydroxyapatite and calcium oxalate dihydrate. Microcalcifications are a feature of particular diagnostic significance on a mammogram and often geographically target the location of the most important abnormality within the breast [Johnson *et al.* 1999]. Due to their diagnostic importance, microcalcifications in fresh breast tissue are not typically made available for scientific research, and thus our studies did not include lesions containing microcalcifications. For this reason, we have investigated the diagnostic power of Raman microscopy of microcalcifications in thin sections of deparaffinized fixed breast tissue [Haka *et al.* 2002]. Using PCA, we were able to distinguish microcalcifications occurring in benign and malignant ducts with a sensitivity of 88% and a specificity of 93%. This is a significant improvement over current X-ray mammography techniques, which are unable to reliable differentiation microcalcifications in benign and malignant lesion.

## *VI. A. Microcalcifications*

Two major types of microcalcifications are found in breast tissue. Type I deposits consist of calcium oxalate dihydrate, a birefringent colorless crystal, while type II deposits are composed of calcium phosphates, mainly calcium hydroxyapatite. Type II microcalcifications are typically basophilic on light microscopic examination of H&E stains and nonbirefringent.

There is no reliable way to distinguish between type I and type II microcalcifications in a clinical mammogram, but the type of microcalcification is thought to correlate with disease [Radi 1989]. Calcium oxalate dihydrate crystals are most frequently seen in benign ductal cysts and are rarely found in foci of carcinoma, while calcium phosphate deposits are most often seen in proliferative lesions, including carcinoma. This distribution is consistent with the hypothesis that type I microcalcifications are a product of secretions, whereas type II calcium deposits result from cellular degradation or necrosis.

Type II microcalcifications are estimated to occur two to three times more frequently than type I [Rosen 1997]. Nonpalpable type II microcalcifications discovered by mammography frequently geographically target the location of the most important abnormality within the breast [Johnson *et al.* 1999]. As such, calcifications are a key component that radiologists look for in a mammogram. Several algorithms have been proposed that attempt to correlate parameters such as the shape, size, number, and roughness of mammographically detected microcalcifications with disease [Markopoulos *et al.* 2001; Betal *et al.* 1997; Shen *et al.* 1994]. However, these studies often exclude cases due to dark mammographic backgrounds, low density calcific flecks, or densely clustered calcifications and thus are limited to only certain patients and mammograms. To our knowledge, the

highest reported sensitivity and specificity for a cross validated algorithm based on mammography is 71% and 74% respectively [Betal *et al.* 1997]. Although these studies show promising results, the diagnosis of breast carcinoma using mammographically detected microcalcifications remains elusive. While the mammographic appearance of microcalcifications bears some relationship to the histological type of the lesion, currently diagnosis cannot be reliably made on this basis.

Because calcium deposits in breast tissue have only been categorized morphologically, significant insight may be gained by examining them using a more rigorous method. Raman spectroscopy is well suited to further the study of microcalcifications in breast tissue, as it can provide a definitive chemical analysis of these morphologic structures *in vitro*. In fact, Raman spectroscopy has been used successfully to study calcium deposits in several other organs, such as the kidney and urinary tract [Kodati *et al.* 1990; Kodati *et al.* 1991; Kodati *et al.* 1993; Pestaner *et al.* 1996; Kontoyannis *et al.* 1997].

In this study, we have employed Raman spectroscopy to highlight differences in the chemical composition or structure of microcalcifications that exist in different lesions in the breast. Results from this study will further our understanding of the chemical changes accompanying the onset and progression of breast disease and provide an important parameter for the diagnosis of breast disease using Raman spectroscopy.

## *VI. B. Sample Preparation and Data Acquisition*

VI. B. a) Sample Preparation

Raman spectra were acquired from 6 μm thick deparaffinized sections of formalin fixed, paraffin embedded breast tissue. Due to their diagnostic importance, microcalcifications in

fresh breast tissue cannot typically be spared for scientific research and thus our study was confined to examining microcalcifications in fixed tissue sections. Since microcalcifications are relatively inert, the protein crosslinking effects of the fixative should be minimal. Furthermore, Raman spectral lineshapes from the calcifications examined in this study are consistent with previously published data acquired from unfixed tissue in other organ systems [Kodati *et al.* 1990; Kodati *et al.* 1991; Kodati *et al.* 1993; Pestaner *et al.* 1996; Kontoyannis *et al.* 1997]. Samples were mounted on $MgF_2$ flats (Moose Hill Enterprises inc., Sperryville, VA). Each microcalcification studied was photographed using a phase contrast microscope. The phase contrast images and H&E stained serial sections were reviewed by an experienced pathologist, who was blinded to the spectroscopy results and rendered a histologic diagnosis of the disease state of regions where data was acquired. A total of 30 type I and 60 type II microcalcifications in breast biopsies from 11 patients were examined using Raman spectroscopy, 74 from histologically benign ducts and 16 from histologically malignant ducts. Histologic diagnoses for benign ducts ranged from ductal epithelial hyperplasia (DEH) (3), sclerosing adenosis (19), fibrocystic change (43), and fibroadenoma (5), to Monckeberg's arteriosclerosis (4), while all 16 malignant ducts were diagnosed as ductal carcinoma in situ (DCIS). No invasive carcinomas were encountered in the regions where data was acquired. All 11 patients were Caucasian females with a mean age of 53.4 years (range 41 to 85 years) and had undergone excisional breast biopsy for suspicious microcalcifications found on mammography. These patients had no palpable breast lesions and, with the exception of the fibroadenomas, had no mass lesion or other significant findings on mammography.

VI. B. b) Data Acquisition

Data was acquired using the laboratory confocal Raman microscopy system detailed in Chapter III.F.2. In short, Raman excitation light, 830 nm, is launched into a confocal microscope and focused to a spot size of approximately 2μm. All Raman spectra in this study were acquired with a 60 sec. integration time and a spectral resolution of 8 $cm^{-1}$. The average laser excitation power used varied between 100 and 150 mW.

## *VI. C. Raman Spectra*

Figure VI.1a is a specimen radiograph which exhibits features indicative of the presence of microcalcifications, while Figure VI.1b displays a phase contrast image collected from a thin section of this specimen. The Raman spectrum of a type I microcalcification acquired from the deposit highlighted by a small box in image VI.1b is shown in Figure VI.1c. Based on the overall histology of this sample as well as the specific features apparent in the phase contrast image, this lesion was diagnosed as fibrocystic change. Vibrational features

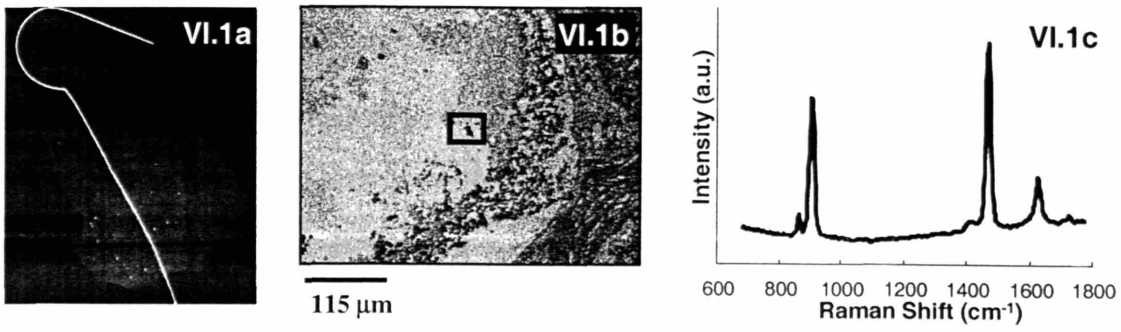


**Figure VI.1.** a) Specimen radiograph and b) phase contrast image taken from a section of the same sample. c) Raman spectrum of a type I calcification arising in association with secretions in the lumen of a duct cyst in a focus of fibrocystic disease. The region from which the Raman spectrum was acquired is highlighted by a box.

characteristic of calcium oxalate dihydrate can be seen at 912 $cm^{-1}$, 1477 $cm^{-1}$, and 1632 $cm^{-1}$. These Raman features are attributed to C-C stretching, and C-O symmetric and asymmetric stretching respectively and are consistent with previously published Raman spectra of calcium oxalate dihydrate [Kodati *et al.* 1990; Pestaner *et al.* 1996; Kontoyannis *et al.* 1997].

Figures VI.2a and VI.2b display a phase contrast image of a type II microcalcification in a malignant duct and the corresponding specimen radiograph. Figure VI.2c shows the Raman spectrum acquired from the deposit highlighted in image VI.2a by a small box. Through examination of this spectrum, it is evident that the microcalcification is not composed of pure calcium hydroxyapatite. The Raman spectrum of pure stoichiometric calcium hydroxyapatite contains four phosphate internal vibrational modes as well as bands due to the hydroxyl ion stretching and librational modes. Two of the phosphate vibrational modes are out of the spectral range we have chosen to examine as well as both of the hydroxyl ion modes. The large band at 960 $cm^{-1}$ is the $v_1(PO_4)$ totally symmetric stretching mode of the 'free' tetrahedral phosphate ion. Another phosphate $v_1$ mode occurs at 948 $cm^{-1}$

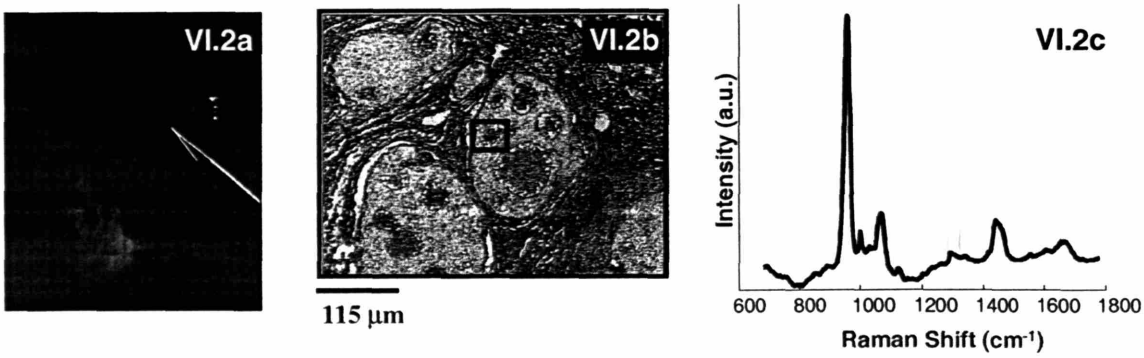


**Figure VI.2.** a) Specimen radiograph and b) phase contrast image taken from a section of the same sample. c) Raman spectrum of a type II calcification in a malignant breast lesion. The region from which the Raman spectrum was acquired is highlighted by a box.

but is obscured by the broad phosphate stretching mode at 960 $cm^{-1}$. Overlapping Raman structure resulting from five $\nu_3(PO_4)$ bands can be seen between 1028 $cm^{-1}$ and 1061 $cm^{-1}$. The sixth $\nu_3(PO_4)$ mode appears at 1075 $cm^{-1}$. The phosphate features present are consistent with previously published Raman spectra of calcium hydroxyapatite [Kodati *et al.* 1991; Kodati *et al.* 1993; Kontoyannis *et al.* 1997]. In addition to the phosphate peaks resulting from calcium hydroxyapatite there are several other vibrational modes present in this spectrum. Protein contributions can be seen at 1445 $cm^{-1}$ and 1650 $cm^{-1}$. Also the sharp peak present at 1004 $cm^{-1}$ can be attributed to phenylalanine. Small contributions from lipid are manifest as a C-C stretch and C-H ($CH_2$) bend at 1130 $cm^{-1}$ and 1300 $cm^{-1}$ respectively.

Initially, data acquired from type I and type II microcalcifications were separated based on their Raman spectra. The presence or absence of vibrational intensity at specific wavenumbers was used to distinguish between type I and type II microcalcifications. Spectra containing large peaks at 912 $cm^{-1}$ and 1477 $cm^{-1}$, characteristic of calcium oxalate dihydrate, were grouped into the type I category while spectra displaying intensity at 960 $cm^{-1}$, characteristic of calcium hydroxyapatite, were grouped into the type II category. In the current analysis, the separation into type I and type II microcalcifications was performed by visual inspection. However, an automated computer algorithm which normalizes the spectra and distinguishes them based upon an intensity value of one occurring at either 960 $cm^{-1}$, type II, or 1477 $cm^{-1}$, type I, could easily be implemented. All 30 type I microcalcifications we examined were formed in loci of fibrocystic disease and thus all 30 type I microcalcifications were diagnosed as benign. This is consistent with the fact that type I microcalcifications are formed as a product of secretions and are typically located in cystic lesions. Although type I microcalcifications have been found in malignant lesions,

specifically lobular carcinoma *in situ*, it is exceedingly rare [Frappart *et al.* 1984; Frappart *et al.* 1986].

## *VI. D. Principal Component Analysis*

In order to differentiate type II microcalcifications occurring in benign and malignant breast lesions, we employed PCA, described in Chapter IV.B.1 [Geladi and Kowalski 1986]. Although PCA provides little physical information in and of itself; however, it is adept at isolating spectral trends that correlate with physical information and thereby provides a basis for development of a diagnostic algorithm. Furthermore, by comparing the lineshapes of the diagnostic PC spectra with the spectra of pure chemicals, it is possible to ascribe meaning to them. More importantly, this method of analysis provides a proof of principle that there is indeed important diagnostic information contained within the Raman spectra of type II microcalcifications.

We used a singular value decomposition algorithm to determine the principal components of our data set. The data set was normalized to the 960 $cm^{-1}$ peak height to remove any possible intensity biases and subsequently mean centered prior to performing PCA in order to remove features common to all spectra thereby further highlighting spectral variance. All 60 spectra could be accurately modeled above the noise level using 9 principal components. The first 6 PCs account for more than 97 % of the total variance in the data. Next, we used logistic regression, a discriminate analysis technique, to generate a diagnostic algorithm that was used to classify the breast lesions into benign and malignant categories [Shama 1996]. Logistic regression correlates the weighting coefficients (scores) of the principal components calculated for each Raman spectrum with the diagnostic categories.

Diagnoses were provided by pathologist blinded to the outcome of the spectroscopic measurements. A leave one out cross-validation analysis was employed in order to obtain a robust diagnostic algorithm.

## *VI. E. Diagnostic Algorithm*

Fibroadenoma is a benign tumor of a completely different lineage than all other lesions we have examined [Rosen 1997]. It is most closely related to phylloides tumors, the malignant counterpart of which is not carcinoma but cystosarcoma phylloides, in which the stroma rather than the epithelium is malignant. Furthermore, the clinician typically knows that a breast lesion is in the fibroadenoma/phylloides tumor family based on physical examination and features other than microcalcification on mammography [Houssami *et al.* 2001]. As these lesions must be surgically excised for treatment, physicians would be unlikely to use a technique like Raman spectroscopy as an adjunct tool for diagnosis of fibroadenoma. For these reasons, we assessed the performance of the algorithm after excluding samples diagnosed as fibroadenoma from our analysis.

Using a combination of PCA and logistic regression, we were able to examine Raman spectral signatures of type II microcalcifications to determine whether or not breast disease diagnosis could be made on this basis. We obtained good diagnostic accuracy with 3 PC scores. The significant scores are associated with $PC_2$, $PC_3$, and $PC_5$. $PC_5$ accounts for 1.0% of the total variance in the data, while $PC_2$ and $PC_3$ account for 8.8% and 5.2% respectively. Using these three principal components and a leave one out cross validation method we were able to predict 14 out of 16 DCIS and 34 out of 39 benign samples correctly. Thus, type II microcalcifications occurring in benign and malignant breast ducts could be distinguished

with a sensitivity of 88% and a specificity of 87%. If we retain all samples, the sensitivity and specificity are only slightly degraded, maintaining a sensitivity of 88% with a drop in sensitivity to 80%. A graphic representation of the diagnostic algorithm for type II microcalcifications is shown in Figure VI.3. In order to condense the algorithm into a two-dimensional representation, $PC_5$ and $PC_2$, which both have higher scores for benign microcalcifications, were added together to form a single axis. Based on this algorithm, all of the samples diagnosed as DEH and sclerosing adenosis, the benign conditions most commonly confused morphologically with carcinoma, were predicted correctly. 4 out of 5 type II stromal calcifications occurring in fibroadenoma were misdiagnosed, as well as 2 of 4 arterial calcifications in Monkeberg's arteriosclerosis and 3 out of 13 ductal calcifications in fibrocystic disease.

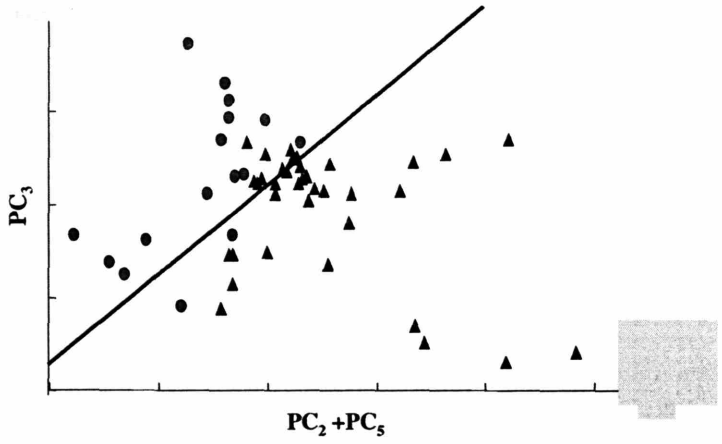


**Figure VI.3.** Diagnostic algorithm for type II microcalcifications based on the scores of three principal components: benign (triangles), malignant (circles).

In general, only one microcalcification was studied from each lesion. However, in two samples, multiple microcalcifications were studied from the same lesion and no significant differences were seen in the spectra for each given lesion. When we combine data acquired from both type I and type II microcalcifications we obtain an overall sensitivity of 88% and a specificity of 93%. This corresponds to a positive predictive value of 74% and a

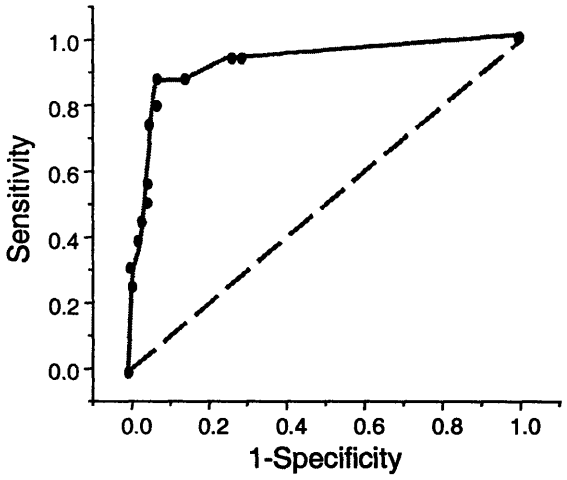


**Figure VI.4.** Receiver operating characteristic (ROC) curve which illustrates the ability of Raman spectroscopy to separate microcalcifications occurring in benign and malignant breast lesions. A simulated ROC curve of two indistinguishable populations, represented by the dashed line, is included for comparison.

negative predictive value of 97%. A receiver operating characteristic curve generated from these results is shown in Figure VI.4. Based on these *in vitro* results in fixed tissue, we believe that Raman spectroscopy has the potential to discriminate microcalcifications associated with benign and malignant breast lesions more accurately than mammography. Further studies performed *in vitro* on fresh tissue and ultimately *in vivo* are planned to better evaluate the clinical utility of Raman spectroscopy as compared to X-ray mammography for the diagnosis of breast cancer.

## *VI. F. Chemical Analysis*

Through examination of the three diagnostic principal component spectra, we can gain insight into the physical basis responsible for this discrimination. The most diagnostically significant PC spectrum was $PC_5$, shown in Figure VI.5a. Examination of this PC spectrum reveals a broadening of the 960 $cm^{-1}$ phosphate stretching peak. This broadening is clearly demonstrated in Figure VI.5b, in which $PC_5$ is overlaid with the mean spectrum from all type II microcalcifications. Broadening of this peak has been reported in the literature to result from the presence of calcium carbonate [Nelson and Williamson 1982; de Mul *et al.* 1998]. In these studies, the application of Raman spectroscopy to carbonated apatite model systems

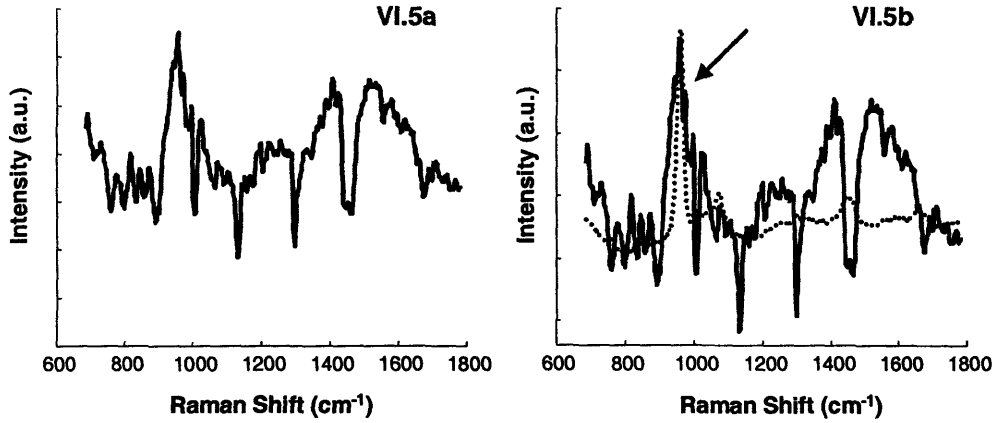


**Figure VI.5.** a) Principal Component spectrum 5. b) Principal Component spectrum 5 (solid line) overlaid with the mean spectrum from all type II microcalcifications (dotted line) to illustrate broadening of the 960 $cm^{-1}$ peak (arrow).

demonstrated a broadening of the phosphate peak with increased carbonate content. The introduction of carbonate ions into the apatite structure reduces the symmetry of its' unit cell. The peak broadening results from a loss of long-range translational order in the apatite structure as the carbonate content of the sample increases. The study found a linear relationship between the Full Width at Half Maximum (FWHM) of the 960 $cm^{-1}$ phosphate stretching mode and the calcium carbonate content of the sample. Evidence that the broadening at 960 $cm^{-1}$ in $PC_5$ may result from variations in the calcium carbonate content of the microcalcifications is manifest in a peak at 1070 $cm^{-1}$ attributable to the calcium carbonate $\nu_1(CO_3)$ mode. However, the difficulty in interpreting PC spectra conferred by the inclusion of both positive and negative features necessitates further investigation.

If indeed $PC_5$ accounts for variations in the amount of calcium carbonate present, then spectra that have a higher score for $PC_5$ will contain a larger amount of calcium carbonate than spectra with a lower weighting coefficient. As benign spectra typically have a larger score for $PC_5$ than malignant spectra, we postulate that type II microcalcifications occurring in benign lesions of the breast contain a larger amount of calcium carbonate than those

deposits found in DCIS. To check our hypothesis, the FWHM was calculated for the 960 $cm^{-1}$ phosphate stretching peak in each Raman spectrum in our study. In accordance with the theory that type II microcalcifications formed in benign lesions have a larger calcium carbonate content, we found that type II microcalcifications occurring in benign breast lesions had an average FWHM of 18.0 ±0.5 $cm^{-1}$, while deposits in lesions diagnosed as DCIS had an average FWHM of 17.0 ±0.5 $cm^{-1}$. The significance of this difference is reflected in a p-value of 0.03. This value was calculated based on the Wilcoxon rank sum test which does not assume a normal distribution of data. Furthermore, if we examine the FWHM of those samples incorrectly diagnosed, we found the opposite trend. The FWHM of benign samples incorrectly diagnosed as malignant was 15.8 ±0.5 $cm^{-1}$ while that of malignant samples incorrectly diagnosed as benign was 17.5 ±0.5 $cm^{-1}$, indicating that the width of the phosphate stretching mode is a key diagnostic feature. However, although the peak height of the 1070 $cm^{-1}$ carbonate stretching mode is on average four times larger in benign samples, it does not correlate linearly with the FWHM of the 960 $cm^{-1}$ phosphate stretching mode. This indicates that additional impurities in the apatite structure contribute to disruption of the symmetry and thereby the broadening of the 960 $cm^{-1}$ peak. These impurities are manifest in the complex vibrational structure of $PC_5$, but presently have not been identified. $PC_5$ also contains several features representative of proteins such as the $CH_2$, $CH_3$ bending mode at 1445 $cm^{-1}$ and the Amide I vibration at 1650 $cm^{-1}$. Unlike the calcium carbonate features, which have a positive intensity, the protein features are negatively directed. This indicates that the protein and carbonate contents are negatively correlated, and thus that benign samples tend to have a lower protein content than malignant samples.

The amount of protein and calcium carbonate present in type II calcifications in benign and malignant lesions is further confirmed by examination of $PC_2$, shown in Figure VI.6. This spectrum also appears to contain positively directed calcium carbonate features, particularly at 1070 $cm^{-1}$, as well as negatively directed protein features and contributes more, on average, to the Raman spectra of microcalcifications formed in benign ducts. Additionally, $PC_2$ exhibits a large, second derivative-like feature around 960 $cm^{-1}$. This type of structure accounts for peak broadening in the data and further supports our hypothesis that type II microcalcifications formed in benign ducts tend to have a larger amount of calcium carbonate, and thus more broadening of the 960 $cm^{-1}$ peak, than those formed in malignant ducts.

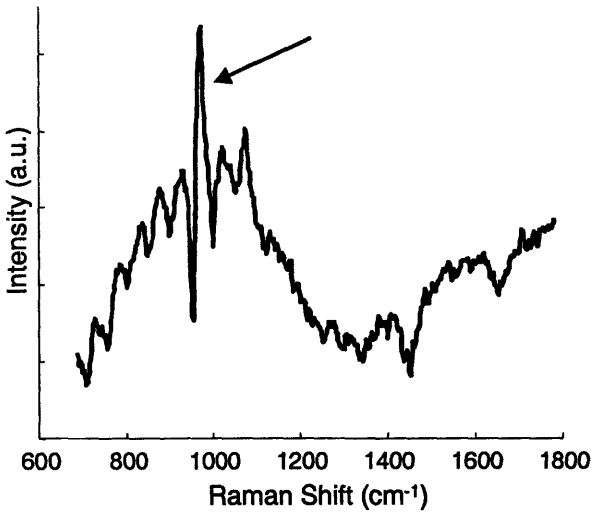


**Figure VI.6.** Principal Component spectrum 2 exhibiting a large, second derivative-like feature around 960 $cm^{-1}$ (arrow).

$PC_3$ was also found to be diagnostically significant. It is shown in Figure VI.7. $PC_3$, however, contributes more to Raman spectra acquired from type II calcifications in malignant ducts. It has positively directed protein features, thus lending further support to the theory that microcalcifications formed in malignant ducts have a larger amount of protein than deposits in benign ducts. The amount of protein in microcalcifications in benign and malignant ducts is confirmed by monitoring the peak height of the Amide I vibration at 1650 $cm^{-1}$. The intensity of this mode is approximately one and a half times greater in type II

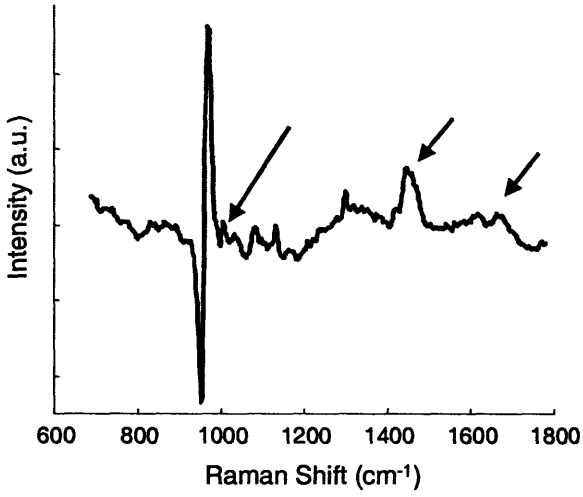


**Figure VI.7.** Principal Component spectrum 3 exhibiting positively directed protein features such as the peak at 1445 $cm^{-1}$, the Amide I vibration at 1650 $cm^{-1}$, and the phenylalnine feature at 1004 $cm^{-1}$

microcalcifications formed in malignant lesions. Additionally, contributions from phenylalanine, an amino acid often found in conjunction with collagen and other proteins, can be seen in $PC_3$ at 1004 $cm^{-1}$. $PC_3$ exhibits a large first derivative-like feature at ~960 $cm^{-1}$. This feature accounts for a peak shift in the phosphate stretching mode which is positively correlated with the protein features. The presence of these protein features may explain the misdiagnosis of stromal calcifications in fibroadenomas and arterial calcifications in Monkeberg's arteriosclerosis, which are the result of stromal or arterial degradation similar to the cellular degradation that occurs in DCIS.

## *VI. G. Summary and Discussion*

This study demonstrated the diagnostic potential of Raman spectroscopy to differentiate microcalcifications found in benign and malignant breast lesions. Additionally, using PCA we have discovered subtle differences in the chemical composition of type II microcalcifications occurring in benign and malignant breast lesions. Based on our results, we postulate that type II microcalcifications occurring in benign lesions of the breast have both a lower protein and a higher calcium carbonate chemical content than those formed in malignant lesions. Although we have identified a few of the chemicals responsible for the

differences between benign and malignant type II microcalcifications, there are several other chemical species represented in the rich structural content of the diagnostic PC spectra which are as yet unidentified. Elucidation of the additional chemical species present in type II breast microcalcifications may yield further insight into the mechanisms by which they are formed.

Further studies are needed to identify these chemical species, and fresh breast tissue may be necessary for these studies. We have found few microcalcifications in the fresh frozen breast tissue from surgical specimens currently available to us for study because they are important for medical diagnosis and therefore not usually released for scientific study. It is for this reason that we used deparaffinized fixed tissue sections for this study. As a result of the fixation process, the fluorescence occurring as a background on the Raman spectrum could not be reliably analyzed. However, the development of fiberoptic probes for Raman spectroscopy may soon allow real time studies of microcalcifications in fresh breast tissue in the clinical setting prior to pathologic examination. Based on the findings of this study, we expect type II calcifications occurring in benign and malignant lesions to have distinct fluorescent properties due to the known fluorescence characteristics of proteins and calcium carbonate [Fujimoto *et al.* 1977; Aminzadeh 1997]. Additional differences in the fluorescence profile of type II microcalcifications formed in benign and malignant lesions due to as yet unidentified chemical species may also become apparent, once microcalcifications in unfixed tissue are studied. Thus, the fluorescence of type II microcalcifications could easily be exploited to increase the diagnostic accuracy of this methodology. Furthermore, we plan to couple these results with a previously described Raman spectroscopic model of breast tissue to create a powerful new tool for the diagnosis of

benign and malignant breast lesions [Shafer-Peltier *et al.* 2002]. The Raman technique may be applied first *in vitro* in breast biopsies in which little tissue is obtained and the lesion may not be well represented but microcalcifications are present. Ultimately, it may be used as an *in vivo* adjunct to mammography to help select those patients with microcalcifications who need to go on to biopsy.

## *Acknowledgements*

Karen Shafer-Peltier initiated the microcalcification study and helped collect much of the data. Dr. Maryann Fitzmaurice analyzed the histological sections and provided valuable insight and feedback for the study. Dr. Ramachandra Dasari insisted that I collect data from type I microcalcifications and although I resisted, it resulted in a much stronger and more comprehensive study. Many of the images in this chapter have been reproduced from *Cancer Research* [Haka *et al.* 2002] with permission from The American Association for Cancer Research. Funding has been provided by the NIH grant P41RR02594. Financial support was also contributed by the Pathology Associates of University Hospitals of Cleveland.

## *References*

Aminzadeh A (1997). "Fluorescence Bands in the FT-Raman Spectra of Some Calcium Minerals." Spectrochim Acta A **53**: 693-697.

Betal D, Roberts N and Whitehouse GH (1997). "Segmentation and Numerical Analysis of Microcalcifications on Mammograms Using Mathematical Morphology." Brit J Radiol **70**: 903-917.

Brennan JF, Wang Y, Dasari RR and Feld MS (1997). "Near Infrared Raman Spectrometer Systems For Human Tissue Studies." Appl Spectrosc **51**: 201-208.

Brown SD (1995). "Chemical Systems Under Indirect Observation: Latent Properties and Chemometrics." Appl Spectrosc **49**: 14A-31A.

Buschman HP, Deinum G, Motz JT, Fitzmaurice M, Kramer JR, van der Laarse A, Bruschke AV and Feld MS (2001). "Raman Microspectroscopy of Human Coronary Atherosclerosis; Biochemical Assessment of Cellular and Extracellular Morphologic Structures *In Situ*." Cardiovasc Pathol **10**: 69-82.

Denium G, Rodriquez D, Römer TJ, Brennan JF, Fitzmaurice M, Myles JL, Kramer J, Lees RS and Feld MS (1999). "Principal Component Analysis As A Method To Correlate the Raman Spectrum and the Pathology of Human Coronary Artery Tissue." Appl Spectrosc **53**: 938-942.

de Mul FFM, Otto C, Greve J, Arends J and ten Bosch JJ (1998). "Calculation of the

Raman Line Broadening on Carbonation in Synthetic Hydroxyapatite." J Raman Spectrosc **19**: 13-21.

Frappart L, Remy I, Lin HC, Bremond A, Raudrant D, Grousson B and Vauzelle JL (1986). "Different Types of Microcalcifications Observed in Breast Pathology. Correlations With Histopathological Diagnosis and Radiological Examination of Operative Specimens." Virchows Arch A **410**: 179-187.

Frappart L, Boudeulle M, Boumendil J, Lin HC, Martinon I, Palayer C, Mallet-Guy Y, Raudrant D, Bremond A and Rochet Y (1984). "Structure and Composition of Microcalcifications in Benign and Malignant Lesions of the Breast: Study by Light Microscopy, Transmission and Scanning Electron Microscopy, Microprobe Analysis, and X-ray Diffraction." Hum Pathol **15**: 880-889.

Fujimoto D, Akiba K and Nakamura N (1977). "Isolation and Characterization of a Fluorescent Material in Bovine Achilles Tendon Collagen." Biochem Bioph Res Co **76**: 1124-1129.

Geladi P and Kowalski BR (1986). "Partial Least-Squares Regression: A Tutorial." Anal Chim Acta **185**: 1-17.

Haka AS, Shafer-Peltier KE, Fitzmaurice M, Crowe J, Dasari RR and Feld MS (2002). "Identifying Microcalcifications in Benign and Malignant Breast Lesions By Probing Differences in their Chemical Composition Using Raman Spectroscopy." Cancer Res **62**: 5375-5380.

Hanlon EB, Manoharan R, Koo TW, Shafer KE, Motz JT, Fitzmaurice M, Kramer JR, Itzkan I, Dasari RR and Feld MS (2000). "Prospects for *In Vivo* Raman Spectroscopy." Phys Med Biol **45**: R1-R59.

Houssami N, Cheung MN and Dixon JM (2001). "Fibroademona of the Breast." Med J Aust **174**: 185-188.

Johnson JM, Dalton RR, Wester SM, Landercasper J and Lambert PJ (1999). "Histological Correlation of Microcalcifications in Breast Biopsy Specimens." Archiv Surg **134**: 712-716.

Kodati VR, Tomasi GE, Turumin JL and Tu AT (1990). "Raman Spectroscopic Identification of Calcium-Oxalate-Type Kidney Stone." Appl Spectrosc **44**: 1408-1411.

Kodati VR, Tomasi GE, Turumin JL and Tu AT (1991). "Raman Spectroscopic Identification of Phosphate-Type Kidney Stones." Appl Spectrosc **45**: 581-583.

Kodati VR, Tu AT, Nath R and Turumin JL (1993). "Analysis of Urinary Calculi of Mixed and Unusual Composition: Raman Spectroscopic Investigation." Appl. Spectrosc **47**: 334-337.

Kontoyannis CG, Bouropoulos NC and Koutsoukos PG (1997). "Use of Raman Spectroscopy for the Quantitative Analysis of Calcium Oxalate Hydrates: Application For the Analysis of Urinary Stones." Appl Spectrosc **51**: 64-67.

Kontoyannis CG, Bouropoulos NC and Koutsoukos PG (1997). "Raman Spectroscopy: A Tool for the Quantitative Analysis of Mineral Components of Solid Mixtures. The Case of Calcium Oxalate Monohydrate and Hydroxyapatite." Vib Spectrosc **15**: 53-60.

Mahadevan A and Richards-Kortum R (1996). "Raman Spectroscopy For the Detection of Cancers and Precancers." J Biomed Opt **1**: 31-70.

Manoharan R, Shafer K, Perelman L, Wu J, Chen K, Deinum G, Fitzmaurice M, Myles J,

Crowe J, Dasari RR and Feld MS (1998). "Raman Spectroscopy and Fluorescence Photon Migration For Breast Cancer Diagnosis and Imaging." Photochem Photobiol **67**: 15-22.

Markopoulos C, Kouskos E, Koufopoulos K, Kyriakou V and Gogas J (2001). "Use of Artificial Neural Networks (Computer Analysis) in the Diagnosis of Microcalcifications on Mammography." Eur J Radiol **39**: 60-65.

Nelson DGA and Williamson BE (1982). "Low-Temperature Laser Raman Spectroscopy of Synthetic Carbonated Apatites and Dental Enamel." Aust J Chem **35**: 715-727.

Pestaner JP, Mullick FG, Johnson FB and Centeno JA (1996). "Calcium Oxalate Crystals in Human Pathology. Molecular Analysis With the Laser Raman Microprobe." Arch Pathol Lab Med **120**: 537-540.

Radi MJ (1989). "Calcium Oxalate Crystals in Breast Biopsies." Arch Pathol Lab Med **113**:1367-1369.

Rosen PP (1997). Breast Pathology Philadelphia, PA, Lippincott-Raven.

Shafer-Peltier KE, Haka AS, Fitzmaurice M, Crowe J, Myles J, Dasari RR and Feld MS (2002). "Raman Microspectroscopic Model of Human Breast Tissue: Implications for Breast Cancer Diagnosis *In Vivo*." J Raman Spectrosc **33**:552-563.

Shama S (1996). Applied Multivariate Techniques. New York, NY: John Wiley and Sons, Inc.

Shen L, Rangayyan RM and Desautels JEL (1994). "Application of Shape-Analysis to Mammographic Calcifications." IEEE T Med Imaging **13**: 263-274.

# Chapter VII. Raman Spectroscopic Breast Cancer Diagnosis: *In Vivo* Studies

Previous studies have demonstrated the ability of Raman spectroscopy to diagnose breast cancer using *ex vivo* tissues. The final objective of this thesis, the *in vivo* application of Raman spectroscopy for diagnosing breast cancer, is described in this chapter. Our *in vivo* studies were performed at the Cleveland Clinic Foundation in collaboration with Dr. Joseph Crowe. Data were collected with our front-viewing Raman optical fiber probes during lumpectomy and mastectomy surgical procedures. The goals of this study were to demonstrate our ability to collect *in vivo* data and make accurate diagnoses using our previously developed diagnostic algorithm, discussed in Chapter V.A. This study represents the first demonstration of *in vivo* collection of Raman spectra of breast tissue. The culmination of this thesis results in an approach that was employed intra-operatively during partial mastectomy surgeries to accurately assess margin status.

## *VII. A. Introduction*

Having established that Raman spectroscopy is a useful technique for evaluating breast cancer *ex vivo*, preliminary *in vivo* investigations are the next step to clinical implementation. To date, only a handful of *in vivo* studies using Raman spectroscopy have been undertaken [Caspers *et al.* 1998; Bakker Schut *et al.* 2000; Caspers *et al.* 2000; Hata *et al.* 2000; Utzinger *et al.* 2001; Shim *et al.* 2000]. The majority have been targeted towards easily accessible organs, such as skin, and require relatively long collection times. However, the recent development of a small diameter high throughput Raman probe provides the ability to study remote organs with real-time diagnostic capability. In this chapter, the first demonstration of *in vivo* collection of Raman spectra of breast tissue is presented. Data were acquired during mastectomy surgeries. Although we ultimately strive for transdermal needle probe measurements, for initial investigations, probe positioning and contact can be more accurately controlled in a surgical environment. However, preliminary results using Raman spectroscopy for intra-operative margin assessment are promising and may represent a viable clinical application in addition to transdermal needle probe measurements.

Because we have demonstrated the safety of this technique, we bypassed animal studies and proceed directly to human investigations [Motz 2003]. Further, animal models, which would normally be used for initial *in vivo* studies, are not appropriate for development of this technology due to species specific variability in the spectra collected.

## *VII. B. Data Acquisition*

The experimental system and optical fiber Raman probes used for these procedures are

described in detail in section III.E.3. All room and surgical lights were turned off during each measurement. The spectrally examined tissue was then excised by the surgeon and underwent conventional pathological examination. Spectra were collected for a total of 1 s. A range of powers, 82-125 mW, were used depending on the probe employed.

Following each procedure, calibration data were collected for spectral corrections. Wavenumber calibration was established with a spectrum of 4-acetamidophenol. Chromatic intensity variations were corrected by collecting the spectrum of a tungsten white light source diffusely scatted by a reflectance standard ($BaSO_4$). The remaining probe background generated in the optical fibers was characterized by collecting the scattered excitation light off of a roughened aluminum surface. This background was optimally subtracted from the data in an iterative loop by using a scaling factor related to the tissue's optical properties [Motz *et al.* 2003]. The tissue fluorescence background was modeled with a sixth-order polynomial. Finally, the data was fit via non-negativity constrained least-squares minimization with our spectral model of breast tissue, described in section IV.C. In order to accurately model the *in vivo* data, spectra of probe components, epoxy and sapphire, were included in the model. In accordance with our initial diagnostic study, the fit coefficients of fat, collagen, cell nucleus, epithelial cell cytoplasm, and cholesterol-like were normalized to sum to a total contribution of one. In the present study, the two types of microcalcifications, calcium hydroxyapatite and calcium oxalate dihydrate, were excluded from this normalization as these species were not present in the tissue samples used for the diagnostic algorithm development. We also observed increased contributions from β-carotene in our *in vivo* data and thus this component was excluded from normalization.

### VII. B. 1. Raman Optical Fiber Probes

Four different probes were used in the *in vivo* clinical studies presented in this chapter. Probes D and F have 15 collection fibers and a diameter of 2.5 mm. Probes G and H have 9 collection fibers and a smaller diameter of 2.0 mm. The throughput of each probe, assessed as the laser power emerging from the distal tip, is give in Table VII.1. These values were obtained with 1260 mV, the maximum laser output.

| Probe | Laser Power |
|---|---|
| D (15 collection fibers) | 161.9 mW |
| F (15 collection fibers) | 118.2 mW |
| G (9 collection fibers) | 109.1 mW |
| H (9 collection fibers) | 78.5 mW |

**Table VII.1.** The throughput of the probes used in the *in vivo* studies.

The day prior to each clinical procedure, the experimental system was aligned and the probes submitted for cold-gas ethylene oxide sterilization. Just before surgery, the proximal ends of the sterilized Raman probe were coupled to the experimental system. The distal end of the probe was kept sterile and placed in gentle contact with the tissue while spectra were acquired. In the studies of atherosclerosis by Motz and coworkers, a single procedure was performed per day [Motz *et al.* submitted]. This allowed alignment of the specific probe to be used and the experimental system the day prior to intra-operative data collection. The probe was then submitted for ethylene oxide cold gas sterilization and the instrumental system aligned for precise coupling of the laser and the sterilized probe. To maximize the data collection in the mastectomy studies, spectra were acquired during as many as 4 surgeries in a single day. Because it is difficult to align the system while ensuring probe sterility, the instrument was aligned for best laser coupling with all 4 probes prior to sterilization. To assess how to optimally align the system for all 4 probes, each probe was

aligned and the throughput of the other 3 probes measured at this alignment. Results are shown in Table VII.2. Based on these results, the system was aligned for either probe H or probe G depending on the number of surgeries scheduled during the next day of data collection.

| Probe Optimally Aligned | Other Probe Throughputs |
|---|---|
| Probe D | Probe F 73.7 mW |
| | Probe G 91.5 mW |
| | Probe H 66.6 mW |
| Probe H | Probe D 169.5 mW |
| | Probe F 91.4 mW |
| | Probe G 99.1 mW |
| Probe G | Probe D 125.9 mW |
| | Probe F 94 mW |
| | Probe H 73.5 mW |

**Table VII.2.** Probe throughputs with different laser coupling alignments.

The linear array of collection fibers are terminated with a modified BNC connector and coupled to the spectrograph with a customized adaptor plate that was built in house. The BNC connector snaps into place on the adaptor plate, however, the coupling does not ensure precise alignment of the linear array with the spectrograph slit Vertical alignment of the linear array is necessary to assure adequate spectral resolution and thus alignment must be checked in the surgical suite prior to data collection. Perpendicular alignment of the linear area of collection fibers can usually be achieved with OR lights. However, OR lights are bright and can saturate the detector. Further, the BNC connector is the portion of the clinical instrumentation that allows the majority of light to enter the system. Each probe also has a different focal plane within the spectrograph. Thus, prior to each procedure the spectrograph must be focused in the OR. Again this can typically be

done using the OR lights. Precision refining of the collection fiber/ spectrograph coupling will result in less instrumental adjustments in the OR and easier clinical implementation.

## *VII. C. Margins*

### VII. C. 1. Introduction

Breast cancer is the most common female cancer in the United States, the second most common cause of cancer death in women (after lung cancer), and the main cause of death in women ages 45 to 55 [Jemal *at al.* 2004]. Breast cancer surgery has changed dramatically over the past several decades, and continues to evolve. With the emergence of the partial mastectomy, women may now preserve their breast without sacrificing oncologic outcome. Partial mastectomy is the surgical removal of the tumor, also known as breast conservation surgery or lumpectomy, followed by radiation therapy to eradicate any residual disease. Several clinical trials directly comparing partial mastectomy with traditional mastectomy, removal of the entire breast, have shown equivalent survival rates between the two treatment approaches [Early Breast Cancer Trialists' Collaborative Group 1995]. The goals of partial mastectomy are to provide a low rate of cancer recurrence in the treated breast while maintaining a cosmetically acceptable breast.

Complete surgical excision of the primary tumor is key to reducing the risk of local recurrence in women undergoing partial mastectomy procedures while minimizing the amount of breast tissue removed is the main factor in preserving cosmetic appearance. Thus, in successful partial mastectomy surgeries, complete resection of the cancer must be balanced with tissue conservation. To ensure that all malignant tissue is removed, a small margin of normal breast tissue surrounding the lesion is also excised. After surgery, a pathologist checks to make sure the surgeon has removed the entire cancerous lesion by

histologic assessment of the tissue margins. Margin status is gauged by pathological examination of the border of the excised lesion. Additionally, six small tissue samples are often taken from locations within the surgical cavity and examined for the presence of malignancy. Negative resection margins, typically defined as the absence of either invasive or intraductal carcinoma, have lower associated rates of local recurrence following partial mastectomy than do positive resection margins [Gage *et al.* 1996; Park *et al.* 2000; Smitt *et al.* 1995; Anscher *et al.* 1993; Borger *et al.* 1994]. Positive or unknown histologic margins usually prompt re-excision of the initial surgical site, since such patients are at higher risk for local recurrence even when radiation therapy is administered. In clinical practice, as many as 20%-55% of patients undergoing partial mastectomy will require a second surgical procedure due to positive margins indicative of incomplete cancer excision [Walls *et al.* 1995; Klimberg *et al.* 1998].

As a consequence of the large number of re-excision surgeries performed, there are numerous approaches under investigation to enhance intra-operative margin assessment. Gross inspection of the specimen in the operating room, with or without frozen section analysis, may permit identification of positive or close margins and immediate re-excision. However, routine frozen section analysis is time consuming and can lead to inadequate assessment of tumor margins in large specimens, and loss of diagnostic material in small specimens [Ferreiro *et al.* 1995; Johnson *et al.* 2001; Rubio *et al.* 1998]. Time intensive techniques, such as frozen section analysis, also have the disadvantage of prolonging the surgical procedure, thereby increasing the time the patient remains anesthetized. Therefore, many intra-operative techniques, which can provide real-time feedback, are under investigation. Intra-operative ultrasound may assist in assuring negative margins, although it

is generally of low resolution and thus its use does not preclude the presence of microscopic tumor on permanent sections [Klimberg et al. 1999]. Sehgal and coworkers used tissue echogenicity, the angular variance in echogenicity around the circumference of the lesion, and the patients age to obtain a sensitivity and specificity of 95% and 63%, respectively [Sehgal *et al.* 2004]. Optical techniques are also capable of providing immediate diagnosis and thus can assist in tumor resection during partial mastectomy surgeries. Currently, a variety of optical imaging and spectroscopic techniques are being explored to improve breast cancer diagnosis. These techniques employ visible or near-infrared light, are of high resolution when compared with ultrasound, and provide chemical information about the tissue being studied. Preliminary *in vivo* investigations have examined the efficacy of diffuse reflectance spectroscopy in the diagnosis of breast lesions, as well as in the assessment of tumor margins [Bown *et al.* 2000]. Diffuse reflectance spectroscopy monitors changes in the absorption and reduced scattering coefficients among tissues with different pathologies. It yielded a sensitivity and specificity of 67% and 79%, respectively.

In this study, we present the first demonstration of *in vivo* collection of Raman spectra of breast tissue. Data were collected during partial mastectomy surgeries to demonstrate the feasibility of *in vivo* Raman spectroscopy for intra-operative margin assessment and diagnosis of breast cancer. The research serves to extend and confirm the results of our *ex vivo* studies. The results of this study indicate that Raman spectroscopy has the potential to aid in intra-operative tumor resection. Accurate *in vivo* margin assessment techniques will allow numerous re-excision surgeries to be avoided. They may also extend partial mastectomy procedures to those women who do not harbor sufficiently small or localized breast cancers to qualify by current standards.

### VII. C. 2. Sample Preparation

The clinical protocol has been approved by both the MIT Committee on the Use Of Humans as Experimental Subjects and the Institutional Review Board of the Cleveland Clinic Foundation. Informed consent was obtained from all subjects prior to the surgical procedures.

This study utilizes partial mastectomy surgery to demonstrate the feasibility of *in vivo* Raman spectroscopy. The standard of care at the Cleveland Clinic Foundation involves the excision of 6 margin specimens from the surgical cavity. Raman spectra were collected from several of these margins prior to excision and thus only tissue that would normally be excised during the procedure was removed. A total of 30 Raman spectra were collected from 9 patients, 29 from margins subsequently found to be negative on pathology examination and 1 spectrum from a margin subsequently found to be positive on pathology examination. Of the 29 negative margins, 21 were comprised of normal breast tissue and 8 contained tissue diagnosed as fibrocystic change. The 1 positive margin was diagnosed as high-grade ductal carcinoma in situ (DCIS). We are able to accurately fit all 30 spectra with our previously developed spectral model of breast [Shafer-Peltier *et al.* 2002].

Two spectra were excluded from the present analysis. The first, a benign papilloma, is a pathology not encountered in our previous studies and thus our diagnostic algorithm does not encompass this type of tissue. The second is a margin noted by the pathologist to harbor significant cautery effects resulting from the surgical procedure. This was the only specimen where cautery of this degree was seen.

## VII. C. 3. Model Fits

Model fits to *in vivo* Raman spectra acquired from normal, benign, and malignant breast tissues are shown in Figure VII.1. The difference between the measured spectrum and the model fit, the residual, is shown below each spectrum. The lack of significant structure in the residuals demonstrates that the model accounts for the majority of the spectroscopic features observed and describes the data well. The fit coefficients, also displayed in Figure VII.1, represent the amount that each model basis spectrum must be weighted in order to recreate the tissue spectrum, thereby providing insight into the chemical/morphological makeup of the tissue.

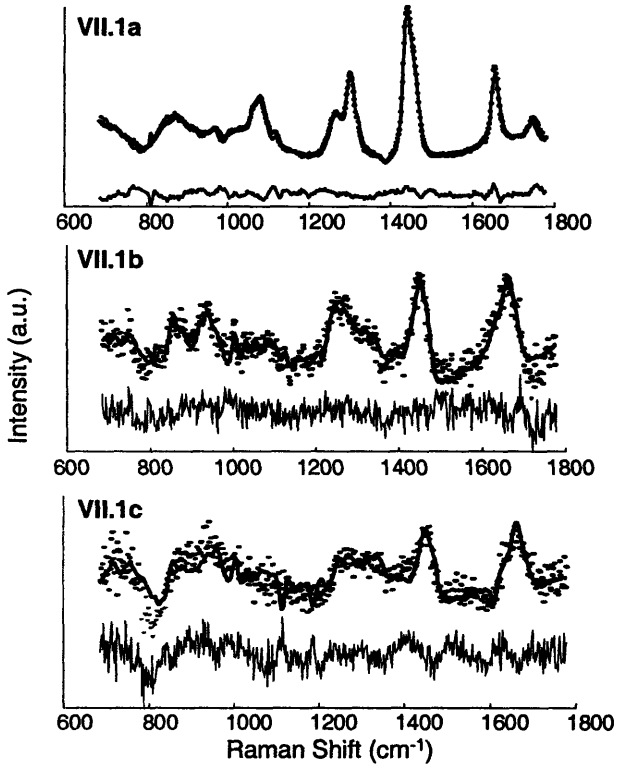


| NORMAL | |
|---|---|
| Cholesterol-like | 0.18 |
| Fat | 0.81 |
| Collagen | 0.01 |
| Cell Nucleus | 0.00 |
| Cell Cytoplasm | 0.00 |

| FIBROCYSTIC CHANGE | |
|---|---|
| Cholesterol-like | 0.12 |
| Fat | 0.02 |
| Collagen | 0.63 |
| Cell Nucleus | 0.01 |
| Cell Cytoplasm | 0.22 |

| DUCTAL CARINOMA IN SITU | |
|---|---|
| Cholesterol-like | 0.14 |
| Fat | 0.09 |
| Collagen | 0.36 |
| Cell Nucleus | 0.09 |
| Cell Cytoplasm | 0.32 |

**Figure VII.1.** Normalized Raman spectra (solid line), model fit (dotted line), residual (shown below), and fit coefficients representative of a) normal breast tissue, b) fibrocystic change, and c) ductal carcinoma in situ.

Fit coefficients are a function of both the concentration of a particular model component and its Raman scattering cross-section (which indicates the strength of the signal

at unit concentration). The fit coefficients of normal breast tissue exhibit a large contribution from fat. This is because normal breast tissue is predominately comprised of adipocytes, cells containing large amounts of cytoplasmic fat, and also because relative to most other model components, fat has a large Raman scattering cross-section. This explains the excellent signal to noise ratio evident in the spectrum acquired from normal breast tissue, Figure VII.1a. Although there is more noise evident in spectra acquired from diseased tissue, data analysis still yielded excellent model fits.

Fibrocystic change is a benign condition that can manifest itself as fibrosis (a scarring process characterized by an increased stromal component, and thus by accumulation of collagen), adenosis (increase in the number of ductules) or cyst formation (dilation of ducts and lobules with fluid). The margin which harbors fibrocystic change shows an increase in the fit coefficients of collagen due to fibrosis and epithelial cell cytoplasm as a consequence of adenosis. The fit coefficients of the positive margin, diagnosed as high-grade ductal carcinoma in situ (DCIS), also display an increase in the amount of epithelial cell cytoplasm. However, a signature of carcinoma is enlargement of cell nuclei, and thus a higher nuclear to cytoplasm (N/C) ratio than in benign conditions. Nuclear enlargement and atypia are hallmarks of cancer. Thus, the N/C ratio is a diagnostic criterion routinely used by pathologists [Elston and Ellis 1991; Hoda and Rosen 2002]. In our studies, the spectroscopic parameter characterizing the N/C ratio, obtained by dividing the fit coefficient of the cell nucleus basis spectrum by the fit coefficient of the epithelial cell cytoplasm basis spectrum, is much larger for the cancerous specimen, shown in Figure VII.1c, than for any of the fibrocystic lesions encountered in this study.

Table VII.3 displays the fit coefficient error associated with each model component. The method used for calculating prediction error is presented in section IV.F. Errors are broken down by diagnosis, as spectra corresponding to different pathologies contained dissimilar amounts of noise. The amount of noise was extremely variable even within pathologies due to collection with different Raman probes as well as day to day variations in laser coupling.

| Model | Signal | OLF | $\Delta c_{normal}$ | $\Delta c_{fibrocystic\ change}$ | $\Delta c_{cancer}$ |
|---|---|---|---|---|---|
| | | | N=0.0451 | N=0.0927 | N=0.1841 |
| Calcium Oxalate Dihydrate | 2.68 | 0.96 | 0.02 | 0.04 | 0.07 |
| Calcium Hydroxyapatite | 2.85 | 0.93 | 0.02 | 0.03 | 0.07 |
| Cholesterol-like | 4.48 | 0.28 | 0.04 | 0.07 | 0.15 |
| Water | 7.04 | 0.64 | 0.01 | 0.02 | 0.04 |
| β-Carotene | 3.67 | 0.84 | 0.01 | 0.03 | 0.06 |
| Fat | 4.97 | 0.40 | 0.02 | 0.05 | 0.09 |
| Collagen | 8.12 | 0.45 | 0.01 | 0.03 | 0.05 |
| Cell Nucleus | 5.96 | 0.69 | 0.01 | 0.02 | 0.04 |
| Epithelial Cell Cytoplasm | 6.32 | 0.31 | 0.02 | 0.05 | 0.09 |

**Table VII.3.** Fit coefficient errors for the *in vivo* data.

## VII. C. 4. Diagnostic Algorithm

Figure VII.2 displays a scatter plot of the fit coefficients for collagen and fat, FC(Coll) and FC(Fat), respectively, for all data acquired in this study. Also shown are the decision lines that separate samples according to diagnoses. The diagnostic algorithm shown in Figure VII.2 was developed previously using 126 spectra from 58 patients and is used in a prospective manner in this study [Haka *et al.* submitted]. Table VII.4 compares the pathologic diagnosis with that of the Raman diagnostic algorithm for our data set. The

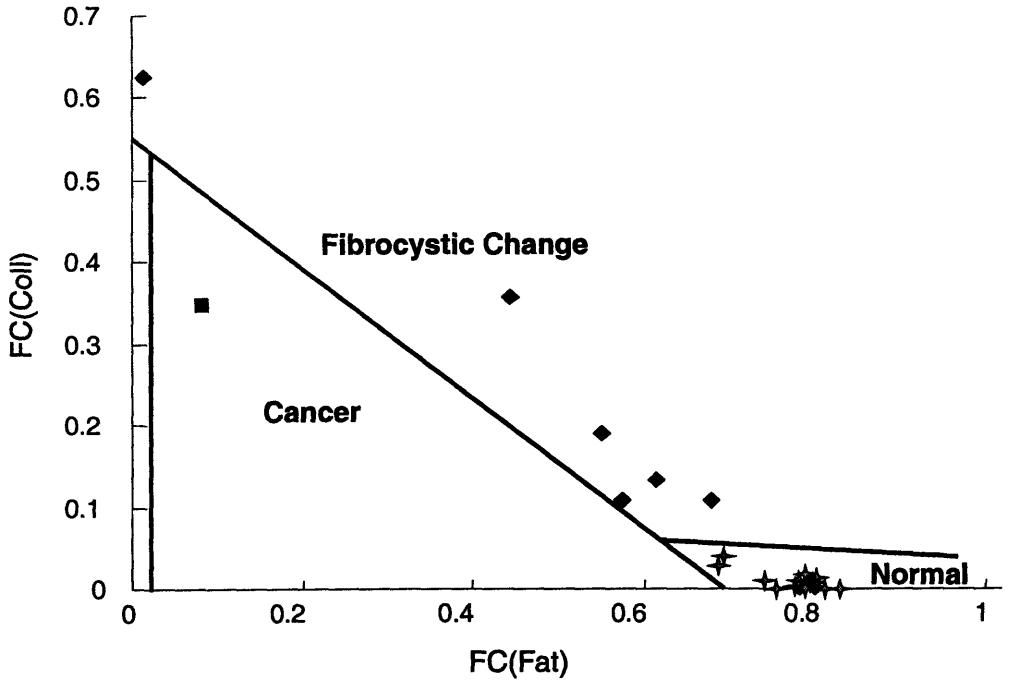


**Figure VII.2.** Scatter plot displaying the fat and collagen content for the *in vivo* Raman spectra acquired margin specimens. Normal (stars), Fibrocystic Change (diamonds), Ductal Carcinoma In Situ (square).

algorithm results in a sensitivity for detecting carcinoma of 100%, a specificity of 100%, and an overall accuracy of 93% (28/30). We note, that although there is only one malignant sample in the present data set, this algorithm has been previously validated with 31 cancerous specimens. The high grade DCIS correctly identified by Raman spectroscopy was grossly invisible. Upon pathologic review, the finding that this margin was positive necessitated that the patient undergo a second surgery to excise the remaining cancerous cells. Had Raman spectroscopy been employed in a real-time fashion to guide excision during the initial surgery, the additional procedure could have been avoided.

| Pathology Diagnosis / Raman Diagnosis | Normal (21 spectra) | Fibrocystic Change (8 spectra) | Cancer (1 spectrum) |
|---|---|---|---|
| Normal | 21 | 2 | 0 |
| Fibrocystic Change | 0 | 6 | 0 |
| Cancer | 0 | 0 | 1 |

**Table VII.4.** Comparison of pathologic diagnosis with that of the Raman diagnostic algorithm for margin specimens. The Raman diagnostic algorithm results in an overall accuracy of 93% (28/30).

### VII. C. 5. Discussion

This pilot study is the first use of Raman spectroscopy to examine breast cancer *in vivo*. It clearly demonstrates the feasibility of Raman spectroscopy as a clinical technique for breast cancer diagnosis. The data exhibit good agreement with our previously developed spectral model and diagnostic algorithm. Studies with a larger patient pool are currently underway to further expand and validate our diagnostic algorithm. Further, we have developed and demonstrated real-time Raman diagnosis with our clinical instrumentation thus allowing its implementation in upcoming studies [Motz *et al.* in press]. These excellent results indicate that Raman spectroscopy has the potential to provide real-time margin assessment thereby reducing the recurrence rate of breast cancer following partial mastectomy surgeries.

As the first *in vivo* demonstration of Raman spectroscopy of breast tissue, this study has implications beyond margin assessment. There are several areas where Raman spectroscopy may aid in breast cancer diagnosis and treatment. In particular, optical techniques are less invasive than current diagnostic procedures. The results of this study illustrate the potential for transdermal needle measurements to provide breast cancer diagnosis. As opposed to standard biopsy, a spectroscopic transdermal needle measurement would have the advantage of providing immediate diagnosis. As a result, Raman

spectroscopy has the potential to reduce both the likelihood of a non-diagnostic biopsy that would require repeat needle or surgical biopsy, and patient anxiety by eliminating the currently unavoidable wait for a traditional histopathology diagnosis. Furthermore, with the development of minimally invasive breast cancer therapies, such as radiofrequency ablation, which relies on insertion of a thin metal probe into the breast, there is the potential that diagnosis and treatment could be performed in a single procedure [Fornage *et al.* 2004].

## *VII. D. Mastectomies*

### VII. D. 1. Sample Preparation

The clinical protocol has been approved by both the MIT Committee on the Use Of Humans as Experimental Subjects and the Institutional Review Board of the Cleveland Clinic Foundation. Informed consent was obtained from all subjects prior to the surgical procedures.

This study utilizes mastectomy surgeries to demonstrate the feasibility of *in vivo* Raman spectroscopy. Spectra were acquired from the mastectomy specimen prior to removal of the breast. Locations of data acquisition were selected by the surgeon. Small samples of tissue were taken from the spectrally examined region of the breast. As the entire breast is excised during a mastectomy procedure, only tissue that would normally be excised during the surgery was removed. A total of 32 Raman spectra from 9 patients was collected, 24 spectra from normal breast tissue, 6 from tissue diagnosed as fibrocystic change, and 2 spectra from cancerous lesions. The malignant tissue was

**Figure VII.3.** Schematic of a mastectomy surgery.

diagnosed as intermediate-grade DCIS. We are able to accurately fit all 32 spectra with our previously developed spectral model of breast [Shafer-Peltier *et al.* 2002]. In the mastectomy procedures, spectra were acquired from more peripheral tissue sites than in the margin specimens. The surgical procedure, diagramed in Figure VII.3, illustrates the area of data collection from deep within the breast, closer to the chest wall.

Seven spectra were excluded from the present analysis. The first, a lesion diagnosed

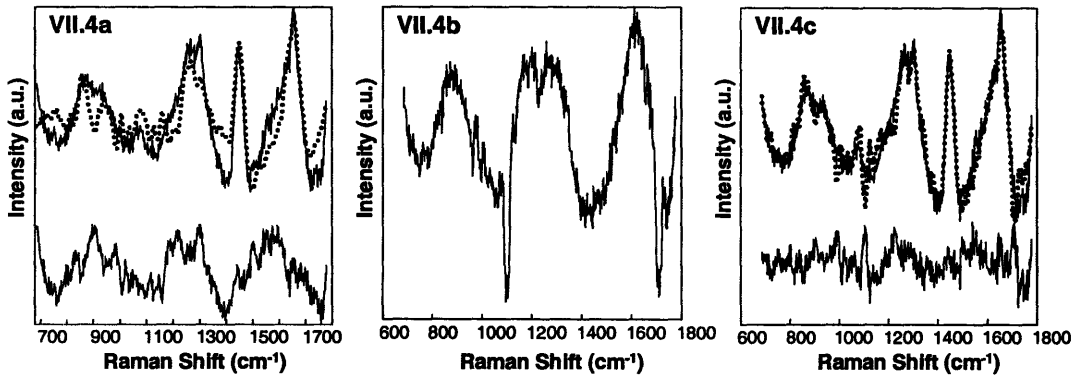


**Figure VII.4.** a) A Raman spectrum contaminated with light. Also shown are the model fit (dotted line) and residual (below). b) A spectrum obtained by shining light onto the probe/ spectrograph connection. c) Raman spectrum shown in a. The light spectrum, shown in b, is included in the model resulting in the fit (dotted line) and residual (below) shown in c.

as granulomatous response, is a pathology not encountered in our previous studies and thus our diagnostic algorithm does not encompass this type of tissue. Six spectra, all from a single patient, were excluded due to distortions from light contamination. Figure VII.4 shows a Raman spectrum contaminated with light. Although the OR lights were turned off during data acquisition, it did not result in complete darkness due to windows in the surgical suite and computer monitors. The light was found to enter through the probe spectrograph BNC connection. Only probe D exhibited this type of light contamination. In latter data collection, the BNC connection was covered with a black cloth. A spectrum of the light entering probe D is shown in Figure VII.4b. When this light spectrum was included in the model, fits were improved as seen in Figure VII.4c. However, all 6 spectra were still

incorrectly diagnosed and thus excluded from the analysis. Refinement of the light spectrum shown in Figure VII.4b may further improve the accuracy of the model fit.

### VII. D. 2. Model Fits

Model fits to *in vivo* Raman spectra acquired from normal, benign, and malignant breast

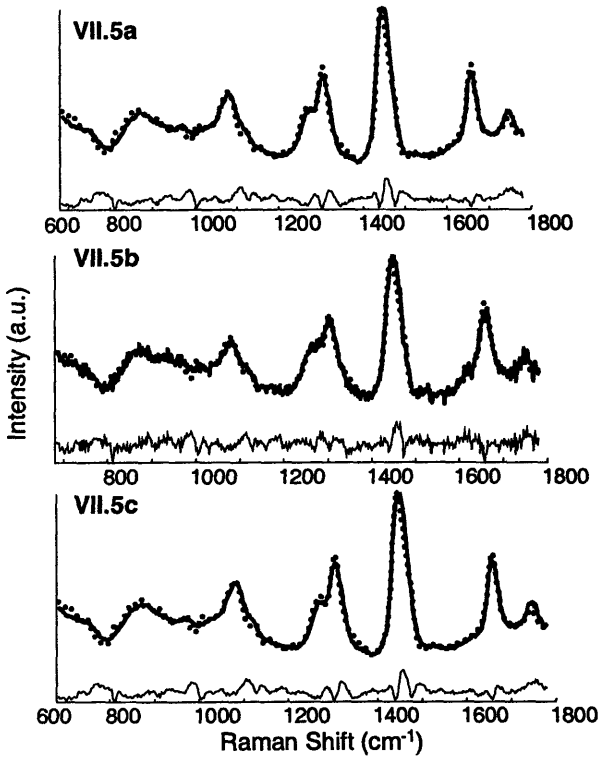


| NORMAL | |
|---|---|
| Cholesterol-like | 0.19 |
| Fat | 0.79 |
| Collagen | 0.01 |
| Cell Nucleus | 0.00 |
| Cell Cytoplasm | 0.01 |

| FIBROCYSTIC CHANGE | |
|---|---|
| Cholesterol-like | 0.12 |
| Fat | 0.73 |
| Collagen | 0.04 |
| Cell Nucleus | 0.00 |
| Cell Cytoplasm | 0.11 |

| DUCTAL CARINOMA IN SITU | |
|---|---|
| Cholesterol-like | 0.14 |
| Fat | 0.81 |
| Collagen | 0.00 |
| Cell Nucleus | 0.00 |
| Cell Cytoplasm | 0.05 |

**Figure VII.5.** Normalized Raman spectra (solid line), model fit (dotted line), residual (shown below), and fit coefficients representative of a) normal breast tissue, b) fibrocystic change, and c) ductal carcinoma in situ.

tissue are shown in Figure VII.5. The difference between the measured spectrum and the model fit, the residual, is shown below each spectrum. All 3 spectra were acquired from the same patient. Some structure is visible in the residuals. Much of the structure in the residuals results from spectral broadening as a consequence of incomplete vertical alignment of the probe fibers and the detector. The BNC connectors on some probes prevent vertical alignment. However, the model still accounts for the majority of the spectroscopic features

observed and describes the data well. It is notable that all 3 spectra, regardless of diagnosis, are predominately composed of fat. Because most spectra acquired in the mastectomy studies contain large signals from fat, the noise in the data is similar regardless of the corresponding diagnosis. Thus, the fit coefficient error for all data, regardless of pathology, is similar to the error shown for normal samples in Table VII.3.

### VII. D. 3. Diagnostic Algorithm

Figure VII.6 displays a scatter plot of the fit coefficients for collagen and fat for the data acquired from mastectomy specimens. Also shown are the decision lines that separate samples according to diagnoses. Table VII.5 compares the pathologic diagnosis with that of the Raman diagnostic algorithm for our data set. The algorithm results in a sensitivity of 0%, a specificity of 100%, and an overall accuracy of 81% (26/32). Clearly, the results from the mastectomy specimens are different than those from the margin tissues. In particular all of the mastectomy data, regardless of pathology, exhibits large contributions from fat. We are currently investigating the reason for the difference between the *in vivo* Raman spectra acquired from mastectomy and margin specimens.

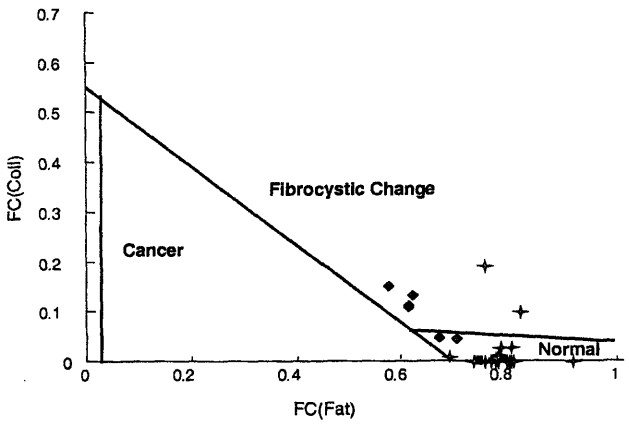


**Figure VII.6.** Scatter plot displaying the fat and collagen content for the *in vivo* Raman spectra acquired during mastectomy surgeries. Normal (stars), Fibrocystic Change (diamonds), Ductal Carcinoma In Situ (squares).

| Pathology Diagnosis / Raman Diagnosis | Normal (24 spectra) | Fibrocystic Change (6 spectra) | Cancer (2 spectra) |
|---|---|---|---|
| Normal | 22 | 2 | 2 |
| Fibrocystic Change | 2 | 4 | 0 |
| Cancer | 0 | 0 | 0 |

**Table VII.5.** Comparison of pathologic diagnosis with that of the Raman diagnostic algorithm for mastectomy specimens. The Raman diagnostic algorithm results in an overall accuracy of 81% (26/32).

One possibility is that the tissue examined in the mastectomy surgeries was more peripheral than the specimens in the lumpectomies. This peripheral tissue is further from the core area of the breast, which contains the ductal system, and thus may have a higher fat content, as shown in Figure VII.7. Future studies of Raman spectra at different locations with in the breast can be used to examine the effect of anatomical position on spectrally extracted composition. Misdiagnoses may also arise from the fact that in the 2 cancerous mastectomy specimens malignant cells only occupied 10% and 20% of the volume of tissue spectrally examined. It is possible that this level of cellularity provides insight into our lower detection limits. Future studies, aimed at obtaining quantitative fit coefficients, will elucidate lower detection limits as well as Raman scattering cross-sections of our model components. However, it is also possible that there was a slight registration error between the excised tissue and the spectroscopic data. Such

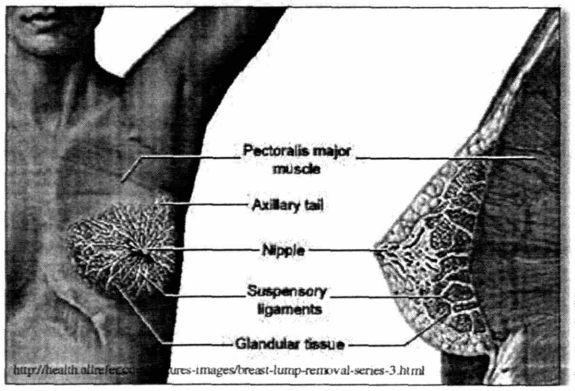


**Figure VII.7.** Schematic of the breast illustrating the distribution of the ductal system.
© ADAM.

registration errors have presented problems in many of our studies, including our *in vivo* examination of atherosclerosis [Motz *et al.* submitted].

## *Acknowledgements*

All of the data in this chapter was collected under the supervision of Dr. Joseph Crowe. This study would not have been possible without the incredible support of the Cleveland Clinic Foundation surgical staff. I especially thank Joanne Woletz for her exceptional efforts. In addition to providing guidance for the clinical protocol, Dr. David Hicks analyzed the histological sections. I would also like to thank Deborah Baynes for helping the study to run smoothly and Jim Stanicky for probe sterilization. Jonathan Nazemi was invaluable in executing this study. He assisted with data acquisition, study planning, equipment transportation, and general troubleshooting. Luis Galindo constructed all the Raman probes used in this study. Thanks to Jason Motz for allowing me to participate in his earlier clinical research, an experience which prepared me to undertake this study. Last, I would like to thank Ramachandra Dasari for his help with study planning and obtaining COUHES approval. This research was sponsored by the NIH grant HL-64675 and the National Center for Research Resources program grant P41-RR-02594.

## *References*

Anscher MS, Jones P, Prosnitz LR, Blackstock W, Herbert M, Reddick R, Tucker A, Dodge R, Leight G, Iglehart JD and Rosenman J (1993). "Local Failure and Margin Status in Early-Stage Breast Carcinoma Treated With Conservation Surgery and Radiation Therapy." Ann Surg **218**(1): 22-28

Bakker Schut TC, Withes MJH, Sternborg HJCM, Speelman OC, Roodenburg JLN, Marple ET, Bruining HA and Puppels GJ (2000). "*In Vivo* Detection of Dysplastic Tissue by Raman Spectroscopy." Anal Chem **72**(24): 6010-6018.

Borger J, Kemperman H, Hart A, Peterse H, Vandongen J and Bartelink H (1994). "Risk Factors in Breast-Conservation Therapy." J Clin Oncol **12**(4): 653-660.

Bown SG, Briggs G, Kelley C, Lakhani S, Pickard D, Ripley PM, Rose IG and Saunders C and Bigio IJ (2000). "Diagnosis of breast cancer using elastic-scattering spectroscopy: preliminary clinic results." J Biomed Opt **5**: 221-228.

Caspers PJ, Lucassan GW, Wolthuis R, Bruining HA and Puppels GJ (1998). "*In Vitro* and *In Vivo* Raman Spectroscopy of Human Skin." Biospectrosc **4**: S31-S39.

Caspers PJ, Lucassen GW, Bruining HA and Puppels GJ (2000). "Automated Depth-Scanning Confocal Raman Microspectrometer for Rapid *In Vivo* Determination of Water Concentration Profiles in Human Skin." J Raman Spectrosc **31**: 813-818.

Early Breast Cancer Trialists' Collaborative Group (1995). "Effects of Radiotherapy and Surgery in Early Breast Cancer. An Overview of the Randomized Trials." N Engl J Med **333**: 1444.

Elston CW and Ellis IO (1991). "Pathological Prognostic Factors in Breast Cancer. I. The

Value of Histological Grade in Breast Cancer: Experience from a Large Study with Long-Term Follow-Up." Histopathology **19**(5): 403-410.

Ferreiro JA, Gisvold JJ and Bostwick DG (1995). "Accuracy of Frozen-Section Diagnosis of Mammographically Directed Breast Biopsies. Results of 1,490 Consecutive Cases." Am J Surg Pathol **19**: 1267.

Fornage BD, Sneige N, Ross MI, Mirza AN, Kuerer HM, Edeiken BS, Ames FC, Newman LA, Babiera GV and Singletary SE (2004). "Small (<= 2 cm) Breast Cancer Treated with US-Guided Radiofrequency Ablation: Feasibility Study." Radiology **231**(1): 215-224.

Gage I, Schnitt SJ, Nixon AJ, Silver B, Recht A, Troyan SL, Eberlein T, Love SM, Gelman R, Harris JR and Connolly JL (1996). "Pathologic Margin Involvement and the Risk of Recurrence in Patients Treated With Breast-Conserving Therapy." Cancer **78**(9): 1921-1928.

Haka AS, Shafer-Peltier KE, Fitzmaurice M, Crowe J, Dasari RR and Feld MS "Detecting Breast Cancer Using Raman Spectroscopy" P Natl Acad Sci USA submitted 2004.

Hata TR, Scholz TA, Ermakov IV, McClane RW, Khachik F, Gellermann W and Pershing LK (2000). "Non-Invasive Raman Spectroscopic Detection of Carotenoids in Human Skin." J Invest Derm **115**: 441-448.

Hoda SA and Rosen PP (2002). "Practical Considerations in the Pathologic Diagnosis of Needle Core Biopsies of Breast." Am J Clinical Pathol **118**(1): 101-108.

Jemal A, Tiwari RC and Murray T (2004) "Cancer statistics 2004." CA Cancer J Clin **54**: 8.

Johnson AT, Henry-Tillman R and Klimberg VS (2001). "Breast Conserving Surgery: Optimizing Local Control in the Breast With Assessment of Margins." Breast Dis **12**: 35.

Klimberg VS, Westbrook KC and Korourain S (1998). "Use of Touch Preps for Diagnosis and Surgical Margins in Breast Cancer." Ann Surg Oncol **5**:220-226.

Klimberg VS, Harms S and Korourian S (1999). "Assessing Margin Status." Surg Oncol **8**: 77.

Motz JT (2003). "Development of *In Vivo* Raman Spectroscopy of Atherosclerosis." Medical Physics Ph.D. Thesis. Cambridge, Massachusetts Institute of Technology.

Motz JT, Hunter M, Galindo LH, Gardecki JA, Kramer JR, Dasari RR and Feld MS (2003). "Optical Fiber Probe for Biomedical Raman Spectroscopy." Appl Opt **43**: 542-554.

Motz JT, Gandhi SJ, Scepanovic OR, Haka AS, Galindo LH, Kramer JR, Dasari RR and Feld MS (2004). "Real-Time Raman System for *In Vivo* Disease Diagnosis." JBO (in press).

Motz JT, Gandhi S, Haka AS, Galindo LH, Kramer, JR, Fitzmaurice M, Dasari RR, Miller A and Feld MS "*In Vivo* Raman Spectroscopy of Human Atherosclerotic Plaques." Nat Med (submitted).

Park CC, Mitsumori M, Nixon A, Recht A, Connolly J, Gelman R, Silver B, Hetelekidis S, Abner A, Harris JR and Schnitt SJ (2000). "Outcome at 8 Years After Breast-Conserving Surgery and Radiation Therapy for Invasive Breast Cancer: Influence of Margin Status and Systemic Therapy on Local Recurrence." J Clin Oncol **18**(8): 1668-1675.

Rubio IT, Klimberg VS and Korourian S (1998). "Use of Touch Preps for Diagnosis and Evaluation of Surgical Margins in Breast Cancer." Ann Surg Oncol **5**: 220.

Sehgal CM and Cary TW (2004). "Computer-Based Margin Analysis of Breast

Sonography for Differentiating Malignant and Benign Masses." J Ultrasound Med **23**: 1201-1209.

Shafer-Peltier KE, Haka AS, Fitzmaurice M, Crowe J, Myles J, Dasari RR and Feld MS (2002). "Raman Microspectroscopic Model of Human Breast Tissue: Implications for Breast Cancer Diagnosis *In Vivo*." J Raman Spec **33**(7): 125-137.

Shim MG, Song L-MWK, Marcon NE and Wilson BC (2000). "*In Vivo* near-Infrared Raman Spectroscopy: Demonstration of Feasibility During Clinical Gastrointestinal Endoscopy." Photochem Photobiol **72**: 146-150.

Smitt MC, Nowels KW, Zdeblick MJ, Jeffrey S, Carlson RW, Stockdale FE, Goffinet DR (1995). "The Importance of the Lumpectomy Surgical Margin Status in Long-Term Results of Breast Conservation." Cancer **76**(2): 259-267.

Utzinger U, Heintzelman dL, Mahadevan-Jansen A, Malpica A, Follen M and Richards-Kortum R (2001). "Near-Infrared Raman Spectroscopy for *In Vivo* Detection of Cervical Precancers." Appl Spectrosc **55**(8): 955-959.

Walls J, Knox F, Baildam AD, Asbury DL, Mansel RE, and Bundred NJ (1995). "Can Preoperative Factors Predict for Residual Malignancy After Breast Biopsy for Invasive Cancer?" Ann R Coll Surg Engl **77**: 248-251.

# Chapter VIII. Other Applications of Raman and Fluorescence Spectroscopies

Although there are many advantages to Raman spectroscopy, other optical techniques may also play a role in breast cancer diagnosis. Preliminary investigations have examined the diagnostic potential of fluorescence and reflectance spectroscopies. Studies have also been conducted on spectroscopic techniques that have only recently been applied to tissue, such as surface enhanced Raman spectroscopy and fluorescence lifetime measurements. Finally, Raman and fluorescence spectroscopies are used in a synergistic manner to elucidate the mechanism of ceroid formation *in situ*. Ceroid is an insoluble lipid-protein complex characteristic of atherosclerotic plaques. The mechanism of ceroid formation has been extensively studied but despite intensive research, ceroid is only defined empirically through its fluorescence properties and its behavior during various staining processes. The synergy of these two types of spectroscopy allows for the identification of ceroid *via* its fluorescence signature and the subsequent elucidation of its chemical composition through the acquisition of a Raman spectrum. A better understanding of the mechanism of ceroid formation may suggest avenues to induce regression or prevent progression of atherosclerotic plaques with medical therapy

## *VIII. A. Fluorescence and Reflectance of Breast*

Although there are many advantages to Raman spectroscopy, other optical techniques may also play a role in breast cancer diagnosis. In particular, several studies examining fluorescence spectroscopy for the diagnosis of cancer have shown promising results, particularly for the detection of precancerous changes. Because fluorescence spectroscopy is fast, easily implemented, and has relatively strong signals, many researchers have employed it for tissue diagnosis. As such, we are investigating the diagnostic role of fluorescence and reflectance spectroscopies in breast cancer. The techniques may provide complementary information to that obtained with Raman spectroscopy. To assess this, each fluorescence and reflectance data set acquired in this study corresponds to a Raman spectrum obtained from the same region of tissue. Preliminary results of the corresponding Raman spectral data set are presented in Chapter V.B. In combination, these techniques may provide a more complete understanding of the biochemical and/or morphological changes that take place during the progression of breast disease. Ultimately all three modalities may be combined into a single spectroscopic technique for the diagnosis of breast cancer. The overall goal of this research project is to develop fluorescence and reflectance spectroscopies as a diagnostic tool for the detection and differentiation of various breast diseases. We have collected a large pool of data from a wide range of samples in order to further our understanding of breast disease progression. Using this data we shall determine the key diagnostic features contained within the fluorescence and reflectance spectra and utilize them in the development of a diagnostic algorithm for the differentiation of normal, benign and malignant breast tissue.

## VIII. A. 1. Introduction

The energy of visible and UV light can elevate the electrons in molecules and atoms to excited energy states. These energy states exist as discrete levels, and can be excited only by photons of a frequency that corresponds to the energy difference between level. The structure of the molecule determines which incident frequencies will be absorbed. In many cases light absorbed by a molecule is converted into heat; however, an absorbed photon can also be re-emitted as fluorescence. Fluorescence emission typically occurs at a lower energy than the absorption energy of the incident photons.

Fluorescence spectra in tissue can be used to identify fluorophores and monitor their concentrations. Various tissue fluorophores include metabolic substances such as NADH and flavins, aromatic amino acids such as tryptophan, tyrosine and phenylalanine, structural proteins such as collagen and elastin, several porphyrins, and lipids such as ceroid and lipofuscin. Each of these fluorophores has specific wavelengths for excitation and emission. The fluorescence emitted by a molecule in tissue depends on the energy level difference between the electronic ground state and excited state and the distribution of vibrational and rotational levels within these states. These energy states can shift in the presence of different local environmental factors, such as pH, temperature and oxygenation. In the progression of disease the local environment in which the fluorophores are embedded changes, as well as their relative concentrations, thus leading to changes in the observed fluorescence intensity and lineshape.

The measured reflectance spectrum contains both diffuse reflectance (multiply scattered) and singly backscattered light. The penetration depth of the diffusive component is 0.5 mm to 1.5 mm, and therefore, diffuse reflectance spectroscopy (DRS) predominately

provides information about the morphology and absorption of the tissue stroma. The absorption spectrum of tissue depends on the type of predominant absorbing molecules or chromophores and therefore, provides information about its chemical composition. Water is a strong tissue absorber in both the UV and IR regions. DNA and proteins absorb in the UV region, while hemoglobin, melanin and β-carotene absorb in the visible region. Other tissue chromophores include porphyrin-like structures such as bilirubin, myoglobin, cytochrome c oxidase and protoporphyrin. For breast tissues, the diffuse reflectance spectra can be analyzed using a mathematical model based on the diffusion approximation to extract the hemoglobin and β-carotene concentrations, oxygen saturation, average diameter and density of scatterers [Zonias *et al.* 1999].

Extraction of the singly backscattered spectrum, which comprises a small fraction (2% to 5%) of the entire reflectance spectrum, can be achieved by subtracting the diffuse reflectance fit from the measured reflectance spectrum [Perelman *et al.* 1998]. The resulting singly backscattered spectrum, referred to as light scattering spectroscopy (LSS), exhibits an oscillatory behavior in wavelength. When arising from epithelium, the frequency of these oscillations corresponds to the nuclear size distribution within the epithelial cells [Perelman *et al.* 1998]. In breast, where the architecture of the tissue examined does not consist of a layer of epithelial cells overlying the stroma, it is not clear what type of information LSS will provide.

Fluorescence photons are scattered and absorbed during their path to the tissue surface where they are collected. Therefore, the spectral features of the collected fluorescence can be significantly distorted, making the extraction of the biochemical composition of the tissue from the measured signal difficult. This is a particular problem in

the presence of strong tissue absorbers such as hemoglobin. Intrinsic fluorescence spectroscopy (IFS) is a technique that extracts the fluorescence of molecules unaffected by absorption and scattering events [Zhang *et al.* 2000; Muller *et al.* 2001]. Because diffuse reflectance undergoes similar absorption and scattering events as fluorescence, information contained within the reflectance spectra can be used to extract the intrinsic fluorescence from the measured fluorescence spectra. An example of measured fluorescence and reflectance data and the corresponding intrinsic fluorescence spectrum is shown in Figure VIII.1. A large dip, due to hemoglobin absorption, can be seen at 420 nm in both the measured reflectance and fluorescence spectra. This feature is not present in the intrinsic fluorescence because effects due to tissue scattering and absorption have been removed. The three techniques, IFS, DRS and LSS, can be combined into a single spectroscopic modality. This technique, known as tri-modal spectroscopy (TMS), provides biochemical, structural, and morphological information simultaneously [Georgakoudi *et al.* 2001, 2002; Muller *et al.* 2002].

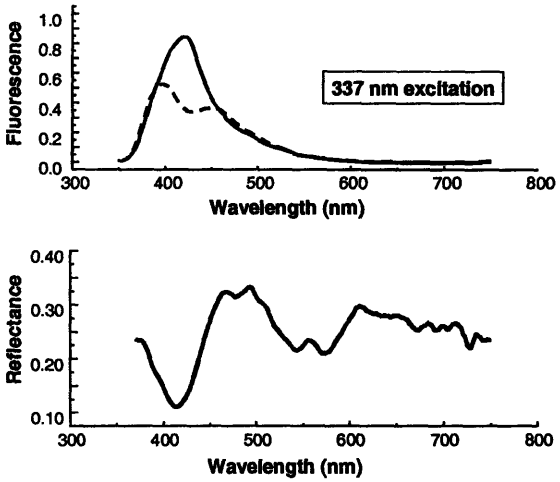


**Figure VIII.1.** Measured tissue fluorescence (dashed line) and reflectance (solid line below) used to extract the intrinsic fluorescence spectrum (solid line above).

Several studies have fueled our interest in the use of fluorescence spectroscopy as a diagnostic tool for the detection of breast disease [Yang *et al.* 1996, 1998; Gupta *et al.* 1997; Majumder *et al.* 1998]. Previous research has demonstrated the ability of fluorescence spectroscopy to differentiate benign and malignant tumors at certain key excitation

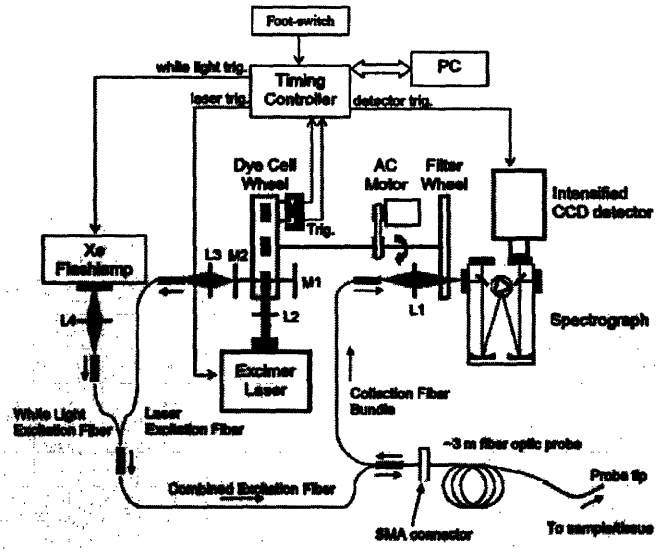


**Figure VIII.2.** Schematic layout of the FastEEM clinical spectrophotometer. L1, L2, L3, L4 are lenses. M1 and M2 are mirrors.

wavelengths. However, there are several questions that these studies have left unanswered. First, their data was acquired at least 4 hours after the tissue was excised, well after key fluorophores, such as NADH, have decayed. This results in diagnostic schemes that may not be applicable to *in vivo* studies. Second, previous studies have only explored a limited number of excitation wavelengths. Third, the groups' results are not consistent, raising questions regarding reproducibility of the data. Our experience in fluorescence spectroscopy of human tissues places us in a good position to take this research a step further. We have optical fiber fluorescence probes, as well as a special instrument, the FastEEM (excitation-emission matrix), shown in Figure VIII.2, for collecting fluorescence and reflectance data [Muller *et al.* 2002]. This instrument provides a broader range of excitation wavelengths than was available in previous studies. Not only can we verify prior published results, but it is possible that we can achieve superior diagnostic information by employing a wider range of excitation wavelengths.

Additionally, a recent publication has indicated the utility of diffuse reflectance spectroscopy for breast cancer diagnosis [Bown *et al.* 2000]. Our FastEEM instrument also allows for the collection of reflectance data. A diagnostic algorithm that combines both

fluorescence and reflectance data could result in significantly more accurate diagnoses. Our current protocol for examining fluorescence spectra allows for the removal of artifacts resulting from tissue absorption and scattering, factors which were not taken into account in previous studies. Removal of features resulting from scattering and absorption is crucial for both an in depth understanding of the origins of tissue fluorescence and for obtaining reproducible data. Further, we have the ability to examine the tissue within minutes of excision. Our capability to examine a wide range of excitation wavelengths, our previous experience with fluorescence and reflectance data processing protocols, and the collection of data immediately following tissue excision should result in more accurate diagnoses and a deeper understanding of the chemical and physical changes accompanying the onset of breast cancer.

### VIII. A. 2. β-Carotene Absorption

Analysis of the FastEEM data of breast tissue revealed contributions from β-carotene, a moiety not encountered in previous studies. We were unable to fit the reflectance data of breast tissue using an absorption spectrum of β-carotene dissolved in hexane [http://omlc.ogi.edu/spectra/photochemCAD/html/beta-carotene.html]. This is because the absorbance properties of carotenoids are highly dependent on their chemical environment [Zang *et al.* 1997]. β-carotene is extremely lipophillic and not soluble in water. In physiologically relevant environments β-carotene is typically dissolved in adipose tissue, and thus it is difficult to select an appropriate solvent for its' examination. For this reason, we employed an absorption spectrum that was obtained by manipulating a diffuse reflectance spectrum of a sample of breast tissue known to contain high concentrations of β-carotene. This reflectance spectrum was inverted, smoothed using a five point adjacent averaging

algorithm, and scaled to encompass a similar intensity range as an absorption spectrum of known β-carotene concentration in hexane. The manipulated reflectance spectrum was subsequently averaged with the absorption spectrum of β-carotene dissolved in hexane. Figure VIII.3 shows the absorption spectrum of β-carotene in hexane, the diffuse reflectance spectrum used in this analysis and the resultant absorption spectrum used to fit our diffuse reflectance data. This absorption spectrum provides superior reflectance fits as it more closely mimics the properties of β-carotene in its natural environment. Reflectance fits

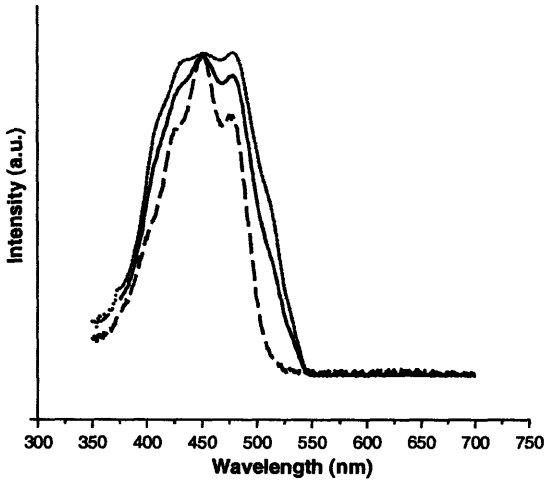


**Figure VIII.3.** Absorption spectrum of b-carotene in hexane (dashed line), inverted reflectance spectrum (dotted line) manipulated to generate the 'b-carotene' absorption spectrum used for fitting diffuse reflectance of breast and artery (solid line).

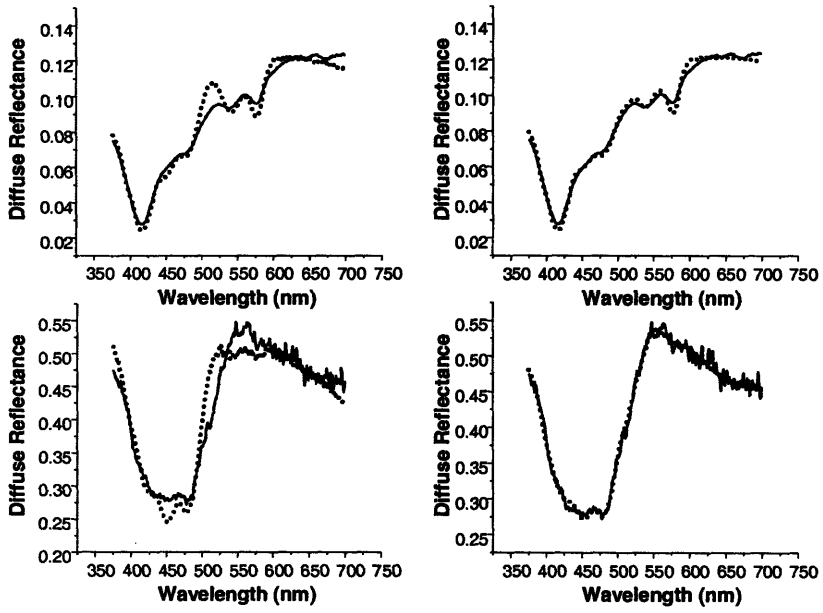


**Figure VIII.4.** Reflectance data (solid lines) model fits (dotted lines) using the absorption spectrum of b-carotene in hexane (left) and the mathematically derived 'b-carotene' absorption spectrum (right).

using the absorption spectrum of β-carotene in hexane and the mathematically derived absorption spectrum are shown in Figure VIII.4. Using an integrating sphere, it should be possible to obtain a more accurate absorption spectrum of β-carotene in its natural environment, tissue.

### VIII. A. 3. Data Acquired at the Cleveland Clinic Foundation

This study was carried out in collaboration with Drs. Crowe and Dawson at the Cleveland Clinic Foundation. All studies involving human tissue were approved by the Cleveland Clinic Foundation Institutional Review Board and the Massachusetts Institute of Technology Committee On the Use of Humans as Experimental Subjects. Informed consent was obtained from all subjects prior to the surgical procedures.

VIII. A. 3. a) Sample Preparation and Data Acquisition

Breast tissue was obtained from patients immediately following surgical lumpectomy or mastectomy procedures. Upon removal, the samples were sectioned per the normal pathology protocol and spectral data acquired in the pathology suite at CCF. Locations for data acquisition were chosen by the pathologist. Several sites were studied per patient (~3 to 4 depending on the size of the sample). Following spectral acquisition, specimens were marked with India ink to indicate the region sampled, and fixed in formalin. The fixed tissue samples were routinely processed, paraffin embedded, cut through the marked locations in 5 μm thick sections, and stained with H&E. The histological slides were examined by an experienced breast pathologist who was blinded to the outcome of the spectroscopy analysis.

Thirteen patients were examined corresponding to 6 FastEEM data sets from normal tissues, 11 from benign and 6 from malignant samples.

Reflectance and fluorescence spectra were obtained with an old version of FastEEM instrumentation [Zangaro *et al.* 1996]. A xenon flash lamp (EG&G Optoelectronics, FX-139, Salem, Massachusetts) was used as a white-light source to acquire reflectance spectra in the 360-700 nm range. Excitation light sources for fluorescence measurements were provided by a 337 nm wavelength nitrogen laser (Laser Science, Inc., Franklin, Massachusetts) and 10 different dye lasers (358 nm to 610 nm), sequentially pumped by the nitrogen laser. The dye cuvettes were mounted on a rotating wheel driven by a stepper motor. Light was delivered to the tissue and collected by means of a probe containing seven optical fibers (200 μm core diameter, 1 fiber used for light delivery and 6 for collection). At the distal tip the collection fibers surrounded the delivery fiber and were fused together, creating a quartz shield approximately 1.5 mm in diameter, which was beveled and then polished at a 17° angle to reduce internal reflections at the boundary between glass and tissue. During a measurement, the probe tip was brought into contact with the sample under investigation, thus providing a fixed light delivery collection geometry. A wheel of long-pass filters was used to prevent reflected laser excitation light from reaching the spectrograph (CP 200, Jobin Yvon SA, Edison, New Jersey) and the intensified diode array detector (EG&G Princeton Applied Research, Trenton, New Jersey). Fluorescence spectra at 11 excitation wavelengths and a reflectance spectrum were collected in less than 5 s. The incident laser light was sufficiently low in energy, ~400 $mJ/cm^2$, that no tissue damage was observed. The wavelength scale was calibrated with a mercury lamp. A concentrated barium sulfate suspension (concentration >20%) was used for reflectance calibration.

VIII. A. 3. b) Results

Figure VIII.5 shows examples of reflectance data, diffuse reflectance model fits, and fit parameters acquired in this study. In Figure VIII.6a raw fluorescence data of breast tissues at 342 nm excitation is shown. A clear trend in intensity can be seen with cancerous specimens having the highest fluorescence intensity and normal samples the lowest. A trend in lineshape can be seen in the intrinsic fluorescence spectra. Normalized intrinsic fluorescence spectra, averaged by pathology, are shown in Figure VIII.6b. The cancerous samples have the smallest FWHM and the normal samples

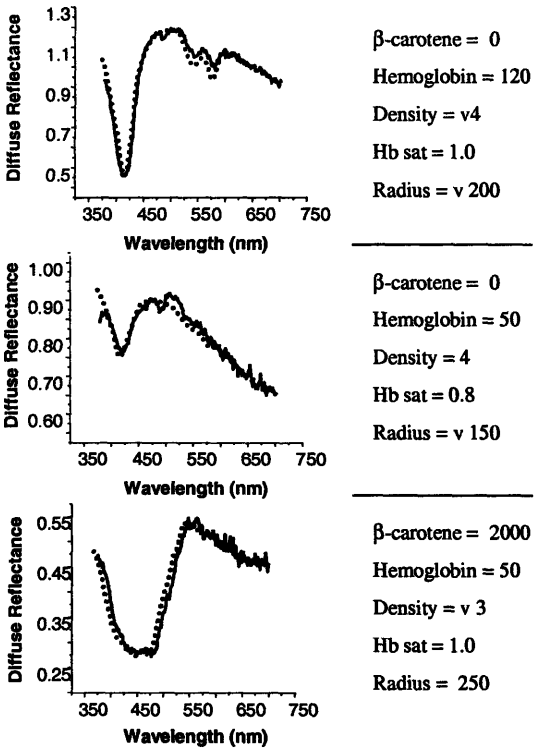


**Figure VIII.5.** Diffuse reflectance spectra of breast tissue.

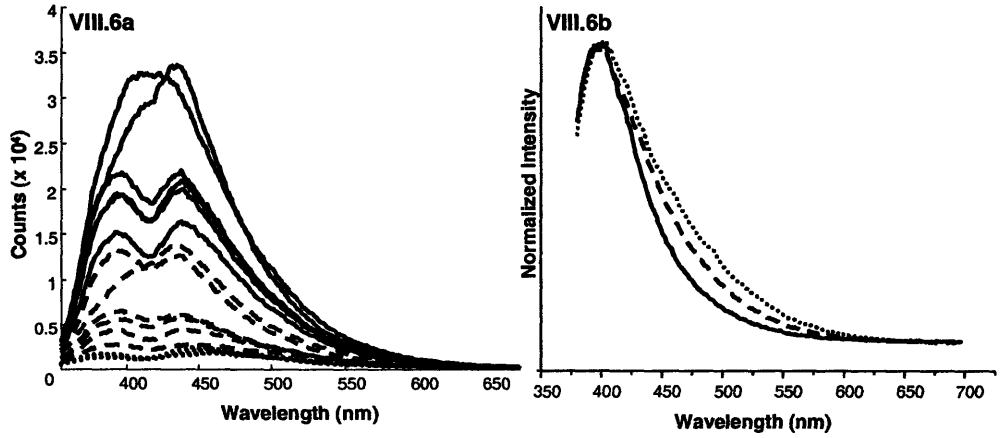


**Figure VIII.6.** a) Raw fluorescence spectra and b) normalized intrinsic fluorescence spectra of breast tissues at 342 nm excitation. Cancer (solid lines), Fibrocystic Change (dashed lines), Normal (dotted lines).

the largest. This is not consistent with previous fluorescence studies in our laboratory. In these studies, cancerous sample typically have the largest FWHM due to increased contributions from NADH. The discrepancy between previous studies and the fluorescence observed in breast is not surprising. Prior work using fluorescence to diagnose cancer has mainly examined dysplasia in epithelial tissues. NADH is observed in higher concentrations in dysplastic tissues, possibly as a result of an increase in epithelial thickness and/ or higher metabolic activity of the cells. In contrast to breast, studies of dysplastic tissues provide a well defined tissue architecture consisting of epithelial tissue overlaying stroma. Although tissue changes occur during dysplasia, the overall tissue architecture, epithelial cells overlying stroma, remains largely unchanged. This is in contrast to breast where samples may be composed of fat, collagen, a cellular tumor, or any combination of features.

### VIII. A. 4. Data Acquired at University Hospitals of Cleveland

This study was carried out in collaboration with Drs. Fitzmaurice, Shenk, and Wang at University Hospitals of Cleveland and Case Western Reserve University. All studies involving human tissue were approved by the University Hospitals of Cleveland and Case Western Reserve University Institutional Review Board and the Massachusetts Institute of Technology Committee On the Use of Humans as Experimental Subjects. Informed consent was obtained from all subjects prior to the surgical procedures.

#### VIII. A. 4. a) Sample Preparation and Data Acquisition

Breast tissue was obtained from patients immediately following surgical lumpectomy, re-excision or mastectomy procedures. Tissue was examined as detailed in section VIII.A.3a.

However, in this study a newer version of the FastEEM instrumentation was employed [Tunnell *et al.* 2003]. Further, two identical FastEEM data sets were acquired from each tissue location to assess measurement error. Raman spectra were also obtained from the same location as the fluorescence and reflectance data.

VIII. 4. b) Results

Preliminary data analysis is promising, indicating that fluorescence and diffuse reflectance not only contain diagnostic information, but may also be most accurate in differentiating pathologies where Raman is least accurate. Figure VIII.7a shows average IFS data from the pathologies encountered in this study. The trend in intensity seen in the CCF data is not recapitulated and no clear trend in intensity is observed. However, lineshape trends, as can be seen in Figure VIII.7b, are similar to those observed in the CCF data with normal samples having a larger FWHM than benign or IDC samples. DCIS, a pathology not encountered in the CCF studies, has the largest FWHM, potentially indicating an increase in NADH. The

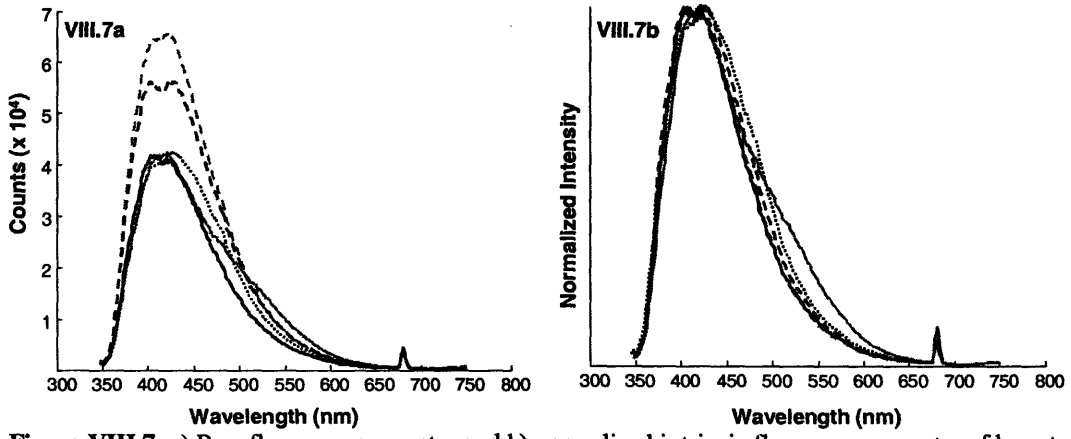


**Figure VIII.7.** a) Raw fluorescence spectra and b) normalized intrinsic fluorescence spectra of breast tissues at 342 nm excitation. IDC (solid black lines), DCIS (solid gray lines), Fibrocystic Change (dashed black lines), Fibroadenoma (dashed gray lines), Normal (dotted lines).

reason for these lineshape trends is currently not well understood.

The basis spectra, used to model the IFS data, were extracted using multiple curve resolution (MCR), an iterative statistical technique [Tauler *et al.* 1994]. The basis spectra obtained using MCR are though to represent NADH and collagen because they have similar, but not identical, lineshapes to spectra of commercially available NADH and collagen. The basis spectra extracted at 340 nm excitation are shown in Figure VIII.8. Also shown for comparison is a spectrum acquired from breast tissue. However, MCR provides no information as to the source of the basis spectra fluorescence. Further, MCR can generate erroneous results if the number of fluorophores present in the tissue, an input parameter, is guessed incorrectly. It is also possible that the basis spectra do indeed represent NADH and collagen and that the amount of NADH seen in normal samples is a consequence of large numbers of adipocytes. The literature should be examined to determine the relative amounts of NADH contained in adipocytes and epithelial cells in order to explore this possibility. Whether the trends observed for the tissue fluorophores are the result of inaccurate basis spectra, additional tissue fluorophores, or unexpected pathology requires further investigation.

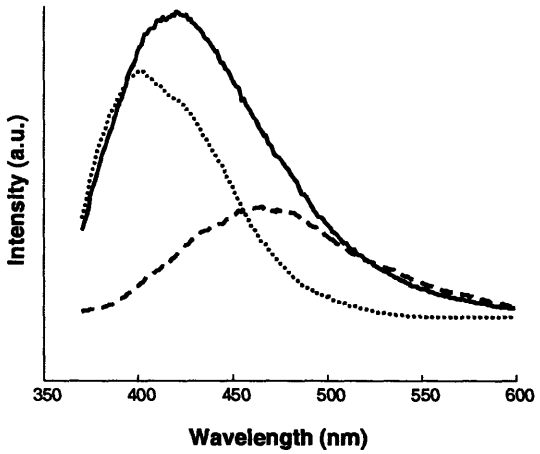

**Figure VIII.8.** Emission spectra of NADH (dashes) and collagen (dots) at 340 nm excitation. Also shown for comparison is a spectrum acquired from breast tissue (solid).

Figure VIII.9 displays the excellent separation obtained between fibroadenoma and cancerous specimens. The separation is based on a single parameter. The diagnostic parameter, A, is extracted from the diffuse reflectance fit. It represents the density of

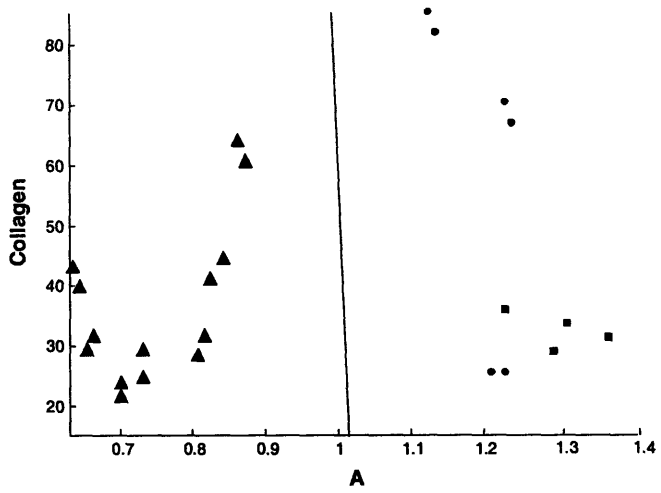


**Figure VIII.9.** Diagnostic plot showing the difference between benign and cancerous tissues. Fibroadenoma (triangles), IDC (squares) and DCIS (circles).

scatterers in the stroma. Two identical FastEEM data sets were acquired of each sample to assess measurement reproducibility. The parameters corresponding to both data sets are shown in Figure VIII.9 to provide insight into the error of the measurements. These diagnostic categories, cancer and fibroadenoma, pertain to the lowest sensitivities and specificities obtained with Raman spectroscopy. Sensitivities and specificities for distinguishing individual pathological categories using intrinsic fluorescence and diffuse reflectance data are displayed in Table VIII.1.

| Normal | Normal | Fibrocystic Change | Fibroadenoma | DCIS |
|---|---|---|---|---|
| Fibrocystic Change | A/β-Carotene Se=100% Sp=75% | | | |
| Fibroadenoma | NADH/β-Carotene Se=100% Sp=100% | A/Collagen Se=94% Sp=87% | | |
| DCIS | A/Collagen Se=100% Sp=100% | A/Hb Se=100% Sp=100% | A/Collagen Se=100% Sp=100% | |
| IDC | A/Collagen Se=100% Sp=100% | A/Hb Se=100% Sp=100% | A/Collagen Se=100% Sp=100% | A/NADH Se=100% Sp=100% |

**Table VIII.1.** Sensitivities and specificities for distinguishing individual pathological categories using IFS and DRS.

### VIII. A. 5. Future Directions

Preliminary results are very promising and convey that fluorescence and reflectance spectroscopies do contain diagnostic information. However, a significant amount of data analysis still remains. Additional cancerous samples must be examined as the algorithms currently only contain 5 malignant data points, 2 IDC and 3 DCIS. A comprehensive diagnostic algorithm must be developed which examines all data simultaneously. Further, there is currently little comprehension of the correlation between the tissue pathology and spectroscopic parameters. The tissue fluorophores and scatterers responsible for differentiation must be identified. Future analysis will also focus on correlating information obtained from FastEEM data and Raman spectroscopy. As a starting point, species that both approaches are sensitive too, such as collagen and β-carotene, can be compared. Ultimately, if the results warrant it, all three modalities (fluorescence, reflectance and Raman) may be combined into a single spectroscopic technique for the diagnosis of breast cancer.

## *VIII. B. Effects of Tissue Freeze-Thaw on Fluorescence and Reflectance*

In developing spectroscopic modalities for the *in vivo* detection of disease, it is often necessary to perform preliminary studies on excised tissue. However, unlike Raman spectroscopy, fluorescence and reflectance spectroscopies are very sensitive to the process of tissue excision and freezing. These processes can have profound effects on the spectroscopic properties of the tissue resulting in significant changes in intensity and lineshape relative to *in vivo* data. Given the frequent necessity of *ex vivo* measurements, it is crucial to understand the effects of tissue removal and freeze-thaw on fluorescence and reflectance data. Although

studies have been conducted which examine these effects, they did not account for distortions of the fluorescence spectra caused by tissue scattering and absorption [Palmer *et al.* 2002]. Accounting for absorption was particularly important in prior studies as they observed increased hemoglobin absorption in freeze-thaw tissues, possibly due to red blood cell lysis. Increased tissue absorption will concomitantly reduce the tissue fluorescence. Indeed less fluorescence was observed in the freeze-thaw samples. However, without correcting the fluorescence data for the effects of scattering and absorption, it is difficult to relate the observed changes to specific parameters. In other words, it is not clear if the decrease in fluorescence intensity resulted solely from increased absorption or if changes in intrinsic tissue fluorescence were also present. Our study examines normal rat esophagus and esophageal papillomas. Further, our analysis allows for disentangling the effects of scattering and absorption from tissue fluorescence.

### VIII. B. 1. Sample Preparation and Data Acquisition

In an effort to examine the effect of tissue removal and the freeze-thaw process on spectral features, a number of rat esophagi were examined as a function of time following tissue removal and pre- and post- tissue freezing. Data was collected with the FastEEM instrumentation described in section VIII.A.4 from both normal esophageal tissue and papillomas. After the removal of the esophagus, the tissue was examined in two ways. To assess the effect of excision, a spectrum was taken immediately following tissue removal, with periodic sampling every 10 min. for a total of 30 min. After 30 min. the intervals were lengthened to every half hour with a total monitoring period of 2 hours. To assess the effect of freeze-thaw, the esophagus was sampled immediately after removal and then snap-frozen

in liquid isopentane for a period of 20 min. after which the tissue sample was thawed and a second spectrum taken.

A rat model for human esophageal squamous cell carcinoma was investigated using DRS and IFS as an opportunity to examine the freeze-thaw process. Fisher 344 rats were injected with the carcinogen N-nitrosomethylbenzylamine (NMBA). Within 15-20 weeks visible polypoid tumors ("papillomas") developed, after proceeding through dysplastic stages characterized by cellular proliferation and keratinization.

## VIII. B. 2. Preliminary Results

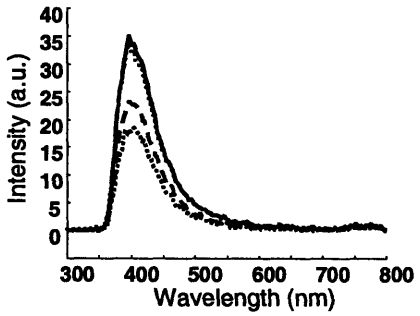


**Figure VIII.10.** Changes in intrinsic fluorescence of normal rat esophagus at 337 nm excitation 20 min. (solid line), 40 min. (dotted line), 60 min.(dashed line), and 80 min.(lower dotted line), following tissue excision.

A decrease in fluorescence intensity was observed as a function of time following tissue excision at all excitation wavelengths. Figure VIII.10 shows an example of the decrease observed at 337 nm excitation for a sample of normal rat esophagus. The magnitude of the intensity decrease varied between samples. No fluorescence lineshape changes occurred with time. The freeze-thaw process was found to cause both intensity and lineshape changes. Figure VIII.11 demonstrates a decrease in the fluorescence intensity at 337 nm excitation, resulting from the freeze-thaw process. Such a decrease was witnessed for all samples. Lineshape changes can also be seen in Figure VIII.11. These lineshape changes were particularly pronounced for esophageal papillomas. A large increase in porphyrin fluorescence was observed in fresh-frozen papillomas compared to that seen in the freshly

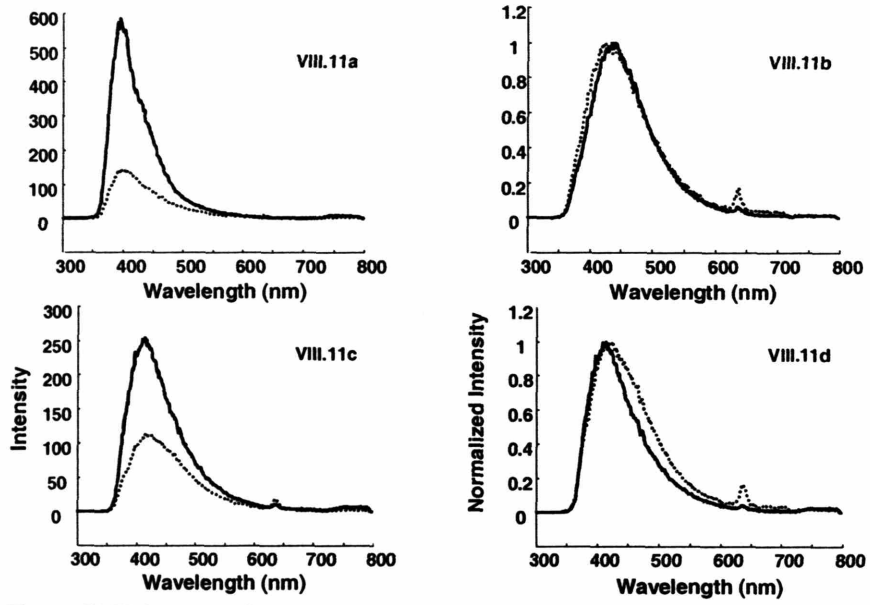


**Figure VIII.11.** Intrinsic fluorescence spectra at 337 nm excitation showing intensity and lineshape changes resulting from the freeze-thaw process in a & b) normal esophagus and c & d) an esophageal papilloma. Fresh tissue (solid line) Fresh-frozen tissue (dotted line)

excised tissue. An example of the increase in porphyrin fluorescence is shown in Figure VIII.12.

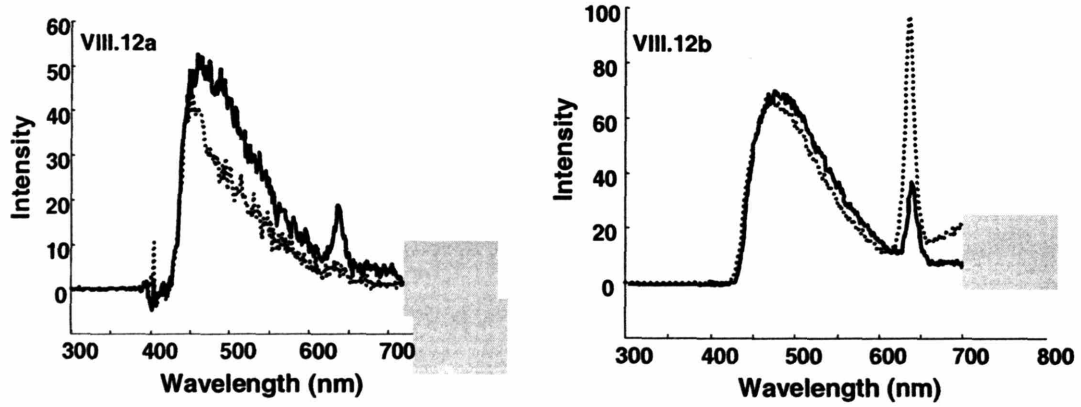


**Figure VIII.12.** Intrinsic fluorescence spectra at 412 nm excitation showing differing effects of the freeze-thaw process on porphyrin fluorescence in a) normal esophagus and b) an esophageal papilloma. Fresh tissue (solid line) Fresh-frozen tissue (dotted line)

The reflectance spectra also exhibited differences between fresh and fresh-frozen tissues. An increase in the oxygen saturation parameter is observed in the fresh-frozen

tissues. Absorption techniques are widely used for the purpose of evaluating tissue oxygenation and are the basis of pulse oxymetry [Takatani and Ling 1994]. The measurement relies on the slight change in the hemoglobin absorption spectrum with oxygenation. Oxy-hemoglobin has a strong absorption peak in the blue region at 415 nm and a smaller double peak at 542 nm and 577 nm, while deoxy-hemoglobin has a strong peak at 430 nm and a single smaller peak at 560 nm. The absorption spectra of oxy- and deoxy-hemoglobin are shown in Figure VIII.13a. Also shown are representative reflectance spectra and model fits of fresh and fresh-frozen tissue. Changes in the hemoglobin oxygen saturation for several different samples are included in Figure VIII.13 as a table. No significant increase in the amount of hemoglobin was observed following the freeze-thaw process, indicating that red blood cell lysis was minimal.

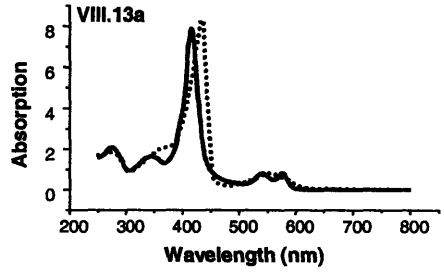


| Hemoglobin Oxygen Saturation Parameter | | |
|---|---|---|
| | *Ex vivo* | Freeze/Thaw |
| Sample 1 | 0.55 | 0.83 |
| Sample 2 | 0.53 | 0.50 |
| Sample 3 | 0.70 | 0.85 |
| Sample 4 | 0.48 | 0.70 |
| Sample 5 | 0.53 | 0.72 |

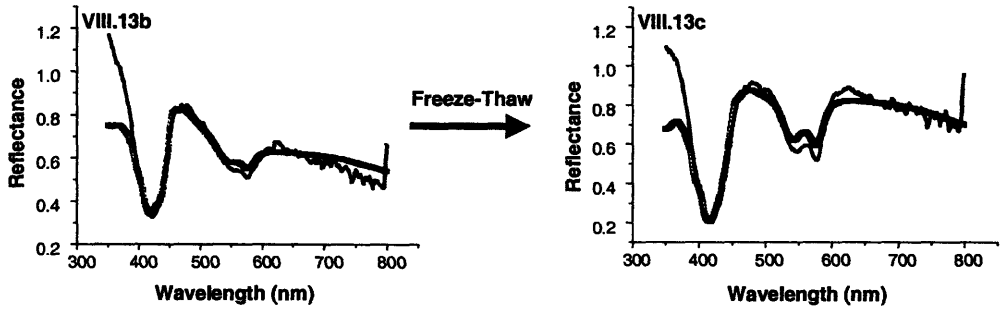


**Figure VIII.13.** Changes in the hemoglobin oxygen saturation induced by the freeze-thaw process. a) Absorption spectra of oxy- (solid line) and deoxy- (dotted line) hemoglobin. b) Diffuse reflectance spectrum (solid line) and model fit (dotted line) of freshly excised tissue and c) fresh-frozen tissue. Also shown are the changes in the hemoglobin oxygen saturation for several different samples.

From these studies, we can conclude that the effects of tissue removal are minimal within a time period of 1.5 hrs. Although changes in intensity occur with tissue excision, we do not observe changes in lineshape or reflectance. However, the freeze-thaw process results in significant differences in both the diffuse reflectance and the intrinsic fluorescence. Consequently, data acquired shortly after tissue excision should accurately mimic an *in vivo* environment while studies on fresh-frozen tissues are not appropriate for extension to clinical data.

## *VIII. C. Fluorescence Lifetime Measurements*

Most *in vivo* fluorescence spectroscopy studies to date have focused on monitoring the steady-state intensity of fluorescence emitted at one or more wavelengths (i.e. the fluorescence induced by constant excitation light). An alternative approach measures the time-resolved fluorescence (the time-decay of the fluorescence excited by a short pulse). Typically, this time-decay is typically on the order of nanoseconds. The method is technically more demanding than steady-state measurements, as it requires the use of a very short excitation pulse and special detectors. However, the time dependence of fluorescence emission can be very sensitive to changes in the environment of the fluorescent species. Furthermore, as time-resolved measurements are unaffected by tissue elastic scattering and absorption, they can provide diagnostic information that might otherwise be convoluted when measured with steady-state fluorescence.

### VIII. C. 1. Sample Preparation and Data Acquisition

Picosecond fluorescence spectra were obtained with the laser system, shown in Figure VIII.14. Excitation wavelengths from 250 nm to 360 nm and 450 nm to 750 nm were available. Most studies presented here employed 330 nm excitation light. The pulse length was 150 fs FWHM however the temporal resolution was limited by the streak camera detection limit of 10 ps. A spot size of 5 mm was used with an average pulse power of <1 mJ per pulse and a repetition rate of 1 KHz. No photobleaching was observed on the samples examined. Average data acquisition times were on the order of 15 min.

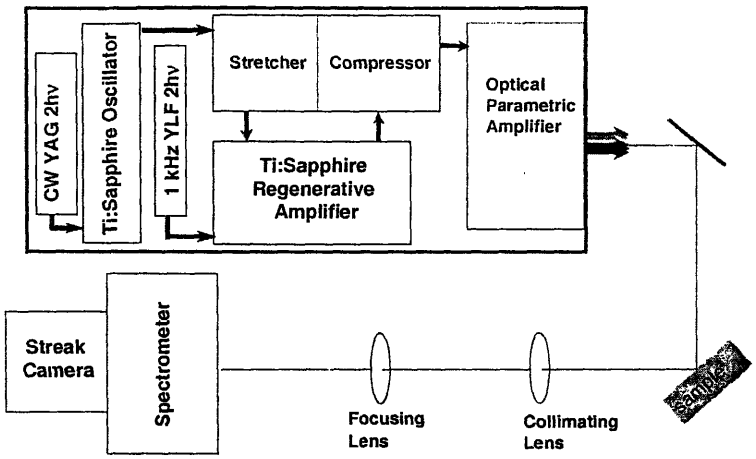


**Figure IIIV.14.** Laser System for Picosecond Spectroscopy

## VIII. C. 2. Preliminary Results

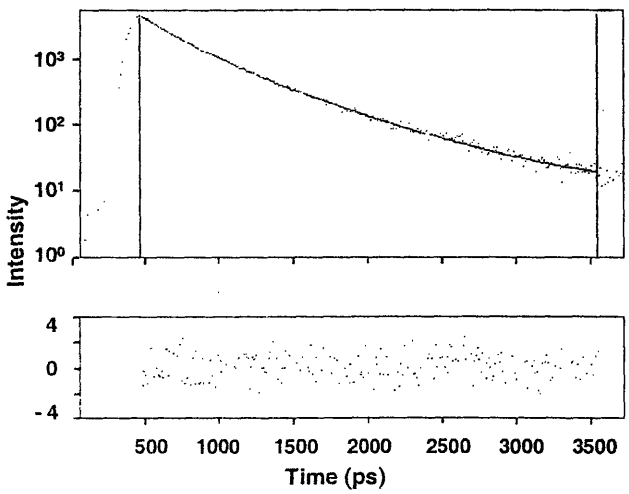


**Figure IIIV.15.** Fluorescence Decay of NADH in PBS: Two Component Fit and Residual

To begin our studies we examined the time-decay spectra of two biological moieties often encountered in our steady-state fluorescence work, NADH and collagen. Data were acquired from NADH in solution. NADH has

two decay times, resulting from different conformations, 240 ps and 550 ps [Couprie *et al.* 1994]. Our data, shown in Figure VIII.15, exhibits excellent agreement with the literature values. We extracted lifetimes of 243 ps and 547 ps. This two component fit corresponded to a $\chi^2$ value of 1.08. We also examined the decay properties of collagen. Commercially available collagen is powdered while collagen is present in the body in a hydrated form. We examined type I collagen in both powered form and as a hydrated collagen gel. A three component fit was necessary to describe the data. Differences in lifetimes were found as a function of environment. Powdered collagen had decay times of 798 ps, 3.54 ns and 10.03 ns, while the collagen get had shorter lifetimes of 442 ps, 2.06 ns and 6.57 ns. $\chi^2$ values were slightly higher for the data acquired from collagen, 1.1 to 1.2, but still good.

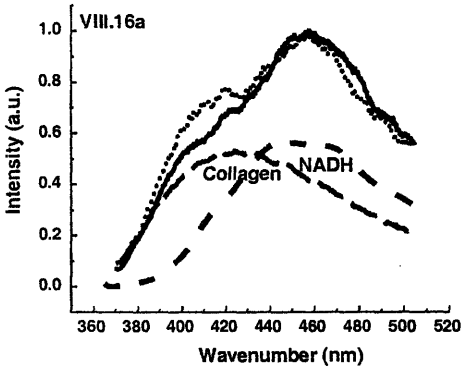


**Figure VIII.16.** Fluorescence time-decay data of cervical tissue. a) Fluorescence lineshape variations as a function of decay time. 100 ps (solid line) 5.7 ns (dotted line). The steady state spectra of collagen and NADH are included for comparison (dashed lines). Also shown are decay rates and their relative amplitudes in spectral regions corresponding to b) collagen and c) NADH.

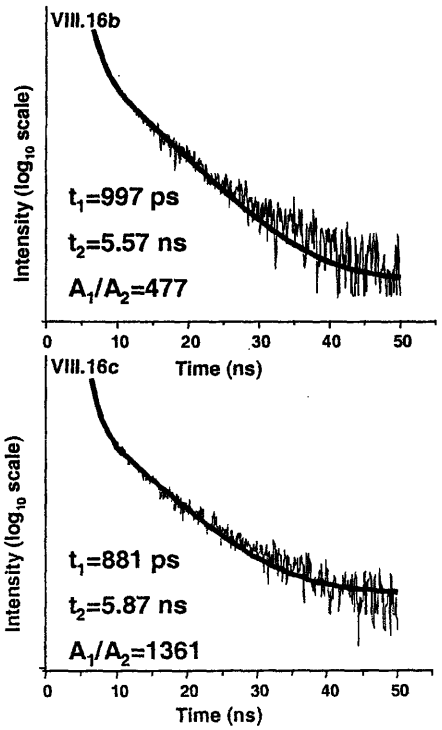


We also examined the fluorescence time-decay properties of cervical tissue. Fluorescence lineshape changes were observed as a function of time. These lineshape changes, shown in Figure VIII.16a, are consistent with a faster decay for

NADH. Decays from two different spectral regions, known to correspond predominately to NADH and collagen fluorescence, were examined. The decay with dominant contributions from collagen fluorescence was obtained by averaging the spectral range from 400 nm to 415 nm and is shown in Figure VIII.16b. Lifetimes found in this spectral region were 997 ps and 5.57 ns with a relative amplitude ratio of 477. In the spectral region from 450 nm to 465 nm, indicative of NADH, comparable lifetimes of 881 ps and 5.87 ns were obtained. However, in this spectral region, shown in Figure VIII.16c, the relative amplitude ratio was 1361. This is indicates a larger contribution from the shorter lifetime decay in the spectral region dominated by NADH fluorescence. The lineshape changes and decay analysis of different spectral ranges are consistent and allow us to conclude that NADH has the faster decay rate and collagen the slower. It is notable that extension of the results from pure component chemicals to tissue was not straightforward. Further studies are necessary to confirm these findings. Also, lifetime variations between tissue types must be examined within a single tissue type and between normal and diseased tissues.

## *VIII. D. Surface Enhanced Raman Scattering*

A great disadvantage of Raman spectroscopy results from the extremely small scattering cross-section of the Raman process. Surface enhanced Raman scattering (SERS) is a spectroscopic technique that results in strongly increased Raman signals when molecules are attached to nanometer-sized gold or silver structures. The effect provides the structural information content of Raman spectroscopy together with ultrasensitive detection limits. Further, since SERS occurs in the local fields of metallic nanostructures, the lateral resolution is determined by the confinement of the local fields and can be orders of

magnitude better than the diffraction limit. Another advantage of SERS is that the fluorescence background, which often complicates the accurate analysis of Raman spectra, is quenched by nonradiative decay channels provided by the metallic nanostructure. For theses reasons, SERS has the possibility to greatly advance biomedical Raman spectroscopy. To this end, we have begun an investigation of SERS of both cells and tissues.

### VIII. D. 1. SERS Cell Studies

Within the recent decade, Raman spectroscopy was successfully applied to living cells [Puppels *et al.* 1990; Peticolas *et al.* 1996; Otto *et al.* 1997; Sijtesema *et al.* 1998, 2000; Feofanov *et al.* 2000; Shafer-Peltier *et al.* 2002]. Measurements on cell monolayers using confocal Raman systems show clear differences in the Raman spectra of the cell nucleus and the cell cytoplasm. Excellent Raman spectra of DNA in the nucleus of a living cell can be obtained using a laser Raman microscope, where the sample is inside the laser cavity [Patapoff *et al.* 1988; Peticolas *et al.* 1990].

Raman scattering is an inefficient effect, with typical non-resonant Raman scattering cross-sections on the order of $10^{-30}$ $cm^2$ per molecule. Typical collection times for a spontaneous Raman spectrum of a living cell (using 5-10 mW laser excitation and a confocal Raman system) can be hundreds of seconds. This results in very long data acquisition times to generate a "Raman map" of a cell [Shafter-Peltier *et al.* 2002], Further, many chemicals are present in a cell at very low concentrations and the excitation laser intensity is limited by effects of cell degeneration, the Raman signal observed from a single cell is extremely weak. Thus it is difficult to study viable cell lines.

In SERS, Raman signals can be enhanced by many orders of magnitude. SERS

occurs when the probed molecules are attached to metallic nanostructures. Raman scattering takes place in the high local optical fields of these nanostructures [Otto *et al.* 1984; Moskovits 1985; Campion and Kambhampati 1998; Kneipp *et al.* 1999]. Areas of enhanced local optical fields occur due to resonances of the applied optical fields with the surface plasmon oscillations of the metallic nanostructures. In addition to this "electromagnetic field enhancement," the electronic interaction between the Raman molecule and the metal can result in an increase of the Raman scattering cross-section itself, called "chemical or electronic enhancement". In the visible and NIR frequency range, silver and gold colloidal clusters or island films of these materials can result in electromagnetic SERS enhancement factors up to 10 to 12 orders of magnitude [Kneipp *et al.* 1995, 1997, 1998].

The field enhancement effect is also operative in fluorescence. Although the effect of surface-enhanced fluorescence has been observed for a few molecules, in many cases, the metal provides strong nonradiative decay channels [Weitz *et al.* 1983; Sokolov *et al.* 1998]. This fluorescence quenching effect can compensate for the field enhancement, resulting in a net fluorescence signal much smaller than that measured without the metal. That explains why in many experiments the surface enhanced resonance Raman (SERRS) spectrum does not show the expected fluorescence background [Bachackashvilli *et al.* 1983, 1984; Kneipp *et al.* 1983; Pettinger 1984].

SERS studies have also been performed on living cells [Manfait *et al.* 1990, 1992; Nabiev *et al.* 1991; Morjani *et al.* 1993]. In these experiments, colloidal silver particles were incorporated inside the cells and SERS was applied to monitor the intracellular distribution of drugs. Surprisingly, these experiments show SERS spectra of the drug but no SERS spectra of the native cell constituents themselves were detected.

In general, due to its chemical inactivity, gold is the more suitable metal for incorporation inside living cells. It has been shown that gold colloidal clusters have SERS enhancement factors comparable to silver clusters when NIR excitation is applied [Kneipp *et al.* 1993]. Moreover, NIR is the desired excitation range for Raman measurements of cells since the lower energy photons reduce the fluorescence background in biological samples and also the risk of cell damage [Hanlon *et al.* 2000; Shafter-Peltier *et al.* 2002].

In this study we report NIR SERS studies of living cells using colloidal gold as the SERS active substrate [Kneipp *et al.* 2002]. In contrast to previous SERS studies using colloidal silver, we measure strong SERS signals from the native chemical constituents of the cell. Thus, this work provides a tool for the sensitive detection of native chemicals inside a cell as well as their intracellular distribution, suggesting many applications in biomedical research.

VIII. D. 1. a) Cell Preparation

Differentiated intestinal epithelial cells HT29 (gift of the Harvard Digestive Diseases Center) were grown on 25 mm round coverglasses for SERS measurements and on formvar-carbon coated grids for electron microscopy studies. Cells were grown with Dulbecco's high-glucose modified Eagle medium (DMEM) supplemented with 10% fetal calf serum, 100 units/ml penicillin and 100 μg/ml streptomycin (Gibco BRL, Life Technologies, Grand Island, NY). Cells were grown to confluency at 37° C in a humidified atmosphere of 5% $CO_2$ in air. Monolayers were loaded with colloidal gold by fluid-phase uptake. Approximately 24 hours prior to data collection, the culture medium was supplemented with the colloidal gold suspension either at either ~3,300 particles/cell or ~330 particles/cell.

Immediately before the experiments, free gold was removed by rinsing the monolayers in Hank's Balanced Salt Solution (HBSS) without sodium bicarbonate or phenol red, buffered at pH 7.4 with 10 mM HEPES (Sigma, St. Louis, MO). Cells remained in the same buffer throughout the measurements. The salts in the buffer solution induce the formation of small colloidal aggregates with sizes of a few hundred nanometers. Cluster-cluster aggregation inside the cell results in the formation of larger gold colloidal clusters, discussed further below.

VIII. D. 1. b) SERS Measurements and Data Processing

Raman measurements were carried out on single cells using the confocal microscope, discussed in Chapter III. 830 nm excitation and a spot size of ~1 μm were employed. Application of 2 to 5 mW NIR excitation did not result in any cell damage. Good SNR SERS spectra were measured with a 1 s. collection time. For mapping experiments, the cell monolayer was moved in 1 μm steps under the laser focus, covering a total area of 30 x 30 μm.

VIII. D. 1. c) Results

Figure VIII.17 shows examples of unprocessed SERS spectra measured at different places on the cell monolayer incubated with colloidal gold. The spectra acquired in 1 s. show a very good SNR

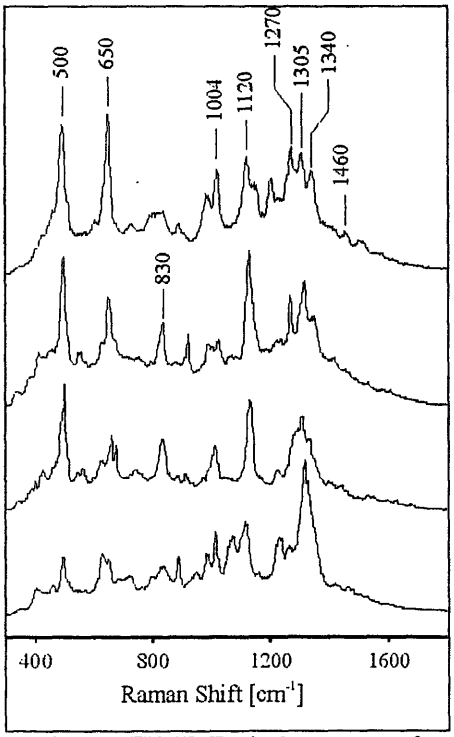


**Figure VIII.17.** Typical unprocessed surface enhanced Raman spectra.

allowing for the possibility of much shorter collection times. The SERS signal appears on the order of thousands of counts per second compared to signals of counts per second measured in "normal" Raman spectroscopy of single cells.

In general, all 900 spectra measured at different locations within the cells are distinct. The variety of lineshapes, relative Raman amplitudes and Raman line widths observed indicate a sensitive means to measure the inhomogenity of a cell. The Raman lines can be assigned to native chemical constituents in the cell nucleus and cytoplasm, such as DNA, RNA, phenylalanine, and tyrosine. The 1120 $cm^{-1}$ line is characteristic of an O-P-O DNA backbone vibration [Puppels *et al.* 1990; Peticolas *et al.* 1996]. Raman lines around 1300 $cm^{-1}$ are related to adenine and guanine vibrations, however, RNA also has strong SERS bands in this frequency region [Kneipp *et al.* 1991]. The spectral region around 1000 $cm^{-1}$ may result from phenylalaline at 1004 $cm^{-1}$ and a C-O DNA backbone vibration at 980 $cm^{-1}$. The bands at about 830 $cm^{-1}$ are likely due to a sugar-phosphate backbone vibration. The frequency of these bands is slightly different for B- and A-forms of DNA [Peticolas *et al.* 1996]. The absence of a strong SERS line at 735 $cm^{-1}$, which arises from the adenine ring breathing mode, indicates that native, and not denatured, DNA contributes to the spectra [Kneipp and Flemming 1986; Chumanov and Cotton 1999]. SERS spectra also show the conformationally sensitive guanine lines around 650 and 670 $cm^{-1}$ [Peticolas *et al.* 1996].

The spectrum in Figure VIII.17a exhibits a strong SERS line at 650 $cm^{-1}$. This peak is likely a guanine vibration superposed with a strong tyrosine vibration and thus also not indicative of DNA denaturation [Peticolas *et al.* 1996]. In contrast to "normal" Raman spectra of living cells, where strong Raman bands appear around 1450 $cm^{-1}$ (protein CH deformation vibration) and at 1650 $cm^{-1}$ (Amide I), in the SERS spectra these bands exhibit

almost no enhancement. In a few spectra, a very weak SERS band appears at about 1450 $cm^{-1}$.

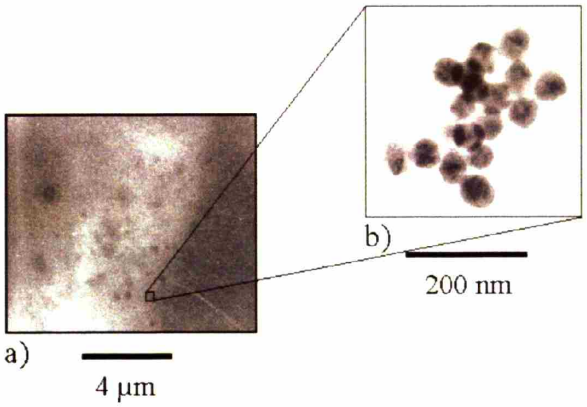


**Figure VIII.18.** Electron micrographs of colloidal gold particles inside a cell monolayer.

Figure VIII.18 displays electron micrographs showing the distribution of colloidal gold particles inside a cell monolayer. The colloidal particles form small colloidal clusters between 100 nm and a few microns in size. The largest clusters can also be seen in the phase contrast microscope views in Figure VIII.19. The higher magnification image, shown in Figure VIII.18b, demonstrates that the gold clusters are made of 60 nm colloidal gold spheres. Extension from NIR SERS experiments performed on DNA attached to similar gold colloidal cluster, allows us to infer a minimum enhancement factors of $10^3$ – $10^4$ for DNA [Kneipp and Flemming 1986]. This estimate is based on the assumption that all DNA molecules contribute to the SERS signal.

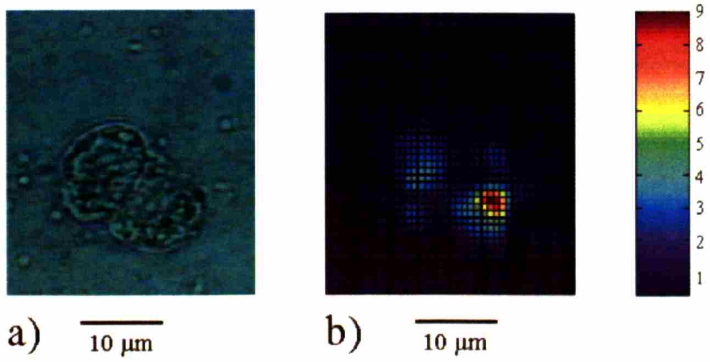


**Figure VIII.19.** a) Phase contrast image of two living cells and b) the image of the total SERS signal.

Figure VIII.19 shows a phase contrast image of two living cells and the Raman map acquired from these cells. The image was created by summing the total Raman

signal obtained at each location. The image shows that the SERS signal does not appear over the entire cell and that parts of the cell show no Raman signal. Since it is unlikely that there are regions of the cell that do not contain Raman scatterers, it follows that the lack of a SERS signal results from the absence of a colloidal gold particle. Variations in the signal strength in the "SERS-active" or gold occupied cell regions may be due to a non uniform electromagnetic SERS enhancement factor within the cell or may reflect a very inhomogeneous distribution of the scattering substance inside the cell.

In order to image the distribution of a particular substance using SERS, the signal of a Raman line resulting from that substance must be normalized to the SERS enhancement factor operative at each location. The SERS features appear on a broad background, which we ascribe to surface-enhanced fluorescence signals from the cell. The lateral distribution of the broad surface-enhanced fluorescence signal (with contributions from many fluorophores) should roughly monitor the distribution of the field enhancement. Therefore, the signals are normalized to the average fluorescence signal between 400 and 1700 $cm^{-1}$.

Example of SERS mapping, Figures VIII.20a and VIII.20b, show the distribution of phenylalanine and DNA over a 30x30 $\mu m^2$ cell monolayer based on the areas of the 1004 $cm^{-1}$ Phe- and

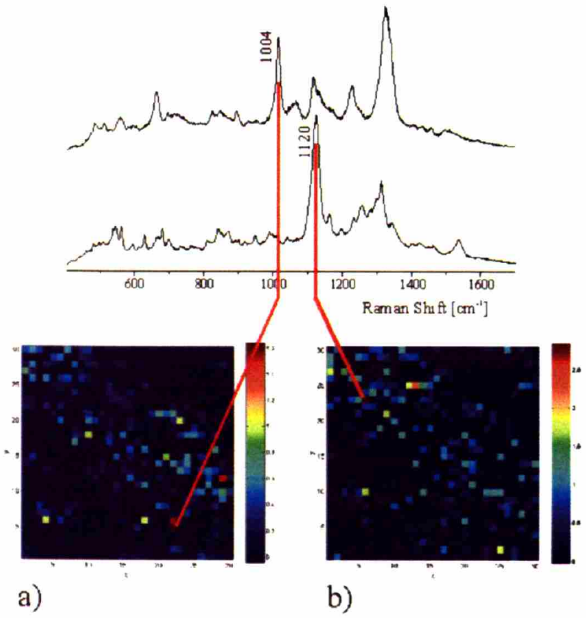


**Figure VIII.20.** Distribution of a) phenylalanine and b) DNA over a 30x30$\mu m^2$ cell monolayer. SERS spectra represent locations of the maximum signals of the two modes used to generate the Raman maps.

1120 $cm^{-1}$ O-P-O DNA backbone peaks, respectively. Also shown in Figure VIII.20 are SERS spectra taken from regions of high intensity in each map. In general, the cell nucleus should contain a larger amount of DNA, whereas phenylalanin should be present mainly in the cytoplasm [Pupples *et al.* 1990; Shafter-Peltier *et al.* 2002].

Figure VIII.20 demonstrates the feasibility of using SERS for generating Raman images. The strongly enhanced Raman signals allow one to generate a surface-enhanced Raman map of a cell (approximately 15x15 $\mu$m) with 1 $\mu$m lateral resolution in about 5 minutes (1 s. per mapping point) using 2 to 5 mW NIR excitation. It should be noted, that these first SERS images are "qualitative". The Raman signal appears as a superposition of the concentration of the Raman molecule and SERS enhancement factor. At present, the normalization scheme accounts for the electromagnetic SERS enhancement. For further development of this technique, nanotechnologies should be explored which generate a uniform distribution of the SERS-active nanostructures over the cell and show only a weak substance-specific chemical SERS enhancement.

To summarize, we have demonstrated the feasibility of measuring SERS spectra of native constituents within a single viable cell and generating a SERS map showing the distribution of specific chemicals within the cell. A SERS spectrum provides rich chemical information about the cell and allows observation of small structural modifications. Moreover, the strong Raman signals allow Raman mapping over single cells in very short times compared to normal Raman measurements. Ultrasensitive Raman spectroscopy inside living cells opens up exciting opportunities for the diagnosis of diseases at a very early stage. It may allow the detection of subcellular chemical changes that are the precursors of larger

morphological changes. In this way, exciting opportunities are opened up for the diagnosis of diseases to be made at very earlier stages.

### VIII. D. 2. SERS Tissue Studies

We have also conducted preliminary investigations of SERS with tissue. Both homogenized and thin slices of tissue were examined using the confocal Raman microscope. Figure VIII.21 shows a SERS spectrum obtained from a sample of homogenized breast tissue. Samples were prepared by spreading homogenized tissue mixed with nanoparticle solution onto an $MgF_2$ flat for microscopy. The spectrum, displayed in Figure VIII.21, was collected in 1 s. with very low levels of laser power (>5 mW). It exhibits a large number of sharp Raman peaks indicating high information content. SERS opens the possibility to examine chemicals present in very low concentrations in the tissue. However, identification of the species responsible for these peaks is challenging.

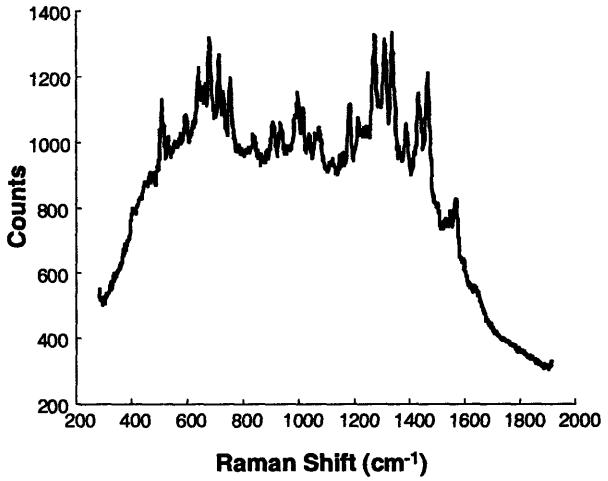


**Figure VIII.21.** SERS spectrum of homogenized breast tissue.

The distribution of chemicals within a tissue can rapidly be probed using SERS. Figure VIII.22 is a SERS map of a thin section of breast tissue. Nanoparticles were applied to the sample by allowing the colloid solution to evaporate from the tissue surface. The nanoparticles form small colloidal clusters, which can be seen in the phase contrast image shown in Figure VIII.22a. The SERS map, displayed in Figure VIII.22b, was generating by

plotting the area under the Raman spectrum acquired at each location. Regions of high SERS intensities correlate well with the colloidal clusters seen in the phase contrast image. SERS spectra obtained from regions of high intensity on the map are shown in Figure VIII.22c. By

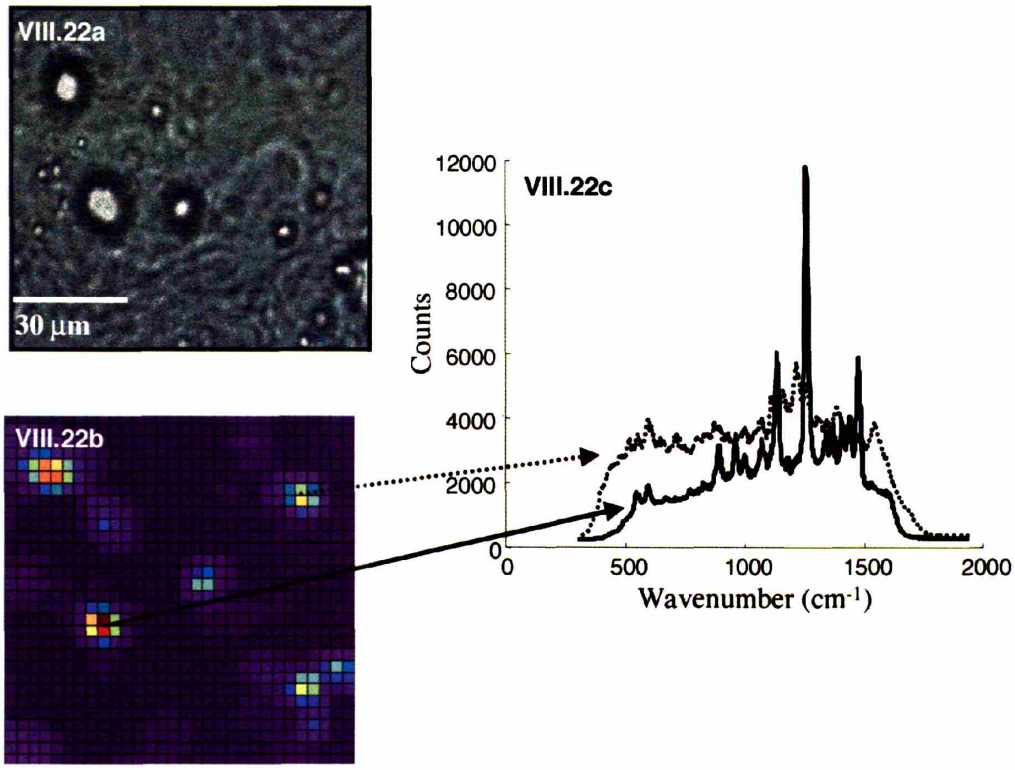


**Figure VIII.22.** SERS map of breast tissue.

utilizing nanotechnology techniques, such as period particle arrays, a uniform distribution of nanoparticles can be achieved thereby providing chemical information at regular intervals across the tissue sample.

During our preliminary investigations into SERS of tissue, we noted unusual spectral behavior. Occasionally, while focusing the microscope to obtain maximum signal, the spectral lineshape would exhibit time dependent fluctuations. An example of such behavior can be seen in SERS spectra of carotid artery. Each of the 4 spectra in Figure VIII.23 was integrated for 1 s. and the spectra were collected sequentially with no change in focus.

Raman peaks grow in size, appear and disappear with time. The cause of these time dependant fluctuations is not known. It may be suggestive of single molecule dynamics as moieties move in and out of the nanoparticle zone of enhancement. Such time dependent fluctuations were also observed in the SERS cells study discussed above.

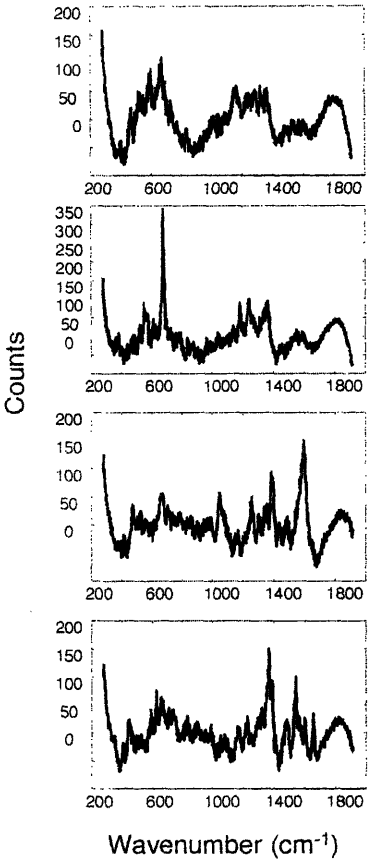


**Figure VIII.23.** SERS spectra of carotid artery exhibiting time dependent fluctuations.

## *VIII. E. Mechanism of Ceroid Formation in Atherosclerotic Plaques: Studies Using a Combination of Raman and Fluorescence Spectroscopy*

Accumulation of the insoluble lipid-protein complex, ceroid, is a characteristic of atherosclerotic plaques. The mechanism of ceroid formation has been extensively studied as the complex is postulated to cause cell injury and necrosis ultimately resulting in plaque irreversibility. Despite intensive research, ceroid is only defined empirically through its fluorescence properties and its behavior during various staining processes, while its precise chemical composition remains unknown. By using our combined Raman and fluorescence microscopy system we have examined the chemical composition of ceroid deposits *in situ* in aorta and coronary artery atherosclerosis. The synergy of these two types of spectroscopy allows for the identification of ceroid *via* its fluorescence signature and the subsequent

elucidation of its chemical composition through the acquisition of a Raman spectrum. Analysis of the Raman spectra from numerous ceroid deposits demonstrates that several different mechanisms contribute to its formation *in vivo*. Data indicate that the primary mode of lipid peroxidation resulting in the production of ceroid occurs through a Fenton reaction while the principal method of protein modification is direct oxidation of amino acids. Furthermore, we compare the chemical composition of intracellular and extracellular ceroid deposits thereby providing a timeframe for the order of chemical reactions which ultimately result in ceroid deposition within atherosclerotic plaques.

### VIII. E. 1. Introduction

It has been suggested that the progression of a fatty streak to an advanced atherosclerotic lesion with necrosis results from toxic products of lipid oxidation produced by macrophages. Incubation of macrophages with oxidized low density lipoprotein (oxLDL) has been shown to induce lipid loading [Steinbrecher *et al.* 1990; Witztum and Steinberg 1991]. Ultimately, most of this lipid is contained within the macropahge lysosomes, primarily in the form of the lipid-protein complex called ceroid [Ball *et al.* 1986]. Ceroid is thought to have detergent properties, which dissolve the foam cell membrane leading to extravasation of the complex into the extracellular space and eventually permanent tissue damage. Ceroid is described as a golden yellow, granular or globular, lipoid pigment. It is histochemically identified by insolubility in a variety of lipid solvents and stainability with lipid dyes [Hartroft and Porta 1965; Porta and Hartroft 1969; Wolman 1980; Pearse 1985]. In addition, ceroid is characterized by the emission of intense yellow autofluorescence when it is excited with ultraviolet (UV) light [Mitchinson *et al.* 1985; Fitzmaurice *et al.* 1989; Verbunt *et al.* 1992].

This definition, however, provides no information as to the origin or definitive chemical nature of ceroid.

Pappenheimer and Victor were the first to report the presence of ceroid in atherosclerotic plaques [Pappenheimer and Victor 1946]. Since then, several reports have described its prevalence in the full spectrum of atherosclerotic lesions [Burt 1952; Hartroft 1953; Slater and Smith 1972; Mitchinson 1982]. Ceroid is not found in normal vessels or thrombi. In small uncomplicated plaques, it initially appears within the cytoplasm of superficial macrophage-like foam cells and is rarely associated with smooth-muscle cells or endothelial cells. It has therefore been suggested that macrophages might be responsible for ceroid accumulation in the plaque, with potentially damaging consequences, such as cell injury, necrosis, and the release of insoluble material into the extracellular space, ultimately causing the plaque to become irreversible. In accordance with this theory, most of the ceroid in advanced plaques is extracellular appearing as solid granules or ring structures in the necrotic base.

Detection of ceroid has proven to be diagnostic of atherosclerotic disease using both standard histopathology and fluorescence spectroscopy. Additionally, several reports suggest that there is a correlation between the amount of ceroid present and the severity of an atherosclerotic lesion [Burt 1952; Slater and Smith 1972]. However, relatively little is known of the chemical composition of ceroid deposits and their role in the progression of atherosclerosis. This is primarily because ceroid is insoluble in organic solvents and cannot be extracted from the plaques and purified for chemical analysis.

Although the definitive mechanisms leading to the production of ceroid are unknown, several routes of formation have been proposed based on biochemical studies, *in vitro* cell

culture experiments, and animal models. These investigations have established that modification of proteins during lipid peroxidation produces fluorescence similar to that observed *in situ* in atherosclerotic lesions and attributed to the presence of ceroid [Kikugawa and Beppu 1987]. Further, experiments in which homogenized tissue or macrophages are exposed to conditions that promote lipid peroxidation witness an increase in the overall fluorescence of the sample consistent with the fluorescence observed in samples containing ceroid [Tsuchida *et al.* 1985; Esterbauer *et al.* 1986; Hoff *et al.* 1992; Nilsson and Yin 1997]]. As a result, protein modifications ensuing during lipid peroxidation have been intensely investigated and implicated in the formation and deposition of ceroid. Mechanistic insight into ceroid formation is further complicated by the wide variety of fluorophores which emulate ceroid fluorescence and can be produced in different *in vitro* model systems using biological materials as substrates. Based on such studies, copious routes of ceroid formation have been proposed [Yin 1996]. In this manuscript, we investigate the presence of chemical moieties from several of these potential routes of formation in ceroid deposits in human aorta and coronary artery.

The majority of experiments which strive to identify the principal route of formation of ceroid focus on modifications of low density lipoprotein (LDL) as clinically, elevated serum LDL levels predict risk of coronary artery atherosclerosis, while elevations of very low density lipoprotein (VLDL) and high density lipoprotein (HDL) levels do not. The Fenton reaction is one of the earliest proposed and most broadly accepted mechanisms of ceroid formation [Dillard and Tappel 1971]. In this schema, hydrogen peroxide, produced by the electron transport chain of mitochondria, forms a hydroxyl radical in the presence of ferrous iron. The highly reactive hydroxyl radical is postulated to peroxidize the

polyunsaturated fatty acids (PUFAs) associated with LDL. Thus, iron and oxygen free radical related peroxidation of LDL may occur inside lysosomes resulting in the formation of cross linked biocomplexes that are undegradable and thought to be ceroid. Also formed during this reaction are lipid hydroperoxides and cyclic peroxides which further decompose into various saturated or unsaturated carbonyl compounds, mainly aldehydes. These reactive aldehydes, such as malondialdehyde and 4-hydroxynonenal, produce fluorescent compounds which exhibit fluorescence characteristic of ceroid [Chio and Tappel 1969; Esterbauer *et al.* 1986].

Further support for this pathway is derived from examining the distribution of iron *in vivo*. Heavy metals such as iron have been found in the lysosomes of most cells as a consequence of normal autophagocytic degradation of metalloproteins [Vatassery *et al.* 1989; Brunk *et al.* 1992]. This mechanism is particularly appealing in the case of atherosclerosis as macrophages may become iron enriched during the phagocytosis of red blood cells or cell debris. Additionally, colocalization of ceroid and iron has been histologically demonstrated [Lee *et al.* 1998]. However, controversy concerning the feasibility of this mechanism *in vivo* stems from the weak prooxidant nature of the ferrous ion. Further, for this mechanism to proceed at a reasonable rate, iron must be present in its reduced form [Dunford 1987]. Conditions capable of converting the ferric ion to its active reduced form are speculative and direct oxidation of pure lipids by iron has not been demonstrated under physiologically relevant conditions.

As a consequence of concerns with the physiological plausibility of the Fenton reaction, studies have focused on alternative pathways of lipoprotein modification. When serum LDL is metabolized by foam cells, the apoproteins are first removed by proteolytic

enzymes, the cholesterol esters are then degraded into free fatty acids and free cholesterol. Free cholesterol is toxic to the foam cells, and is either exported from the cells or detoxified by re-esterification into cholesterol esters. The accumulation of free cholesterol eventually causes the foam cells to lyse thus releasing free fatty acids, free cholesterol, cholesterol esters, phospholipids, and enzymes, such as myeloperoxidase, into the extracellular space. Hypochlorite, a two-electron oxidant produced by myeloperoxidase, generates a high uptake form of LDL primarily by oxidizing the protein component [Hazel and Stocker 1993]. The peroxidation of LDL produces, among other things, HOOA and HODA, two molecules reported to have similar fluorescence properties to ceroid. Other protein oxidation products, such as dityrosine, the oxidation product of tyrosine, have also been suggested as possible sources of ceroid fluorescence [Amado *et al.* 1984].

Whereas the majority of mechanistic studies examine LDL associated fluorophores, reactions between various carbohydrates also give rise to a group of molecules with ceroid like fluorescence. These reactions are termed glycation or Maillard reactions [Maillard 1912]. This pathway involves the production of Schiff bases through the interaction of reducing sugars, such as glucose or fructose, and amino compounds. The Schiff bases rearrange to more stable ketoamine compounds called Amadori products. Although fairly stable, deamidation or dehydration of the Amadori complex may occur resulting in a variety of unsaturated carbonyls. Further reactions between these carbonyls results in the formation of yellow brown advanced glycation end-products (AGEs), which have fluorescence analogous to ceroid [Baynes and Monnier 1989].

Several molecules have been implicated in both the inhibition and the promotion of ceroid formation. For example, ascorbic acid is a water soluble antioxidant which has been

implicated in the recycling of α-tocopherol [Frei *et al.* 1989; Vatassery *et al.* 1989]. However, ascorbic acid can alternatively induce free radical related lipid peroxidation in the presence of transition metals, such as iron and copper. Further, it has been reported that ceroid like fluorophores have been observed in reaction products between ascorbic acid and various amino acids [Yin and Brunk 1999]. Additionally, α-tocopherol, generally considered an endogenous LDL antioxidant, has been implicated in the reduction of the ferric ion necessary to initiate peroxidation of LDL through a Fenton reaction [Yamamoto and Niki 1988]. There are other antioxidants whose roles in atherogenesis and particularly ceroid formation are controversial including several polyenic compounds. Among these we have included β-carotene and retinal palmitate in our study [Karnaukhov *et al.* 1972; Szweda 1994].

The purpose of this study is to more completely characterize the chemical nature of ceroid deposits in human atherosclerotic plaques in an effort to shed light on the process of ceroid formation. This is accomplished by the acquisition of Raman spectra from ceroid deposits *in situ* in samples of coronary artery and aorta. Raman spectra consist of unique combinations of sharp bands, resulting from molecular vibrations, which allow for identification of the chemical species in the sample. The utility of NIR Raman spectroscopy for probing the biochemical composition of human tissue has been well established [Mahadevan and Richards-Kortum 1996; Manoharan *et al.* 1996; Hanlon *et al.* 2000]. Furthermore, a preliminary study illustrating the utility of this approach for the characterization of the chemical makeup of ceroid *in situ* has recently been published [van de Poll 2002]. Although the study provides a comprehensive illustration of the approach, few deposits were examined thus precluding an insightful analysis of the mechanisms leading to

ceroid formation *in vivo*. Our work extends this approach by examining the chemical makeup of numerous ceroid deposits in samples of both aorta and coronary artery.

Due to the strong correlation between the presence and amount of ceroid and the severity of atherosclerotic lesions, it is of crucial importance to fully understand the mechanism of ceroid formation. Insight into the chemical composition of ceroid will shed light on the process of lipoprotein degradation and deposition in atherosclerotic plaques and will address the validity of several theories that have been proposed for ceroid formation. Additionally, a better understanding of the mechanism of ceroid formation may suggest avenues to induce regression or prevent progression of atherosclerotic plaques with medical therapy.

## VIII. E. 2. Sample Preparation and Data Acquisition

### VIII. E. 2. a) Tissue Samples

Raman spectra were collected from frozen sections of coronary artery and aorta obtained from either explanted recipient heart specimens or at the time of autopsy. The samples were rinsed with phosphate-buffered saline (PBS), pH 7.4, frozen in liquid nitrogen, and stored at –85°C until use. The samples were then mounted in histoprep (Fisher Diagnostics, Orangeburg, NY), sectioned, 6 μm thick, on a cryomicrotome (Leica), and mounted on 1 mm thick $MgF_2$ flats (Moose Hill Enterprises Inc., Sperryville, VA) for microscopy. Contiguous 6 μm thick frozen tissue sections were mounted on glass microscope slides, underwent lipid extraction, and were then stained with Oil Red O (ORO) (Poly Scientific R&D Corporation, Bay Shore, NY). Lipid extraction was accomplished by passing the sections through 50%, 75%, and 100% ethanol for 5 minutes each, followed by rehydration in 50% and 25%

ethanol. Ceroid deposits were identified by a combination of histology (lipid extraction and ORO staining) and fluorescence spectroscopy and their chemical composition subsequently examined using Raman spectroscopy. A total of 39 ceroid deposits were examined in 5 samples of coronary artery and 27 ceroid deposits in 6 samples of aorta from 11 patients.

VIII. E. 2. b) Instrumentation

The fluorescence and Raman spectra of both tissues and reagent chemicals used in the model described below were acquired using the confocal microscope, section III.F.2. The microscope itself is equipped with a range of objectives, both normal and phase contrast. For the studies presented here we used a 63x infinity-corrected water immersion objective (0.9 NA), although water immersion was not used. Raman excitation at 830 nm with output powers of approximately 150 mW was employed. The spectrograph itself has an adjustable slit and a turret, which holds three gratings for a range of measurements. For the Raman studies a 600 grooves/mm grating blazed at 1 μm was used along with the 140 μm spectrograph entrance slit setting, providing ~ 8 $cm^{-1}$ resolution. Simply by changing the excitation source, the filters/beamsplitters, and spectrograph grating, the system can be adapted for fluorescence spectroscopy. For the fluorescence measurements, 476 nm excitation light, typically 5 mW, was delivered to the system *via* fiber optics from an argon ion laser (Coherent Innova 700, Coherent Inc., Santa Clara, CA) in an adjacent laboratory. A 600 grooves/mm grating blazed at 500 nm was used for the fluorescence measurements. The switch between Raman and fluorescence is made in less than one min.

VIII. E. 2. c) Data Processing

Fluorescence data were typically collected for 0.5 sec. to 5 sec. Raman spectral data were collected for 60 sec. to 500 sec. depending on the Raman scattering cross-section of the deposit. Often it was necessary for the ceroid deposits to be photobleached for several minutes to reduce the background fluorescence before acquiring a Raman spectrum. All spectral data processing was preformed in MATLAB 5.31 (MathWorks, Inc.). Both Raman and fluorescence data were corrected for the spectral response of the system using a tungsten light source. The data was next frequency calibrated using the known Raman lines of toluene or, in the case of fluorescence, a mercury lamp. Cosmic rays were removed with a derivative filter and the small background from the $MgF_2$ flat was subtracted. Raman data were fit with a fifth order polynomial which was subtracted from the spectrum in order to remove any fluorescence background.

VIII. E. 2. d) Chemical Samples and Spectral Modeling

The chemical composition of the ceroid deposits was determined by analyzing each Raman spectrum with a model. The model contains Raman spectra of several chemicals postulated in the literature to comprise ceroid deposits. These spectra, called basis spectra, are linearly combined with the appropriate weighting factors to recreate the Raman spectrum acquired from a deposit. These weighting factors, called fit coefficients, indicate the amount of each chemical present in the ceroid deposit. Modeling is based on the assumptions that the Raman spectrum of a mixture is a linear superposition of the spectra of its components and that signal intensity and chemical concentration are linearly related. Non-negative OLS fitting of the Raman spectrum of ceroid yields the contribution of each basis spectrum to the entire data spectrum. Model basis spectra are derived by directly taking the Raman spectra of chemicals either synthesized in the laboratory or purchased from commercial sources.

Similar modeling approaches have been used previously to extract the chemical composition of both artery and breast tissues [Buschman *et al.* 2001; Shafter-Peltier 2002].

The Raman model used in this analysis contains chemicals often found in arterial tissue as well as chemicals representative of several of the pathways of ceroid formation discussed above. Acquisition of the first six model components; β-carotene, calcium hydroxyapatite, cholesterol linoleate, cholesterol oleate, free cholesterol, and collagen has been previously described [Buschman *et al.* 2001]. All chemicals listed below were purchased from Sigma (St. Louis, MO) unless otherwise stated. Spectra of HDL (human plasma) and LDL (human plasma) were obtained using the instrumentation described above. The Raman spectrum of a sample of $Cu^{2+}$ oxLDL (courtesy of Dr. H. Hoff, Cleveland Clinic Foundation, Department of Vascular Cell Biology and Atherosclerosis) was incorporated to assess the contribution of the Fenton reaction to ceroid formation. The importance of protein oxidation was assessed through the inclusion of myeloperoxidase/$NO_2$ oxLDL (courtesy of Dr. H. Hoff) and diacetyl dityrosine (courtesey of Dr. L. Sayer). The Maillard reaction is represented by the Raman spectrum acquired from the product of human serum albumin (fatty acid free) and D(-) fructose synthesized according to the method of

| Model | Signal | OLF | Δc |
|---|---|---|---|
| | | | N=0.056 |
| α-Tocopherol | 5.09 | 0.49 | 2.2 |
| β-Carotene | 4.22 | 0.54 | 2.5 |
| Ascorbic Acid | 5.62 | 0.74 | 1.3 |
| Retinal Palmitate | 3.28 | 0.89 | 1.9 |
| Collagen | 7.68 | 0.43 | 1.7 |
| Hemoglobin | 8.34 | 0.84 | 0.8 |
| Cholesterol | 4.15 | 0.45 | 3.0 |
| Cholesterol Linoleate | 4.25 | 0.21 | 6.4 |
| Cholesterol Oleate | 4.36 | 0.27 | 4.7 |
| HDL | 6.37 | 0.34 | 2.6 |
| LDL | 5.08 | 0.41 | 2.7 |
| Fenton Reaction | 4.72 | 0.23 | 5. 1 |
| Protein oxLDL | 6.36 | 0.23 | 3.8 |
| Diacetyl Dityrosine | 5.50 | 0.24 | 4.3 |
| Ascorbic Acid Ox | 4.42 | 0.18 | 7.2 |
| Maillard Reaction | 8.14 | 0.74 | 0.9 |
| Calcification | 2.38 | 0.78 | 3.0 |

**Table VIII.2.** Fit coefficient errors for the ceroid data.

McPherson *et al.* [McPherson *et al.* 1988]. To investigate the role of ascorbic acid in ceroid formation, the Raman spectrum of both L-ascorbic acid and a mixture of L-ascorbic acid and L-Glutamine incubated in PBS was included in our model [Yin 1992]. This pathway represents the proposed route of fluorophore formation during ascorbic acid initiated peroxidation. Ceroid like fluorescence was observed following incubation. In addition to β-carotene, α-tocopherol and retinal palmitate (all trans) were incorporated into the analysis as representative polyenic molecules. Also, the Raman spectrum of hemoglobin (Human, $A_0$ ferrous) was included to examine the distribution heme or heme degradation products within the deposits. Table VIII.2 displays fit coefficient errors calculated using the analytical equation derived in Chapter IV. Also shown are the parameters used for error calculation. The noise in Table VIII.2 is the mean noise from all data. Noise in the coronary and aorta data sets was comparable, N=0.06±0.02 and 0.05±0.02, respectively.

### VIII. E. 3. Results

Ceroid rich regions in each tissue section were identified through a combination of histology and fluorescence spectroscopy. Our combined Raman and fluorescence microscopy instrumentation allows for the identification of ceroid, through its fluorescence signature, and the subsequent acquisition of Raman spectroscopic data from the same region. Ceroid deposits were presumptively identified by comparison of the phase contrast image of the unstained section used for spectroscopy and lipid extracted ORO stained serial sections. A fluorescence spectrum was obtained from each ceroid deposit so identified, to confirm the presence of fluorescence features characteristic of ceroid. Figure VIII.24 shows one example of the data used to identify ceroid deposits. Figure VIII.24a displays a phase contrast image

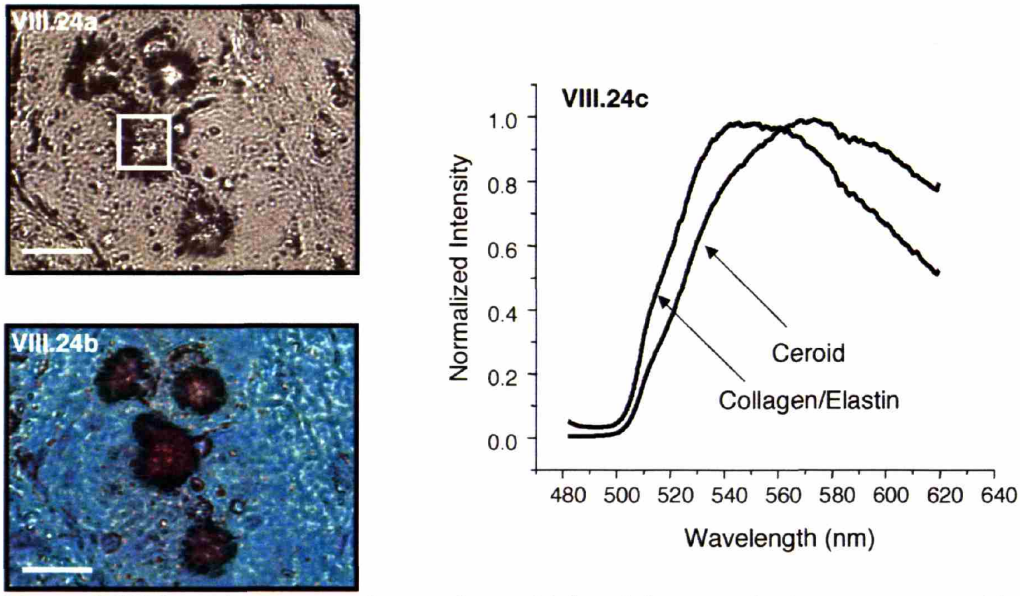


**Figure VIII.24.** a) Phase contrast image of a ceroid deposit in a sample of coronary artery (size bar 25 μm). b) White light image demonstrating a positive ORO stain for ceroid. c) Fluorescence spectrum acquired from the deposit and exhibiting a red shift when compared with the fluorescence spectrum of collagen or elastin.

of a ceroid deposit as identified through comparison with a lipid extracted ORO stained section, shown in Figure VIII.24b. Figure VIII.24c shows the fluorescence spectrum acquired from the deposit shown in image VIII.24a and highlighted by a small box. The fluorescence spectrum of the ceroid deposit exhibits a red shift compared to the fluorescence spectrum of collagen or elastin, the two major fluorophores found in artery at this excitation wavelength. Their spectra, which have similar fluorescence characteristics at this excitation wavelength, are also shown in Figure VIII.24c. A Raman spectrum was subsequently collected from each of the ceroid deposits that exhibited both stainablity with ORO following lipid extraction and a red shifted fluorescence spectrum characteristic of ceroid.

After acquisition of a Raman spectrum, the chemical composition of the ceroid deposit is extracted through modeling. The advantage of this approach is that the basis spectra are correlated with the presence of specific chemicals, thereby providing information about ceroid composition *in situ*. The accuracy of a given model can be qualitatively

determined by observing the residual, calculated by subtracting the model fit from the Raman spectrum of the deposit. The smaller the residual, the more completely the model has accounted for all of the observed spectral features and thus the better the chemical analysis. Figure VIII.25a shows the Raman spectrum of the ceroid deposit pictured in Figure VIII.24a. Also shown are the model fit and the residual. The small size of the residual and its lack of structure indicate a good fit. Although the model employed in this analysis was generally able to account for the majority of the spectral features observed, several Raman spectra exhibited a broadening of the 1650 $cm^{-1}$ peak which was not present in any of the basis spectra. A spectrum of ceroid displaying this broadening is shown in Figure VIII.25b along with its model fit and residual. The persistence of the broadened feature in the residual

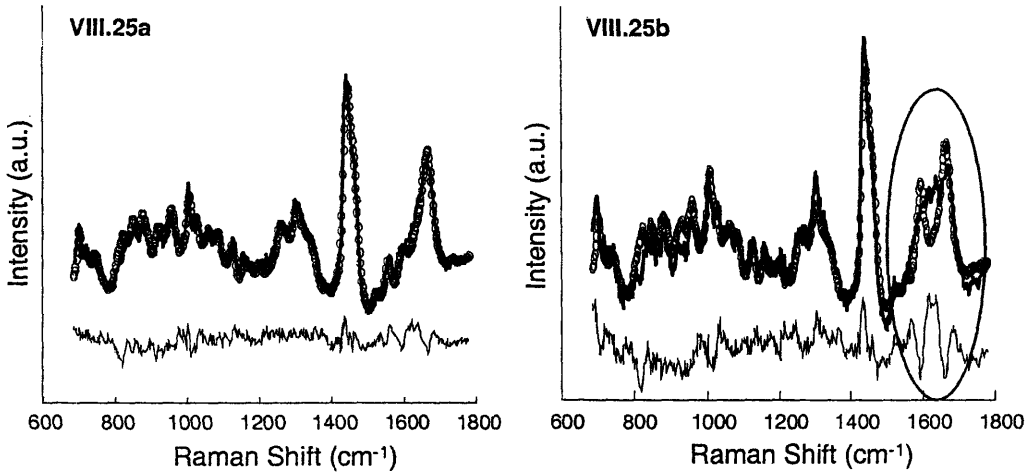


**Figure VIII.25.** a) Raman spectrum acquired from the ceroid deposit pictured in image 2A. The corresponding model fit (open circles) and residual are also pictured. b) Raman spectrum displaying a broadening of the 1650 cm-1 peak highlighted by the black circle.

attests to the inability of the model to account for this element.

From the model fit we can extract the chemical composition of the ceroid deposit. Bar graphs showing the chemical compositions of all of the ceroid deposits examined in coronary arteries and aorta are shown in Figures VIII.26 and VIII.27, respectively. The fit coefficients are normalized to sum to one and thus each bar represents the percentage

contribution of the corresponding basis spectrum to the deposit composition. Variation in the

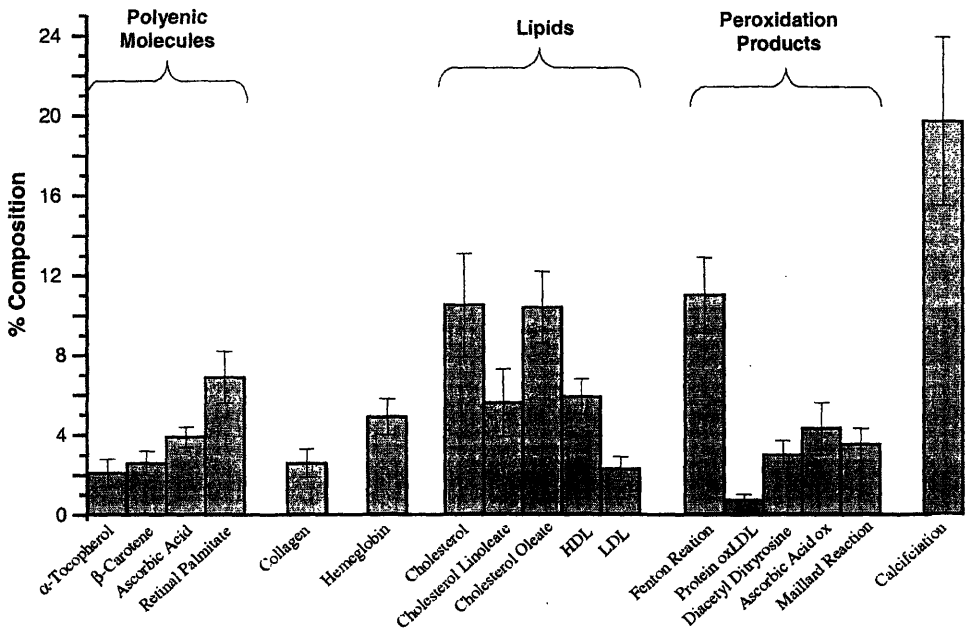


**Figure VIII.26.** Bar graph showing the chemical compositions of all of the ceroid deposits examined in coronary arteries. The error bars represent the standard error of the mean and display variation in the amount of a particular chemical between the deposits examined.

amount of a particular chemical between the deposits examined is displayed in the figure as error bars calculated as the standard error of the mean. The smaller the error bar, the more consistently the component of interest is incorporated in similar quantities into all of the ceroid deposits examined. Many error bars are large, indicating that the chemical composition of the deposits examined has significant variability. Chemical heterogeneity among ceroid deposits was also observed in the preliminary study by Puppels and coworkers [van de Poll *et al.* 2002].

The most notable feature of the bar graphs is that a variety of mechanisms suggested by *in vitro* studies contribute to ceroid formation *in vivo*. Moieties from the Fenton reaction, the Maillard reaction, protein oxidation, and ascorbic acid peroxidation are all present. In accordance with theory, LDL appears within the deposits primarily in its peroxidized form.

Large amounts of free cholesterol are seen in several of the deposits which may indicate foam cell lysis. α-tocopherol is present within ceroid deposits in extremely small quantities, supporting its role as the primary antioxidant associated with LDL. Further, the results support the role of β-carotene as an antioxidant. If, as conjectured, β-carotene prevents oxidation of LDL you would not expect it to be present in ceroid, since presumable only those lipoproteins deficient in β-carotene are susceptible to oxidization. Although small contributions from β-carotene are seen, these correspond to extremely low concentrations as β-carotene is resonance enhanced at this excitation wavelength. As a result, extremely small concentrations generate an intense Raman signal. Conversely, retinal palmitate is present in relatively high concentrations within the deposits indicating that either it plays a role in the formation of ceroid rather than as an antioxidant or it is a less important antioxidant than other polyenic molecules examined. The contribution of collagen to deposit composition is in agreement with electron microscopy studies of ceroid which have shown a core of collagen and elastin-like fibers. Further, hemoglobin is present in the deposits, consistent with both previous Raman studies of ceroid and histochemical studies reporting the co-localization of ceroid and hemoglobin [Nahiev *et al.* 1991: van de Poll *et al.* 2002]. Lastly, many deposits contain contributions from calcium mineral salts. Therefore, it is possible that ceroid deposition may provide a basis for hydroxyapatite nucleation and ultimately formation of calcifications.

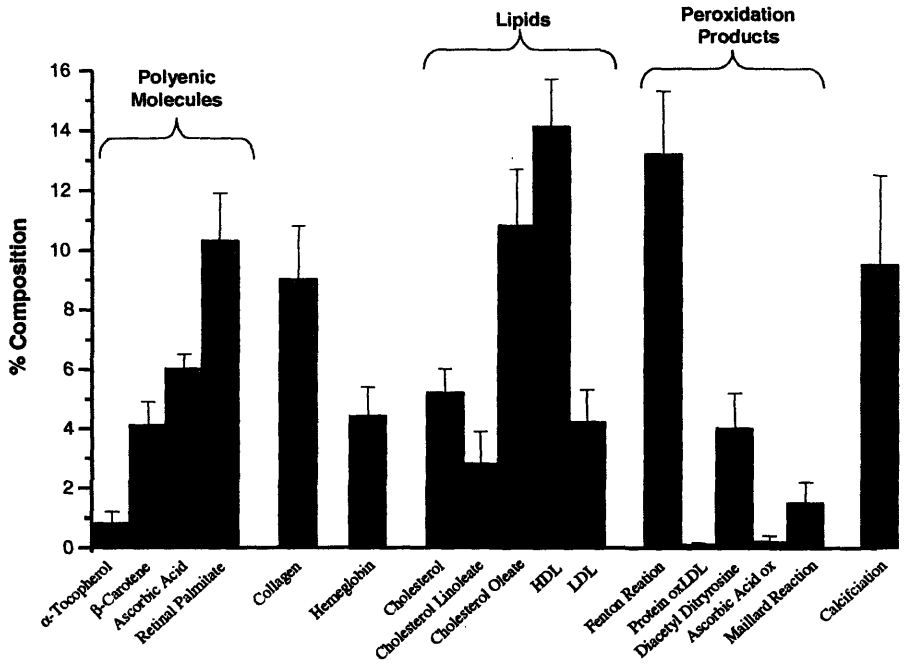


**Figure VIII.27.** Histogram showing the chemical compositions of all of the ceroid deposits examined in aorta. The error bars represent the standard error of the mean and display variation in the amount of a particular chemical between the deposits examined.

Because the overall Raman signal intensity is a function of both the Raman scattering cross-section and the amount of the molecule of interest, fit coefficients are not direct reflections of chemical concentration. Although the absolute Raman scattering cross-section of these model components is not known, and thus a rigorous quantitative analysis cannot presently be preformed, basis spectra with a high degree of spectral similarity should have comparable Raman scattering cross-sections. Thus the fit coefficients of these pathways can be directly compared. For instance, in ceroid deposits occurring in both aorta and coronary arteries, the predominate mode of lipid peroxidation appears to be mediated by transition metals. Ascorbic acid initiated free radical lipid peroxidation also contributes but only as a minor pathway as witnessed by the smaller percent contribution of this model component compared to the model component representative of the Fenton reaction. Likewise, protein oxidation is present and appears to proceed mainly through direct modification of amino

acids while LDL oxidation by myeloperoxidase is not witnessed to a large degree. Again, these two pathways can be compared due to their large degree of spectral overlap, olf=0.39, and thus similar Raman scattering cross-sections. It should be noted that LDL oxidation by myeloperoxidase was present with a contribution of 10.3% in one deposit examined. The significance of this observation and the role of myeloperoxidase in ceroid formation are not clear from this study. Although the relative importance of certain mechanisms can be assessed, direct comparison between the extent of lipid peroxidation and protein oxidation is not feasible without knowledge of the Raman scattering cross-sections of these molecules.

Much of the wide variation in chemical composition among the ceroid deposits can be attributed to examination of the deposits during different stages of formation. In an effort to provide additional insight into the mechanism of ceroid formation, we have compared data acquired from intra- and extra-cellular deposits. The separation into intra- and extra-cellular ceroid is based on the amount of cholesterol linoleate and cholesterol oleate present in each deposit as determined by their fit coefficients. Deposits containing predominately cholesterol oleate were labeled as intracellular while those containing mainly cholesterol linoleate were categorized as occurring extracellularly. Deposits with roughly equal amounts of cholesterol linoleate and cholesterol oleate (less than 10% difference) or with neither molecule, were omitted from this analysis. 10% was chosen as our experimental errors are typically twice that predicted by the analytical formula, section IV.F.6. This distinction is based on the fact that incubation of mouse peritoneal macrophages with cholesteryl linoleate/ bovine serum albumin emulsions induces significant cell damage whereas the addition of cholesteryl oleate/ bovine serum albumin does not [Reid *et al.* 1992]. The separation results in 13 intracellular and 6 extracellular deposits in coronary arteries. Only 2 ceroid deposits

examined in aorta contained cholesterol linoleate in a 10% excess over cholesterol oleate. For this reason, the chemical composition of ceroid deposits occurring intra- and extracellularly was only examined in coronary arteries.

The disproportionately larger amount of intracellular ceroid deposits examined in aorta provides some insight into the differences in fit coefficients, seen in Figures VIII.26 and VIII.27, between coronary arteries and aorta. First, the polyenic molecules are present in smaller amounts in coronary arteries. This is consistent with their role as antioxidants as the depletion of protective molecules should be greater in more advanced deposits. Another molecule postulated to play a protective role in atherosclerosis is HDL. Again, we see much smaller contributions from HDL in the deposits examined in coronary arteries than in those examined in aorta.

While this classification of intracellular and extracllular deposits may seem somewhat arbitrary, differences in chemical composition and morphology of the two types of deposits were observed and provide further confirmation of the validity of this separation. Structural examination of the deposits by an experienced pathologist indicates that all intracellular deposits appear to have a similar globular morphology, whereas the extracellular deposits

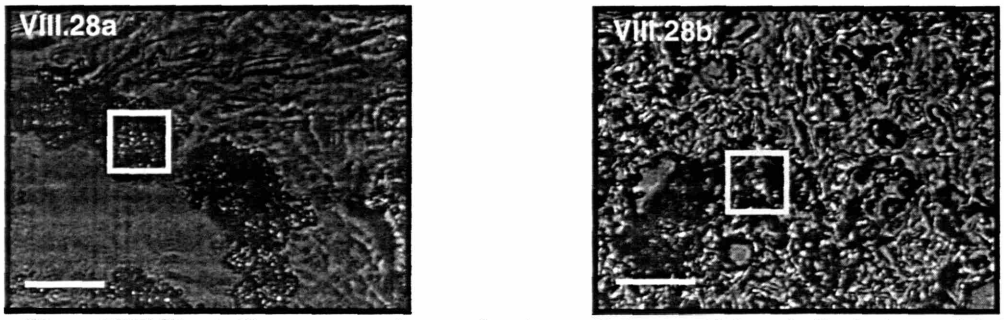


**Figure VIII.28.** a) Phase contrast image of an intracellular ceroid deposit displaying a globular morphology. b) Phase contrast image of an extracellular ceroid deposit displaying a diffuse morphology. (Size bar 25 μm)

have a different diffuse morphology. Figure VIII.28 displays phase contrast images demonstrating the noted intra- and extra- cellular morphologies. A bar graph comparing the composition of intra- and extra-cellular ceroid deposits in coronary artery is shown in Figure VIII.29. The white bars in the figures correspond to intracellular deposits while the shaded lines represent extracellular deposits. Chemicals which did not vary significantly between extracellular and intracellular deposits are excluded from the figure. From this analysis, it is evident that the presence of β-carotene is slightly higher in intra- than extra- cellular deposits. This provides further support for its role as an antioxidant and contradicts suggestions that carotenoids do not play a significant role in protecting LDL against oxidation [Halliwell 1990]. Retinal palmitate is also present in higher quantities

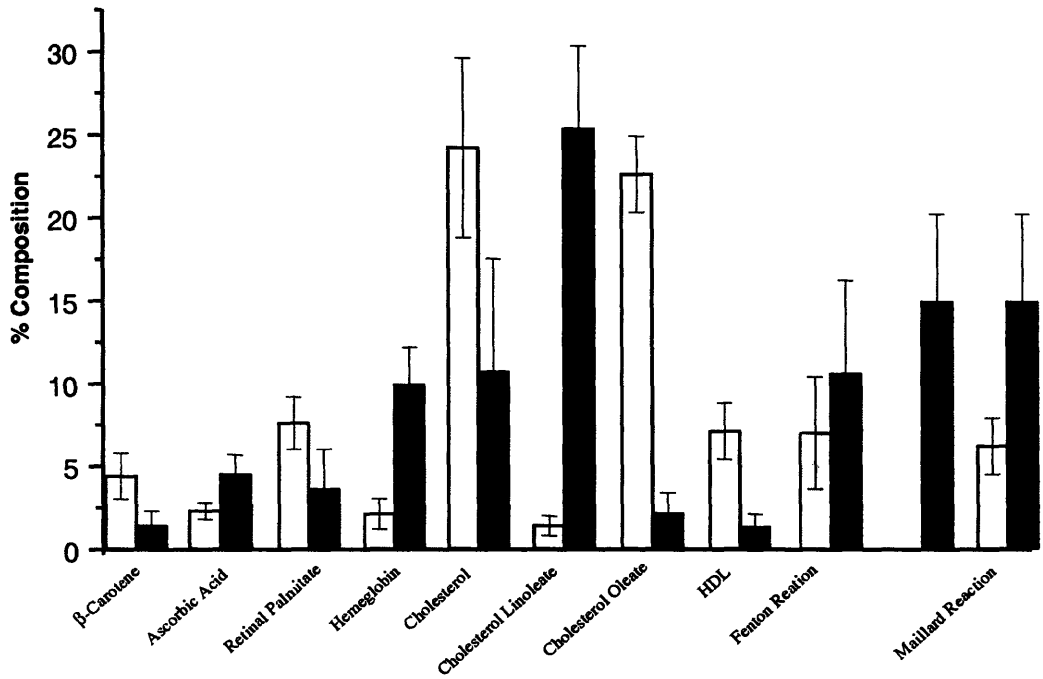


**Figure VIII.29** Histogram showing the chemical compositions of intra- (white bars) and extra- (gray bars) cellular ceroid deposits occurring in coronary arteries. The error bars represent the standard error of the mean and display variation in the amount of a particular chemical between the deposits examined.

intracellularly. This may suggest that it plays a less crucial role as an antioxidant than β-carotene and thus is consumed in latter stages of ceroid formation. α-tocopherol is not present in appreciable quantities in either intra- or extra- cellular deposits, again indicating that it is the principal antioxidant associated with LDL and has been consumed prior to the initiation of lipid peroxidation. Also as expected, free cholesterol is higher intracellularly. This is in accordance with previous literature which reported that incubation with oxLDL led to macrophage accumulation of unesterified cholesterol [Maor and Aviram 1994]. Peroxidized lipids, such as transition metal oxLDL and ascorbic acid initiated lipid peroxidation, are more prevalent extracellularly. This observation lends support to theories which link ceroid accumulation to cell death and necrosis. In fact, ascorbic acid initiated lipid peroxidation appears to occur entirely extracellularly. This observation can also explain why little contribution from this pathway is seen in the predominately intracellular deposits examined in aorta. The reason for this trend is presently not known. It is possible that ceroid induced macrophage lysis results in extravasation of the ferrous ion contained within the deposits thereby providing the heavy metal needed for ascorbic acid initiated lipid peroxidation. Consistent with this theory, hemoglobin contributes to ceroid composition predominately extracellularly. No significant differences were observed in the fluorescence characteristics of the intracellular and extracellular deposits.

### VIII. E. 4. Conclusions

In this study, we analyze the chemical composition of ceroid deposits within atherosclerotic plaques, without the need for extraction or purification, using Raman microscopy. This allows assessment of the physiological relevance of several of the *in vitro* model studies

undertaken in an effort to elucidate the chemical composition of ceroid. Results demonstrate that a variety of mechanisms play a role in ceroid formation *in vivo*. Further, our studies show that the predominate mode of lipid oxidation occurs through a Fenton reaction while oxidative modification of proteins proceeds mainly through direct oxidation of amino acids. Data support the roles of α-tocopherol and β-carotene as antioxidants. The elucidation of the composition of ceroid deposits provides insight into the underlying biochemical mechanism of ceroid formation thereby advancing the understanding of the atherosclerotic disease process.

## *Acknowledgements*

Dr. Maryann Fitzmaurice provided the pathological diagnoses for the UHC FastEEM data. She also helped devise the clinical protocol and collect data from freshly excised tissues. This study would not have been possible without the patience and support of the entire pathology staff at UHC. Jonathan Nazemi was also invaluable in executing the studies carried out in Cleveland. He taught me how to use the FastEEM instrumentation and assisted with data acquisition, study planning, equipment transportation, and general troubleshooting. Zoya Volynskaya helped to collect the UHC FastEEM data and performed much of the analysis presented in this chapter. Joeseph Arendt and George Angheloiu collected the CCF FastEEM data and Dr. Andrea Dawson provided the pathological diagnoses. Sasha McGee and Jelena Mirkovic acquired the FastEEM freeze-thaw data. Irene Georgakoudi and Scott Miller assisted with data acquisition and analysis for the fluorescence lifetime measurements. Irene also provided guidance for generating the new β-carotene absorption spectrum. Katrin Kneipp and I worked together on the SERS cell project. Dr. Maryann Fitzmaurice preformed the histologic analysis for the ceroid studies. Drs. Henry Hoff and Lawrence Sayer provided guidance as well as materials for the ceroid studies. I would like to thank Maryann, Henry, Lawrence, and Ramachandra for taking time to discuss the ceroid project. Many of the images in this chapter have been reproduced from *Applied Spectroscopy* [Kniepp *et al.* 2002] with permission from The Society for Applied Spectroscopy and *Technology in Cancer Research and Treatment* [Manoharan *et al.* 1998] with permission from Adenine press.

## *References*


Amado R, Aeschbach R and Neukom H (1984). "Dityrosine: *In Vitro* Production and Characterization." Methods Enzymol **107**: 377-388.

Bachackashvilli A, Efrima S, Katz B and Priel Z (1983). "Is There Surface Enhancement of Raman-Scattering by Molecules at Resonance." Chemical Physics Letters **94**(6): 571-575.

Bacackashvilli A, Katz B, Priel Z and Efrima S (1984). "Surface Raman-Scattering of Azo Dyes." J Phys Chem **88**(25): 6185-6190.

Ball RY, Bindman JP, Carpenter KLH and Mitchinson MJ (1986). "Oxidized Low Density Lipoprotein Induces Ceroid Accumulation by Murine Peritoneal Macrophages *In Vitro*" Atherosclerosis **60**:173-181.

Baynes JW and Monnier VM (1989). "The Maillard Reaction in Ageing, Diabetes, and Nutrition." New York, Alan R. Liss, Inc.

Bown SG, Briggs G, Kelley C, Lakhani S, Picard D, Ripley PM, Rose IG, Saunders C and Bigio IJ (2000). "Diagnosis of Breast Cancer Using Elastic-Scattering Spectroscopy: Preliminary Clinical Results." J Biomed Opt **5**(2): 221-228.

Brunk UT, Marzabadi MR and Jones CB (1992). "Lipofuscin, Lysosomes, and Iron." Ed. Lauffer RB Iron and Human Disease. London: CRC Press: 237-260.

Burt RC (1952). "The Incidence of Acid-Fast Pigment (Ceroid) in Aortic Atherosclerosis." Am J Clin Pathol **22**:135-139.

Buschman HP, Deinum G, Motz JT, Fitzmaurice M, Kramer JR, van der Laarse A, Bruschke AV and Feld MS (2001). "Raman Microspectroscopy of Human Coronary Atherosclerosis: Biochemical Assessment of Cellular and Extracellular Morphologic Structures *In Situ*." Cardiovascular Pathology **10**: 69-82.

Chio KS and Tappel AL (1969). "Synthesis and Characterization of the Fluorescent Products Derived From Malondialdehyde and Amino Acids." Biochemistry **8**:2821-2827.

Constantino CJL and Aroca RF (2000). "Surface-Enhanced Resonance Raman Scattering Imaging of Langmuir-Blodgett Monolayers of Bis(benzimidazo)perylene on Silver Island Films." J Raman Spectrosc **31**(10): 887-U3.

Couprie ME, Merola F, Tauc P, Garzella D, Delboulbe A, Hara T and Bilardon M (1994). "1st Use of the UV Super-Aco Free-Electron Laser - Fluorescence Decays and Rotational-Dynamics of the NADH Coenzyme." Rev Sci Instrum **65**(5): 1485-1495.

Dillard CJ and Tappel AL (1971). "Fluorescent Products of Lipid Peroxidation of Mitochondria and Microsomes." Lipids **6**: 715-721.

Dunford HB (1987). "Free Radicals in Iron-Containing Systems." Free Rad Biol Med **3**: 405-421.

Esterbauer H, Koller E, Slee G and Koster JF (1986). "Possible Involvement of the Lipid Peroxidation Product 4-Hydroxynonenal in the Formation of Fluorescent Chromolipids." Biochem J **239**: 405-409.

Feofanov AV, Grichine AI, Shitova LA, Karmakova TA, Yakubovskaya RA, Egret-Charlier M and Vigny P (2000). "Confocal Raman Microspectroscopy and Imaging Study of Theraphthal in Living Cancer Cells." Biophysical **78**(1): 499-512.

Fitzmaurice MA, Bordagaray JO, Engelmann GL, Richards-Kortum RR, Kolubayev T, Feld

MS, Ratliff NB and Kramer JR (1989). "Argon Ion Laser-Excited Autofluorescence in Normal and Atherosclerotic Aorta and Coronary Arteries: Morphologic Studies." American Heart Journal **118**(5).

Frei B, England L and Ames BN (1989). "Ascorbate is an Outstanding Antioxidant in Human-Blood Plasma." Proc Natl Acad Sci USA **86**(16): 6377-6381.

Georgakoudi I, Jacobson BC, Van Dam J, Backman V, Wallace MB, Thomas GA, Perelman LT and Feld MS (2001). "Fluorescence, Reflectance, and Light-Scattering Spectroscopy for Evaluating Dysplasia in Patients with Barrett's Esophagus." Gastroenterology **120**: 1620-1629.

Georgakoudi I, Sheets EE, Muller MG, Backman V, Crum CP, Badizadegan K, Dasari RR and Feld MS (2002). "Trimodal Spectroscopy For the Detection and Characterization of Cervical Precancers *In Vivo*." Am J Obstet Gynecol **186**(3): 374-382.

Gupta PK, Majumder SK, and Uppal A (1997). "Breast Cancer Diagnosis Using $N_2$ Laser Excited Autofluorescence Spectroscopy." Lasers Surg Med **21**: 417-422. Halliwell B (1990). "How to Characterize a Biological Antioxidant." Free Rad. Res Comm **9**:1-32.

Hanlon EB, Manoharan R, Koo TW, Shafer KE, Motz JT, Fitzmaurice M, Kramer JR, Itzkan I, Dasari RR and Feld MS (2000). "Prospects for *In Vivo* Raman Spectroscopy." Phys Med Biol **45**: R1-R59.

Hartroft WS (1953). "Pathogenesis and Significance of Hemoceroid and Hyaloceroid, Two Types of Ceroidlike Pigment Found in Human Atheromatous Lesions." J Gerontol **8**: 158-166.

Hartroft WS and Porta EA (1965). "Ceroid." Am J Med Sci **250**: 324-349.

Hazell LJ and Stocker R (1993). "Oxidation of Low-Density Lipoprotein With Hypocholorite Causes Transformation of the Lipoprotein Into a High-Uptake Form For Macrophages." Biochem J **290**:165-172.

Hoff HF, Whitaker TE and O'Neil J (1992). "Oxidation of Low-Density-Lipoprotein Leads to Particle Aggregation and Altered Macrophage Recongnition." J Biol Chem **267**(1): 602-609.

http://omlc.ogi.edu/spectra/photochemCAD/html/beta-carotene.html

Karnaukhov VN, Tataryunas TB and Petrunyaka VV (1972). "Accumulation of Carotenoids in Brain and Heart of Animals on Aging; The Role of Carotenoids in Lipofuscin Formation." Mech Ageing Dev **2**:201-210.

Kikugawa K and Beppu M (1987). "Involvement of Lipid Oxidation-Products in the Formation of Fluorescent and Cross-Linked Proteins." Chem Phys Lipids 44(2-4): 277-296.

Kneipp K, Haka AS, Kneipp H, Badizadegan K, Yoshizawa N, Boone C, Shafer KE, Motz JT, Dasari RR and Feld MS (2002). "Surface-Enhanced Raman Spectroscopy and Raman Imaging in Single Living Cells Using Gold Nanoparticles." Appl Spec 56(2).

Kneipp K, Hinzmann G and Fassler D (1983). "Surface-Enhanced Raman-Scattering of Polymethine Dyes on Silver Colloidal Particles." Chemical Physics Letters **99**(5-6): 503-506.

Kneipp K and Flemming J (1986). "Surface Enhanced Raman-Scattering (SERS) of Nucleic-Acids Adsorbed on Colloidal Silver Particles." J Mol Struct **145**(1-2): 173-179.

Kneipp K, Pohle W and Fabian H (1991). "Surface Enhanced Raman-Spectroscopy on

Nucleic-Acids and Related-Compounds Adsorbed on Colloidal Silver Particles." J Mol Struct **244**: 183-192.

Kneipp K, Wang Y, Dasari RR and Feld MS (1995). "Approach To Single-Molecule Detection Using Surface-Enhanced Resonance Raman-Scattering (SERRS) - A Study Using Rhodamine 6G on Colloidal Silver." Appl Spectrosc **49**(6): 780-784.

Kneipp K, Kneipp H, Kartha VB, Manoharan R, Deinum G, Itzkan I, Dasari RR and Feld MS (1998). "Detection and Identification of a Single DNA Base Molecule Using Surface-Enhanced Raman Scattering (SERS) Phys Rev E **57**(6): R6281-R6284.

Kneipp K, Kneipp H, Manoharan R, Hanlon EB, Itzkan I, Dasari RR and Feld MS (1998). "Extremely Large Enhancement Factors in Surface-Enhanced Raman Scattering for Molecules on Colloidal Gold Clusters." Appl Spectrosc **52**(12): 1493-1497.

Kneipp K, Kneipp H, Deinum G, Itzkan I, Dasari RR and Feld MS (1998)."Single-Molecule Detection of a Cyanine Dye in Silver Colloidal Solution Using Near-Infrared Surface-Enhanced Raman Scattering." Appl Spectrosc **52**(2): 175-178.

Lee FY, Lee TS, Pan CC, Huang AL and Chau LY (1998). "Colocalization of Iron and Ceroid in Human Atherosclerotic Lesions." Atherosclerosis **138**: 281-288.

Mahadevan A and Richards-Kortum R (1996). "Raman Spectroscopy For the Detection of Cancers and Precancers." J Biomed Opt **1**: 31-70.

Maillard LC (1912). "Action des Acides Amines sur les Sucres: Formation des Melanoidines par Voie Methodique." Ed. Hebd CR Seances Acad Sci **154**: 66-68.

Majumder SK, Gupta PK, Jain B and Uppal A (1998). "UV Excited Autofluorescence Spectroscopy of Human Breast Tissues for Discriminating Cancerous Tissue from Benign Tumor and Normal Tissue." Lasers Life Sci **00**: 1-16.

Manoharan R, Wang Y and Feld MS (1996). "Review: Histochemical Analysis of Biological Tissues Using Raman Spectroscopy." Spectrochemica Acta Part A **52**: 215-249.

Maor I and Aviram M (1994). "Oxidized Low Density Lipoprotein Leads to Macrophage Accumulation of Unesterified Cholesterol as a Result of Lysosomal Trapping of the Lipoprotein Hydrolyzed Cholesteryl Ester." J Lipid Res **35**: 803-819.

McPherson JD, Shilton BH and Walton DJ (1988). "Role of Fructose in Glycation and Cross-Linking of Proteins." Biochemistry **27**: 1901-1907.

Mitchinson MJ (1982). "Insoluble Lipids in Human Atherosclerotic Plaques." Atherosclerosis **45**(1): 11-15.

Mitchinson MJ, Hothersall DC, Brooks PN and Deburbure CY (1985). "The Distribution of Ceroid in Human Atherosclerosis." J Pathol **145**(2): 177-183.

Morjani H, Riou JF, Nabiev I, Lavelle F and Manfait M (1993). "Molecular and Cellular Interactions Between Intoplicine, DNA, and Topoisomerase-II Studied by Surface-Enhanced Raman-Scattering Spectroscopy." Cancer Research **53**(20): 4784-4790.

Moskovits M (1985). "Surface-Enhanced Spectroscopy." Reviews of Modern Physics **7**(3): 783-826.

Muller MG, Georgakoudi I, Zhang Q, Wu J and Feld MS (2001). "Intrinsic Fluorescence Spectroscopy in Turbid Media: Disentangling the Effects of Scattering and Absorption" Appl Opt **40**(25): 4633-4646.

Muller MG, Wax A, Georgakoudi I, Dasari RR and Feld MS (2002). "A Reflectance Spectrofluorimeter for Real-Time Spectral Diagnosis of Disease." Rev Sci Instrum **73**(11): 3933-3937.

Muller MG, Valdez TA, Georgakoudi I, Backman V, Fuentes C, Kabani S, Laver N, Wang ZM, Boone CW, Dasari RR, Shapshay SM and Feld MS (2003). "Spectroscopic Detection and Evaluation of Morphologic and Biochemical Changes in Early Human Oral Carcinoma." Cancer **97**(7): 1681-1692.

Otto C, de Grauw CJ, Duindam JJ, Sijtsema NM, Otto C and Greve J (1997). "Applications of Micro-Raman Imaging in Biomedical Research." J Raman Spectrosc **28**(2-3): 143-150

Palmer GM, Marshek CL, Vrostsos KM and Ramanujam N (2002). "Optimal Methods for Fluorescence and Diffuse Reflectance Measurements of Tissue Biopsy Samples." Lasers in Surgery and Medicine **30**(3): 191-200.

Pappenheimer AM and Victor J (1946). "Ceroid Pigment in Human Tissues." Am J Pathol **22**: 395-413.

Patapoff TW, Thomas GA, Wang Y and Peticolas WL (1988). "Polarized Raman-Scattering From Oriented Single Microcrystals of D(A5T5)2 and D(PTPT)." Biopolymers **27**(3): 493-507.

Pearse AGE (1985). "Pigments and Pigment Precursors." Ed. Analytic Technology Histochemistry, Theoretical and Applied 4th Ed. New York, Churchill Livingstone Inc. **2**: 874-928.

Perelman LT, Backman V, Wallace M, Zonios G, Manoharan R, Nusrat A, Shields S, Seiler M, Lima C, Hamano T, Itzkan I, Van Dam J, Crawford JM and Feld MS (1998). "Observation of Periodic Fine Structure in Reflectance from Biological Tissue: A New Technique for Measuring Nuclear Size Distribution." Phys Rev Lett **80**(3): 627-630.

Peticolas WL, Patapoff TW, Thomas GA, Postlewait J and Powell JW (1996). "Laser Raman Microscopy of Chromosomes in Living Eukaryotic Cells: DNA Polymorphism *In Vivo*." J Raman Spectrosc **27**(8): 571-578.

Pettinger B (1984). "The Role of Energy-Transfer Processes in Surface (Enhanced) Inelastic Light-Scattering." Chemical Physics Letters **110**(6): 576-581.

Porta EA and Hartroft WS (1969). "Lipid Pigment in Relation to Aging and Dietary Factors (Lipofuscins)." Ed. Wolman M Pigments in Pathology. Orlando FL, Academic Press Inc: 191-235.

Puppels GJ, de Mull FFM, Otto C, Greve J, Robert-Nicoud M, Arndt-Jovin DJ and Jovin TM (1990). "Studying Single Living Cells and Chromosomes by Confocal Raman Microscpectroscopy." Nature **347**(6290): 301-303.

Reid VC, Brabbs CE and Mitchinson MJ (1992). "Cellular Damage in Mouse Peritoneal Macrophages Exposed to Cholesteryl Linoleate." Atherosclerosis **92**: 251-260.

Selvan ST, Hayakawa T and Nogami M (1999). "Block Copolymer Mediated Synthesis of Gold Quantum Dots and Novel Gold-Polypyrrole Nanocomposites." J Phys Chem B **103**(35): 7441-7448.

Shafer-Peltier KE, Haka AS, Fitzmaurice M, Crowe J, Myles J, Dasari RR and Feld MS (2002). "Raman Microspectroscopic Model of Human Breast Tissue: Implications for Breast Cancer Diagnosis *In Vivo*." J Raman Spec **33**(7): 125-137.

Sijtsema NM, Otto C, Segers-Nolten GMJ, Verhoeven AJ and Greve J (1998). "Resonance Raman Microspectroscopy of Myeloperoxidase and Cytochrome b(558) in Human Neutrophilic Granulocytes." Biophysical J **74**(6): 3250-3255.

Sijtsema NM, Tibbbe AGJ, Segers-Nolten J, Verhoeven AJ, Weening RS, Greve J and Otto

C (2000). "Intracellular Reactions in Single Human Granulocytes Upon Phorbol Myristate Acetate Activation Using Confocal Raman Microspectroscopy." Biophysical J **78**(5): 2606-2613.

Slater RS and EB Smith (1972). "The Microdissection of Large Atherosclerotic Plaques to Give Morphologically and Topographically Defined Fractions For Analysis: II Studies on 'Nile Blue' Cells." Atherosclerosis **15**: 57-69.

Sokolov K, Chumanov G and Cotton TM (1998). "Enhancement of Molecular Fluorescence Near the Surface of Colloidal Metal Films." Anal Chem **70**(18): 3898-3905.

Steinbrecher UP, Zhang H and Lougheed M (1990). "Role of Oxidatively Modified LDL in Atherosclerosis" Free Radical Biol and Med **38**(9): 155-168.

Szweda L (1994). "Age-Related Increase in Liver Retinyl Palmate: Relationship to Lipofuscin." J Biol Chem **269**: 8712-8715.

Takatani S and Ling JA (1994). "Optical Oximetry Sensors for Whole-Blood and Tissue." IEEE Eng Med Biol **13**: 347-357.

Tauler R, Smilde AK, Henshaw JM, Burgess LW and Kowalski BR (1994)."Multicomponent Determination of Chlorinated Hydrocarbons Using a Reaction-Based Chemical Sensor. 2. Chemical Speciation Using Multivariate Curve Resolution." Anal Chem **66**: 3337-3344.

Tsuchida M, Miura T, Mizutani K and Aibara K (1985). "Fluorescent Substances in Mouse and Human-Sera as a Parameter of *In Vivo* Lipid-Peroxidation Biochim Biophys Acta **834**(2): 196-204.

Tunnell JW, Desjardins AE, Galindo L, Georgakoudi I, McGee SA, Mirkovic J, Mueller MG, Nazemi J, Nguyen FT, Wax A, Zhang QG, Dasari RR and Feld MS (2003). "Instrumentation for Multi-Modal Spectroscopic Diagnosis of Epithelial Dysplasia." Tech Canc Res Treat **2**(6): 505-514.

van de Poll SWE, Bakker Schut TC, van der Laarse A and Puppels GJ (2002). "*In Situ* Investigation of the Chemical Composition of Ceroid in Human Atherosclerosis by Raman Spectroscopy." J Raman Spectrosc **33**: 544-551.

Vatassery GT (1989). "Oxidation of Vitamin-E in Red-Cell Membranes by Fatty-Acids, Hydroperoxides and Selected Oxidants." Lipids **24**(4): 299-304.

Verbunt RJAM, Fitzmaurice M, Kramer JR, Ratliff NB, Kittrell C, Taroni P, Cothren RM, Baraga J and Feld MS (1992). "Characterization of Ultraviolet Laser-Induced Autofluorescence of Ceroid Deposits and Other Structures in Atherosclerotic Plaques as a Potential Diagnostic for Laser Angiosurgery." American Heart Journal **123**(1).

Weitz DA, Garoff S, Gersten JI and Nitzan A (1983). "The Enhancement of Raman-Scattering, Resonance Raman-Scattering, and Fluorescence from Molecules Adsorbed on a Rough Silver Surface." J Chem Phys **78**(9): 5324-5338.

Witztum JL and Steinberg D (1991). "Role of Oxidized Low Density Lipoprotein in Atherogenesis." J Clin. Invest **88**:1785-1792.

Wolman M (1980). "Lipid Pigments (Chromolipids): Their Origin, Nature, and Significance." Pathobiol Ann **10**: 253-267.

Yamamoto K and Niki E (1988). "Interaction of α-tocopherol With Iron: Antioxidant and Prooxidant Effects of α-tocopherol in the Oxidation of Lipids in Aqueous Dispersions in the Presence of Iron." Biochem Biophys Acta **958**: 19-23.

Yang Y, Katz A, Celmer EJ, Zurawska-Szczepaniak M and Alfano RR (1997). "Excitation

Spectrum of Malignant and Benign Breast Tissues: A Potential Optical Biopsy Approach." Lasers Life Sci **7**(2): 115-127.

Yang Y, Katz A, Celmer EJ, Koutcher JA and Alfano RR (1998). "Excitation Spectroscopy of Proteins in Malignant and Benign Tissues." OSA TOPS **22**.

Yin D and Brunk UT (1991). "Oxidized Ascorbic Acid and Reaction Products Between Ascorbic and Amino Acids Might Constitute Part of Age Pigments." Mech Ageing Dev **61**: 99-112.

Yin D (1992). "Lipofuscin-Like Fluorophores Can Result From Reactions Between Oxidized Ascorbic Acid and Glutamine. Carbonyl-Protein Cross-Linking May Represent a Common Reaction in Oxygen Radical and Glycosylation-Related Ageing Processes." Mech Ageing Dev **62**: 35-46.

Yin D (1996). "Biochemical Basis of Lipofuscin, Ceroid, and Age Pigment-Like Fluorophores." Free Rad Biol Med **21**(6): 871-888.

Zang LY, Sommerburg O and van Kuijk FJGM (1997). "Absorbance Changes of Carotenoids in Different Solvents." Free Rad Biol and Med **23**(7): 1086-1089.

Zangaro RA, Silveira L, Manoharan R, Zonios G, Itzkan I, Dasari RR, Dam JV and Feld MS (1996). "Rapid Multiexcitation Fluorescence Spectroscopy System for *In Vivo* Tissue Diagnosis." Applied Optics **35**:5211-19.

Zhang Q, Muller MG, Wu J and Feld MS (2000). "Turbidity-Free Fluorescence Spectroscopy of Biological Tissue." Opt Lett **25**(19): 1451-1453.

Zonios G, Perelman LT, Backman VM, Manoharan R, Fitzmaurice M, Van Dam J and Feld MS (1999). "Diffuse Reflectance Spectroscopy of Human Adenomatous Colon Polyps *In Vivo*." Applied Optics **38**: 6628-6637.

# Chapter IX. Future Directions

This chapter discusses the future of Raman spectroscopy in breast cancer diagnosis and treatment. Upcoming clinical and basic studies are detailed. With the successful demonstration of *in vivo* Raman spectroscopy for breast cancer diagnosis, there are many clinical applications that can be addressed. Approaches to transdermal needle measurements for breast cancer diagnosis are presented as well as future intra-operative studies for margin assessment. These clinical studies will be accompanied by diagnostic algorithm validation and extension using our data set acquired from freshly excised tissue. Basic experiments will focus on quantitative analysis and spectral model refinement. Finally, the prospects for a multi-spectroscopic optical fiber probe that may provide enhanced optical diagnosis are presented.

## *IX. A. The Future of Raman Spectroscopy in Breast Cancer Diagnosis*

The experiments and theory presented throughout this thesis demonstrate that Raman spectroscopy can be used to accurately diagnosis breast cancer and breast disease. Furthermore, we have demonstrated extension of the technique to preliminary *in vivo* clinical applications with excellent results. However, additional clinical studies are needed to fully assess the utility of Raman spectroscopy for breast cancer diagnosis and treatment.

### IX. A. 1. Transdermal Needle Measurements

Optical techniques are less invasive than current diagnostic procedures. The results of our initial *in vivo* studies illustrate the potential for Raman spectroscopic transdermal needle measurements to provide breast cancer diagnosis. As opposed to standard biopsy, a spectroscopic transdermal needle measurement would have the advantage of providing immediate diagnosis. As a result, Raman spectroscopy has the potential to reduce both the likelihood of a non-diagnostic biopsy that would require repeat needle or surgical biopsy, and patient anxiety by eliminating the currently unavoidable wait for a traditional histopathology diagnosis. Furthermore, with the development of minimally invasive breast cancer therapies, such as radiofrequency ablation, which relies on insertion of a thin metal probe into the breast, there is the potential that diagnosis and treatment could be performed in a single procedure [Fornage *et al.* 2004]. Spectroscopic diagnosis also confers economic advantages. There are numerous people as well as supplies and equipment involved in the biopsy procedure, tissue processing, and histopathology diagnosis making needle biopsy an expensive enterprise.

Transdermal needle measurements can be preformed with either a front-viewing or a side-viewing Raman optical fiber probe. A front-viewing probe can be used in conjunction with a vacuum-assisted biopsy procedure, discussed in section II.E.3e. A schematic of a transdermal needle measurement that employs the front-viewing Raman probe is shown in Figure IX.1a. In this configuration, the spectroscopic measurement will always sample the proximal end of the biopsy tissue. Although the current reduced diameter front-viewing Raman probe is compatible with an 11 gauge needle, often used in these procedures, studies must be undertaken to investigate whether the vacuum device and overall setup can be used in conjunction with the probe.

A side-viewing Raman probe can also be used for transdermal needle measurements, as depicted in Figure IX.1b. The laboratory has a side-viewing probe prototype based on a design that replaces the sapphire ball lens with a half-ball lens backed by a mirror. Lens and mirror are configured at 45° providing collection capabilities similar to the front-viewing probe. The performance of the side-viewing probe is currently being tested. The side-viewing Raman probe can be used in conjunction with either a spring deployed or a vacuum-assisted biopsy needle. However, side-viewing measurements will necessitate a method for registering the tissue examined spectroscopically, which will lie somewhere in the middle of

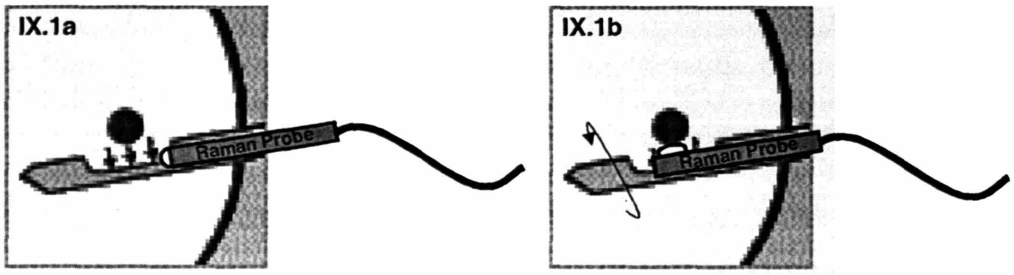


**Figure IX.1.** Transdermal needle measurements with the a) front-viewing and b) side-viewing Raman optical fiber probe.

the biopsy sample, with that examined by the pathologist. Ultimately, a side-viewing implementation is preferable as it allows spectral interrogation of a larger tissue volume. Successive measurements can be performed over 360° around the axis of the needle and depth information obtained as the needle is inserted or withdrawn.

Another potential implementation of Raman spectroscopy is in conjunction with ductoscopy. Fiberoptic ductoscopy adapts endoscopes developed to detect cancer in organs such as the colon, cervix, and esophagus to the study of breast ducts [Berna *et al.* 1991]. It is used to directly visualize the epithelial lining of the breast ducts. Because the majority of both benign and malignant breast disease originates in the epithelium, development of a minimally invasive procedure which can directly assess early epithelial changes has important applications to the detection and treatment of these conditions. Adding spectral information to the white light images recorded during ductoscopy provides the ability to detect pre-cancerous changes in the breast. However, a reduced diameter side-viewing probe, less than 1 mm in diameter, must be developed for incorporation in the ductoscope.

### IX. A. 2. Intra-Operative Margin Assessment

Our pilot study, presented in Chapter VII, is the first use of Raman spectroscopy to examine breast cancer *in vivo*. In addition to establishing Raman spectroscopy as a viable clinical technique, the study also revealed a new application for the approach. The results indicate that Raman spectroscopy has the potential to aid in intra-operative tumor resection. Accurate *in vivo* margin assessment techniques will reduce the recurrence rate of breast cancer following partial mastectomy surgeries and allow numerous re-excision surgeries to be avoided. They may also extend partial mastectomy procedures to those women who do not

harbor sufficiently small or localized breast cancers to qualify by current standards. However a larger data set with additional positive margin specimens is necessary to fully investigate the ability of Raman spectroscopy to aid in intra-operative tumor resection.

Further, for such an implementation to be successful, a thorough understanding of the lower detection limits of the approach is necessary. Experiments that determine the Raman scattering-cross sections of our model components as well as the volume of probed tissue which must harbor malignant cells to be correctly diagnosed are presented below. Future studies may be preformed with the existing Raman optical fiber probe or alternatively, an imaging device could be developed. An imaging modality, which samples a larger surface area, may be preferable for intra-operative margin assessment.

### IX. A. 3. Real-Time Analysis

We have recently developed and demonstrated real-time Raman diagnosis with our clinical instrumentation thus allowing its implementation in upcoming studies [Motz *et al.* in press]. Both clinical studies presented above should employ real-time analysis. This will provide a basis for testing the real-time system as well as feedback from clinicians for display improvement. The real-time Raman system also provides a means to target features of interest during data collection. For example, collecting data from microcalcifications will allow us to couple the results from our Raman microscopy studies of microcalcifications with our *ex vivo* diagnostic algorithm to create a powerful new tool for the diagnosis of benign and malignant breast lesions, as discussed in Chapter V. Ultimately, our real-time diagnostics may be used as a guide to biopsy or tumor resection.

### IX. A. 4. Diagnostic Algorithm Validation and Extension

Studies with a large patient pool are currently underway to further expand and validate our diagnostic algorithm. Preliminary results are presented in Chapter V. Upcoming studies will focus on analysis of the clinical data set containing Raman spectra of fresh tissues. The research serves to extend and confirm the results of our *ex vivo* studies on fresh-frozen tissue.

New diagnostic algorithms will be developed which incorporate additional model parameters, microcalcifications, and intensity information. These algorithms will be used to identify DCIS and possibly different manifestations of a single pathology. The incorporation of microcalcifications and intensity information are expected to strengthen the performance of our diagnostic algorithms. The Raman optical fiber probe provides a reproducible geometry for data collection, allowing examination of spectral data that has not been normalized. Ultimately, we strive to obtain quantitative information by incorporating the Raman scattering cross-sections of the model components into the data analysis routine. Studies to extract quantitative morphological information are discussed below.

## *IX. B. Spectral Model Refinement*

Although our current morphological spectral model of breast tissue provides excellent diagnostic information, there are several areas where the model can be improved.

### IX. B. 1. Quantitative Studies

Our current spectral model of breast only provides relatively quantitative morphological information. Thus, our present diagnostic schemes incorporate structural information and do not utilize intensity information. Although strict quantification is desirable, it is challenging to establish Raman scattering cross-sections for the components present in biological tissue.

However, with instrumental advances and a deeper understanding of the theoretical accuracy of our approach we have planned a study to make our morphological models quantitative.

In this study, data will be acquired from thin sections of fresh-frozen breast tissue using our Raman microscope. This data will be acquired using a low magnification objective to ensure that the spectroscopic signal is representative of the entire breast tissue section. Data will be acquired for long integration times conferring high SNR Raman data. Each thin section of breast tissue spectroscopically examined will then be reviewed by a pathologist. A combination of staining techniques and morphometric analysis will be used to obtain an estimate of the volume occupied by each morphological feature represented in our Raman spectral model. These volumes will then be correlated with the fit coefficients from the corresponding spectrum. Half of the data will be used to scale the model basis spectra such that the fit coefficients are representative of the pathologically determined volumes. The remaining data will be used for validation of the intensity corrected model. The prediction error equation, presented in Chapter IV, can be used to estimate reasonable fit coefficient errors. This study will also provide insight into the lower detection limits of the approach.

### IX. B. 2. Microscopy Studies

Studies to make our spectral model quantitative will also provide a basis for model refinement. I anticipate that some model elements, such as fat and microcalcifications, will quite accurately reflect their morphological volumes while others, such as epithelial cell cytoplasm and cholesterol-like, will not. This will allow us to identify basis spectra that are representative of a variety of morphological features thereby providing a basis for model refinement. Ensuing microscopy studies can be used to update the morphological spectral model. Such studies may begin with the examination of normal and cancerous cell lines. A

key signature of carcinoma is enlargement of cell nuclei, and thus a higher nuclear to cytoplasm (N/C) ratio than in benign conditions. Although we observe disease dependent trends in the spectroscopically obtained N/C parameter, these trends have not translated into diagnostic information. Microscopy studies of cell lines may shed light on ways to extract diagnostic information from the Raman spectrum that are related to tissue cellularity. Microscopy studies can also be used to examine changes in the stroma induced by disease. Ability to detect desmoplastic changes may be of particular importance as previous results indicate that Raman spectroscopy is more sensitive to stromal rather then cellular changes. As instrumentation and data analysis techniques improve, new components corresponding to smaller chemical variations will need to be included in our model.

### *IX. C. Combining Fluorescence, Reflectance and Raman Spectroscopies*

Preliminary results examining fluorescence and reflectance spectroscopies of breast tissues are very promising and convey that the techniques contain diagnostic information. However, a more rigorous understanding of the relationship between data analysis parameters and tissue morphology is necessary. Microscopy studies, similar to those used to develop the Raman spectral model, may provide a basis for understanding the fluorescence and reflectance signals obtained from breast tissue. As a starting point the fluorescence of adipocytes and epithelial cells should be examined. This will shed light on whether the fluorescence trends observed are the result of inaccurate basis spectra, additional tissue fluorophores, or unexpected pathology.

Future analysis will focus on correlating information obtained from FastEEM data and Raman spectroscopy. In order to successfully combine the optical modalities, a rigorous

understanding of the probe volume and sensitivity of each technique is necessary. As a starting point, species that both approaches are sensitive too, such as collagen and β-carotene, can be compared. Ultimately, if the results warrant it, all three modalities (fluorescence, reflectance and Raman) may be combined into a single spectroscopic technique for the diagnosis of breast cancer.

## *References*


Berna JD, Garcia-Medina V and Kuni CC (1991). "Ductoscopy: A New Technique for Ductal Exploration." Eur J Radiol **12**(2): 127-9.

Fornage BD, Sneige N, Ross MI, Mirza AN, Kuerer HM, Edeiken BS, Ames FC, Newman LA, Babiera GV and Singletary SE (2004). "Small (<= 2 cm) Breast Cancer Treated with US-Guided Radiofrequency Ablation: Feasibility Study." Radiology **231**(1): 215-224.

# Chapter X. Conclusion

## *X. A. Review of Goals and Accomplishments*

The overall goal of this thesis was to develop Raman spectroscopy into a clinical tool for breast cancer diagnosis. This process involved many steps, including model and diagnostic algorithm development in the laboratory with subsequent extension of these experimental approaches to a clinical environment. Each of these steps has been addressed in separate chapters, supported by sections that delve deeply into fundamental considerations important for attaining these goals.

The spectral model that was developed in Chapter IV provides a new approach to analyzing Raman spectra. A diagnostic algorithm which utilizes this spectral model, was developed in the laboratory with samples of fresh-frozen breast tissue. This diagnostic algorithm, that encompasses all data and classifies samples according to specific pathological diagnoses, results in high sensitivity and specificity. Based on the excellent results of these laboratory studies, we sought to employ Raman spectroscopy clinically. Studies were undertaken to validate our algorithm on a large data set of freshly excised tissue as well as demonstrate *in vivo* data acquisition.

The clinical studies translate Raman spectroscopy from a laboratory technique into a clinically useful tool. The first study, tests the diagnostic algorithm in a prospective manner on freshly excised tissue. Preliminary results are promising. In the second study, data were acquired *in vivo* during partial mastectomy surgeries. This is the first demonstration of *in*

*vivo* collection of Raman spectra of breast tissue. These advances culminated in an approach that was employed intra-operatively during partial mastectomy surgeries to accurately assess margin status.

## *X. B. Final Remarks*

The research presented in this thesis has brought the powerful analytical technique of Raman spectroscopy into a new regime where it can be employed clinically. We have demonstrated the use of Raman spectroscopy for the intra-operative identification of positive margins. Minor modifications to our Raman probe design will readily allow transdermal needle measurements, thereby opening additional clinical applications of Raman spectroscopy. The experiments and theory presented throughout this thesis demonstrate that Raman spectroscopy can be used to accurately diagnosis breast cancer and breast disease. Thus, Raman spectroscopy has the potential to play a diagnostic role in several aspects of breast cancer evaluation and treatment.